Novel Asymmetric Atomic Sites Semiconductor Catalysts for Enhanced Solar Water Splitting

Thesis submitted in partial fulfillment

for the Award of Degree

Doctor of Philosophy

by

Dileep Kumar

RAJIV GANDHI INSTITUTE OF PETROLEUM TECHNOLOGY

JAIS, -229304

21BS0015 **2026**

CERTIFICATE

It is certified that the work contained in the thesis titled **"*Novel Asymmetric Atomic Sites Semiconductor Catalysts for Enhanced Solar Water Splitting*"** by "Dileep Kumar" has been carried out under my supervision and this work has not been submitted elsewhere for a degree.

It is further certified that the student has fulfilled all the requirements of Comprehensive, Candidacy, and SOTA.

Supervisor
Dr. Vipin Amoli

DECLARATION BY THE CANDIDATE

I, "Dileep Kumar", certify that the work embodied in this thesis is my own bona fide work and carried out by me under the supervision of **"Dr. Vipin Amoli"** from "August 2021" to "June 2026", at Rajiv Gandhi Institute of Petroleum Technology, Jais.

The matter embodied in this thesis has not been submitted for the award of any other degree. I declare that I have faithfully acknowledged and given credits to the research workers wherever their works have been cited in my work in this thesis. I further declare that I have not willfully copied any other's work, paragraphs, text, data, results, etc., reported in journals, books, magazines, reports dissertations, thesis, etc., or available at websites and have not included them in this thesis and have not cited as my own work.

Place: RGIPT, Jais, Amethi
Date:

Dileep Kumar
Roll No.-21BS0015

CERTIFICATE BY THE SUPERVISOR(S)

It is certified that the above statement made by the student is correct to the best of my knowledge.

Dr. Vipin Amoli
(Supervisor)

Prof. Atul Sharma
(Head of Department, E&HS)

CERTIFICATE

Certified that the work contained in the thesis titled **"*Novel Asymmetric Atomic Sites Semiconductor Catalysts for Enhanced Solar Water Splitting*"** by "Dileep Kumar" has been carried out under my supervision. It is also certified that he fulfilled the mandatory requirement of TWO quality publications arose out of his thesis work.
It is further certified that the two publications (copies enclosed) of the aforesaid Mr. Dileep Kumar have been published in the Journals indexed by —

(a) SCI

(b) SCI Extended

(c) SCOPUS

(Supervisor)
Dr. Vipin Amoli

(Convenor, DPGC)
Dr. Omvir Singh

COPYRIGHT TRANSFER CERTIFICATE

Title of the thesis: "Novel Asymmetric Atomic Sites Semiconductor Catalysts for Enhanced Solar Water Splitting"
Name of the student: Dileep Kumar

Copyright Transfer

The undersigned hereby assigns to the Rajiv Gandhi Institute of Petroleum Technology, Jais all rights under copyright that may exist in and for the above thesis submitted for the award of the" Doctor of Philosophy".

Place: RGIPT, Jais, Amethi
Date:

Dileep Kumar
Roll No. 21BS0015

Dedicated to my parents & nature

Acknowledgement

Submitting my doctoral thesis fills my heart with profound happiness. Before doing so, I pause to offer my sincere gratitude to “NATURE” for gifting me with all the right circumstances that allowed me to walk this decisive path in life with grace and ease.

First and foremost, I would like to express my sincere gratitude to Rajiv Gandhi Institute of Petroleum Technology (RGIPT), Jais, Amethi, for providing me with the Institute Fellowship throughout the duration of my doctoral research.

In particular, I express my deepest gratitude to Dr. Vipin Amoli for his constant guidance, encouragement, and support throughout my Ph.D. journey. I am deeply grateful for his numerous helpful discussions and insights that extended well beyond the academic journey. I will always cherish his words, 'We need to dig pits every day...' " I will never forget his dedication towards the perfection of work like writing, figure improvement, critical & logical thinking that will always encourage me.

I would like to express my sincere gratitude to the Head of the Department, DPGC, and the E&HS office for their continuous support and assistance throughout my research journey.

I would like to express my gratitude to my RPEC committee members, Dr. Karan Malik and Dr. Tathamay Basu, for their valuable suggestions and insightful feedback. I am sincerely grateful to Dr. Shikha Singh and Dr. Milan Kumar at RGIPT for generously providing the experimental facilities essential to this work.

I gratefully acknowledge the Central Instrumentation Facility (CIF), RGIPT, for providing the necessary material characterization facilities that greatly contributed to this research.

I would also like to extend my sincere thanks to Prof. Anil Kumar Sinha (Research Collaborator), CSIR–Indian Institute of Petroleum, Dehradun, India, for providing computational facilities for DFT calculations and for his valuable support in the photocatalytic experiments. I would also like to express my sincere gratitude to Prof. Asim Bhaumik (Research Collaborator), Indian Association for the Cultivation of Science (IACS), Kolkata, India, for high-resolution transmission electron microscopy (HRTEM) analysis of the samples.

I gratefully acknowledge Raja Ramanna Centre for Advanced Technology (RRCAT), Indore for providing access to beamline experimental facilities. I also acknowledge the Central Research Facility, Indian Institute of Technology (IIT), Delhi for providing access to in situ EPR measurements. Furthermore, I sincerely acknowledge the Institute of Nano Science and Technology (INST), Chandigarh for their valuable assistance in time-resolved photoluminescence (TRPL) characterizations.

Finally, I would like to thank my lab members: Shubham, Hemant, Amit Verma, Siddhi Agrawal, and Preena Tripathi for their continuous support, cooperation, and the memorable moments shared throughout this journey.

I am forever grateful to my parents, my wife, and my beloved daughter Nandita Chaudhary, whose enduring love, unwavering confidence, and constant support have driven me forward in both my studies and career. Their warmth, affection, and encouragement have always filled me with peace and positivity.

Contents

List of Abbreviations

SA	Single-Atom
SAC	Single-Atom Catalyst
AAS	Asymmetric Atomic Site
AASC	Asymmetric Atomic Sites Catalyst
AASSC	Asymmetric Atomic Site Semiconductor Catalyst
HAAS	Highly Asymmetric Atomic Sites
HAASC	Highly Asymmetric Atomic Sites Catalyst
FT	Faceted TiO_2
PV	Solar Photovoltaic
SWS	Solar Water Splitting
PC	Photocatalytic
PEC	Photoelectrochemical
HER	Hydrogen Evolution Reaction
OER	Oxygen Evolution Reaction
STH	Solar-To-Hydrogen
VB	Valence Band
CB	Conduction Band
CBM	Conduction Band Minimum
VBM	Valence Band Maximum
MOFs	Metal–Organic Frameworks
GaN	Gallium Nitride
CNTs	Carbon Nanotubes
CQDs	Carbon Quantum Dots
CTAB	Cetyltrimethylammonium Bromide
PVP	Polyvinylpyrrolidone
DFT	Density Functional Theory
MD	Molecular Dynamics

List of Figures

List of Tables

Scope of Thesis

The rapid increase in greenhouse gas emissions due to extensive fossil fuel consumption has created an urgent demand for sustainable and carbon-neutral energy technologies. Among the available alternatives, solar energy stands out as an abundant and renewable resource. In this context, solar-driven hydrogen production through photocatalytic and photoelectrochemical (PEC) water splitting has emerged as promising strategies. However, their large-scale implementation remains constrained by the lack of efficient catalysts, primarily due to poor visible light response, unfavorable band structures, rapid recombination of photogenerated charge carriers, and sluggish surface reaction kinetics.

Single-atom catalysts (SACs) involving metal single atoms are trapped on semiconductor supports, have demonstrated maximum atomic utilization efficiency and great potential in catalytic activity. The stabilization of single atoms requires specific anchoring sites that can be surface defects, unsaturated atoms, and any heteroatoms that stabilize single atoms through metal-support interactions. Recently, defect-rich metal oxides have been identified as more suitable platforms in which oxygen or metal vacancies act as trap centers for single atoms. In particular, asymmetric atomic sites (AAS), generally expressed as M_{SA}-O_v-M_2 (where M_{SA} denotes the trapped metal single atom, O_v is an oxygen vacancy, and M_2 represents the semiconductor support), are identified as the most preferable active catalytic sites for catalytic activity. However, the generation of defect-rich supports involves undesired consumption of H_2 gas and/or H_2/Ar gas and energy-intensive processes rendering them impractical and uneconomic. Moreover, achieving precise control over AAS remains a significant challenge with current capabilities in infancy. To harness the intriguing chemistry of AASC for photocatalytic H_2 production, judicious selection of support is essential while ensuring precise defect control. Furthermore, this approach should aim to achieve both high performance and cost-effectiveness, which are the ultimate goals in photocatalyst design for H_2 production.

This thesis focuses on the development of asymmetric atomic site catalysts (AASCs) for efficient photocatalytic hydrogen production using faceted semiconductor nanostructures as

support materials. Conventional approaches for constructing AASCs often rely on defect engineering to create anchoring sites for isolated metal atoms; however, achieving precise defect control remains challenging. To address this limitation, this work explores faceted nanostructured semiconductors as alternative platforms, leveraging their intrinsically under-coordinated surface atoms as natural anchoring sites for single metal atoms.

Among various semiconductor materials, anatase TiO_2 was selected as the model support owing to its excellent photocatalytic properties, chemical stability, abundance, and tunable crystal facets. TiO_2 can be synthesized with different exposed facets, including (101), (010), (001), and (111), each possessing distinct atomic arrangements and surface characteristics. Notably, the anatase TiO_2 (111) facet exhibits a high density of under-coordinated titanium atoms compared with other commonly exposed facets. The increased degree of under-coordination results in higher surface energy and stronger interactions with adsorbed species, making the (111) facet particularly suitable for trapping and stabilizing isolated metal atoms. These unique structural features motivated the selection of the TiO_2 (111) facet as the support platform for constructing AASCs in this study. Copper (Cu) was chosen as the dopant metal due to its variable oxidation states (Cu^0, Cu^+, and Cu^{2+}), reversible redox behavior, earth abundance, and tunable electronic and optical properties. These characteristics make Cu an attractive candidate for engineering asymmetric atomic sites and enhancing photocatalytic activity. The research therefore investigates the rational design of Cu-based AASCs through the incorporation of isolated Cu atoms onto faceted TiO_2 nanostructures, thereby combining the advantages of crystal-facet engineering and single-atom catalysis within a single material system. The catalysts were synthesized using a simple, scalable hydrothermal approach and comprehensively characterized using advanced state-of-the-art experimental techniques to determine their structural, electronic, optical, and photocatalytic properties. Experimental observations were further complemented by

theoretical calculations to establish the fundamental structure–activity relationships governing photocatalytic hydrogen evolution. The performance of the developed catalysts was systematically evaluated and benchmarked against contemporary state-of-the-art photocatalytic systems reported in the literature.

Overall, this thesis aims to provide fundamental insights into the role of asymmetric atomic sites in solar-driven hydrogen generation while demonstrating a practical strategy for designing efficient, stable, and cost-effective photocatalysts. The findings contribute to both the scientific understanding of AASCs and the advancement of next-generation materials for sustainable solar fuel production.

Chapter: 1

Introduction

This chapter introduces the fundamental principles of solar water splitting, including both photocatalytic and PEC approaches. It discusses the working mechanisms, commonly used catalysts, and their inherent limitations. The chapter further reviews recent advancements in SACs, asymmetric atomic sites, and facet engineering. Special emphasis is placed on TiO_2-based systems, including facet-dependent properties and strategies for stabilizing single atoms.

1.1. Introduction

The global energy landscape is under unprecedented pressure due to rapidly rising energy demand and the continued depletion of fossil fuel reserves. As a result, modern society is facing escalating challenges, including energy insecurity, fluctuating fuel prices, and geopolitical tensions linked to resource scarcity **[1, 2]**.

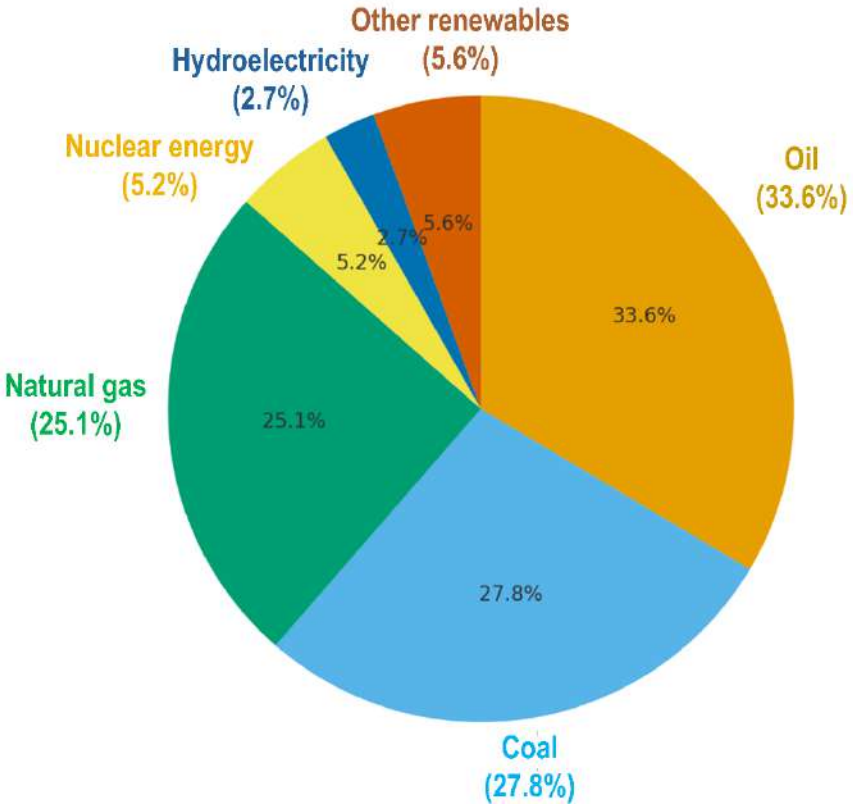

Figure 1.1. Global energy sources by statistical review of World Energy in 2025.**[2]**

Even today, a significant majority of the world's energy supply relies on fossil fuel combustion, which releases vast quantities of greenhouse gases, primarily CO_2 and NO_2, into the atmosphere. The Energy Institute published the 75th edition of the Statistical Review of World Energy in 2025, which ranks various energy sources by their CO_2 emissions (**Figure 1.1**). The report indicates that the global energy demand increased by approximately 2%, with fossil fuels accounting for about 87% of the total energy consumption in 2024. In addition, electricity demand continues to outpace total energy demand **[3]**. These emissions are the driving force behind climate change, rising global temperatures, and a cascade of

environmental issues, including air pollution, Weather-related disasters, sea level rise, and biodiversity loss. As the negative impacts of fossil fuel dependency intensify, there is now an urgent, worldwide impetus to transition to clean, sustainable energy solutions to ensure global energy security and mitigate climate change **[3]**. In this context, renewable energy technologies such as solar, wind, and hydroelectric power have gained prominence, yet the intermittent nature of solar and wind energy presents challenges for consistent supply and integration with existing energy infrastructure **[4].** Among the various renewable energy options, hydroelectric and wind power are constrained by geographic and environmental factors. The generation of hydroelectric power requires specific topographical conditions and an adequate, continuous water source **[5]**. Similarly, wind energy production depends on favorable wind regimes, which are typically found in open, elevated, or coastal areas. Sparsely populated regions are preferred for safety and to minimize noise disturbances **[6]**. In contrast, solar energy presents the greatest potential to meet future global energy demand, owing to its universal availability, ease of scalability, and continuous technological advancements that have improved both efficiency and cost-effectiveness. Consequently, solar energy stands out as a vital component in the global transition toward sustainable and low-carbon energy systems **[7]**.

1.1.1. Solar energy: A clean and abundant source of energy

The Sun is the largest and most abundant renewable energy source available to humanity, providing energy freely and continuously. The solar energy incident on Earth is enormous, approximately 1.25×10^6 TW, which is nearly 10,000 times greater than the current global energy consumption **[7]**. In comparison, the average worldwide energy consumption rate was 13 TW in 2001 and is projected to reach 28 TW by 2050. In 2002, the estimated global fossil fuel reserves were expected to last about 40 years for oil, 60 years for natural gas, and 200 years for coal, highlighting the urgent need for alternative sustainable energy sources **[8]**. It

would be sufficient to meet the world's current energy demand. Solar energy refers to the radiant light and heat emitted by the Sun, which can be harnessed through various advanced technologies, including solar heating systems, photovoltaic cells, solar thermal systems, and artificial photosynthesis. Among these, solar photovoltaics and solar water splitting are considered the most efficient and environmentally friendly approaches for utilizing solar energy **[9, 10]**.

Solar photovoltaic (PV) technology is a renewable energy approach that directly converts sunlight into electricity using solar panels coated with semiconductor materials via the photovoltaic effect **[11]**, as shown in **the Figure 1.2**.

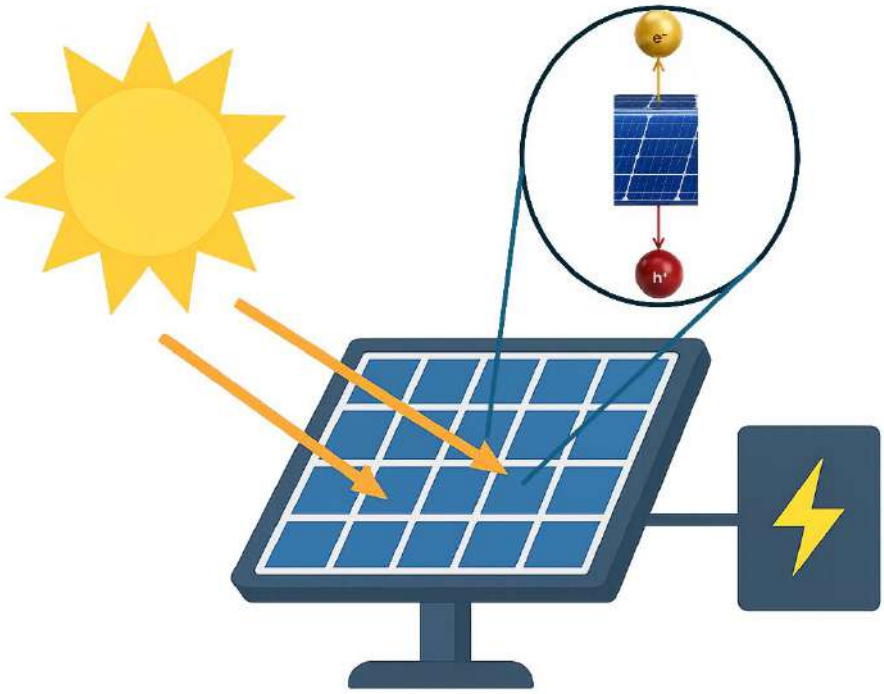

Figure 1.2. Schematic representation of the solar photovoltaic (PV) technology: conversion of sunlight into electricity using semiconductor materials through the photoelectric effect.

When sunlight strikes the semiconductor surface, photons generate electron–hole pairs that create an electric current. Commonly used semiconductor materials include silicon, cadmium telluride (CdTe), and perovskite-based compounds **[12]**. PV systems can be installed on various scales from rooftops to large solar farms and offer advantages such as low

maintenance, long operational life (20–30 years), and decentralized energy generation that enhances energy independence **[12]**. Continuous improvements in materials and device design, including perovskite and tandem solar cells, are further increasing efficiency and lowering costs **[13].** However, PV technology still faces challenges such as limited sunlight availability, reliance on energy storage systems for uninterrupted power supply, high initial installation costs, limited conversion efficiency, and concerns about panel recycling and disposal.

Solar photocatalysis, on the other hand, involves using semiconductor materials as photocatalysts to harness solar energy for driving chemical reactions such as CO_2 reduction, water splitting, natural water purification, and pollutant degradation **[14, 15]**. Among these, solar water splitting (SWS) is particularly promising because it enables the direct conversion of sunlight into hydrogen and oxygen, providing a clean and sustainable route for future energy generation **[16]** as illustrate in the **Figure 1.3**. Unlike photovoltaic (PV) systems, which require batteries with limited capacity and lifespan to store electricity, solar water splitting (SWS) produces hydrogen that can be safely stored for long periods without energy loss **[17]**.

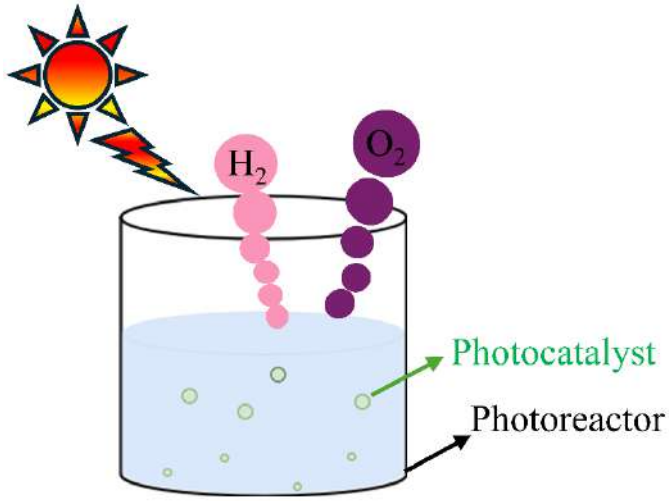

Figure 1.3. Schematic illustration of solar water splitting process using a powdered catalyst.

This enables reliable, long-term energy storage and on-demand use of hydrogen, supporting decentralized production without the need for complex and costly electrical storage infrastructure **[18]**. Hence, SWS offers a more flexible and scalable storage solution compared to conventional PV-battery systems, especially for large-scale and long-term energy needs. The hydrogen generated can be used for power generation, fuel cell vehicles, and industrial applications. Hydrogen gas (H_2) is a clean alternative to fossil fuels. It can be burned to produce heat and steam, used in modified internal combustion engines, or serve as an energy carrier in fuel cells, where the only by-product is water. In fact, hydrogen fuel cells are already in use in certain vehicles, such as those operating in California **[19].**

1.1.2. Solar Water Splitting

Solar water splitting is a photocatalytic process that utilizes semiconductor materials as catalysts to decompose water (H_2O) molecules into hydrogen (H_2) and oxygen (O_2) gases under solar irradiation. The process is typically carried out by dispersing semiconductor catalysts in water within a photoreactor and exposing the suspension to simulated solar light, as schematically illustrated in the **Figure 1.4**. The overall process involves three fundamental steps: (i) absorption of sunlight by the semiconductor catalyst, resulting in the excitation of electrons from the valence band (VB) to the conduction band (CB) and the generating electron–hole (e^-/h^+) pairs; (ii) separation and migration of these photogenerated charge carriers to the surface of the catalyst; and (iii) participation of electrons and holes in redox reactions with the adsorbed water molecules, resulting in the reduction of protons to H_2 and the oxidation of water to O_2 **[20].** The overall mechanism can be represented by the following set of equations.

$$H_2O + 2h^+ \rightarrow 2H^+ + \frac{1}{2}O_2 \qquad \text{(Oxidation)} \qquad (1.1)$$

$$2H^+ + 2e^- \rightarrow H_2 \qquad \text{(Reduction)} \qquad (1.2)$$

$$2H_2O + 4h\upsilon \rightarrow 2H_2 + O_2 \qquad \text{(Overall reaction)} \qquad (1.3)$$

The total efficiency of the photocatalytic water-splitting process is determined by the efficiencies of the individual steps involved.

$$\phi_{total} = \phi_{absorption} \times \phi_{seperation} \times \phi_{reaction} \quad (1.4)$$

$\phi_{absorption}$ denotes the photon absorption efficiency, defined as the number of e^-/h^+ generated by the incident photon flux; $\phi_{seperation}$ represents the fraction of generated e^-/h^+ pairs that migrate to the photocatalyst surface; $\phi_{reaction}$ represents the fraction of migrated e^-/h^+ pairs that participate in reactions with H_2O molecules.

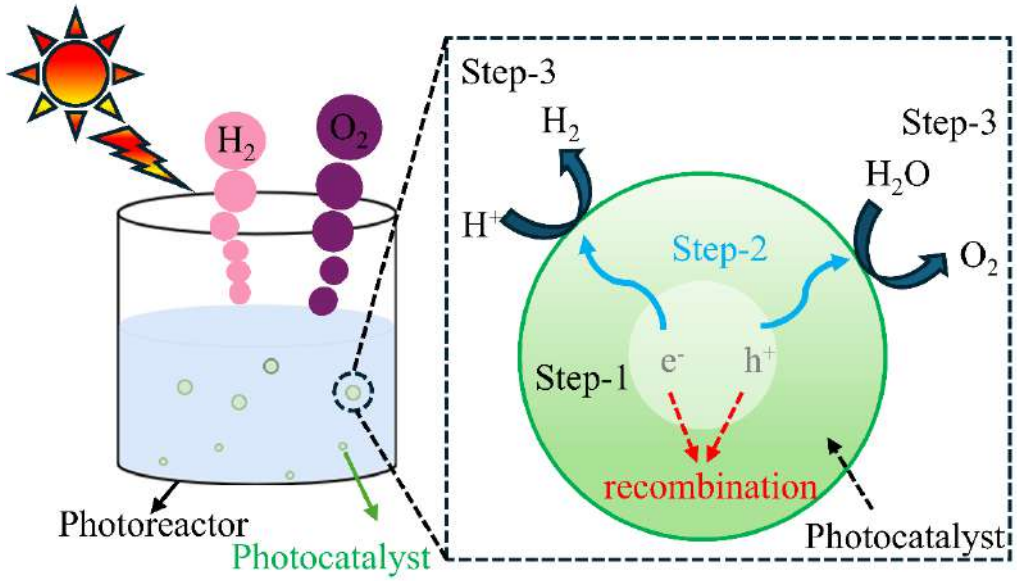

Figure 1.4. Schematic representation of the photocatalytic water-splitting mechanism. The enlarged view illustrates the generation, recombination, and transfer of photogenerated charge carriers.

To achieve overall solar water splitting, a semiconductor catalyst must satisfy several critical requirements: (i) it should possess an appropriate band gap to absorb incident solar radiation effectively; (ii) the conduction band minimum (CBM) should be more negative than the reduction potential of H^+/H_2 (0 V vs. the Normal Hydrogen Electrode, NHE, at pH 0), while the valence band maximum (VBM) must be more positive than the oxidation potential of H_2O/O_2 (+1.23 V vs. NHE at pH 0), as illustrated in **Figure 1.5**. In addition, the catalyst should exhibit excellent physicochemical stability under both oxidative and reductive

environments. An ideal photocatalyst is expected to efficiently harvest solar energy, facilitate rapid charge separation and migration, support surface redox reactions, and maintain long-term structural integrity. Thermodynamically, overall solar water splitting is an uphill, non-spontaneous process with a large positive Gibbs free energy change ($\Delta G° = 238\ kJ \cdot mol^{-1}$ or 1.23 eV), and the energy required to drive this reaction is supplied by solar irradiation **[21].**

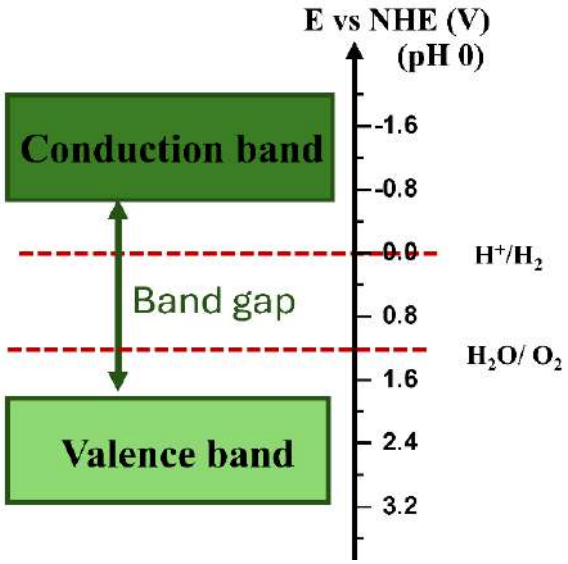

Figure 1.5. Energy-level diagram illustrating the positions of the conduction band (CB) and valence band (VB) of a semiconductor photocatalyst relative to the H^+/H_2 reduction potential and H_2O/O_2 oxidation on the NHE scale.

Therefore, the semiconductor band gap should be > 1.23 eV theoretically and > 2.0 eV practically to overcome thermodynamic and kinetic losses **[22].**

Photoelectrochemical (PEC) water splitting combines solar and electrochemical processes in one device to split water into hydrogen and oxygen under illumination **[23]**. It uses a semiconductor photoelectrode, a counter electrode, and a reference electrode immersed in an electrolyte. When sunlight hits on the surface of the semiconductor electrode with enough energy, it generates electron-hole pairs that are separated by an electric field at the semiconductor-electrolyte interface. These charge carriers drive electrochemical reactions, either the hydrogen evolution reaction (HER) or oxygen evolution reaction (OER), at the

semiconductor electrode, which acts as a photocathode or photoanode, respectively **[24].** The opposite half-reaction occurs at the counter electrode, often in a separate chamber to keep hydrogen and oxygen gases apart. Sometimes, a small external voltage, called "small biasing," is applied to assist the reaction when sunlight energy alone is insufficient, improving efficiency by helping charge separation and reaction kinetics **(Figure 1.6).** Materials commonly used for fabricating photoelectrodes in photoelectrochemical (PEC) water splitting include TiO_2, Fe_2O_3, WO_3, $BiVO_4$, Ta_3N_5, and emerging materials such as perovskite oxynitrides, sulfides, and metal–organic frameworks (MOFs) **[25]**.

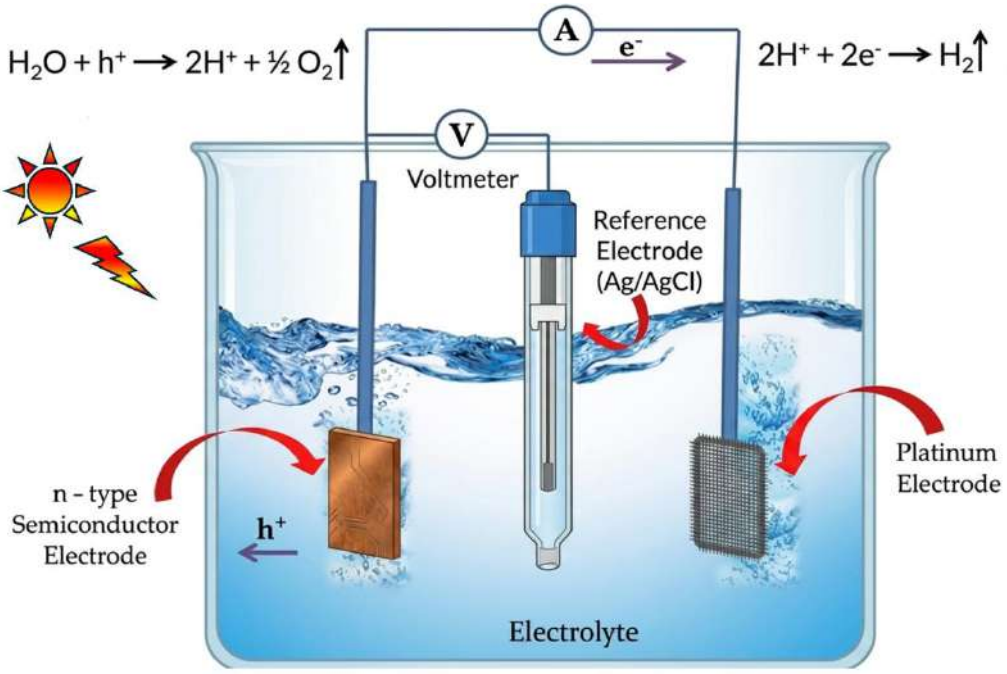

Figure 1.6. Schematic representation of the PEC water-splitting system, illustrating the key components and the underlying mechanism of H_2 and O_2 generation.

To boost interfacial charge transfer and catalytic efficiency, co-catalysts like Pt, RuO_2, NiO_x, or Co-Pi are frequently integrated. Additional enhancement approaches include doping to modify electronic properties, creating heterojunctions to facilitate charge separation, nano structuring to increase surface area and light absorption, and surface passivation to reduce

charge recombination **[26, 27]**. These combined strategies significantly improve charge carrier transport, reduce recombination losses, and elevate the overall catalytic performance of the photoelectrodes for efficient solar water splitting.

Photoelectrochemical (PEC) water splitting systems, despite notable progress, continue to face several critical challenges such as photoelectrode degradation due to corrosion, high fabrication costs, and complex device architecture **[28]**. Both photocatalytic (PC) and PEC approaches utilize semiconductor materials to absorb sunlight and initiate the redox reactions required for water splitting; however, they differ significantly in their structural configuration, charge carrier transport mechanisms, and practical applicability **[29]**.

PEC systems provide superior control over charge separation, interfacial reaction kinetics, and overall efficiency through the use of an externally applied bias voltage. This capability makes them particularly valuable for studying fundamental mechanisms and conducting controlled laboratory-scale investigations **[30, 31]**. Nevertheless, the intricate fabrication process, dependence on costly electrode materials, and limited operational stability restrict their suitability for large-scale implementation **[32, 33]**.

In contrast, photocatalytic water splitting offers a simpler, more economical, and scalable approach. It employs dispersed semiconductor powder catalysts suspended in an aqueous medium, eliminating the need for external bias, complex circuitry, or electrode assembly. This simplicity enables easy deployment in large-area solar reactors **[20, 33]**. Furthermore, recent advancements in high-index faceted nanostructures **[34]**, single-atom catalysts **[35]**, heterojunction engineering **[36]**, and co-catalyst integration **[37]** have greatly enhanced light absorption, charge separation efficiency, and surface reaction kinetics in photocatalytic systems.

In conclusion, while PEC systems are indispensable for gaining mechanistic insights and achieving high efficiencies under controlled conditions, photocatalytic water splitting

presents a more promising route for sustainable and large-scale solar hydrogen generation. Its inherently simple configuration, scalability, and compatibility with natural sunlight position it as a leading candidate for the development of future renewable hydrogen technologies.

1.2. Semiconductor Materials for Solar Water Splitting

Solar water splitting is recognized as an environmentally friendly approach for generating hydrogen energy, which is crucial for the sustainable development of the global economy and society. This process enables the direct conversion of solar energy into hydrogen, a clean and renewable fuel, thereby reducing dependence on fossil fuels and minimizing greenhouse gas emissions **[38]**. Efficient hydrogen production via solar water splitting relies heavily on the use of high-performance semiconductor materials as photocatalysts to achieve optimal photocatalytic activity and energy conversion efficiency **[39]**.

In 1972, Fujishima and Honda first reported the electrochemical splitting of water using titanium dioxide (TiO_2) as a photoanode in a photoelectrochemical (PEC) cell **[23]**. This pioneering work laid the foundation for the field of semiconductor-based photocatalysis and inspired extensive research into diverse semiconductor materials, including metal oxides (e.g., ZnO, TiO_2, ZrO_2, SnO_2, WO_3, Fe_2O_3, RuO_2), metal sulfides (e.g., CdS, ZnS, $ZnIn_2S_4$), metal nitrides (e.g., GaN, Ta_3N_5), oxynitrides (e.g., $BaTaO_2N$), metal phosphides, carbon-based materials (e.g., g-C_3N_4, graphene, carbon nanotubes, carbon quantum dots), organic semiconductors, and perovskite-type compounds **[40-42]**.

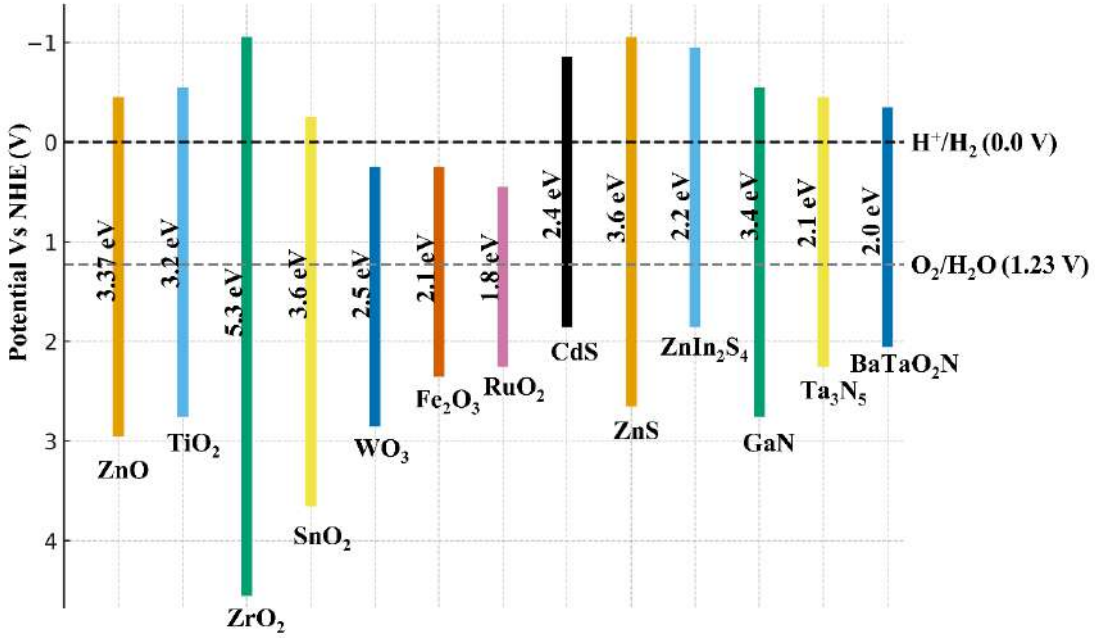

Figure 1.7. Positions of conduction and valence band edges of various semiconductor photocatalysts relative to water splitting redox potentials.**[22]**

An effective photocatalyst including metal oxides, metal sulfides, and metal nitrides must meet two basic thermodynamic criteria: a suitable band gap and suitable band edge positions. The band gap filters the part of the solar spectrum that can be absorbed. A too wide value limits the absorption only to the ultraviolet light and an excessively narrow band gap reduces the thermodynamic driving force for the redox reactions. An optimum band gap is generally considered to be around 1.8-2.2 eV, which is a good compromise between harvesting visible light and providing sufficient reaction feasibility. The band edge location is also important. In the case of water splitting the conduction band minimum must be at a more negative potential than the $2H^+ + 2e^- \rightarrow H_2$ reduction level (0 V vs. NHE) and the valence band maximum must be more positive than the $H_2O + 2h^+ \rightarrow 2H^+ + \frac{1}{2} O_2$ oxidation potential (+1.23 V vs. NHE) as shown in the **Figure 1.7.** This alignment provides the electrochemical energy required for photogenerated electrons and holes to drive both half-reactions. The material that satisfies both criteria simultaneously provides a basis for practical photocatalytical application.

1.2.1. Metal Oxides

Metal oxides have been widely explored as photocatalysts for solar water splitting owing to their non-toxicity, chemical stability, earth abundance, and suitable band structures **[42]**. Titanium dioxide (TiO_2); the anatase phase of TiO_2 has been the most extensively investigated photocatalyst since the 1970s **[43]**. Despite its excellent stability and favorable band edge positions, TiO_2 suffers from a wide bandgap (~3.2 eV), restricting its absorption to the ultraviolet region (only ~4% of the solar spectrum). Moreover, rapid electron–hole recombination limits its solar-to-hydrogen (STH) efficiency [10]. TiO_2 is widely used as a sensor because surface reactions at defects modulate its resistance. Its high stability and tunable surface properties make it effective despite its wide band gap **[44].** Hematite (α-Fe_2O_3); Hematite is an N-type semiconductor with a narrower bandgap (~2.1 eV), making it responsive to visible light. However, its practical performance is constrained by short hole diffusion lengths (2–4 nm), poor conductivity, photo corrosion, and high recombination rates **[45]**. Bismuth Vanadate ($BiVO_4$); $BiVO_4$ is considered one of the most promising metal oxides for photoanodic water oxidation, with a narrow bandgap (~2.4 eV) and visible-light activity. Its primary drawback is poor charge carrier mobility, which researchers have addressed through strategies such as heterojunction formation and doping **[46, 47]**. Tungsten Trioxide (WO_3); WO_3 exhibits a moderate bandgap (2.6–2.8 eV), allowing partial visible light absorption and excellent chemical stability in acidic conditions. However, its limited absorption range and instability in neutral or basic electrolytes remain challenges **[48]**.

There are the different types of strategies to enhance photocatalytic efficiency including: (i) Doping: Introducing metal (e.g., Fe, Ni, Au, Ag) or non-metal dopants (e.g., N, C, S) to create mid-gap states and extend light absorption into the visible range **[49]**; (ii) Nanostructuring: Designing nanorods, nanowires, and nanosheets to increase active surface area and shorten charge transport paths; and (iii) Heterojunction Formation: Combining

semiconductors (e.g., TiO_2/WO_3, $Fe_2O_3/BiVO_4$) to promote charge separation and broaden light absorption **[50,51]**.

1.2.2. Metal Sulfides

Metal sulfides have suitable band edge positions, tunable photoelectrochemical properties, and narrow band gaps, making them ideal for photocatalytic hydrogen production and photoelectrochemical applications. However, they often suffer from photocorrosion in aqueous environments. Cadmium Sulfide (CdS); CdS has a smaller bandgap of ~2.4 eV than metal oxide semiconductor and exhibits good visible light absorption but is prone to photocorrosion due to oxidation of sulfide ions by photogenerated holes **[52]**. Yang et al. synthesized a TiO_2-CdS nanocomposite, achieving a hydrogen generation rate of 954 μmol g^{-1} h^{-1}, 1.4 and 1.7 times higher than pure CdS and TiO_2, respectively **[53].** Zinc Sulfide (ZnS); Although ZnS is non-toxic and abundant, its wide bandgap (~3.6 eV) limits its absorption to the UV region, making it less suitable for solar applications unless modified **[54]**. Zinc Indium Sulfide ($ZnIn_2S_4$); This ternary sulfide shows improved stability compared to binary sulfides but still suffers from high charge carrier recombination **[55].**

1.2.3 Metal Nitrides and Oxynitrides

Metal nitrides and oxynitrides exhibit narrow bandgaps and suitable band positions for visible-light-driven water splitting. However, they often have high defect densities and limited stability under oxidative conditions. Gallium Nitride (GaN); GaN and its doped variants possess tunable bandgaps but are expensive to fabricate, which limits large-scale applications. Tantalum Nitride (Ta_3N_5); With a bandgap of ~2.1 eV, Ta_3N_5 shows excellent visible light activity but faces challenges such as oxidation-induced degradation. Barium Tantalum Oxynitride ($BaTaO_2N$); $BaTaO_2N$ has a suitable bandgap (~1.9 eV) for visible light absorption and can perform overall water splitting via a single-step photoexcitation, though

its quantum efficiency remains low **[56]**.

1.2.4. Carbon-Based Semiconductors

Carbon-based materials are increasingly employed as supports, co-catalysts, or hybrid components due to their excellent conductivity and tunable band structures. Graphitic Carbon Nitride (g-C_3N_4); A metal-free polymeric semiconductor with a bandgap of ~2.7 eV, g-C_3N_4 exhibits visible light absorption but suffers from high charge recombination rates **[57].** Graphene and Carbon Nanotubes (CNTs); Graphene provides a high surface area and superior electron mobility, serving as an effective electron acceptor when combined with semiconductors. CNTs enhance charge transport, facilitating efficient electron–hole separation **[58].** Carbon Quantum Dots (CQDs); CQDs act as photosensitizers and electron mediators, improving visible light absorption and charge carrier dynamics in hybrid photocatalysts.

Although metal sulfides and nitrides offer narrower band gaps and strong visible-light absorption, metal oxides continue to dominate photocatalytic research because of their exceptional chemical stability, environmental benignity, low cost, and structural versatility. A comparative summary of metal oxides, sulfides, and nitrides is presented in the **Table 1**. Their physicochemical properties can be effectively tuned through doping, defect engineering, facet exposure control, and heterojunction construction, which improve charge separation and extend light absorption into the visible region. Among various oxides, TiO_2, Fe_2O_3, and WO_3 are widely explored for photoelectrochemical and photocatalytic hydrogen generation due to their robustness under oxidative conditions. In particular, TiO_2 remains the benchmark photocatalyst owing to its high stability, abundance, and well-aligned band edges suitable for water splitting. Nevertheless, its wide band gap and rapid electron–hole recombination restrict visible-light activity and reduce efficiency. Therefore, extensive efforts have been directed toward band-gap narrowing and charge separation enhancement through

metal or non-metal doping, defect modulation, and the design of asymmetric atomic sites or heterostructures, significantly improving its photocatalytic performance under solar illumination **[20, 59].**

Table 1 Comparison of the band gap energies of various semiconductor materials.

Property	**Metal Oxides**	**Metal Sulfides**	**Metal Nitrides**
Band gap	3.0–3.5 eV (wide, but tunable via doping)	1.0–2.5 eV (narrow)	1.5–2.5 eV
Light absorption	UV, extendable to visible by modification	Visible	Visible–IR
Stability	Excellent (highly durable)	Poor (photocorrosion)	Moderate (oxidation sensitive)
Environmental safety	Non-toxic, abundant	Often toxic	Moderate
Scalability	High (cost-effective synthesis)	Limited	Limited

1.3. Material Engineering Strategies for Performance Enhancement

To achieve efficient solar water splitting, various material engineering strategies have been developed to optimize the structural, electronic, and interfacial properties of semiconductor photocatalysts. Among these, single-atom catalysts (SACs), defect/vacancy engineering, heterojunctions and Z-scheme structures, and facet engineering have emerged as some of the most promising approaches for enhancing photocatalytic activity, stability, and charge separation efficiency.

1.3.1. Defect/Vacancy Engineering

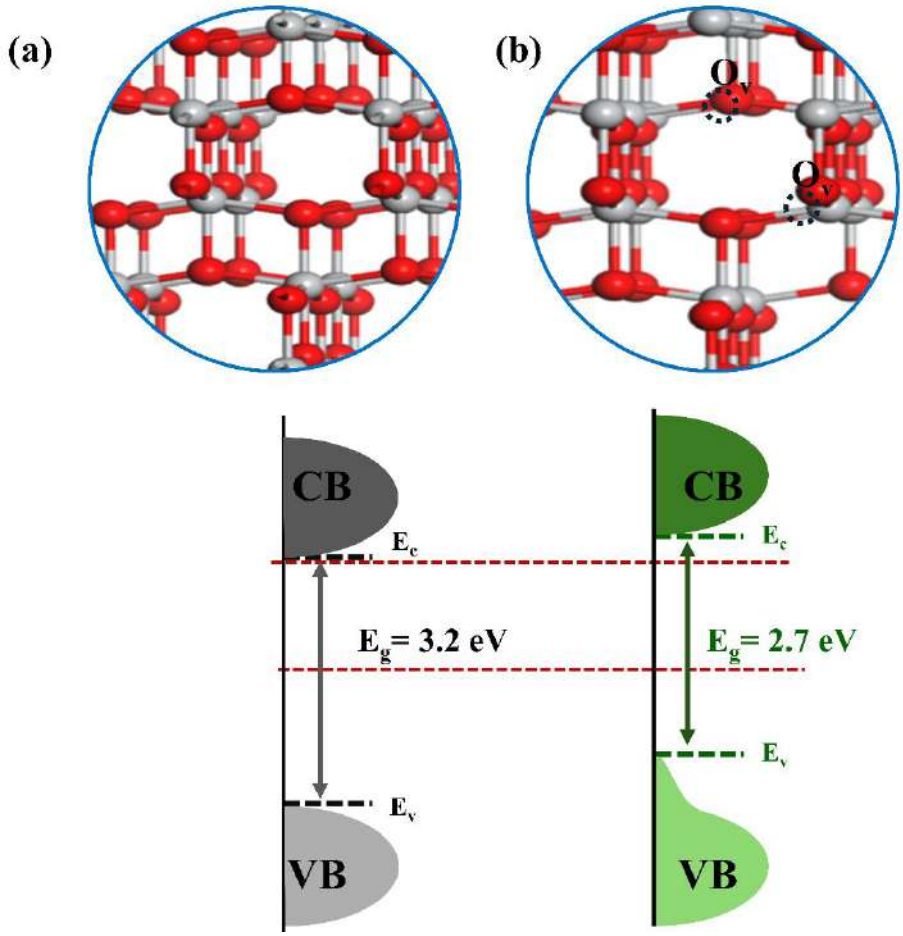

Figure 1.8. A schematic illustration of the band edge and band gap in **(a)** Pristine TiO_2 **(b)** defective TiO_2 (defects alter the band structure) with Ti, and O atoms represented in gray, and red colors, respectively.**[34]**

This approach involves introducing structural defects by creating oxygen, nitrogen, carbon, and metal vacancies within the semiconductor. In general vacancies on the metal oxides surface can be created through thermal treatment, metal or non-metal doping, and high energy particles bombardment **[60]**. These defects alter the band structure and increase the number of active sites for catalytic processes. The modified band structure can generate intermediate energy levels within the band gap, thereby extending light absorption and enhancing charge carrier separation (**Figure 1.8**). The semiconductor's active sites act as adsorption and activation centers **[61]**. However, poorly controlled defects may serve as

recombination centers deep traps that diminish the catalyst's performance. Achieving reproducibility in defect concentration and precisely characterizing the nature of vacancies, whether surface, bulk, or both, remains a significant challenge in the field of defect engineering.

1.3.2. Heterojunctions and Z-Scheme Structures

This structure has great potential to overcome the rapid recombination of photogenerated electron–hole pairs in semiconductor catalysts. When two semiconductors with distinct band structures interact, a Type-II heterojunction is formed at their interface, as shown in the **Figure 1.9a**. The resulting band bending and internal electric field facilitate the separation of photogenerated charge carriers **[62]**. During this process, electrons move from the higher conduction band (CB) to the lower CB, causing them to possess lower energy and become less reactive for reduction reactions. Similarly, holes migrate from the lower valence band (VB) to the higher VB, resulting in holes with higher energy that are less effective for oxidation reactions. Hence, although charge separation is improved, the overall rate of photocatalytic activity decreases due to the weakened redox potentials of the charge carriers **[63]**. To address this limitation, researchers developed the Z-scheme photocatalytic system, inspired by the natural photosynthetic process **[66]**. In a Z-scheme configuration **(Figure 1.9b**), the photogenerated electron in the CB of one semiconductor recombines with the hole in the VB of the other. This selective recombination eliminates the weaker charge carriers and leaves behind highly energetic electrons and holes in the respective CB and VB of the two components. As a result, the system simultaneously achieves efficient charge separation while maintaining strong redox capability **[65].** Building upon this concept, the S-scheme heterojunction further refines the charge-transfer mechanism by introducing band bending and Fermi-level equilibration at the semiconductor interface, as illustrated in the **Figure 1.9c**.

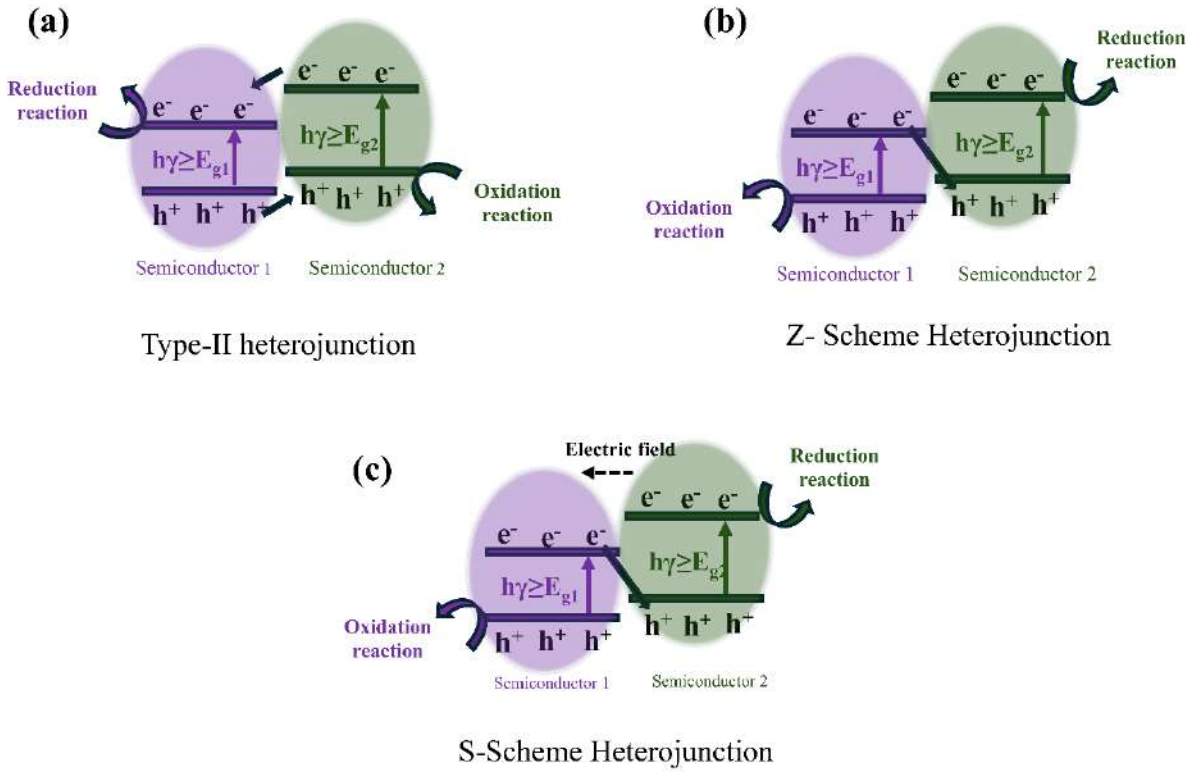

Figure 1.9. A schematic representation of the three distinct mechanisms for the separation of electron-hole pairs in **(a)** type-II **(b)** Z-scheme **(c)** S-scheme heterojunctions.

These effects generate a built-in internal electric field that drives the selective migration of high-energy charge carriers while suppressing unwanted recombination **[66].** Unlike traditional Z-schemes, S-schemes eliminate the need for external redox mediators and exhibit enhanced interfacial contact, structural stability, and quantum efficiency. However, despite their superior photocatalytic performance, both Z- and S-scheme architectures face challenges such as complex synthesis procedures, difficulties in achieving ideal band alignment, possible interface recombination, and long-term structural instability under continuous illumination. Nevertheless, when rationally designed, such advanced heterostructures exhibit excellent charge-transfer dynamics and durability, making them promising candidates for solar-driven hydrogen evolution and other photocatalytic applications **[67, 68]**.

1.3.3. Facet Engineering

Reduction and Oxidation reaction activities directly depend on the nanostructure of the catalyst. At the nanoscale, the surface area and number of active sites can be increased. Facet engineering at this scale can optimize catalytic performance, as each exposed facet has unique atomic coordination, surface energy, electronic properties, and physical and chemical activities **[69]**. Spatial separation of reduction and oxidation reaction on different facets of a semiconductor is a promising approach because it enables efficient charge-carrier separation for overall solar water splitting as shown in **Figure 1.10**. Facets with higher surface energy tend to grow rapidly, but they either occupy only a small part of the final nanocrystal or disappear altogether. In contrast, facets with lower surface energy grow more slowly but are preserved in the final nanocrystal, as described by the Gibbs–Wulff theorem **[70]**. However, synthesizing high-index facets is challenging due to their high surface energy. Despite this, the undercoordinated atoms and elevated surface energy of these facets can significantly enhance catalytic kinetics, provide more absorption sites for HER and OER, and allow selective control over the reaction products **[71]**. Anatase TiO_2, a widely studied semiconductor, has been engineered to expose various facets that show distinct photocatalytic activities, including (101), (010), (001), and (111) **[72, 73]**. The exposed facets can be adjusted by carefully controlling the nucleation and growth rates along different crystallographic directions during crystal formation **[74]**. Fortunately, specific capping agents such as hydrofluoric acid (HF), cetyltrimethylammonium bromide (CTAB), and polyvinylpyrrolidone (PVP) play a crucial role in tailoring the morphology of nanocrystals. These agents selectively adsorb onto particular crystallographic planes, especially the high-energy facets, thereby reducing their surface energy and stabilizing them against dissolution or transformation. By effectively controlling the relative growth rates of different crystal facets, these capping agents prevent the high-energy facets from vanishing during the

synthesis process, resulting in well-defined and thermodynamically stable crystal morphologies **[75-77]**.

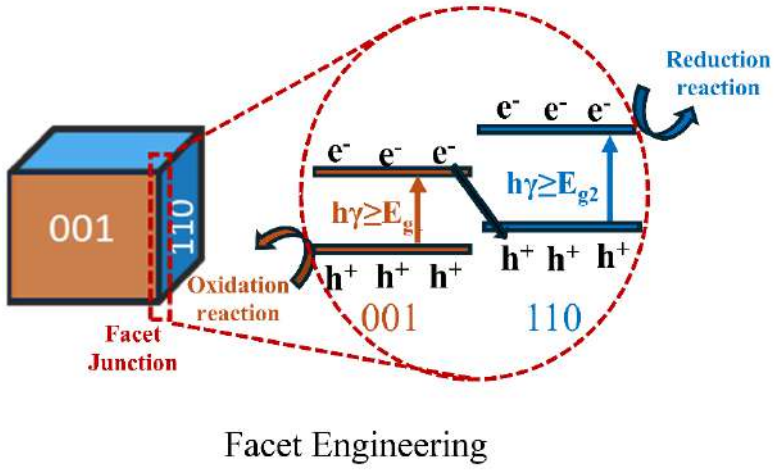

Figure 1.10. Schematic illustrations of spatial separation of electrons-holes pair at the facet junction of the (001) and (110) exposed facets.

For instance, under normal synthesis conditions, anatase TiO_2 crystals predominantly expose the thermodynamically stable {101} facets, whereas the more reactive {001} facets are particularly advantageous for solar energy conversion applications **[74]**. Lu and co-workers demonstrated that the introduction of fluorine ions can selectively adsorb onto the {001} crystal surfaces, thereby altering the relative surface energies and promoting the formation of anatase TiO_2 crystals enriched with approximately 47% {001} facet exposure **[34]**. Crystal facet engineering in different semiconductor materials often requires the use of specific capping agents, as the exposed crystal facets are highly sensitive to their concentration. By tuning the amount of capping agents such as polyvinylpyrrolidone (PVP) or hydroxylamine hydrochloride ($NH_2OH \cdot HCl$) during synthesis, Cu_2O crystals with distinct facet orientations can be obtained **[78]**. Similarly, $BiVO_4$ crystals with controlled ratios of {040}/{110} facets can be synthesized by adjusting both the $TiCl_3$ capping agent concentration and the solution pH **[79]**.

Although facet engineering significantly improves the photocatalytic and electrocatalytic

efficiency of semiconductor nanomaterials, several challenges hinder its large-scale application. High-energy facets are thermodynamically unstable and tend to reconstruct or dissolve during synthesis or operation due to elevated surface energy **[80]**. Achieving uniform exposure of such facets requires precise control of growth parameters, which is difficult to reproduce consistently **[81]**. Moreover, capping agents like HF, CTAB, and PVP, while stabilizing reactive facets, can leave residual impurities or block active sites, reducing catalytic efficiency **[78]**. Facet-dependent charge separation and limited understanding of surface electronic structures further complicate reaction optimization. Thus, maintaining facet stability, reproducibility, and purity remains a major obstacle for practical photocatalytic applications **[82]**.

1.3.4. Single-Atom Catalysts (SACs)

In this strategy, a single metal atom is either anchored or doped on or within semiconductor support without forming clusters or nanoparticles **(Figure 1.11a, b).** These isolated metal atoms act as highly active and well-defined catalytic sites for the hydrogen evolution reaction (HER). Owing to their atomically dispersed nature, single-atom catalysts (SACs) can effectively tailor the local coordination environment at the metal-support interface or defect anchoring sites. This modification fine-tunes the catalytic activity, selectivity, and electronic structure, thereby facilitating efficient charge separation and transfer at the atomic level. As a result, SACs can significantly lower the overpotential required for hydrogen evolution and improve overall photocatalytic efficiency **[83]**. Despite their remarkable advantages, achieving stable and high-loading single-atom dispersion remains a considerable challenge. Under operating conditions such as heat, illumination, or solvent exposure, single atoms may migrate or aggregate into clusters, leading to a reduction in catalytic performance **[84]**. Moreover, the synthesis of SACs requires precise control over atomic dispersion, and their characterization demands advanced techniques such as high-angle annular dark-field

scanning transmission electron microscopy (HAADF–STEM) and X-ray absorption spectroscopy (XAS/EXAFS). However, these techniques are often complex, resource-intensive, and not always readily accessible **[85]**.

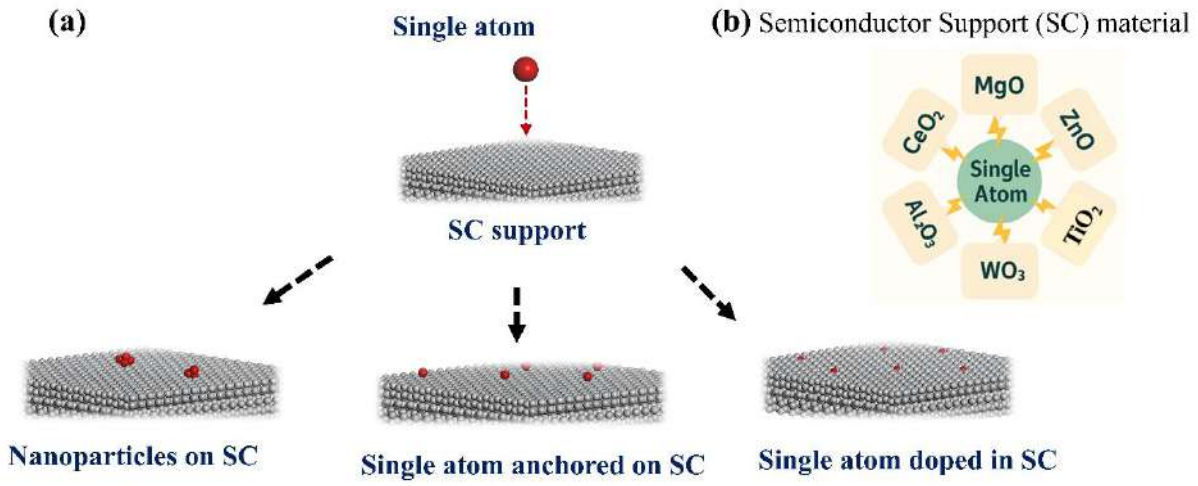

Figure 1.11. (a) Schematic depiction of the interaction between a single atom and SC support. **(b)** Different type of metal oxide SC supports for single atom.

1.4. Asymmetric Atomic Sites

Single-atom catalysts (SACs) have great potential for solar water splitting. In SACs, single metal atoms anchored on semiconductor supports increase the number of active sites, broaden the light absorption range, and enhance charge transfer/separation efficiency in heterogeneous catalysis **[86-88]**. For the first time, Qingxia Liu *et al.* reported that isolated Pt single atoms dispersed on TiO_2 exhibited superior photocatalytic H_2 evolution activity compared to conventional Pt nanoparticles **[89]**. Xie *et al.* demonstrated that the longer lifetime of photoexcited electrons in isolated Pt sites decorated on g-C_3N_4 significantly enhanced photocatalytic hydrogen production **[84]**. Furthermore, Li *et al.* revealed that Cu single atoms (SAs) trapped within a Cu/TiO_2 photocatalyst exhibited reversible and cooperative photocatalytic water-splitting activity, resulting in enhanced H_2 generation [**90**]. Single-atom doping requires specific sites on the support that contain under-coordinated

atoms, surface defects, or heteroatoms to enable strong metal–support interactions [**90]**. The local environment formed through such metal–support interactions can result in asymmetric atomic sites. These asymmetric atomic sites where a single atom experiences an uneven geometric or electronic environment. This asymmetry facilitates local charge polarization, generating built-in electric fields that promote directional charge transfer, optimize intermediate binding energies, and significantly enhance the kinetics of photocatalytic reactions, thereby considerably enhancing H_2 evolution efficiency **[91]**. Generally, single-atom supports can be either non-metal-oxide or Metal-oxide supports. On non-metal-oxide supports such as N-doped carbon, g-C_3N_4, or metal-organic frameworks, asymmetric atomic sites are typically created via coordination to heteroatoms or structural defects, producing uneven charge distributions that facilitate proton reduction. Zhang et al. reported the synthesis of a single-atom Ni–N_3–C catalyst anchored on a pre-designed N-doped carbon support derived from metal-organic frameworks. The catalyst exhibited exceptional performance in CO_2 electroreduction, achieving a maximum CO Faradaic efficiency of 95.6%, highlighting the effectiveness of atomically dispersed Ni centers in promoting selective CO production **[92]**. Metal-oxide supports, including TiO_2, In_2O_3, $W_{18}O_{49}$, and Fe_2O_3, offer additional structural and electronic complexities, including lattice distortions, mixed-valence cations, surface steps, and oxygen vacancies, which are the origin of diverse forms of asymmetry around an anchored single atom. This asymmetry can be (i) Geometric asymmetry arises from deviations in coordination number or bond angles, creating undercoordinated metal sites favorable for reactant adsorption **[93]**. (ii) Electronic asymmetry results from uneven electron density due to different oxidation states or coordination environments of metal sites, establishing localized electronic states that promote efficient charge separation and enhance catalytic activity. M. Sun et al. demonstrated that the electronic asymmetry of lattice oxygen sites in ZnO enhances the methane conversion rate

exceeding 16000μmolg $^{-1}$ h^{-1}**[94]**. (iii) Interfacial asymmetry occurs at material boundaries, such as between metal clusters and oxide supports, generating built-in electric fields that facilitate charge separation **[95]**. (iv) Vacancy-Induced Asymmetry is an oxygen vacancy around a metal site. This asymmetry alters the coordination environment of the metal site, induces lattice distortion, and perturbs the local electronic structure. These vacancies break the original lattice symmetry and often serve as anchoring sites for single atoms, stabilizing them and enhancing their catalytic activity **[96]**. More specifically, asymmetric atomic sites (AAS), typically represented as M_{SA}–O_v–M_2, are commonly used to describe metal-oxide-supported single-atom catalysts **(Figure 1.12)**. In this configuration, M_{SA} refers to the trapped metal single atom, which serves as the primary active site for the adsorption and activation of reactants, such as water molecules, during photocatalytic H_2 evolution. O_v denotes an oxygen vacancy in the support, creating a localized electron-rich site, while M_2 represents the semiconductor support that influences the electronic structure of the trapped metal atom through coordination interactions and contributes to geometric and electronic asymmetry.

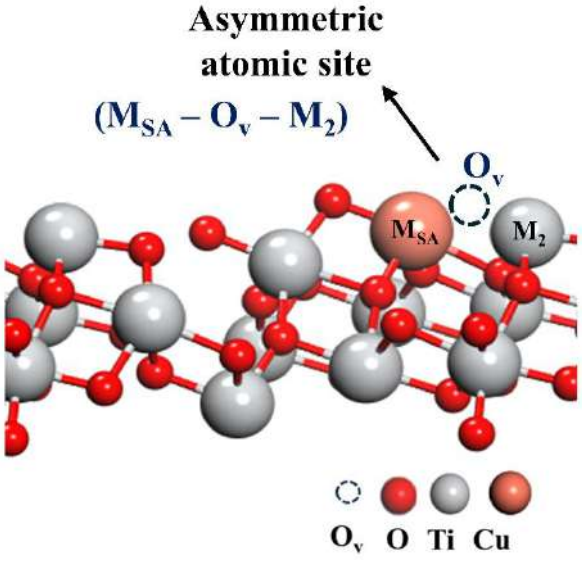

Figure 1.12. Schematic illustration of asymmetric atomic sites on metal oxide support.

Collectively, the M_{SA}–O_v–M_2 configuration has been recognized as one of the most favourable catalytic architectures for achieving superior performance in asymmetric atomic site catalysts (AASC) **[97]**. For instance, Nie et al. demonstrated that Pt^{2+}–O_v–Ce sites in Pt^{2+}-doped CeO_2 catalysts exhibit high CO oxidation activity and excellent thermal stability [**90]**. Tao et al. reported that Ir–O–Ru sites in Ir-doped RuO_2 (IrSA/RuO_2) exhibit excellent hydrogen and oxygen evolution reaction (HER/OER) activity and stability in acidic media, as the dual active sites modify the electronic structures of both Ru and Ir atoms **[98]**. Wang et al. reported that Co–O–Pt dimer sites in Co/Pt dual single-atom catalysts supported on TiO_2 exhibited a photocatalytic activity of 43.467 mmol g^{-1} h^{-1} due to the coupling between the dimer sites, which mutually enhanced the electronic states of Pt and Co atoms, thereby weakening the H* binding **[99]**. Even with these impressive breakthroughs on asymmetric atomic sites (AAS) in photocatalytic hydrogen production has mainly relied on defect-rich metal oxides as supports, which often demand the use of hydrogen and/or hydrogen/argon gases **[84, 100, 101, 102**]. This results in significant practical drawbacks, such as excessive resource consumption, making these approaches less suitable for large-scale sustainable hydrogen production. In addition, current techniques for achieving precise and uniform control over AAS formation remain quite limited and underdeveloped, posing a major challenge to the rational design and effective deployment of advanced catalysts. To fully leverage the unique reactivity of asymmetric atomic site semiconductor catalysts (AASSC) for photocatalytic hydrogen evolution, it becomes crucial to carefully select support materials that not only promote the stabilization of desired AAS but also allow for rigorous regulation of defect types and distributions. Faceted Nanostructure is a good candidate to create AASC because facet nanostructures contain intrinsic defective sites **[73]**; for example, anatase TiO_2 exhibits various facet like 101, 001, & 111. 101 is most stable facet TiO_2. in nature 90 % of TiO_2 is available 101 facet. But with the help of chemical modification another facet is also

explored like 001, 111. If facet Nanostructures can be utilized in appropriate way to create AAS, it will overcome the previous issue with defect rich metal oxide. So, this is my motivation to work on faceted nanostructure.

1.5. Facet Nanostructures: Wonderful support materials to create AASC

After the pioneering work of Fujishima and Honda in 1972 **[23]** to enhanced performance of solar water splitting, semiconductor material is used as doping or anchoring single atom. a myriad of semiconductor materials including metal oxides **[103]** (TiO_2, ZnO, SnO_2, CuO, Cu_2O, ZrO_2, WO_3), metal sulfides (CdS, ZnS), metal nitrides, carbon materials (*g*-C_3N_4, carbon nanotubes, carbon dots), organic semiconductors, and their composites have been fabricated and used extensively for solar water splitting to produce H_2. Titanium dioxide (TiO_2) has always been one of the most used photocatalysts for water splitting due to its high physiochemical stability, non-toxic nature, low cost, and ability to absorb ultraviolet light. TiO_2 commonly has three different phases including rutile, anatase, and brookite as shown in **Figure 1.13.** The three phases of TiO_2 contain TiO_6 octahedra as basic units connecting with shared edges and corners in different orientations and distortion. The different orders of the TiO_6 octahedra determine the atomic structures, surface structures, and electronic structures of each phase of TiO_2. Anatase is tetragonal, with the lattice parameters $a = b = 0.376$ nm, $c = 0.951$ nm; Rutile is tetragonal, with the lattice parameters $a = b = 0.459$ nm, $c = 0.296$ nm; Brookite is rhombohedral, with the lattice parameters are $a = 0.918$ nm, $b = 0.545$ nm, and $c = 0.515$ nm. Rutile is the most stable phase at high temperatures (> 800° C) and naturally occurring form of TiO_2. Brookite is less stable than rutile and anatase and is rarely reported. Anatase is commonly observed, stable up to ~600° C, and converts to rutile at high temperatures **[43].** The bandgap energy for rutile, brookite, and anatase is 3.0, 3.2, and 3.3 eV respectively. Among all these phases, Anatase is known for its high surface area and photocatalytic properties, making it useful in solar water splitting. However, the anatase TiO_2

has also several challenges including a wide band gap (3.2 eV), partial ability to adsorb visible light, low quantum efficiency, etc. therefore, researchers have been focusing on surface engineering to enhance the photocatalytic characteristics of the material. To regulate the surface and interface structures, the selection of facets to form the surface and interface is a crucial parameter.

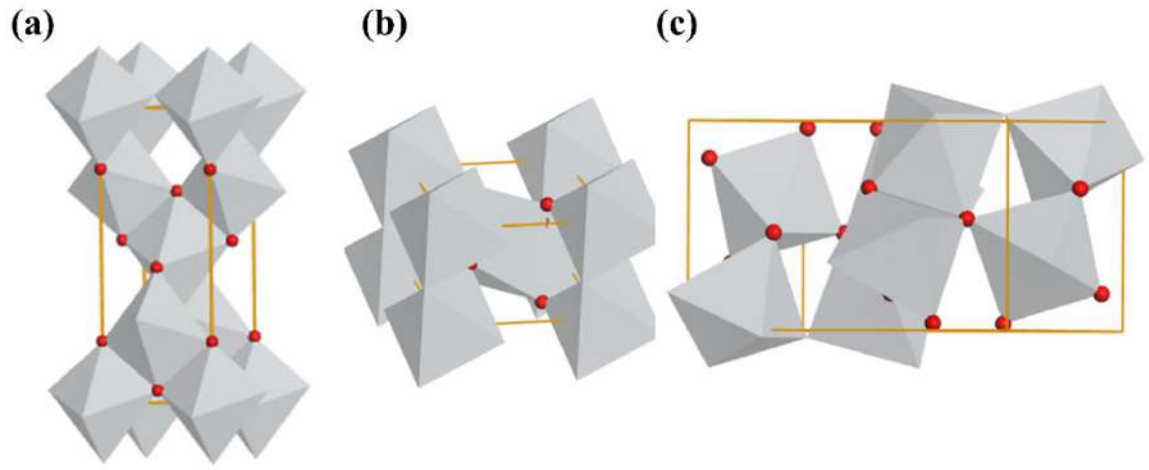

Figure 1.13. Crystal structures of anatase **(a)** rutile **(b)** brookite **(c)** of TiO_2. (red spheres are O atoms, gray atoms within octahedra are Ti atoms, and yellow lines represent the unit cell).

Design and morphological control of crystal facets is a commonly employed strategy to optimize the performance of various crystalline catalysts from noble metals to semiconductors. The basis of this strategy is that surface atomic configuration and coordination, which inherently determines their heterogeneous reactivity, can be finely tuned by morphological control.

1.5.1. Faceted Nanostructures of TiO_2

TiO_2 faceted nanostructures are nano-sized structures of titanium dioxide that exhibit defined crystal facets on their surfaces, corresponding to distinct crystallographic planes or orientations. Material properties such as optical, electronic, electrochemical, and adsorption behavior strongly depend on the types of exposed facets, which result in variable photocatalytic activity **[73]**. Among the three phases of TiO_2 (anatase, rutile, brookite),

anatase widely investigated in nanomaterials, can present (001), (010), (101), and (111) facets for solar water splitting. The surface energy of each facet depends on under-coordinated Ti and O atoms. As illustrated in **Figure 1.14a**, on the (001) facet, five-coordinated Ti (Ti_{5c}) and two or three-coordinated O (O_{2c}, O_{3c}) are interconnected, yielding a high surface energy (0.90 $J \cdot m^{-2}$); this causes the (001) facet to disappear during crystal growth. Yang et al. successfully synthesized microscale (001) facets with abundant reactive sites using TiF_4 and HF as precursors and capping agents **[34]**. In contrast, the (010) facet, in addition to the outermost Ti_{5c} atoms on the top layer, the fully (6-fold)-coordinated Ti (Ti_{6c}) atoms are also exposed on the second layer. Moreover, both O_{2c} and O_{3c} atoms exist on the surface of (010) (**Figure 1.14b)**. Its surface energy is 0.57 $J.m^{-2}$. While not present in equilibrium by the Wulff construction, formation of (010) facet is theoretically possible in basic solutions.

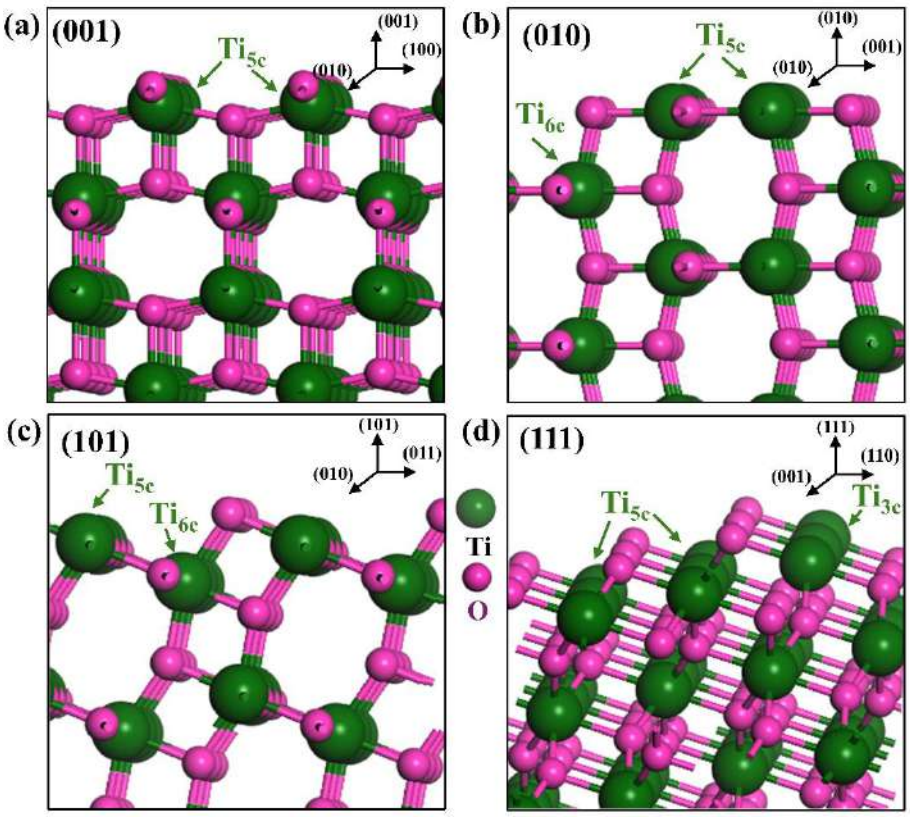

Figure 1.14. (a-d) Surface structures of (001), (010), (101), and (111) facets of anatase TiO_2.

Pan et al. produced single-crystalline anatase TiO_2 rods with dominant (010) facets via hydrothermal treatment and controlled solution pH between 10.1 and 11.8 **[104].** The stable

(101) facet contains both Ti_{5c} and Ti_{6c} in a 1:1 ratio along with O_{2c} and O_{3c} atoms and features the lowest surface energy (0.43 $J \cdot m^{-2}$), mainly due to under-coordinated Ti_{5c} atoms (**Figure 1.14c)**. Growth of anatase crystals exposing (101) facets is tunable by varying synthetic parameters, including precursor, solvent, capping agent, reaction time, and temperature. Surfactants and capping agents, such as titanium butoxide, Oleic acid, and Oleylamine, also control nanocrystal shape **[105].** Large single crystals are fostered at low nucleation densities and gradual growth rates, achieved via low supersaturation. Ti(III) has been commonly selected as a precursor since it requires oxidation to Ti(IV) prior to hydrolysis, proceeding slowly due to limited dissolved oxygen **[74]**. Hosono et al. synthesized octahedral anatase crystals with nearly 100% (101) exposure by hydrolyzing $TiCl_3$ and using sodium dodecyl sulfate; gases released during sodium dodecyl sulfate decomposition aid in growth equilibrium. H_2SO_4 yields similar results but different morphologies **[106].** Li et al. used $TiCl_3$, HCl, and H_2O_2 for hydrothermal synthesis of (101) facet crystals **[107]**. Amoli et al. generated indium oxide nanocluster-doped TiO_2 rice-grain nanocrystals with six {101} and two {001} facets **[108].** For the (111) facet, all Ti atoms are under-coordinated: 75% are five-coordinated (Ti_{5c}) and 25% are three-coordinated (Ti_{3c}), yielding the highest surface energy (1.61 $J \cdot m^{-2}$) and lowest surface area (**Figure 1.14d)**. The order of facet surface energies is: (111) > (001) > (010) > (101). Xu et al. first synthesized anatase crystals with well-defined (111) facets by employing F^- and ammonia as capping agents. These crystals exhibit markedly enhanced photocatalytic activity (405.2 $\mu mol \cdot h^{-1}$), approximately 5, 9, and 13 times higher than those dominated by (010), (101), and (001) facets, respectively, attributable to the abundance of under-coordinated atoms serving as active sites **[73]**. Thus, High index facet (111) nanostructures of TiO_2 can be used as support material to stabilize SA to create AASC.

1.6. Motivation

To move beyond the limitations associated with conventional defect-rich metal oxides, I turned my attention to a more controlled and structurally defined alternative: faceted nanostructure. Faceted nanostructure is an interesting class of materials for the design of asymmetric atomic site catalysts (AASCs), primarily owing to the presence of intrinsic undercoordinated defects at their crystallographic surfaces. Among various metal oxides, anatase TiO_2 metal oxide is naturally expose multiple well-defined facets. Its crystal structure can expose different facets, including the most prominent (101), (001), and (111) facets, each with distinct surface atomic configurations and energy. Under ambient conditions, the thermodynamically stable (101) facet dominates the surface of anatase TiO_2, having approximately 90% of the total surface area. This arises due to its relatively low surface energy. However, through chemical and synthesis process modifications, higher energy facets such as (001) and (111) can be selectively engineered and stabilized. A critical distinction among these facets lies in the coordination environment of the surface titanium (Ti) atoms.

On the (101) facet, the surface comprises both five-fold undercoordinated (Ti_{5c}) and six-fold fully coordinated (Ti_{6c}) titanium atoms. The (001) facet, in contrast, exclusively presents five-fold undercoordinated Ti atoms. The (111) facet is particularly noteworthy: approximately 75% of its surface Ti atoms are five-fold undercoordinated, while the remaining 25% are three-fold undercoordinated. The (111) facet has the more undercoordinated Ti atoms among the three facets. The more undercoordinated the surface atoms, the higher the surface energy, and the more strongly the (111) facet interacts with incoming species. These structural characteristics motivated the selection of the (111) facet of anatase TiO_2 as the support material in this thesis.

These undercoordinated surface atoms make it an ideal platform to trap and stabilize

isolated single metal atoms, which is an essential for the construction of asymmetric atomic site catalysts (AASCs). Copper (Cu) was selected as the doping metal atom species due to Cu exhibits variable oxidation states (Cu^0, Cu^{1+}, Cu^{2+}), reversible catalytic cycles, and tunable electronic and optical properties, making it an attractive candidate.

Therefore, in this thesis replacing undercoordinated Ti atoms with Cu atoms on the (111) exposed facet of TiO_2 to create AASC to overcome the limitations associated with conventional defect-rich metal oxide supports.

High index facet (111) nanostructure and SA: To create AASC

This approach focuses on tailoring both the surface crystallographic facets and the atomic coordination environment to achieve enhanced light utilization, charge dynamics, and surface reaction kinetics. In this strategy involves the integration of single-atom catalysis (SAC) with high-index facet engineering in a single semiconductor system. In this design, AASC are introduced within a rationally engineered single-atom-trapped (111)-faceted TiO_2 structure **(Figure 1.15).** This hybrid configuration couples the multiple advantages of high-index faceted nanostructures rich in reactive step, edge, and kink sites with the unique reactivity and precision of isolated single-atom active centers. The AASC may play multiple synergistic roles that collectively enhance photocatalytic water splitting efficiency (i) Enhanced light harvesting and charge dynamics**:** The asymmetric local coordination around the single atoms modifies the electronic band structure, promoting improved photon absorption, efficient charge carrier separation, and reduced electron hole recombination. (ii) Facilitated adsorption and polarization of Water Molecules: The intrinsic charge heterogeneity at the AASC strengthens the adsorption and polarization of H_2O molecules, improving their activation for redox reactions. (iii) Accelerated electron transfer: The single-atom centers act as active bridges, facilitating rapid electron transfer from the semiconductor conduction band to surface-adsorbed intermediates, thereby boosting the hydrogen evolution reaction (HER)

kinetics. (iv) Electronic structure optimization: The asymmetric coordination environment shifts the d-band center closer to the fermi level, improving the binding of key intermediates (H*, OH*) and lowering the reaction energy barriers for both reduction and oxidation steps.

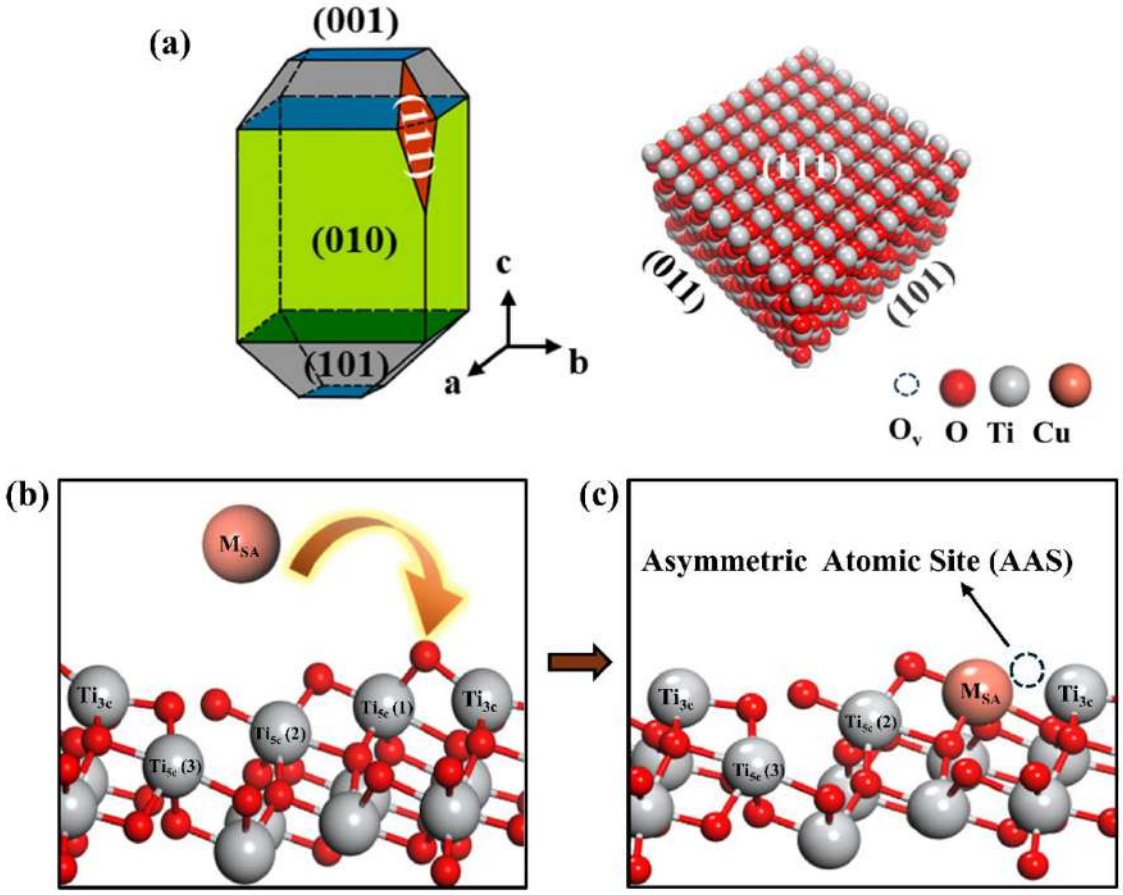

Figure 1.15. (a) A model of TiO_2 with (111) exposed facet, where titanium and oxygen atoms are represented in grey and red colors, respectively. **(b, c)** Schematic representation of the creation of AAS. There are primarily two types of titanium atom sites: five-coordinated titanium atoms (Ti_{5c}, 75%) and three-coordinated titanium atoms (Ti_{3c}, 25%).

Chapter: 2

Materials, Synthesis Methods, Characterization Techniques, and Photocatalytic & Photoelectrochemical Testing Setup

---

This chapter presents a comprehensive description of the materials used, synthesis procedures, characterization techniques, and experimental setups employed for evaluating photocatalytic and PEC performance of the materials presented in the thesis. The chapter begins with details of the precursor chemicals and materials, synthesis methodology highlighting the conditions optimized for achieving controlled facet exposure and stable incorporation of single metal atoms. The chapter further outlines the various characterization techniques used to investigate the structural, morphological, optical, and electronic properties of the synthesized materials. Techniques such as X-ray diffraction (XRD), scanning and transmission electron microscopy (SEM/TEM), nitrogen adsorption–desorption analysis, UV–Vis spectroscopy, and X-ray absorption spectroscopy (XAS) are described to provide insights into crystallinity, surface morphology, electronic structure, and defect states. In addition, charge carrier dynamics are analyzed using time-resolved photoluminescence (TRPL) and electrochemical measurements to understand charge separation and transport behaviour.

Finally, the chapter details the experimental setups used for evaluating the photocatalytic and PEC water splitting performance of the developed materials. This includes device designs, light sources, experimental conditions, gas analysis using gas chromatography (GC). The configuration of PEC systems including electrode fabrication using spray pyrolysis deposition, electrolyte selection, and measurement conditions are outlined.

2.1. Materials and Reagents

Tetra-n-butyl orthotitanate (TNBT) with 23-24% TiO_2 and Oleylamine ($C_{18}H_{37}N$) 95% purity were sourced from Sisco Research Laboratories (SRL), India. Hydrofluoric acid (HF) 48% AR, ammonia solution (NH_3) 25% LR, hydrazine hydrate ($NH_2NH_2.H_2O$) 80% LR, N-cetyl-N,N,N-trimethylammonium bromide (CTAB), cupric sulfate pentahydrate ($CuSO_4 \cdot 5H_2O$) LR, and sodium sulfate (Na_2SO_4, 0.1 M) were obtained from Molychem. Poly (vinyl alcohol) (PVA) powder 87-90% hydrolysed was purchased from Sigma Aldrich. Isopropyl alcohol (IPA) and anhydrous ethanol were purchased from Merck. Indium Tin Oxide (ITO) glass was purchased from Sigma Aldrich. All chemicals were used as received without further purification.

2.2. Synthesis Methods

The catalyst was synthesized by a simple sol-gel assisted hydrothermal method. Thin film photoelectrodes were prepared using spray pyrolysis deposition system (Model HO-TH-04, HolmarcOpto Mechatronics Pvt. Ltd., India). The system includes a 20 mL syringe pump for precursor delivery, an ultrasonic atomising nozzle, an air compressor for carrier gas and a heated base plate to keep the substrate temperature constant. The details process is given in chapter 3 & 4.

2.3. Characterization Techniques

In recent years, notable advancements have been made in the development of asymmetric atomic-site semiconductor materials, enabling the design of structures with tailored properties for specific applications. These developments have been greatly supported by the rapid progress in advanced analytical techniques used to investigate nanostructured materials.

The characterization of asymmetric atomic-site semiconductors typically involves analyzing

their size, morphology, crystalline structure, porosity, electronic configuration, local environment of absorbing atom, lifetime of carriers, and other essential physicochemical properties. The characterization techniques such as X-ray diffraction, electron microscopy, optical spectroscopy, N_2 sorption analysis, X-ray absorption spectroscopy, electron paramagnetic resonance, time-resolved photoluminescence (TRPL), and various electronics measurements are commonly employed for this purpose.

In this context, this chapter provides a comprehensive and detailed discussion of the characterization techniques utilized during the investigation of the newly developed asymmetric atomic-site semiconductor materials.

2.3.1. Powder X-Ray Diffraction

X-ray powder diffraction, first introduced by Debye and Scherrer in 1916 **[109]**, is a non-contact and non-destructive technique widely used to determine grain size, strain, and phase composition of nanostructured materials. The method works on the principle that when electromagnetic radiation interacts with a periodic atomic lattice, diffraction occurs if the spacing of the lattice planes is comparable to the wavelength of the radiation **[110].**

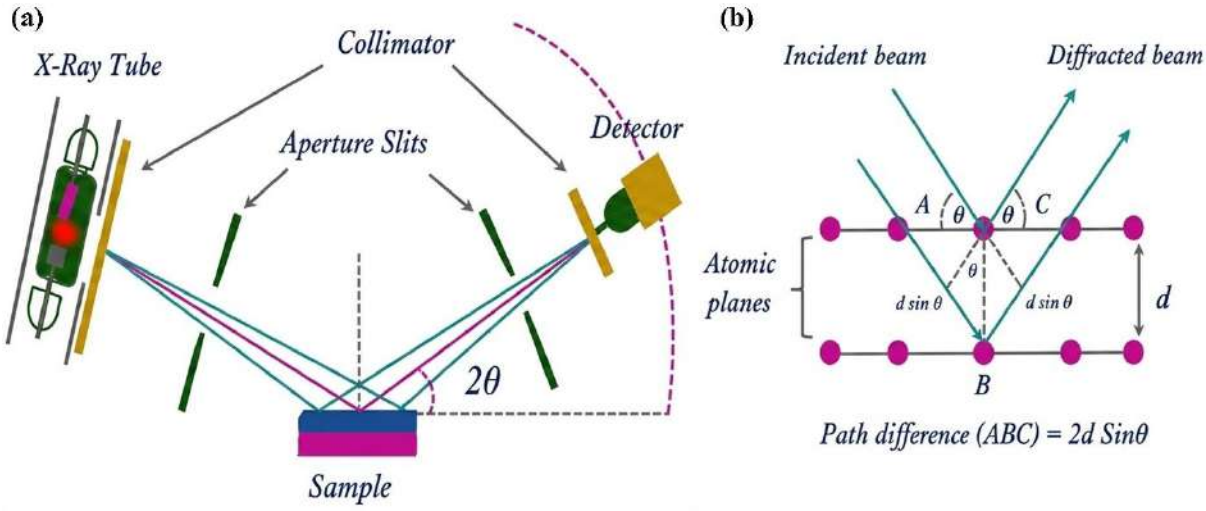

Figure 2.1. (a) Schematic illustration of an X-ray diffractometer. **(b)** Bragg scattering from crystalline planes.

Figure 2.1a illustrates the essential components of an X-ray diffractometer. A collimated X-ray beam is directed onto the sample, and when the Bragg condition is fulfilled, the incoming radiation is diffracted. As shown in **Figure 2.1b**, Bragg diffraction takes place when X-rays with wavelengths similar to atomic distances are specularly scattered by the crystal planes and undergo constructive interference.

Bragg's law describes the relationship between the X-ray wavelength (λ), the distance between lattice planes (d), and the diffraction angle (ɵ). The law is expressed as: $\lambda = 2dsin\theta$, where λ is the X-ray wavelength, d is the interplanar spacing, and θ is the angle of incidence. In XRD measurements, the intensity of diffracted X-rays is recorded as a function of the diffraction angle 2θ. The diffraction pattern of a material is determined by its crystal structure. Specifically, the unit cell dimensions determine the angular positions of the diffraction peaks, while the arrangement of atoms within the unit cell affects the relative intensities of the peaks.

One important feature of XRD in nanomaterials is peak broadening. The broadening of a peak, usually measured as the full width at half maximum (FWHM), is directly related to the crystallite size (D) of the nanoparticles. This relationship is described by the Debye-Scherrer equation 2.1. **[111].**

$$D = \frac{0.89\lambda}{\beta\ cos\theta} \qquad (2.1)$$

where β is the FWHM (in radians), θ is the Bragg angle, and λ is the X-ray wavelength used.

XRD analysis of the developed materials in this this was performed at the Central Instrumentation Facility (CIF) of Rajiv Gandhi Institute of Petroleum Technology (RGIPT), Jais, Amethi, Uttar Pradesh, India. The measurements were conducted using Malvaran PANalytical Empyrean X-ray diffractometer with Cu-Kα (λ = 1.540598 Ǻ) radiation and

scan step size (0.0032826) operated at room temperature. Phase identification of all samples was carried out by comparing the observed diffraction peak positions and intensities with standard patterns available in the JCPDS (Joint Committee on Powder Diffraction Standards) database. The indexed peaks were deconvoluted using Lorentzian fitting through peak analysis software, and the full width at half maximum (FWHM) was determined. The average crystallite size (D) was then calculated using the Debye–Scherrer equation.

2.3.2. Electron Microscopy

Electron microscopes employ electrons instead of photons because electrons possess significantly shorter wavelengths, enabling imaging of materials with atomic-scale resolution. In these instruments, electromagnetic lenses are used to control and focus the electron beam, analogous to the role of optical lenses in conventional light microscopes. Because the wavelength of accelerated electrons can be up to five orders of magnitude shorter than that of visible light, electron microscopes exhibit a much higher resolving power and are capable of revealing fine structural details that are beyond the limits of optical microscopy. During electron microscopy, the interaction of the incident electron beam with the specimen through elastic and inelastic scattering processes generates various signals that provide valuable structural, compositional, and electronic information about the material **[112]**. Depending on the nature of these interactions and the imaging configuration, several types of electron microscopes are employed, including the Scanning Electron Microscope (SEM), Transmission Electron Microscope (TEM), and Scanning Transmission Electron Microscope (STEM).

2.3.2.1. Scanning Electron Microscope (SEM)

The Scanning Electron Microscope (SEM) is one of the most widely used analytical instruments for the characterization of materials at the micro and nanoscale level. It is

extensively employed to study surface-related physical properties such as morphology, surface texture, particle shape, particle size, and size distribution. SEM provides high-resolution images of the specimen surface and is particularly effective for understanding surface features and structural details. In SEM, a finely focused electron beam is generated by an electron gun and accelerated by an applied voltage typically ranging from 1 to 20 kV. This electron beam is focused and scanned in a raster pattern across the surface of the specimen using a series of electromagnetic lenses and scanning coils. When the incident electron beam strikes the specimen surface, it interacts with the atoms of the material through elastic and inelastic scattering processes, resulting in the generation of various detectable signals. These interactions produce several types of signals, including secondary electrons, backscattered electrons, characteristic X-rays, and photons. Among these, secondary electrons (SEs) are most commonly used for imaging purposes. Secondary electrons are low-energy electrons generated from the near-surface region of the specimen and can escape due to their shallow origin depth. As a result, they provide detailed information about the surface topography and fine morphological features of the sample.

The emitted signals are collected by suitable detectors and converted into electrical signals, which are then processed to form an image displayed on a monitor. SEM images exhibit a large depth of field, giving them a characteristic three-dimensional appearance, which is highly advantageous for visualizing surface structures and roughness. The spatial resolution of an SEM image is mainly determined by the diameter of the focused electron probe. This probe size depends on several factors, including the wavelength of the electrons, the accelerating voltage, and the performance of the electromagnetic lens system used to focus and control the electron beam. With optimized operating conditions, SEM can achieve nanoscale level resolution, making it a powerful tool for materials characterization **[113-115]**.

2.3.2.1.1 Energy Dispersive X-ray Analysis (EDX)

This technique is commonly used in combination with SEM to analyze the near-surface elemental composition and to estimate the relative abundance of elements at different locations, thereby providing a clear representation of the surface elemental distribution **[116, 117]**. When a high-energy electron beam interacts with the sample, it excites the atoms uniformly, resulting in the emission of characteristic X-rays with energies specific to each element. These X-rays arise from electronic transitions between atomic shells following the ejection of inner-shell electrons and subsequent relaxation of higher-energy electrons. The emitted X-rays carry information not only about the parent element but also about the electronic shells involved in the transition, enabling accurate identification of the elemental composition of the specimen **[118].** The EDX technique allows elemental analysis to be expressed in terms of normalized atomic percentage as well as normalized weight percentage. X-rays with sufficient energy to escape from the specimen surface are detected and recorded as a spectrum containing distinct peaks at characteristic energies corresponding to the elements present. Additionally, the integrated peak areas can be used to obtain semi-quantitative elemental composition data. Moreover, EDX elemental mapping provides a meaningful visualization of the spatial distribution of elements across the surface of the specimen **[119].**

FESEM images were obtained using a field-emission scanning electron microscope (FE-SEM, JEOL JSM-7900F) equipped with an energy-dispersive X-ray (EDX) system for elemental analysis at CIF, RGIPT. For cross-sectional imaging, the sample was positioned perpendicular to the electron beam.

2.3.2.2. Transmission Electron Microscope (TEM)

In Transmission Electron Microscopy (TEM), a high-energy electron beam is transmitted through an ultrathin specimen using an accelerating voltage (100–200 kV). The interaction

between the electrons and the sample produces images that provide detailed structural information **[120-122]**. Modern TEM instruments offer very high spatial resolution, often better than 0.1 nm, allowing observation at the atomic scale. By combining bright-field (BF) and dark-field (DF) imaging with electron diffraction, it is possible to identify crystalline regions and determine their size, orientation, and structural quality. A standard TEM operates mainly in two imaging modes: bright field and dark field. In BF-TEM, images are formed using transmitted electrons, resulting in a dark specimen on a bright background, where darker areas correspond to regions with greater thickness, higher mass, or stronger diffraction. In contrast, DF-TEM images are formed using scattered or diffracted electrons, producing an inverted contrast, where the specimen appears bright against a dark background **[123]**. In addition to these conventional modes, TEM also offers advanced techniques such as high-resolution TEM (HRTEM) for atomic-scale imaging, selected area electron diffraction (SAED) for crystal structure analysis, scanning TEM (STEM) for combined imaging and analysis, and energy-filtered TEM (EFTEM) for elemental and chemical mapping **[122]**.

The morphology of the materials developed in the thesis was studied at CIF of RGIPT. TEM and HRTEM were conducted on a JEOL TEM-2010 field emission gun transmission electron microscope operated at 200kV. HAADF-STEM images were obtained using an ultrahigh-resolution field emission gun with a HAADF detector. **Figure 2.2** is a representative TEM image **(Figure 2.2 (a))** of the material with HRTEM **(Figure 2.2 (b))** and SAED **(Figure 2.2 (c))** modes (detail of the sample is given in Chapter 3).

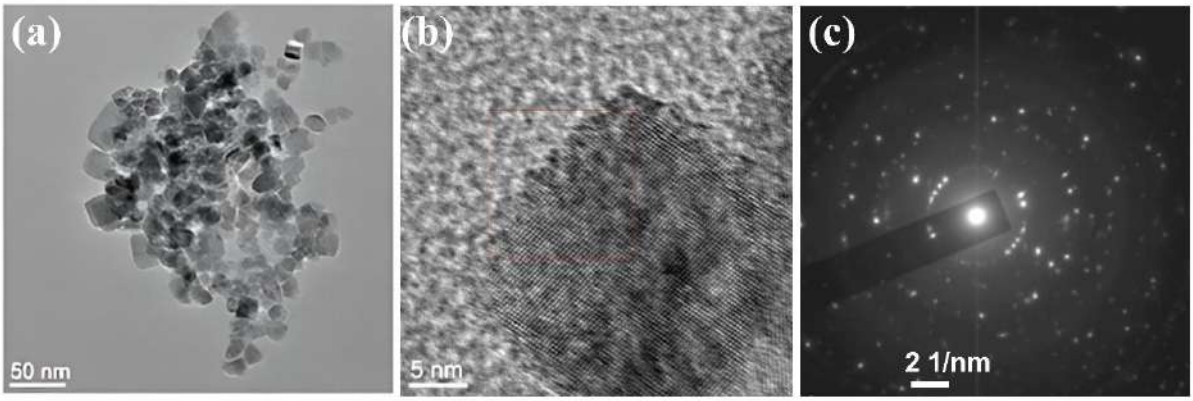

Figure 2.2. (a) Representative TEM image of a sample. **(b)** HRTEM image. **(c)** SAED image of the specimen

2.3.2.2.1. High-Resolution Transmission Electron Microscope (HR-TEM)

High-resolution transmission electron microscopy (HRTEM) is a phase-contrast imaging technique in TEM that enables direct visualization of atomic arrangements. It allows determination of local crystal orientations, identification of lattice planes, and observation of structural defects within a sample **[124, 125]**. Due to its ability to resolve features at the atomic scale, HRTEM is a powerful technique for investigating the structural properties of nanostructured materials **[126].**

2.3.2.2.2. Selected Area Electron Diffraction (SAED)

The SAED (Selected Area Electron Diffraction) pattern provides crystallographic information from a specific selected region of the sample **[127]**. In the TEM–SAED mode, electrons scattered or diffracted from a chosen area of the specimen are collected to form an electron diffraction pattern, which typically appears as a series of distinct spots. Each diffraction spot represents a specific diffraction condition satisfied by the crystal structure of the sample. The spacing between the diffraction spots is related to the interplanar spacings of the crystal lattice, while the arrangement and orientation of the spots provide information about the crystal orientation. Thus, SAED is a useful technique for analyzing the crystal

structure and orientation of materials at the nanoscale **[122].**

2.3.2.3. Scanning Transmission Electron Microscopy (STEM)

Scanning Transmission Electron Microscopy (STEM) involves scanning a finely focused electron beam across the sample, similar to SEM. As the beam scans point by point, detectors collect the electrons transmitted through the specimen to construct an image. In conventional HR-TEM, detecting metal nanoparticles with sizes of about 1 nm or smaller on strongly scattering crystalline oxide supports can be challenging due to the overlap of mass-thickness contrast and diffraction contrast. In such cases, an aberration-corrected STEM equipped with bright-field (BF), dark-field (DF), and secondary electron detectors offers a more effective approach, enabling clearer detection and visualization of ultrasmall nanoparticles **[128, 129]**.

2.3.2.3.1. High Angle Annular Dark Field Scanning Transmission Electron Microscopy (HAADF STEM)

In HAADF-STEM, images are obtained by collecting electrons scattered to high angles using an annular dark-field detector, which is different from conventional dark-field imaging. The HAADF image is formed mainly from incoherently scattered electrons rather than Bragg-diffracted electrons. As a result, HAADF images show minimal diffraction contrast, and the image intensity is roughly proportional to the square of the atomic number (Z^2) **[130, 131]**. Due to this strong Z-contrast, small metal nanoparticles, even those with sizes around 1 nm or smaller, appear as bright spots in HAADF-STEM images, while they appear dark in bright-field STEM images.

2.3.2.3.2. Elemental Mapping in STEM

In STEM, two-dimensional atomic-scale chemical mapping can be achieved using electron energy loss spectroscopy (EELS) and energy-dispersive X-ray spectroscopy (EDX). With the introduction of aberration-corrected electron optics, probe sizes smaller than 0.1 nm have

become possible, enabling chemical mapping of crystalline materials with atomic resolution **[132, 133]**. However, EELS-based maps are sometimes difficult to interpret directly because the electron-matter interaction is nonlocal, which can complicate the analysis **[134]**. In contrast, EDX-STEM functions in a similar manner to STEM-EELS but uses a detector that effectively collects signals over a large solid angle. This wide-angle detection averages out phase-related effects, resulting in incoherent imaging, and therefore the obtained chemical maps are more straightforward and easier to interpret **[135]**.

TEM and HRTEM were performed on a Field Emission Gun Transmission Electron Microscope JEOL-TEM-2010, operating at 200 kV. HAADF-STEM images were obtained by an ultrahigh-resolution field emission gun coupled with a HAADF detector.

2.3.3. BET Characterization: Surface Area and Porosity

Surface area and porosity of materials are important properties that impact the quality and utility in various practical applications **[136]**. Differences in the surface area and porosity of particles within the material, which otherwise may have the same physical dimensions; can greatly influence its performance characteristics. N_2 sorption is commonly used technique to determine surface area and porous texture of the powdered nanoparticle and microparticle samples **[137]**. When gas is passed through the materials, exposed surface of material and gas molecules interact to each other. The result of this interaction is characterized as physical adsorption due the presence of an intrinsic surface energy. Adsorption is a reversible phenomenon due the weak Vander Waals bonds between gas molecules and the surface the material (less than 15 KJ/mole). Gas physisorption is considered non-selective, thus filling the surface layer by layer depending on the available solid surface and the relative pressure. The surface area of the material includes both the external surface and the internal surface of the pores depends on filling the first layer because the amount of gas adsorbed when the

mono-layer is saturated is proportional to the entire surface area of the sample. The complete adsorption/desorption analysis is called an adsorption isotherm.

When a material is exposed to a gas, an attractive force acts between the exposed surface of the solid and the gas molecules. The result of these forces is characterized as physical adsorption. Adsorption takes place because of the presence of an intrinsic surface energy. Due to the weak Vander Waals bonds involved between gas molecules and the surface (less than 15 KJ/mole), adsorption is a reversible phenomenon. Gas physisorption is considered non-selective, thus filling the surface layer by layer depending on the available solid surface and the relative pressure. Filling the first layer enables the measurement of the surface area of the material, because the amount of gas adsorbed when the mono-layer is saturated is proportional to the entire surface area of the sample. The surface area of a solid includes both the external surface and the internal surface of the pores. The complete adsorption/desorption analysis is called an adsorption isotherm. The six IUPAC standard adsorption isotherms are shown in **Figure 2.3a [138]**. The Type I isotherm is typical of microporous solids (pore diameter < 2nm). Type II is shown by finely divided non-porous solids. Type III implies a relatively weak interaction between adsorbent and adsorbate (i.e. water vapour on hydrophobic materials). Type VI and V feature a hysteresis loop generated by the capillary condensation of the adsorbate in the mesoporous material (pore diameter 2─50 nm). Type VI step-like isotherm represents step-by-step adsorption of multilayers (i.e. nitrogen adsorbed on special carbon). Isotherm shape depends on the porous texture of the material. Once the isotherm is obtained, a number of calculation models can be applied to different regions of the adsorption isotherm to evaluate the specific surface area (i.e. Brunauer–Emmett–Teller (BET), Dubinin, Langmuir, etc.) and pore size distributions (i.e. Barrett-Joyner-Halenda (BJH), DH, H&K, S&F, etc.) of the material. IUPAC classification of the hysteresis loops for mesoporous materials (type IV isotherm) several types of hysteresis are shown in **Figure**

2.3b, based on the pressure range over which the main boundary loop extends **[139]**. H1 type of hysteresis is associated with capillary tubes shaped pores open at both ends. H2 type of hysteresis loop is associated with open slit shaped pores with parallel walls. H3 type of hysteresis loop is associated with heterogeneous distribution of pores in the shape of capillary tubes with open ends. H4 type of hysteresis loop is associated with heterogeneous distribution of pores in the shape of capillary tubes with wide bodies and narrow necks. N_2 adsorption/desorption measurements on all the samples developed during the course of this research program were carried out by using BELSORB max (Japan) instrument at liquid nitrogen temperature (77K). BET and BJH methods were used for the determination of surface area and pore size distribution of the samples. The samples were degassed and dried under a vacuum system at 150°C for 2-3 h before the measurements.

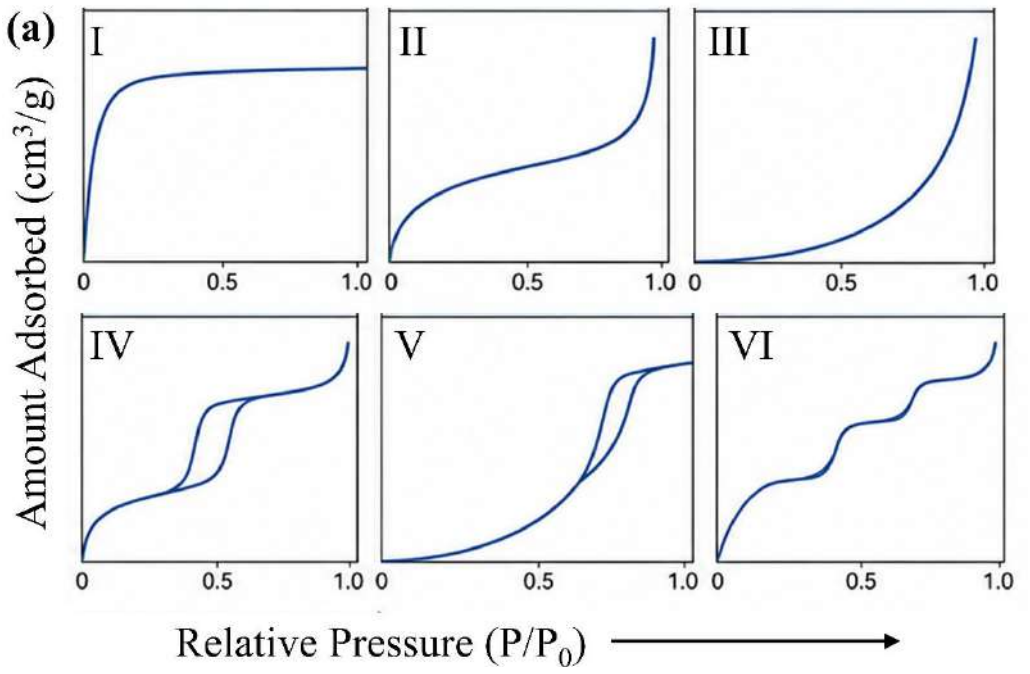

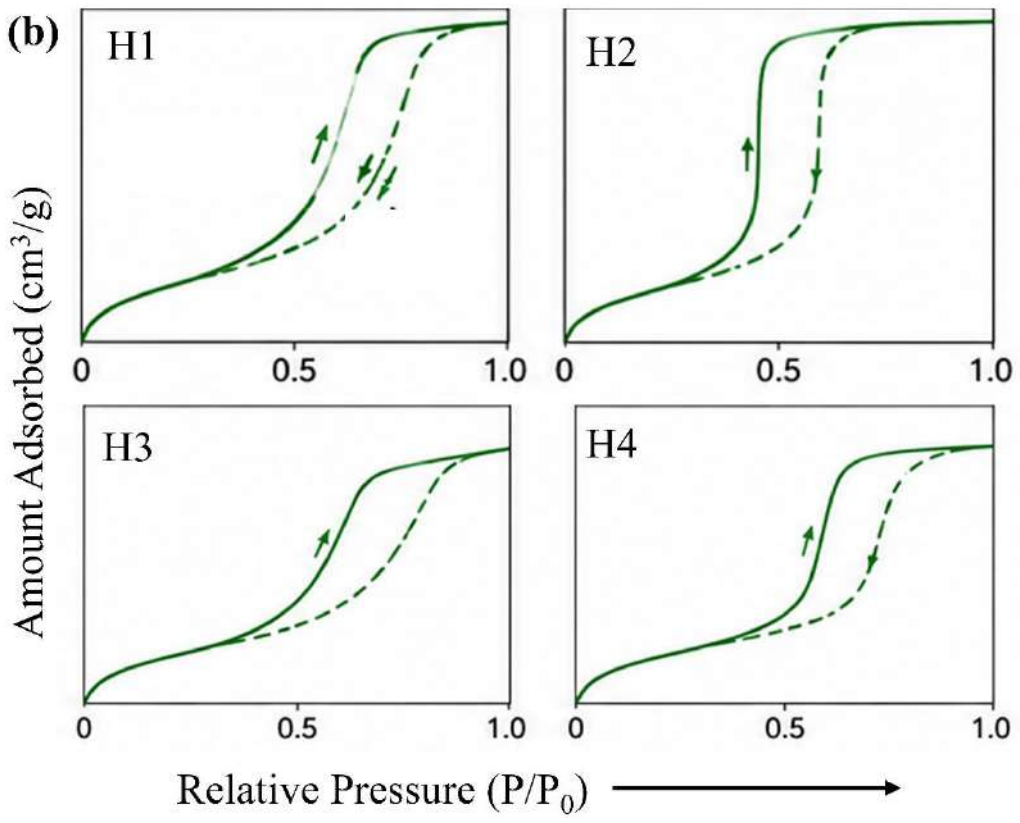

Figure 2.3. Types of sorption isotherms **(a)** and hysteresis loops **(b)** according to International Union of Pure and Applied Chemistry (IUPAC)

The Brunauer–Emmett–Teller (BET) specific surface area, BJH average pore size, and pore volume of the samples were obtained from the N2 adsorption/desorption isotherms recorded on BELSORP max (Japan) at 77 K. The samples were degassed and dried under a vacuum system at 150 °C for 2–3 h before the measurements.

2.3.4. Nanomaterials Characterization by Spectroscopy

2.3.4.1. Ultraviolet-visible Spectroscopy

UV/Vis spectroscopy is a powerful analytical technique for identifying, characterizing, and studying nanostructured materials **[140, 141, 39]**. Since UV/Vis spectroscopy involves the transition electrons from the ground state to the higher energy or excited state, it is also known as electronic spectroscopy. UV/visible spectroscopy is a method for measuring the amount of light that a sample absorbs and scatters (a quantity called the extinction, which is

defined as the sum of absorbed and scattered light). In its most basic version, a sample is positioned between a light source and a photodetector, and the intensity of a UV/visible light beam is measured both before and after it passes through the sample. The foundation of UV/visible spectroscopy is Beer Lambert law **[142]**, which states that when a monochromatic light beam passes through an absorbing substance solution, the rate at which the radiation intensity decreases is proportional to the incident radiation, the thickness of the absorbing solution, and the solution's concentration.

$$A = \log_{10}\left(\frac{I_0}{I}\right) = \varepsilon c l \qquad (2.2)$$

where A is the measured absorbance, I_0 is the incident light intensity, I is the transmitted light intensity, c is the molar concentration of the absorbing species, l is the route length through the sample, and ε is the extinction coefficient or molar absorptivity.

A UV/Vis spectrophotometer is a device used in ultraviolet-visible spectroscopy that consists of a light source, reference and sample beams, a monochromator, and a detector. The absorption edge for semiconductor nanomaterials with optical absorption in the UV-Vis range can be determined from diffused reflectance spectra obtained in UV-Vis spectroscopy. Tauc Plots can then be used to calculate the band gap energy of the materials using these absorption edge values **[143]**. The effects of quantum confinement in nanostructured materials can be shown via UV-Vis spectroscopy, as seen by the systematic blue shift of the absorption edge to a lower wavelength with decreasing particle size **[144]**.

UV-vis absorption spectra presented in this thesis were recorded were collected on a UV-vis-NIR spectrophotometer (Agilent Technologies, Cary 5000 with DRS 2500) in the 200–800 nm spectral region, at the CIF, RGIPT.

2.3.4.2. Fluorescence Spectroscopy

Photoluminescence (PL) spectroscopy is an optical characterization technique commonly

used to study the emission characteristics and recombination behaviour of emitted photons in luminescent materials. PL spectra were recorded on the Cary Eclipse Fluorescence Spectrophotometer (Agilent Technologies, Cary Series) instrument. The Cary Eclipse uses xenon flash lamp excitation, which provides high-intensity illumination pulse. The instrument has dual Czerny-Turner monochromators for the excitation and emission channels that provide accurate wavelength selection and efficient light rejection. The detection is done by a photomultiplier tube (PMT) which is a right angle to the excitation beam. This reduces the effect of scattered excitation light on the signal being measured. the PL spectra of developed material were recorded at room temperature with an appropriate excitation wavelength which was selected according to the absorption characteristics of the developed material **[145]**.

The PL spectra presented in this thesis were recorded using a Cary Eclipse Fluorescence Spectrophotometer (Agilent Technologies, Cary Series) at the Central Instrumentation Facility (CIF), Rajiv Gandhi Institute of Petroleum Technology (RGIPT).

2.3.4.3. Time-Resolved Photoluminescence Spectroscopy

Time-Resolved Photoluminescence (TRPL) is an optical spectroscopy technique for determining the dynamics of excited states in materials. In TRPL, a short LASER pulse excites electrons from the ground state to higher energy states and then these electrons relax back to the ground state emitting photons as light. This emitted light is called photoluminescence (PL). A detector records the intensity of emitted light as a function of time **[146]**. The result is a decay curve which shows the emission fades over time. The PL intensity, $I(t)$ typically decays exponentially and is given as:

$$I(t) = I_0 \times e^{-}\frac{t}{\tau} \qquad (2.3)$$

where τ is the carrier lifetime, which is the average time an excited electron survives before recombining.

The TRPL experiment was done at the Institute of Nano Science and Technology (INST), Mohali (Punjab), India. TRPL spectra of the photocatalyst were obtained using a Fluorolog HORIBA instrument at an excitation wavelength of 300 nm.

2.3.4.4. Raman Spectroscopy

Raman spectroscopy provides crucial information on the molecular structures of both inorganic and organic systems by examining the vibrational levels of molecules. Raman spectroscopy is very useful in the characterization of nanomaterials because it makes it easy to detect minute differences. Raman spectroscopy was once primarily used for fundamental research, but advancements in instruments (such as laser miniaturization, charge coupled device detection (CCD), notch filters, and data processing software) have transformed it into a useful tool for material characterization. Raman spectroscopy is a special instrument for characterizing micromechanical behaviour and assessing nano-scale structural changes. It may also give basic phase identification and modest spectra rectifications. Thus, Raman spectroscopy is an effective method for examining biological elements in bacteria **[147]**, nanophases distributed in a matrix **[148]**, surface-formed nanophases **[149]**, and solid-state electronics **[150, 151]**. Inelastic scattering, or Raman scattering of monochromatic laser light in the UV-visible region, is the foundation of Raman spectroscopy **[152]**. The energy of the laser photons is pushed up or down when the laser light interacts with a sample that has undergone a change in energy due to a transition to another higher energy level. The energy shift provides details on the system's vibrational modes.

Raman spectra of the samples were recorded in a Triple Raman spectrometer (model-T64000; J-Y Horiba) equipped with 1800 grooves/mm gratings, TE Cooled Synapse CCD (J-Y Horiba) and with an open-stage Olympus microscope with 50×objective. The samples were excited with a 514.5 nm wavelength laser from an Ar+ laser (model: Stabilite 2017, Spectra-

Physics). The integration time, number of accumulation (averaging), and laser power used for the analysis were 20 s, 4 times, and 500 micro-watts, respectively.

2.3.4.5. X-ray Photoelectron Spectroscopy

A surface-sensitive quantitative spectroscopic method for determining the elemental composition, empirical formula, chemical state, and electronic state of the elements on a material's surface is X-ray photoelectron spectroscopy **[45]**.

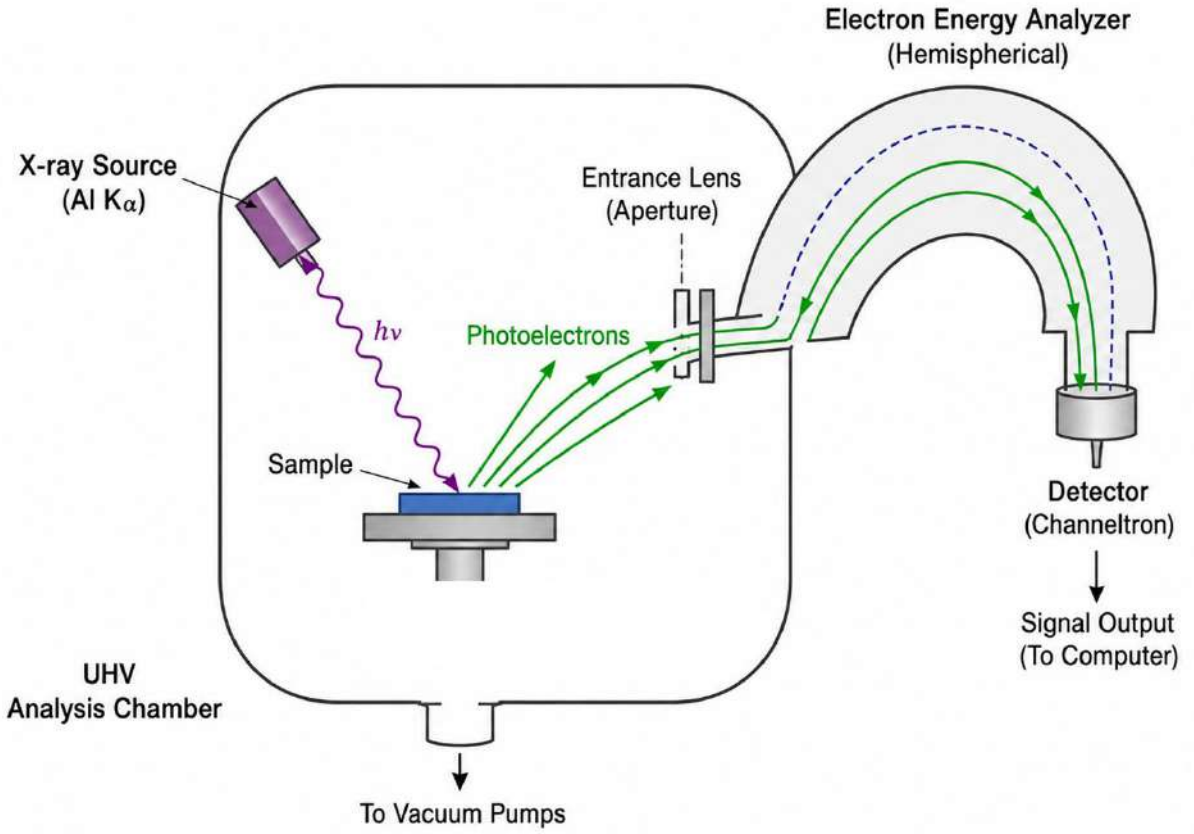

Figure 2.4. Schematic representation of an X-ray photoelectron spectroscopy (XPS) instrument, illustrating its major components, including the X-ray source, ultra-high-vacuum chamber, sample holder, electron energy analyser, detector, and data acquisition system.

As illustrated in **Figure 2.4**, XPS is usually done by stimulating a sample surface with mono-energetic Al-Kα X-rays, which causes photoelectrons to be released from the sample surface. The kinetic energy of the released photoelectrons is measured using an electron energy

analyser. An equation based on Ernest Rutherford's work from 1914 is used to determine the binding energy (EBE) of each of the released electrons **[153]**.

$$E_{B.E.} = E_{incident\ photon} - (E_{K.E.} + \Phi) \quad (2.4)$$

where $E_{K.E.}$ is the electron's kinetic energy as determined by the device, $E_{B.E.}$ is the electron's binding energy, $E_{incident\ photon}$ is the energy of the incident X-ray photons being employed, and Φ is the material's work function.

The elemental identification, chemical state, and quantity of a detected element can be ascertained from the binding energy and intensity of a photoelectron peak. XPS is a surface analysis method that is better suited for the compositional study of ultra-thin layers and thin microscale sample features since its normal analysis depth is less than 5 nm **[154]**.

XPS survey spectra were recorded on a thermos scientific K-ALAPHA+ surface analysis with Al-Kα X-ray (1486.6 eV) as the excitation source and the spectra were corrected by C1s spectra (284.8 eV).

2.3.4.6. Electron Paramagnetic Resonance (EPR)

Electron paramagnetic resonance is a spectroscopic technique used to analysis materials with unpaired electrons. Generally unpaired electrons are present in some systems like free radicals, transition metal ions (Cu^{2+}, Fe^{3+}, Mn^{2+}), defects, etc. When these systems are placed in an external magnetic field (B_0), unpaired electrons behave like tiny bar magnets and split into two spin states. The energy gap between the two spin states is:

$$\Delta E = g \times \mu_B \times B_0 \quad (2.5)$$

Where g is g-factor (~2.0023 for free electron, μ_B is Bohr magneton (9.274×10^{-24} J/T), and B_0 is applied magnetic field strength.

This splitting is called the Zeeman effect. In the technique a fixed microwave frequency is applied to the sample. The magnetic field is slowly swept until the exact resonance field is

reached and absorption occurs. The detector recording the signal is usually the first derivative of the absorption **[155].**

EPR analysis of developed materials was performed at IIT Delhi (Sonipat campus). EPR spectra were carried out at room temperature using a Bruker (A300-9.5/12/S/W) instrument operating in the X-band (9.8 GHz) and DC magnetic field (0-13 KG). This instrument consisted of an X-band, Q-band, ENDOR, and dual-mode resonator.

2.3.4.7 Electrochemical Impedance Spectroscopy (EIS) Analysis

Electrochemical Impedance Spectroscopy (EIS) is a powerful instrument to examine charge transfer and transport mechanisms in different electrochemical systems **[156-158]**. All impedance techniques are based on the concept of applying a small-amplitude sinusoidal excitation signal to the system under examination and measuring the current or voltage response of the device. For the impedance measurement, a frequency response analyzer (FRA) is employed to apply a small amplitude AC signal on the as-prepared samples as working electrodes. The FRA examines the working electrodes AC voltage and current response to calculate the resistive, capacitive, and inductive impedance **[158, 160]**. In this thesis work, Electrochemical Impedance Spectroscopy (EIS) measurements were performed on an electrochemical workstation (Metrohm Nova 2.1 Autolab) with a frequency range of 0.05 Hz – 10 kHz in the dark at an applied voltage of 0.5 V vs Ag/AgCl. Mott-Schottky (M-S) study was done in applied potential range from 1 to -1 V (vs Ag/AgCl) @ 1 kHz frequency.

2.3.5. X-Ray Absorption Spectroscopy (XAS)

XAS experiment is often performed at synchrotron facilities in the energy range of 5 to 25 keV. The main component of XAS beamline is Double Crystal Monochromator (DCM) which is used for energy selection from the white synchrotron beam. The beamline energy

range is useful for K-edge studies of elements with atomic numbers in the range 20<Z<47 and for L-edge studies of high-Z elements (Z>47). XAS is an element specific analytical technique for determine the oxidation state, coordination environment, electronic structure, and local atomic structure of materials. In addition, in-situ XAFS studies can be performed to monitoring the growth of nanoparticles in the solution phase **[161].** Generally, this analysis is mainly divided into two regions including X-ray absorption near-edge structure (XANES) and extended X-ray absorption fine-structure (EXAFS).

The experimental setup is capable of recording EXAFS spectra of the samples in transmission as well as in fluorescence mode. In the transmission mode there are three ionization chamber1, 2, and 3. Sample is placed between the ionization chamber-1 and 2. Ionization chamber 3 is used as reference metal foils for energy calibration. Ionization chamber 1 measures the incident flux and the ionization chamber 2 measures the transmitted intensity. In the fluorescence mode the sample is placed in front of the silicon drift detectors at 45º degree geometry.

The XAS experiments were performed using EXAFS Scanning beamline (BL-9) of Indus-2 Synchrotron Source (2.5 GeV, 200 mA) at Raja Ramanna Centre for Advanced Technology (RRCAT), Indore, India **[161].** Beamline optics involved the use of two long mirrors on both sides of a Double Crystal Monochromator (DCM). Meridional cylindrical pre-mirror made from Rh/Pt coating was employed for the purpose of collimating the X-rays and rejecting the higher harmonics in the vertical direction. This collimated beam was monochromated by using a Si (111) double crystal monochromator (2d = 6.2709 Å). The beam was focused vertically and horizontally at the sample location using a faced-down Rh/Pt-coated flexible post mirror and a sagittal cylindrical second crystal of the DCM, respectively. For the reduction in higher harmonics present in the X-rays, the second crystal of the DCM was detuned. The samples of pure powders were uniformly mixed with cellulose powder and then

made into a pellet form which was placed inside kapton tape. Copper foil was used for calibration purposes. Cu K-edge data were acquired using the fluorescence mode at room temperature. Using the fluorescence mode, the RaySpec 4 Channel SDD detector and sample were oriented at right angles and at 45° to the X-ray beam respectively. Ti K-edge data were acquired using the fluorescence mode at room temperature. Athena/Artemis software package 68, which is based on FEFF6, was used to analyze EXAFS data, including calibration, merging, and analysis. The fitting results were optimized using bond length (R), energy shift (ΔE_0), amplitude factor (S_0^2), and Debye–Waller factor (σ^2).

2.4. Material Studio: Density Functional Theory (DFT) calculations

DFT calculations presented in this thesis were carried out using the Materials Studio computational package. It integrates different products like CASTEP, DMol³, and Adsorption Locator under the Modules tab within a single platform. There are around 10–15 modules under the Modules tab of material studio. It provides user friendly interface to design and analyze next generation materials at the atomic level using computational methods like DFT. Material studio cover most of application area like pharmaceuticals, catalysts, polymers and composites, metals and alloys, batteries and hydrogen fuel cells, semiconductor, electronics, and consumer packaged goods. We have mainly used two modules: 1) DMol³ and 2)

These calculations were performed to gain atomistic insights into the structural, electronic, and catalytic properties of the investigated photocatalytic systems and to complement the experimental findings. The computational studies enabled a deeper understanding of the interactions between single metal atoms and faceted TiO_2 surfaces, as well as the underlying structure–activity relationships governing photocatalytic hydrogen production.

All computational studies presented in this thesis were carried out using Materials Studio software, utilizing the high-performance computing facilities available at the laboratory of

Prof. Anil Kumar Sinha at the Council of Scientific and Industrial Research–Indian Institute of Petroleum (CSIR-IIP), Dehradun, India.

2.5. Photocatalytic & Photoelectrochemical Testing Setup for performance testing of the developed materials

2.5.1. Photocatalytic water splitting experimental set-up

The experiments of the photocatalytic H_2 production were carried out in a photocatalytic reactor, which consisted of a 50 ml round bottom glass vessel made of borosilicate glass tightly sealed at the opening with silicon rubber septum at ambient temperature and atmospheric pressure and a high Power 450-W Xe lamp [Newport 94023A Oriel Sol3A, AM 1.5G (1000 W/m^2), solar simulator]. For a typical run, a glass vessel with 0.1 g of the photocatalyst sample suspended in 15 mL of pure water under continuous stirring using a magnetic stirrer was placed below the solar simulator and lit from the top of the glass vessel. The developed gases were collected after 2 h using an airtight gas syringe (Hamilton) and quantified with a gas chromatograph (Agilent 490 micro-GC) equipped with a thermal conductivity detector. The amounts of H_2 and O_2 generated were calculated by comparing the integrated area of the gas analyzer peaks with that of the known amounts of standard pure H_2 and O_2 gases.

2.5.2. PEC experimental set-up

PEC water splitting experiments were performed in a 200 mL three-electrode cell utilizing a μ-AUTOLAB type-III potentiostat in conjunction with a 75-W Xenon light source (Model LH-S-075X, SCIENCETECH, Canada) fitted with UV cutoff and visible light filters. The photocatalytic reactor possessed a light-irradiated surface area of 12.57 cm^2. The electrolyte consisted of 0.1 M H_2SO_4 (pH~1). A platinum mesh functioned as the counter electrode, Ag/AgCl as the reference electrode, and the photoelectrodes as a working electrode. Linear

sweep voltammetry (LSV) measurements were conducted across a potential range of −1.0 to 1.5 V relative to Ag/AgCl at a scan rate of 10 mV s^{-1} under both dark and simulated illumination conditions. Chronoamperometry (CA) assessments were conducted at –1.0 V relative to Ag/AgCl in both dark and illuminated conditions to quantify steady-state photocurrents for all photoelectrodes. Photocurrent and open-circuit potential measurements were conducted at various wavelengths.

PEC measurements were performed in an H-type glass cell to verify the nature of the gas generated at the working electrode, with the cathodic and anodic compartments isolated by a Nafion proton-exchange membrane (NRE-212, Sigma-Aldrich) to avoid product crossover. A 75-W Xenon lamp, fitted with a UV cutoff filter and visible-light-pass filters, used as the illumination source. The light intensity from the Xe lamp was quantified using a PVM210 irradiance meter (Megger Limited, Archcliffe Road, Dover, Kent, England). Before each PEC run, high-purity N_2 gas was introduced into both compartments for 30 minutes to eliminate dissolved oxygen and provide an inert atmosphere. The hydrogen produced in the cathodic compartment was analyzed using a Newchrom 6800 GC equipped with a thermal conductivity detector. The equipment was calibrated using standard H_2 gas (99.99%) prior to quantifying the gaseous products to achieve precise measurements.

2.5.3. Open circuit voltage decay (OCVD) measurement

During OCVD, the electrodes were maintained in darkness until the voltage stabilized. A 75-W Xenon light source (Model LH-S-075X, SCIENCETECH, Canada) was turned on the electrode-electrolyte interface of the electrode. After achieving steady photovoltage, the light source was switched off and subsequent photovoltage decrease was recorded.

2.5.4. Gas Analyzer

The gas analyzer is equipment that qualitatively and quantitatively analyses the species of

chemical gases in the sample **[163, 164].** It identifies the species and offers the numerical or graphical measurement value of the quantity. There are numerous forms of gas analysis depending upon the principle adopted for gas analysis like gas chromatograph, IR Gas analyser, thermal conductivity gas analyser, paramagnetic gas analyser etc. Gas chromatograph is a prevalent technique among them. **Figure 2.5** shows a typical gas chromatograph (GC) composed of several key parts: a supply of carrier gas for the mobile phase; a sample injection port; a column housed in an oven which can be temperature-controlled during the separation process; and a detector to monitor the eluent coming from the column. The GC columns are housed inside a temperature-controlled oven.

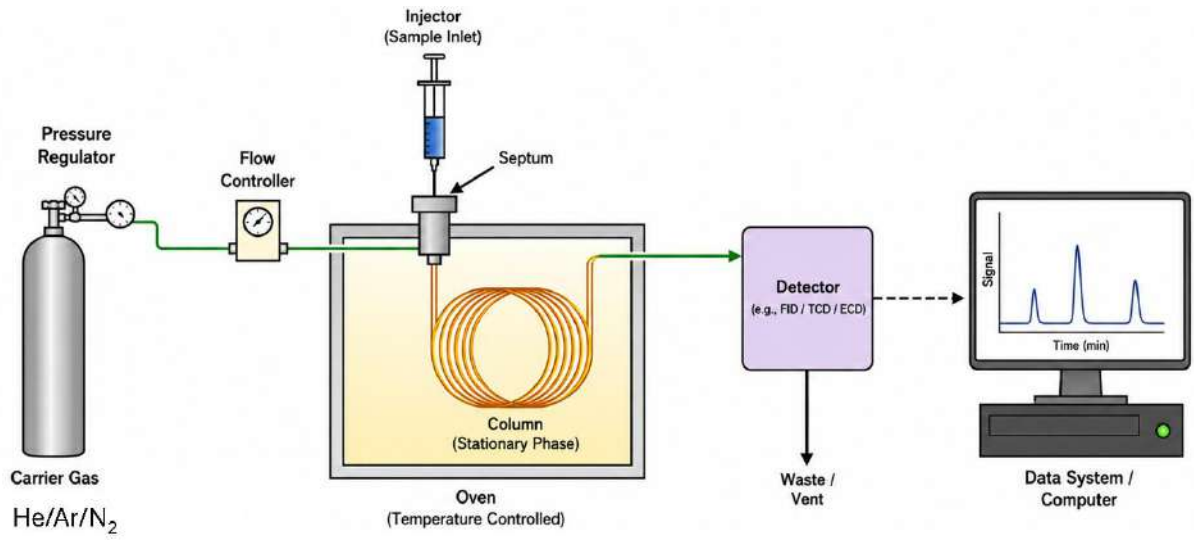

Figure 2.5. Schematic representation of a gas chromatograph (GC), illustrating its major components, including the carrier-gas supply, injector, chromatographic column, oven, detector, and data acquisition system.

The column is attached at one end to the inlet and at the other end to the detector. Columns are available in varying lengths, diameters and interior coatings. various columns are intended for various chemicals. The column and oven are used to separate the injected material into distinct compounds as it passes through the column.

In this thesis work, we have used a refinery gas analyser (Agilent 490 micro-GC) and a

Newchrom 6800 GC for the determination of evolved gases as a result of photocatalytic and photoelectrochemical water splitting, respectively. As each compound enters the detector, an electrical signal proportional to the amount of compound detected is generated. This signal is generally sent to a data analysis system such as Agilent ChemStation, where it shows up as a peak on a chromatogram.

Chapter: 3

Cu_{SA}-O_v-Ti_{3c} Atomic Sites Catalyst for Enhanced Photocatalytic Water Splitting

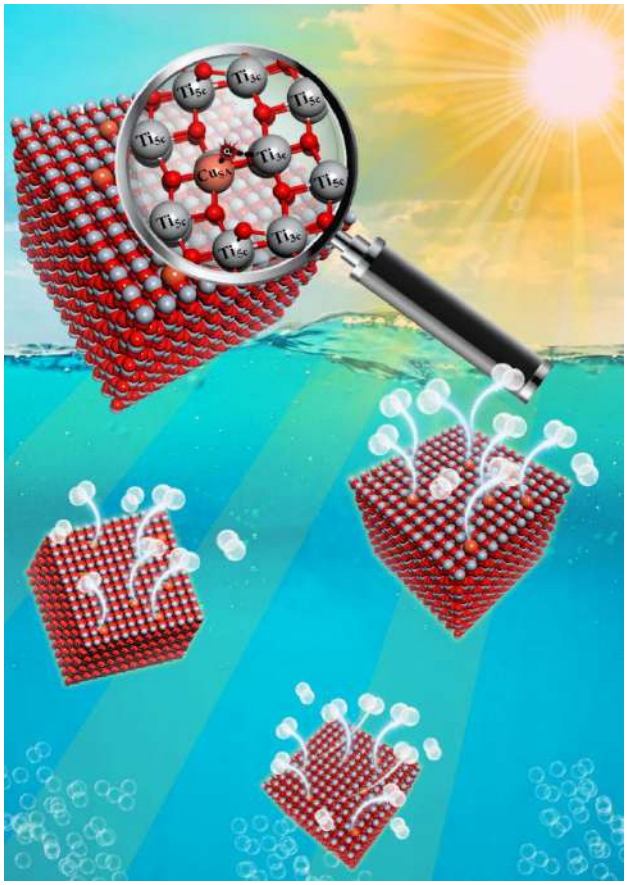

This chapter presents the development of Cu_{SA}-O_v-Ti_{3c} AASC by doping Cu-single atoms on (111)-faceted TiO_2. Experimental results and density functional theory (DFT) calculations reveal that Cu_{SA} specifically substitutes for the five-coordinated Ti atoms (Ti_{5c}) next to three-coordinated Ti atoms (Ti_{3c}), with the creation of oxygen vacancy (O_v) resulting in the formation of Cu_{SA}–O_v–Ti_{3c} AAS. The optimized catalyst demonstrates excellent visible-light-driven photocatalytic performance, achieving hydrogen evolution rates of 8.3 mmol $h^{-1}g^{-1}$, approximately 250 times higher than pristine TiO_2-based catalysts. Experimental and theoretical investigations reveal that Cu_{SA}-O_v-Ti_{3c} sites play multiple roles in (i) enhancing light harvesting, charge transfer dynamics and redox capability of photoexcited electrons; (ii) enhanced adsorption and polarization of H_2O molecules due to intrinsic charge heterogeneity at HAAS; (iii) facilitating electron transfer from Cu_{SA}-O_v-Ti_{3c} to H_2O molecules; and (iv) elevating the d-band center towards the Fermi level, thus facilitating the better adsorption of intermediates. Furthermore, a comparative analysis with recent Cu/TiO_2-based photocatalysts is provided to highlight the superior performance of the developed system.

3.1. Introduction

Photocatalytic water splitting to produce hydrogen (H_2) fuel offers a clean and sustainable approach for sustainable energy generation and environmental remediation concomitantly **[165, 166]**. Despite numerous efforts devoted to developing high-performance photocatalytic H_2-evolution systems, the activity of most of the photocatalysts developed so far is still limited, which should be attributed to their inappropriate band structures, fast recombination of photogenerated charge carriers, and sluggish surface reactions **[41, 167, 168]**. Furthermore, the use of expensive rare-earth elements such as Pt, Rh, Pd, and Au, significantly impedes the realization of such systems for any practical application **[169]**. Recently, Single-atom catalysts (SACs) involving metal single atoms (SAs) trapped on semiconductor supports have demonstrated maximum atomic utilization efficiency and tremendously high activity in heterogeneous catalysis and thus are expected to have great potential in photocatalytic water splitting **[83, 170]**. For example, Xie and coworkers demonstrated that the isolated Pt SAs anchored on g-C_3N_4 exhibited 8.6-fold higher photocatalytic H_2 production activity than Pt nanoparticles **[84]**. Li *et al.* demonstrated that Cu SAs trapped in Ti vacancies in a Cu/TiO_2 photocatalyst exhibited reversible and cooperative photocatalytic water splitting activity for enhanced H_2 production *i.e.*, 36-folds higher than pristine TiO_2 **[90]**. Stabilization of SAs demands specific anchoring sites on the supports that can be unsaturated surface atoms, surface defects, and any heteroatoms that can stabilize SAs through metal-support interactions **[171]**.

Recently, defects-rich metal oxides including TiO_2, In_2O_3, $W_{18}O_{49}$, and Fe_2O_3 have been identified as more suitable platforms in which oxygen/metal vacancies act as trap centers to effectively anchor SAs through enhanced metal-support interactions for better adsorption and activation of targeted molecules **[100, 172]**. More specifically, asymmetric atomic sites (AAS), generally expressed as M_{SA}-O_v-M_2 (where M_{SA} denotes the trapped

metal SA, O_v is the oxygen vacancy, and M_2 denotes semiconductor support) have been identified as the most preferable catalytic sites for enhanced catalytic/photocatalytic of these AASC **[97]**. For instance, Nie *et al.* reported atomically dispersed Pt^{2+}-O_v-Ce sites in Pt^{2+} doped CeO_2 catalysts with high CO oxidation activity and high thermal stability **[101]**. Gao *et al.* reported Pt/Fe_2O_3 catalyst with atomically dispersed Pt-Fe pair sites in which strong electronic coupling between Pt and Fe facilitates the adsorption and dissociation of O_2 molecules for high oxygen reduction reactions **[102]**. Hejazi *et al.* elucidated that Pt SA decorated on defective TiO_2 with surface Ti^{3+}/O_v vacancies (obtained by reducing TiO_2 films in Ar/H_2 environment at different temperatures) exhibited 150 times higher H_2 generation rate than Pt nanoparticles/TiO_2 catalyst **[173]**. Zhao *et al.* reported Cu SAs doped O_v-rich In_2O_3 ($Cu\text{-}In_2O_3/O_v$), which exhibited 31.8-fold peroxymonosulfate (PMS) activation than In_2O_3/O_v. This is attributed to the enhanced interfacial charge transfer between the PMS and $Cu\text{-}In_2O_3/O_v$ due to the presence of Cu-O_v-In asymmetric sites on the catalyst surface **[100]**. Similarly, Shen *et al.* predicted the strong electronic coupling between Cu SAs and adjacent Ti atoms to form Cu-Ti-O_v sites in $Cu/Ti_{0.91}O_2$ catalyst that allowed efficient and selective photoreduction of CO_2 to C_3H_8 **[174-176].** Despite these wonderful advances, the utilization of AASC in photocatalytic H_2 production remains constrained. Previous studies have predominantly utilized defects-rich metal oxides as support materials for creating AAS, which involve undesired consumption of H_2 gas and/or H_2/Ar gas, rendering them impractical for photocatalytic H_2 production **[84, 100, 101, 102]**. Moreover, achieving precise control over AAS remains a significant challenge with current capabilities in infancy. To harness the intriguing chemistry of AASC for photocatalytic H_2 production, judicious selection of support is essential while ensuring precise defect control. Furthermore, this approach should aim to achieve both high performance and cost-effectiveness, which are the ultimate goals in photocatalyst design.

High-index faceted nanostructures with intrinsic under-coordinated atoms on the surfaces have been explored for a myriad of applications **[177].** Anatase TiO_2, an extensively studied semiconductor, has been engineered to exhibit various exposed facets such as (101), (010), (001), and (111) as illustrated schematically in **Figure 3.1a [72, 73, 178, 179]**. Each facet owns its own unique surface atomic arrangement. Among all these facets ((101), (010), (001)), (111) is more promising because on (111) surface, all the Ti atoms are under-coordinated; *i.e.,* 75% atoms are five-coordinated Ti atoms (Ti_{5c}) and 25% atoms are three-coordinated Ti atoms (Ti_{3c}) with non-equivalent co-ordination environments as illustrated in Figure 3.1a. Furthermore, it is important to note that Ti_{5c} atoms on (111) facet marked as $Ti_{5c}(1)$ and $Ti_{5c}(2)$ (rightmost, Figure 3.1a) also have non-equivalent coordination environments **[73]**; $Ti_{5c}(2)$ is linked with $Ti_{5c}(1)$ on one side and $Ti_{5c}(3)$ on another side through Oxygen (O), and both $Ti_{5c}(1)$ and $Ti_{5c}(3)$ are five-coordinated Ti atoms. However, the $Ti_{5c}(1)$ atom is linked with one Ti_{5c} (*i.e.*, $Ti_{5c}(2)$) Ton one side and Ti_{3c} atom on the other side through O and thus gives rise to $Ti_{5c}(1)$-O-Ti_{3c} atomic sites near to Ti_{3c} atoms. It is worth mentioning that $Ti_{5c}(1)$-O-Ti_{3c} is an asymmetric atomic site (AAS) as the two Ti atoms *i.e.*, $Ti_{5c}(1)$ and Ti_{3c} around O have different coordination numbers. These findings indicate that (111) faceted TiO_2 contains intrinsic AAS and if these sites are utilized judiciously these sites can serve as excellent trapping centers for stabilizing metal SA for fabricating advanced AASC in contrast to conventional defect-rich metal oxides. Despite its fascinating surface chemistry, (111) faceted TiO_2 has not been even explored yet for stabilizing metal SA which may be due to the difficulties in synergetic coupling of crystal facet engineering with SA doping in a single material.

Inspired by the aforementioned advances, Cu_{SA}-O_v-Ti_{3c} highly asymmetric atomic sites (HAAS) were introduced in a rationally designed Cu-single atom trapped (111)-faceted TiO_2 ($Cu_{SA}FT_{111}$) HAASC, coupling the multiple advantages of high-index faceted

nanostructures and SAC in a single material for unprecedented H_2 production. As a proof of concept, 111 faceted TiO_2 with intrinsically undercoordinated Ti surface atoms is employed for Cu_{SA} trapping. Experimental results and density functional theory (DFT) calculations reveal that Cu_{SA} specifically substitutes for the five-coordinated Ti atoms (Ti_{5c}) next to three-coordinated Ti atoms (Ti_{3c}), with the creation of oxygen vacancy (O_v) resulting in the formation of Cu_{SA}–O_v–Ti_{3c} HAAS. In contrast to the conventional AAS, which generally includes two dissimilar atoms around O/O_v, HAAS designed in the presented work are highly asymmetric in two aspects: (i) these sites consist of two dissimilar metal atoms around O_v; and also (ii) the two metal atoms which constitute Cu_{SA}-O_v-Ti_{3c} sites have different coordination environments. Our investigations reveal that Cu_{SA}-O_v-Ti_{3c} HAAS play multiple roles in (i) enhancing light harvesting, charge transfer dynamics and redox capability of photoexcited electrons; (ii) enhanced adsorption and polarization of H_2O molecules due to intrinsic charge heterogeneity at HAAS; (iii) facilitating electron transfer from Cu_{SA}-O_v-Ti_{3c} to H_2O molecules; and (iv) elevating the *d*-band center towards the Fermi level, thus facilitating the better adsorption of intermediates. As a result, 0.9 at% of Cu in HAASC achieves an H_2 production rate of 8.3 $mmolh^{-1}g^{-1}$ in pure water and 784.5 $mmolh^{-1}g^{-1}$ in water/methanol (10:1, v/v) mixture, ~250 fold higher than AASC under stimulated AM 1.5G light irradiation.

3.2. Experimental Section

3.2.1. Synthesis of HAASC

HAASC was synthesized through a facile sol-gel assisted hydrothermal method, taking inspiration from our work on (111) faceted TiO_2 **[179]**. In a controlled synthesis procedure, first, 2 ml oleylamine (Sisco Research Laboratories, India) was dissolved in 90 ml of ethanol (Merck) under continuous stirring at ambient conditions. Subsequently, 6 ml Tetra-n-butyl orthotitanate (TNBT, Sisco Research Laboratories, India) was added in the solution which

was further stirred for 15 min. Thereafter a solution of 30 ml H_2O and 30 ml ethanol was added to the reaction mixture and further stirred for 3 hr at 500 rpm. The resulting product was separated by centrifugation and the obtained precipitates were washed several times with H_2O and then mixed with 160 ml ethanol and 80 ml H_2O. Thereafter 2 ml NH_3 solution (25%, Molychem) and 1 ml HF (48%, Molychem) solution were added dropwise, and the resulting mixture was further stirred for 30 min (solution A).

Cu precursor solution was prepared by mixing 0.092 gm cetyltrimethylammonium bromide (CTAB, Molychem), and 0.059 gm $CuSO_4.5H_2O$ (Molychem) in 10 ml of H_2O under continuous stirring. Thereafter a solution of 1 ml hydrazine hydrate in 10 ml H_2O was mixed under continuous stirring, which was further stirred for 15 min at 300 rpm (solution B).

Solution B was mixed with solution A dropwise under continuous stirring at 500 rpm. After 30 min, the mixture was transferred into a 250 ml Teflon-lined autoclave, which was sealed and heated at 160 °C in an electric oven. After the autoclave had cooled down to room temperature, the resultant product was separated by centrifugation and washed with H_2O and anhydrous ethanol several times. Finally, the product was dried at 100 °C for 24 hr and 550 °C for 2.30 hr at a heating rate of 10 °C/min in the electrical furnace to obtain $Cu_{SA}FT_{111}$ HAASC. FT_{111} was synthesized by following the same procedure for HAASC, without using Cu precursors. **Table 3.1**, summarizes the Ti, and Cu precursor concentrations used for the synthesis of different Cu(x)FT_{111} HAASC samples. Table 3.1, represents the calculated atomic concentration of Ti, and Cu in different Cu_{SA}(x)FT_{111} samples using Inductively coupled plasma-optical emission spectrometry (ICP-OES).

Table 3.1. Summary of precursor concentrations used for different $Cu_{SA}(x)FT_{111}$ HAASC samples

Sample	FT_{111}	$Cu_{SA}(0.61)FT_{111}$	$Cu_{SA}(0.9)FT_{111}$	$Cu_{SA}(1.24)FT_{111}$	$Cu_{SA}(1.28)FT_{111}$
TNBT	6 *ml*	6 *ml*	6 *ml*	6 *ml*	6 *ml*
$CuSO_4.5H_2O$	0 *gm*	0.029 *gm*	0.059 *gm*	0.12 *gm*	0.18 *gm*

3.2.2. EIS Experiment

EIS experiments were performed on an electrochemical workstation (Metrohm Nova 2.1 Autolab) with as-synthesized samples as working electrodes, a Pt mesh (1.5 × 1.5 cm) as the counter electrode and Ag/AgCl (saturated KCl) as a reference electrode. A Na_2SO_4 (0.1 M, Molychem) aqueous solution was used as an electrolyte. The working electrodes were prepared as follows: 50 mg photocatalyst was ground with 0.1 ml acetic acid (Merck), 0.2 ml ethanol, and 0.3 ml triton X-100 (Molychem) to make a homogeneous paste. Then the paste was coated on indium tin oxide (ITO) coated glass (0.5 × 0.5 cm) by the doctor blade technique. Subsequently, these electrodes were dried at 120°C and calcined at 500°C in a furnace for 30 min. EIS measurements were obtained at an applied voltage of (0.5 V vs. Ag/AgCl) in the dark in the frequency range of 0.05 Hz – 10 kHz. M-S analysis was performed in an applied potential range from 1 to –1 V (vs. Ag/AgCl) @ 1 kHz frequency. The donor density was obtained from the slope of the *M-S* plots using the following equation **[180]**:

$$Slope\ of\ MS\ plot = \frac{2}{e\epsilon\epsilon_0 A^2 N_D} \qquad (3.1)$$

Where ϵ is the dielectric constant (31 for TiO_2) **[181]**, ϵ_0 is the permittivity of vacuum, N_D donor density of *n*-type semiconductor, A is the area of the working electrode, and e is the electronic charge.

3.2.3. Photocatalytic measurements

The photocatalytic water splitting experiments were performed at room temperature. Typically, 0.1 g of the photocatalyst sample was dispersed in 15 mL of pure water in a 50 mL round bottom glass vessel made of borosilicate glass. The vessel was tightly sealed and purged with N_2 for 30 min. Subsequently, the suspension was irradiated by a 450-W Xe lamp (Newport 94023A Oriel Sol3A, AM 1.5G, solar simulator). During the photocatalytic experiments, the reaction mixture was continuously stirred using a magnetic stirrer. The gaseous products were collected using an airtight gas syringe (Hamilton) and quantified with a gas chromatograph (Agilent 490 micro-GC) equipped with a thermal conductivity detector. The amounts of H_2 and O_2 generated were calculated by comparing the integrated area of the GC peaks with that of the known amounts of standard pure H_2 and O_2 gases. The solar-to-hydrogen conversion efficiency (η_{STH}) was calculated by following equation **[182]**:

$$\eta_{STH} = \left[\frac{(\text{mmol } H_2 \text{ per s}) \times (237000 \text{ Jmol}^{-1})}{P_{Total} (\text{mW cm}^{-2}) \times \text{Area (cm}^2)}\right]_{AM1.5G} \quad (3.2)$$

For cyclic experiments and post-catalysis characterizations, the photocatalyst was collected from the reaction vessel after photocatalytic reactions via centrifugation and subsequently dried at 100 °C for 12 h without undergoing any additional treatment.

3.2.4. DFT Calculations

DFT calculations were performed using the Perdew-Burke-Ernzerhof (PBE) exchange-correlation function in the DMol3 module of Material Studio. Additionally, spin-polarized calculations were conducted using a plane wave pseudopotential method within the framework of the generalized gradient approximation (GGA) **[183, 184]**. The DFT-D correction using the (Tkatchenko-Scheffler) TS scheme was applied for dispersion (D) corrections. The 1 × 1 × 1 Monkhorst–Park scheme *k*-point set was used to integrate the

wavefunction in reciprocal lattice for all calculations. The structural models of FT_{111} (anatase TiO_2 with (111) exposed facets, space group: I41/amd) were built as 2 × 2 × 1 supercells with lattice constants of *a* =10.68 Å, *b* =10.20 Å, *c* =22.60 Å. A vacuum slab of 15 Å was created to eliminate interlayer interaction between the neighboring slabs. To create the structural model for $Cu_{SA}FT_{111}$ (Cu_{SA} trapped on (111) faceted anatase TiO_2), One Ti_{5c} atom ($Ti_{5c}(1)$), next to the Ti_{3c} atom was replaced by Cu_{SA} with the creation of O_v following the EXAFS results. The crystal structures and atom coordinates were also optimized firstly under the principle of energy minimization to obtain the appropriate cell parameters with stable structures for the models. The geometry optimization approached the convergence criteria for energy, maximum force, and maximum displacement on each atom was 5.4 × 10^{-4} eV, 0.1 eV/Å, and 0.005 Å respectively. We optimized the surface structure after fixing the atoms of the bottom two layers. Energy band gap, density of states (DoS), charge density difference (CDD), thermodynamic properties, and population analysis of optimized structures were studied.

To study the adsorption of H_2O on FT_{111} and $Cu_{SA}FT_{111}$, firstly Adsorption locator module **[185]** in Material Studio was employed to identify the possible adsorption sites and corresponding energies by carrying out Monte Carlo searches of the configuration space of the substrate-adsorbate system as the temperature is slowly decreased within the simulated annealing process of a molecular dynamics (MD) run. The lowest energy Configuration space using Monte Carlo simulations was returned after each annealing cycle of the MD run. Five cycles containing 50000 steps per cycle with annealing temperatures of 100 to 5000 *K* were used for reproducible results. The Monte Carlo parameters were set to a probability of 0.32 (ratio = 1) for 'conformer', 'rotate', and 'translate' while 'regrow' was set to 0.03 (ratio = 0.1). The COMPASS force field was used in conjunction with atomic charges calculated using CASTEP single-point energy calculations. Ewald and atom-based summation methods were

chosen for the electrostatic and van der Waals energy components respectively with the cut-off's set at 15.5 Å as validated by Zhao *et al* **[186]**. **Figures 3.19 and 3.20**, represent various structure models with H_2O adsorbed on different sites on FT_{111} and $Cu_{SA}FT_{111}$ respectively with corresponding energy values given in **Table 3.9**, which establish that Ti_{5c}-O-Ti_{3c} and Cu_{SA}-O_v-Ti_{3c} sites were identified as most preferable sites for FT_{111} and $Cu_{SA}FT_{111}$ respectively. These results were further used for geometry optimization and adsorption energy calculation, and Gibb's free energy calculations using the PBE exchange-correlation function in the DMol^3 module of Material Studio.

The adsorption energy of H_2O on the catalyst surface was calculated using Equation 3.3. **[102]**:

$$\triangle E_{A-H_2O} = E_{A-H_2O} - E_A - E_{H_2O} \quad (3.3)$$

Where E_{A-H_2O}, and E_A are the total energies of the photocatalyst surface with and without adsorbed H_2O respectively; E_{H_2O} is the total energies of H_2O molecules.

The Gibb's free energy ($\triangle G_H$) of hydrogen evolution reaction (HER) and complete H_2O reaction on the photocatalyst surface can be determined as: **[102]**

$$\triangle G_H = \triangle E_H + \triangle ZPE - T \triangle S \quad (3.4)$$

$\triangle E_H$ is the change of hydrogen adsorption energy, which can be calculated as **[102]**:

$$\triangle E_H = E_{*H} - E_* - \frac{1}{2}E_{H_2} \quad (3.5)$$

Where E_{*H}, and E_* are the total energies of photocatalysts with and without adsorbed atomic H, respectively; E_{H_2} is the total energy of hydrogen in gas.

$\triangle ZPE$ is the change of zero-point energy, which can be calculated as follows **[102]**:

$$\triangle ZPE = ZPE_{*H} - ZPE_* - \frac{1}{2}ZPE_{H_2} \quad (3.6)$$

Where ZPE_{*H} and ZPE_* are the zero-point energies of the photocatalyst with and without absorbed H atoms; ZPE_{H_2} is the zero-point energies of H_2 in the gas phase.

$\triangle S$ is the difference in entropy between the photocatalyst absorbed H atom and $\frac{1}{2}H_2$ in the gas phase and *T* denotes Temperature; Here, T = 298.15 K was considered.

3.3. Results and Discussion

3.3.1. Design of $Cu_{SA}FT_{111}$ HAASC and Materials Characterization

HAASC was synthesized through a facile sol-gel assisted hydrothermal method **[179]**. The synthesis procedure for $Cu_{SA}FT_{111}$ HAASC is illustrated in **Figure 3.1b**. First, a facile sol-gel assisted hydrothermal method was employed to synthesize sol-type TiO_2 in ethanol-H_2O solution using HF and NH_3 solution as facet-controlling agents **[179]**.

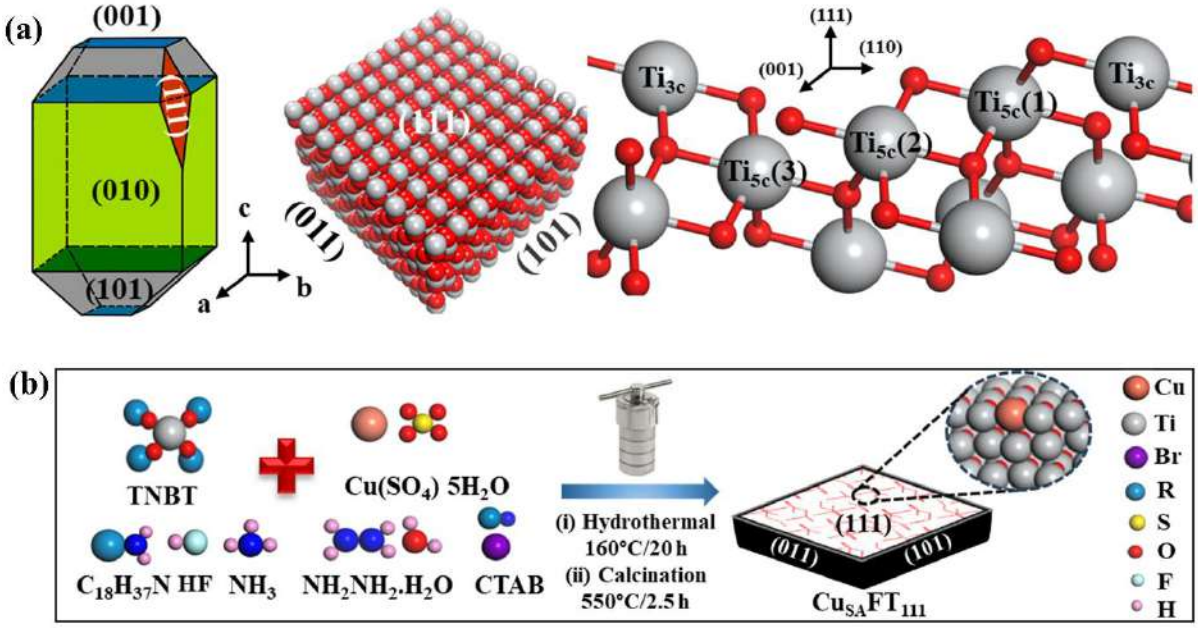

Figure 3.1. Synthesis of $Cu_{SA}FT_{111}$ HAASC**. (a)** A model of (111)-facet exposed TiO_2. Ti and O atoms are shown in grey and red colors. The right side is the top view of (111) surface atoms. There are mainly two types of Ti atom sites; five-coordinated Ti atoms (Ti_{5c}, 75%) and three-coordinated Ti atoms (Ti_{3c}, 25%) with non-equivalent coordination environments. Furthermore, $Ti_{5c}(2)$ is linked with $Ti_{5c}(1)$ on one side and $Ti_{5c}(3)$ on another side through oxygen (O). However, the $Ti_{5c}(1)$ atom is linked with one Ti_{5c} (*i.e.*, $Ti_{5c}(2)$) on one side and Ti_{3c} atom on the other side through O and thus gives rise to $Ti_{5c}(1)$-O-Ti_{3c} atomic sites near Ti_{3c} atoms. **(b)** Brief schematic of the HAASC synthesis process.

The Cu_{SA} were loaded on as-synthesized sol-type TiO_2 by mixing it with copper sulfate pentahydrate ($CuSO_4.5H_2O$) solution at room temperature. Subsequently, a hydrothermal process followed by controlled calcination allowed the fabrication of $Cu_{SA}FT_{111}$ nanostructures (for details see experimental 3.2.1). By changing the amount of $CuSO_4.5H_2O$, a series of $Cu_{SA}(x)FT_{111}$ catalysts with different Cu contents were synthesized. The $Cu_{SA}FT_{111}$ samples are named $Cu_{SA}(x)FT_{111}$, where x represents the atomic percentage (at%) of Cu obtained from the X-ray photoelectron spectroscopy (XPS) analysis. For comparison, (111-faceted TiO_2) (termed as FT_{111}, AASC) was also prepared by the same method without using Cu precursors. **Figure 3.2a** represents the Transmission electron microscopy (TEM) image of $Cu_{SA}(0.9)FT_{111}$ in which well-defined nanostructures (~20–30 nm) can be seen.

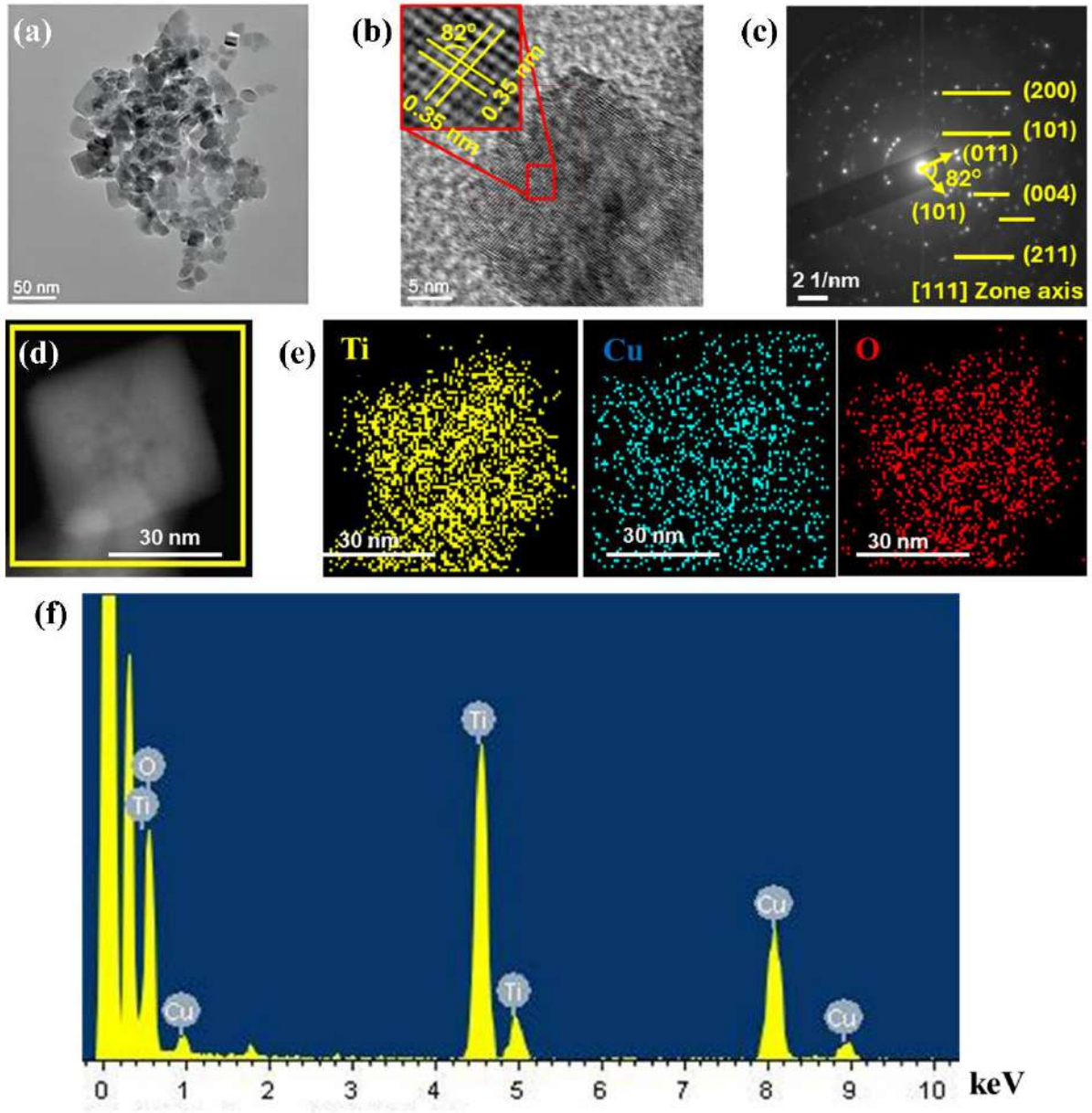

Figure 3.2. (a) A low-resolution TEM image of $Cu_{SA}(0.9)FT_{111}$. **(b)** A high-resolution TEM image. The inset shows the zoom-in view of the region marked in red color. **(c)** SAED pattern. **(d)** HAADF-STEM image. **(e)** Selected area EDS elemental maps of Ti, Cu, and O respectively. **(f)** EDS spectra of $Cu_{SA}(0.9)FT_{111}$, confirm the presence of Ti, O, and Cu elements.

Figure 3.2b shows a lattice-resolved high resolution (HR)-TEM image of a typical nanoparticle with a nanocuboid shape. A pair of lattice fringes of 0.35 nm with an interfacial angle of 82°, which could be ascribed to the (101) and (011) planes of anatase TiO_2. Importantly, even at the lattice-resolved resolution, no features corresponding to any of the

copper species (*i.e.*, Cu, CuO, and Cu_2O) are observed which can be ascribed to the atomically-dispersed nature of Cu species in $Cu_{SA}(0.9)FT_{111}$. The diffraction spots in the selected area electron diffraction (SAED) pattern **(Figure 3.2c)** can be indexed to (101), (004), (200), and (211) crystal planes of anatase TiO_2. A pair of different spots corresponding to (101) and (011) planes with an angle of 82° indicate [111] zone axis **[73, 179]**. These results indicate that $Cu_{SA}(0.9)FT_{111}$ nanostructures are (111) exposed facets **(Figure 3.2a).** Energy-dispersive X-ray spectroscopy (EDS) spectrum confirms the presence of Ti, Cu, and O elements in $Cu_{SA}(0.9)FT_{111}$ **(Figure 3.2f)**. Aberration-corrected High-angle annular dark-field scanning electron microscopy (HAADF-STEM) is then employed to probe the fine copper distribution. While the instrumental limitations prevented atomically resolved HAADF-STEM images for Cu_{SA} **(Figure 3.2d)**, EDS elemental maps **(Figures 3.2e)** reveal the homogeneous dispersion of Cu in $Cu_{SA}(0.9)FT_{111}$. The extension of the copper signal beyond the cubic boundaries of the particle is ascribed to the presence of the copper grid employed for TEM analysis. The elemental maps for Ti and O accurately mirror the cubic shape of the particle observed in the HAADF-STEM, validating that this discrepancy specifically pertains to copper and is a result of the copper grid utilized in the experimental procedure. **Figure 3.3a** shows Power X-ray Diffraction **(**XRD) patterns of $Cu_{SA}(0.9)FT_{111}$ and FT_{111}, where the diffraction peaks are mainly attributed to anatase TiO_2 with tetragonal structure (I41/amd, JCPDS no. 21-2172) **[34]**, without any Cu crystalline phase any (*i.e.*, Cu, CuO, Cu_2O), indicating that Cu doping does not alter the crystal structure of FT_{111}. Furthermore, it also suggests the highly dispersed nature of Cu species in $Cu_{SA}FT_{111}$. Raman spectra of $Cu_{SA}(0.9)FT_{111}$ **(Figure 3.3b)** closely resemble FT_{111}, with five dominant major peaks which can be ascribed to E_g (144, 196, 636 cm^{-1}) and $B1_g$ (396 cm^{-1}) modes of anatase TiO_2 **[187]**. No peaks of Cu oxide species are observed, in agreement with the absence of Cu-related peaks in XRD.

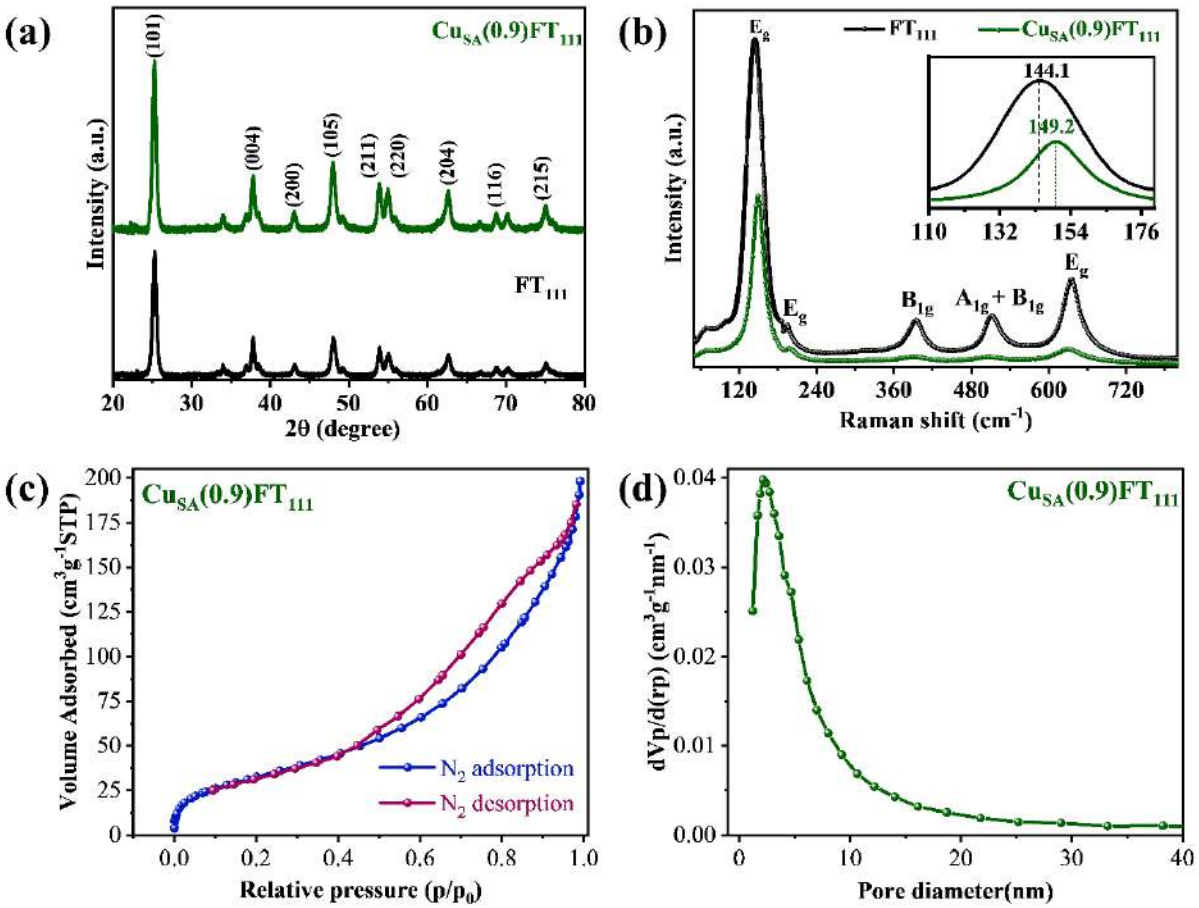

Figure 3.3. (a) Powder XRD patterns of FT_{111} and $Cu_{SA}(0.9)FT_{111}$. **(b)** Raman spectra of FT_{111} and $Cu_{SA}FT_{111}$. The inset shows the close-up view in the range of 110-180 cm^{-1}. **(c)** N_2 adsorption-desorption isotherm. **(d)** Corresponding BJH pore-size distribution curve of $Cu_{SA}(0.9)FT_{111}$ HAASC. It exhibits a type IV isotherm with a hysteresis loop, which is a typical characteristic of mesoporous materials. The single peak in the BJH pore size distribution curve indicates uniform porosity in the material.

The significant decrease in intensity of Raman peaks and their shifting towards high wavenumber **(Inset, Figure 3.3b)** in $Cu_{SA}(0.9)FT_{111}$ can be correlated with the formation of oxygen vacancies (O_v) as a result of the charge compensation effect when Cu_{SA} are trapped on the TiO_2 surface **[188]**. These material characterization results confirm the formation of Cu-single atom trapped (111) faceted TiO_2 nanostructures ($Cu_{SA}FT_{111}$) in the presented work. Thanks to our synthesis procedure which allowed the successful integration of two different approaches *i.e.*, facets engineering (maintaining high-index (111) exposed facets) and metal

single atom (*i.e.*, Cu_{SA}) doping in a single material which is rarely reported to the best of our knowledge.

Table 3.2. Surface and porous characteristics measured from N_2 adsorption/desorption isotherms for FT_{111} and $Cu_{SA}(0.9)FT_{111}$ photocatalyst.

Sample	Surface area (S_{BET}) (m^2/g)	Mean pore diameter ($<d_p>$) (nm)	Pore Volume (cm^3/g)
FT_{111}	122.3	6.7	0.38
$Cu_{SA}(0.9)FT_{111}$	138.9	2.1	0.31

N_2 adsorption-desorption isotherms **(Figure 3.3c, d)** along with Barrett-Joyner-Halenda (BJH) pore size distribution confirm the inter-particle mesoporosity in $Cu_{SA}(0.9)FT_{111}$ **[189]**. The specific surface area (S_{BET}), mean pore diameter ($<d_p>$), and pore volume (V_p) are calculated as 138.9 m^2/g, 2.1 nm, and 0.31 cm^3/g respectively as given in **Table 3.2**. Room-temperature electron paramagnetic resonance (EPR) spectra **(Figure 3.4a)** were obtained to evaluate the paramagnetic properties of $Cu_{SA}(0.9)FT_{111}$. **Figure 3.4a** shows the EPR spectra of FT_{111} and $Cu_{SA}(0.9)FT_{111}$. For FT_{111}, a typical peak is observed at $g_{\perp} = 2.002$, which can be ascribed to intrinsic under-coordinated Ti^{3+} species present on the surface of FT_{111} **[190]**. However, $Cu_{SA}(0.9)FT_{111}$ shows an intense asymmetric peak ($g_{\perp} = 2.211$) with hyperfine lines ($g_{\parallel} = 2.365$) in the low field region which is the characteristic of Cu^{2+} ions being located in tetragonally elongated octahedral sites **[191-194]**. The disappearance of the Ti^{3+} EPR peak after Cu doping indicates that Cu^{2+} ions have substituted for Ti^{3+} ions in $Cu_{SA}FT_{111}$. The $g_{\parallel} > g_{\perp}$ indicates that the ground state of Cu species is $d_{x^2-y^2}$ **[191]**.

3.3.2. Site-specific location of Cu and formation of Cu_{SA}-O_v-Ti_{3c} HAAS

XPS analysis was used to investigate the chemical state of elements. The high-resolution Ti2p spectrum of FT_{111} and $Cu_{SA}(0.9)FT_{111}$ **(Figure 3.4b)** displays two main peaks at 458.4 eV ($Ti2p_{3/2}$) and 464.2 eV ($Ti2p_{1/2}$). The O1s spectra **(Figure 3.4c)** revealed three peaks, including lattice oxygen (O_I) at approximately 529.3 eV, oxygen vacancies (O_v) around 531.1 eV, and surface adsorbed water or hydrocarbons (O_{II}) at 532.6 eV **[192, 193]**.

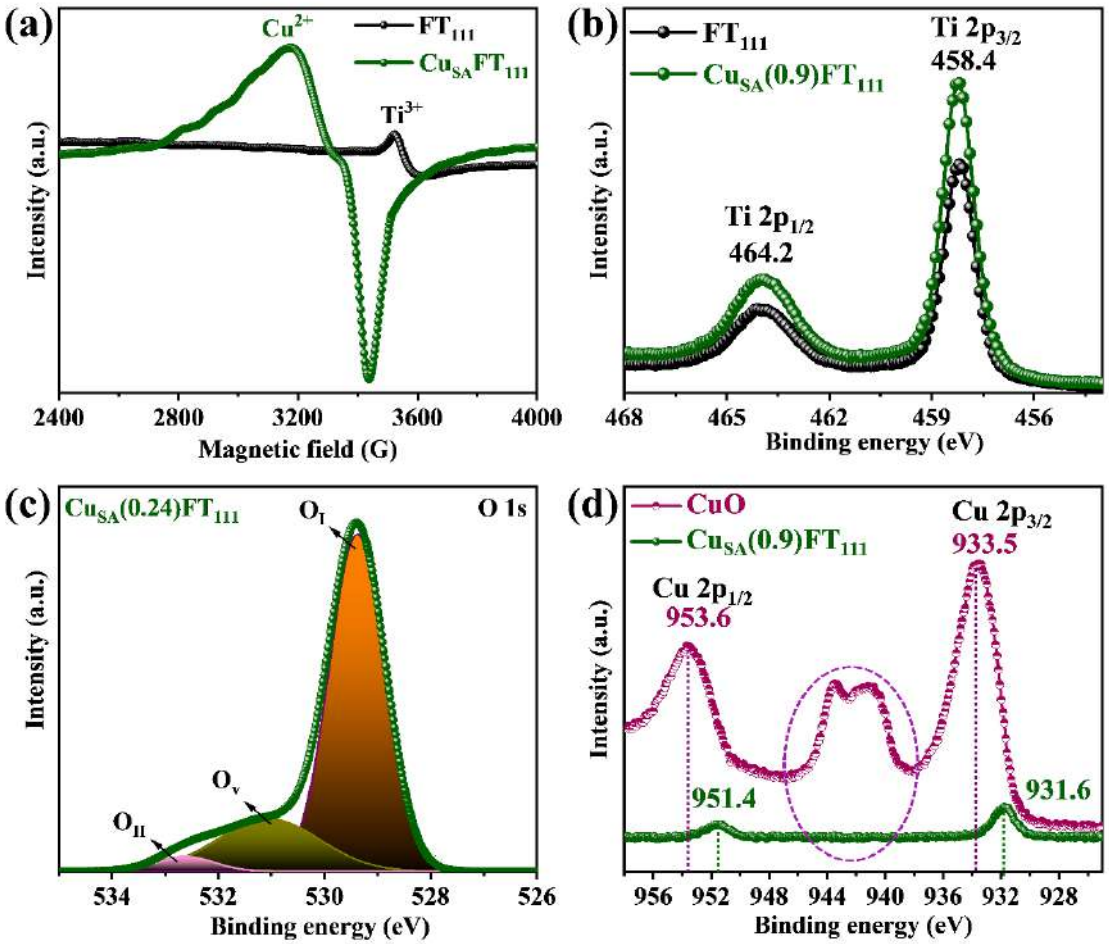

Figure 3.4. (a) EPR spectra of FT_{111} and $Cu_{SA}(0.9)FT_{111}$. **(b)** High-resolution XPS spectra of Ti*2p* for FT_{111} and $Cu_{SA}(0.9)FT_{111}$. **(c)** High-resolution XPS spectra of O1s spectra $Cu_{SA}(0.9)FT_{111}$. Three peaks signify lattice oxygen (O_I), oxygen vacancies (O_v), and surface adsorbed water or hydrocarbons (O_{II}). **(d)** High-resolution XPS spectra of Cu*2p* of CuO (used as reference material) and $Cu_{SA}(0.9)FT_{111}$.

To find the chemical state of Cu dopants in $Cu_{SA}FT_{111}$, another sample (CuO) was prepared by the same hydrothermal method without using TiO_2 precursors. **Figure 3.4d** shows the high-resolution Cu2p spectra of CuT_0 and $Cu_{SA}(0.9)FT_{111}$. The binding energy peaks centered at 933.5 ($Cu2p_{3/2}$) and 953.6 eV ($Cu2p_{1/2}$) in CuO with the characteristic shake-up satellite peak at around 942 eV declare that Cu exists in +2 oxidation state, mainly as bulk CuO **[195].** Notably, Cu2p peaks in $Cu_{SA}(0.9)FT_{111}$ exhibit two distinct features; first, the satellite peak is completely disappeared and second, the Cu2p peaks are shifted to lower binding energy values. These results can be ascribed to (i) the atomically-dispersed/isolated nature of Cu^{2+} species in $Cu_{SA}(0.9)FT_{111}$, as it is reported that Cu^{2+} isolated species exhibit lower binding energy compared to bulk Cu^{2+} in CuO; **[195]** (ii) the existence of strong electronic coupling between Cu_{SA} and Ti species *via* O_v, as identified through Raman analysis **(Figure 3.3b)**.

Extended X-ray absorption fine structure (EXAFS) spectroscopy was utilized to further probe the chemical state and local environment of Cu_{SA} in $Cu_{SA}(0.9)FT_{111}$. **Figure 3.5a** shows the normalized Cu K-edge X-ray absorption near-edge (XANES) profiles of FT_{111} and $Cu_{SA}(0.9)FT_{111}$ with Cu foil, CuO, and Cu_2O used as reference materials. Notably, the XANES absorption edge of $Cu_{SA}(0.9)FT_{111}$ overlays with reference CuO, indicating that the oxidation state of Cu species in $Cu_{SA}(0.9)FT_{111}$ is +2. The pronounced differences in the XANES profiles between the $Cu_{SA}(0.9)FT_{111}$ and Cu foil exclude the possibility of Cu-Cu coordination in $Cu_{SA}FT_{111}$. Extended X-ray absorption fine-structure (EXAFS) analysis was used to evaluate the precise location of Cu_{SA} and its local environment. **Figure 3.5b** shows the Fourier transform (FT) of Cu K-edge EXAFS spectra of $Cu_{SA}(0.9)FT_{111}$, which shows a dominating Cu-O peak at ~1.35 Å, which nearly overlays with the Cu-O peak at ~1.45 Å of the CuO. Interestingly, a minor scattering peak at ~2.25 Å is attributed to Cu-Ti coordination in the second coordination sphere. Notably, no signal for Cu-Cu/Cu-O-Cu bonding is observed in $Cu_{SA}(0.9)FT_{111}$. These results confirm that Cu atoms replace Ti atoms in

$Cu_{SA}(0.9)FT_{111}$ and these trapped Cu atoms are isolated without any aggregation in the form of Cu/Cu_xO_y. EXAFS fitting results for $Cu_{SA}(0.9)FT_{111}$ give a coordination number (CN) of 4 for Cu-O contribution in the first coordination sphere with a bond length of ~1.92 Å and CN of 4 for Cu-Ti contribution in the second coordination sphere with a bond length of ~2.86 Å **(Figure 3.6a, b and Table 3.3)**.

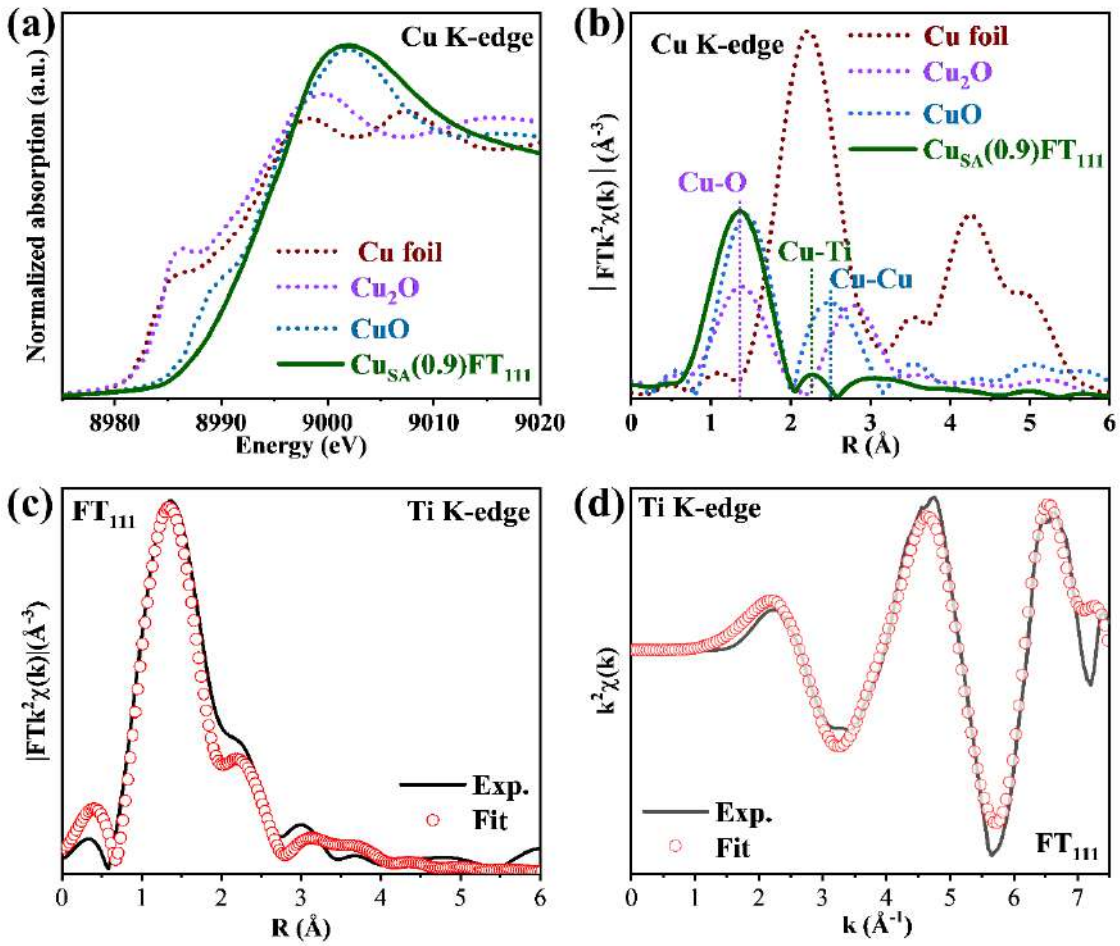

Figure 3.5. (a) Normalized XANES spectra of Cu *K*-edge for Cu foil, CuO, Cu_2O, and $Cu_{SA}(0.9)FT_{111}$. **(b)** Cu *K*-edge k^2-weighted Fourier transform EXAFS spectra. **(c, d)** Experimental (solid grey line) and best-fitted (red circle line) Ti K-edge EXAFS spectra of FT_{111} in *R* space, *k* space respectively. The obtained best-fitted parameters are given in **Table 3.3.**

Whereas the EXAFS fitting results for FT_{111} verify a CN of 5 for Ti-O contribution in the first coordination sphere with a bond length of ~1.92 Å and CN of 4 for Ti-Ti contribution in

the second coordination sphere with a bond length of ~3.06 Å **(Figure 3.5c, d and Table 3.3)**. The lower CN for Cu-O in $Cu_{SA}(0.9)FT_{111}$ indicates the formation of O_v upon the substitution of Ti atoms by Cu_{SA}. Moreover, a reduction in bond length between Cu and Ti indicates significant distortion in the second coordination sphere of $Cu_{SA,}$ suggesting the formation of Cu_{SA}-O_v-Ti sites. The obtained best-fitted parameters are given in **Table 3.3**. It is worth mentioning that, in the presented work we are dealing with the trapping of Cu_{SA} on the TiO_2 (111) surface, an aspect that has not been previously investigated. On the (111) surface, there are mainly two types of five-coordinated Ti atoms (*i.e.*, $Ti_{5c}(1)$ and $Ti_{5c}(2)$, **(Figure 3.1a)** and three-coordinated Ti atoms (Ti_{3c}) with non-equivalent coordination environments **[73]**.

Table 3.3. Detailed information on M-O and Ti-M contributions from EXAFS fitting.

Sample	Scattering Path	N	R (Å)	σ^2 (Å^2)	R-factor (%)
FT_{111}	Ti-O	5	1.92±0.015	0.001	0.019
	Ti-Ti	4	3.06±0.029	0.002	
$Cu_{SA}FT_{111}$	Cu-O	4	1.92±0.005	0.001	0.014
	Cu-Ti	4	2.86±0.061	0.040	

N= Coordination number, R= Interatomic distance, σ^2 = Debye-Waller factor (bond disorder)
R-factor = A measure of the quality of EXAFS fitting

A close comparison of FT-EXAFS spectra of Ti K-edge and Cu K-edge in FT_{111} and $Cu_{SA}(0.9)FT_{111}$ can provide more insight into the site-specific location of Cu_{SA} in $Cu_{SA}(0.9)FT_{111}$. As revealed in **Figures 3.6c, d**, the EXAFS spectrum of Ti K-edge in FT_{111} and $Cu_{SA}(0.9)FT_{111}$ is very similar, whereas Ti K-edge and Cu K-edge spectra in $Cu_{SA}FT_{111}$ are significantly different. These results are quite interesting compared to the previous reports on single-atom Cu/TiO_2 systems, which claimed similar Ti K-edge and Cu K-edge

when Cu_{SA} replaced Ti atoms **[90]**. As mentioned already, we are dealing with the TiO_2 (111) surface for trapping of Cu_{SA} (not studied so far), the results obtained in our work can be explained based on the exclusive replacement of $Ti_{5c}(1)$ atoms (*i.e.*, Ti_{5c} atoms next to Ti_{3c} atoms) by Cu_{SA} as follows: the similarity between Ti K-edge in $Cu_{SA}(0.9)FT_{111}$ and FT_{111} can be attributed to $Ti_{5c}(2)$ and $Ti_{5c}(3)$ atoms, which have identical surroundings in both the materials.

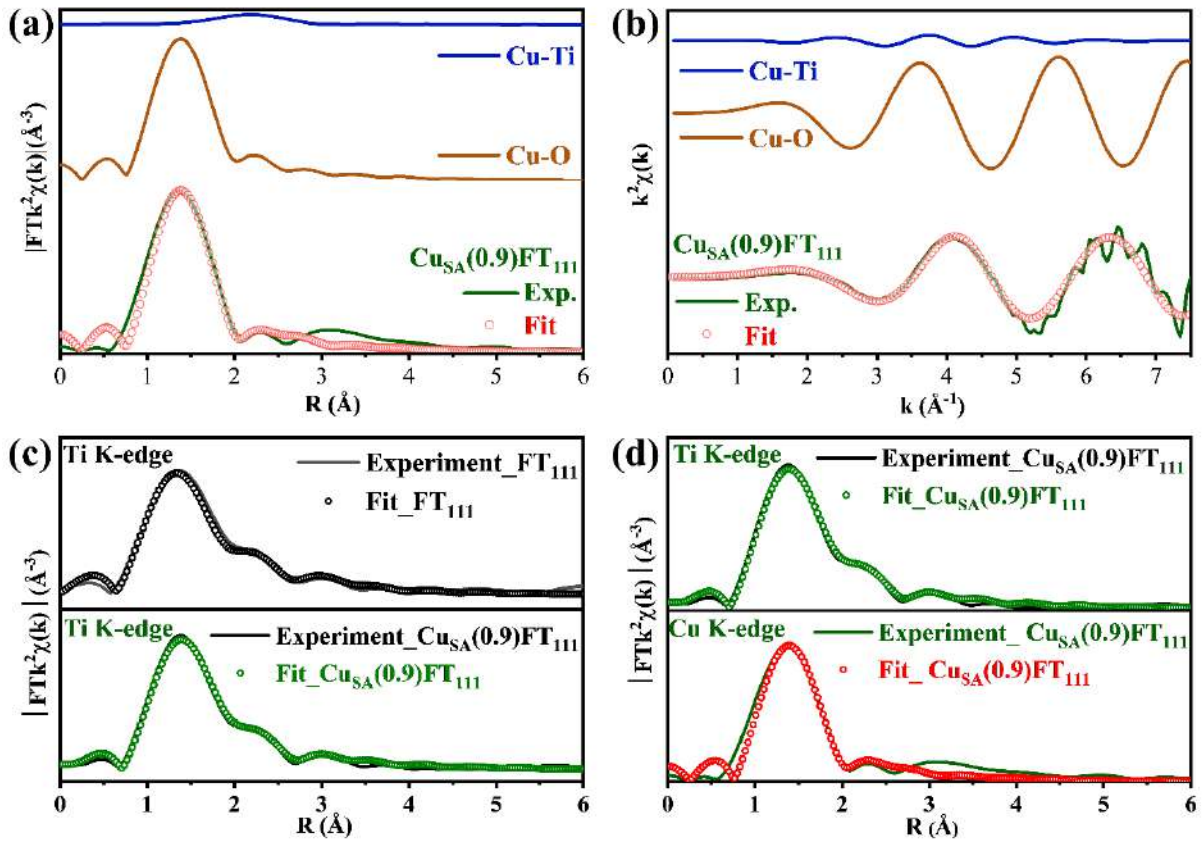

Figure 3.6. Experimental (solid green line) and best fitted (red circle line) Cu K-edge EXAFS spectra of $Cu_{SA}(0.90)FT_{111}$ in **(a)** *R* space; **(b)** *k* space. For clarity, Cu-O (solid brown line) and Cu-Ti (solid blue line) contributions in the fitted spectra are also highlighted. The obtained best-fitted parameters are given in Table 3.2. **(c)** Best-fitted EXAFS spectra of Ti *K*-edge for FT_{111} and $Cu_{SA}(0.9)FT_{111}$. **(d)** Best-fitted EXAFS spectra of Ti *K*-edge and Cu K-edge of $Cu_{SA}(0.9)FT_{111}$.

However, the mismatch between the Ti K-edge and Cu K-edge in $Cu_{SA}FT_{111}$ can be attributed to the replacement of $Ti_{5c}(1)$ by Cu_{SA} and the formation of Cu_{SA}-O_v-Ti_{3c} HAAS, resulting in

an obvious change in the two spectra. The Cu_{SA}-O_v-Ti_{3c} sites formed in our rationally designed $Cu_{SA}FT_{111}$ are highly asymmetric in two aspects: (i) these sites consist of two dissimilar metal atoms around O_v; and also (ii) the two metal atoms that constitute these sites have different coordination environments. To date, only the asymmetric sites M_1-O_v-M_2, with different metal atoms only (similar coordination environments) have been reported as reactive sites in several redox reactions **[196-198]**.

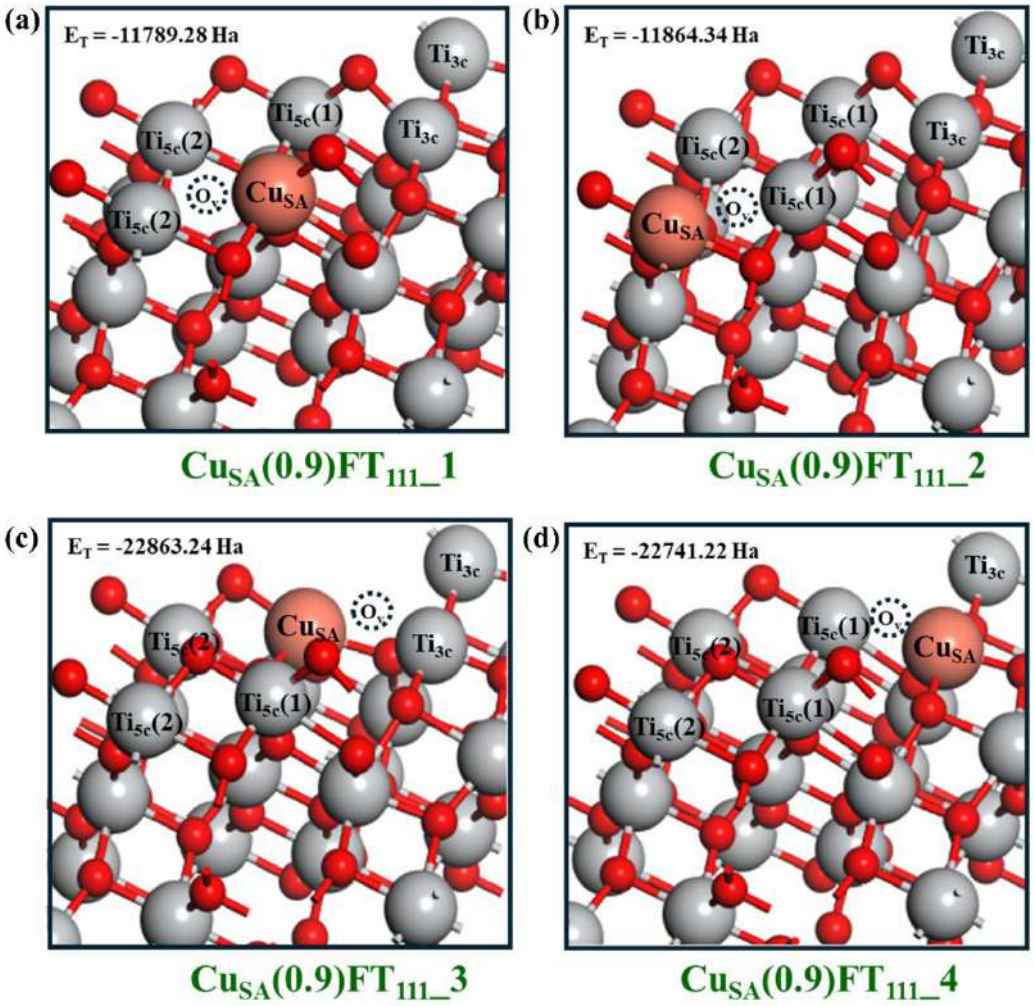

Figure 3.7. (a-d) Optimized structures when Cu_{SA} is substituted for different undercoordinated Ti atoms ($Ti_{5c}(1)$, $Ti_{5c}(2)$, and Ti_{3c} atoms) on (111) facets of TiO_2 and corresponding total energy. The total energy of the system is lowest, when Cu_{SA} substitutes specifically for $Ti_{5c}(1)$ atoms (i.e., Ti_{5c} atoms next to Ti_{3c} atoms) compared to $Ti_{5c}(2)$ atoms and/or Ti_{3c} atoms itself.

Density Functional Theory (DFT) calculations further support the formation of Cu_{SA}-O_v-Ti_{3c} HAAS sites in $Cu_{SA}FT_{111}$. We tried Cu substitution for different under-coordinated Ti atoms ($Ti_{5c}(1)$, $Ti_{5c}(2)$, and Ti_{3c} atoms, **Figure 3.8**) on the TiO_2 (111) surface and calculated the total energy of these systems using the DMol3 module **(Figures 3.7a-d and Table 3.4)**.

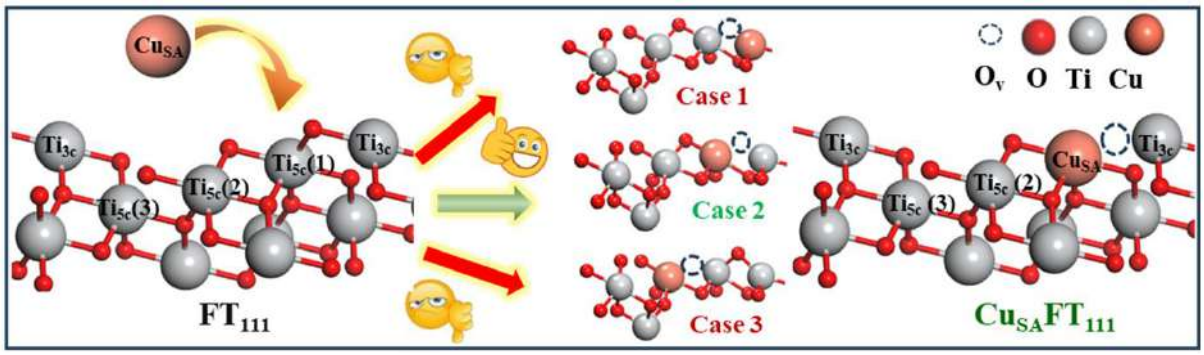

Figure 3.8 Schematic representation of the creation of Cu_{SA}-O_v-Ti_{5c} HAAS when Cu_{SA} specifically replaces Ti_{5c} atoms adjacent to Ti_{3c} atoms based on EXAFS results.

Table 3.4. Total energy of the optimized structures after the Cu_{SA} substitution on different undercoordinated Ti atoms on (111) faceted TiO_2.

Sr. No.	Optimized Structure	Total energy (E_T), Ha
1	$Cu_{SA}FT_{111}$_1	−11789.28
2	$Cu_{SA}FT_{111}$_2	−11864.34
3	$Cu_{SA}FT_{111}$_3	−22863.24
4	$Cu_{SA}FT_{111}$_4	−22741.22

$DMol^3$ allows efficient and accurate determination of the most stable configuration for a variety of systems including metal oxides as reported previously **[199, 200]**. It is found that the total energy of the system is lowest when Cu_{SA} substitutes specifically for $Ti_{5c}(1)$ atoms

(*i.e.*, Ti_{5c} atoms next to Ti_{3c} atoms) compared to $Ti_{5c}(2)$ atoms and/or Ti_{3c} atoms itself *i.e.*, case 2 is easiest to form as illustrated in **Figure 3.8.** These simulation results indicate that the formation of Cu_{SA}-O_v-Ti_{3c} HAAS sites is thermodynamically favorable and supports the EXAFS results.

3.3.3. Photocatalytic performance of HAASC for water splitting under visible light

The $Cu_{SA}(x)FT_{111}$ catalysts were evaluated for photocatalytic water-splitting reactions under visible light irradiation (AM1.5, 100 mW/cm^2) using pure water (unless otherwise specified). Firstly, $Cu_{SA}(x)FT_{111}$ catalysts with varied amounts of Cu (0, 0.61, 0.9, 1.24, and 1.28 at%) were investigated for 4 hr and it was found that the photocatalyst with 0.9 at% of Cu exhibited the highest activity **(Figure 3.9a)**. Thereafter catalyst dosages were optimized **(Figure 3.9b)** for further photocatalytic studies. It is important to note that only H_2 and O_2 gases were detected in the gaseous product **(Figure 3.10)**.

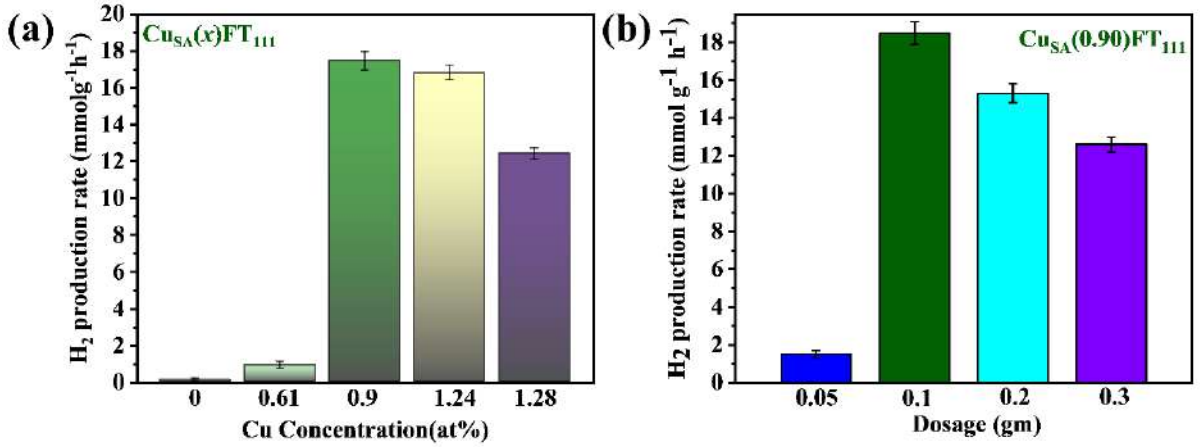

Figure 3.9. Photocatalytic H_2 production activity of HAASC. **(a)** Photocatalytic H_2 production in different HAASC catalysts (Cu at%, 0, 0.61, 0.9, 1.24, and 1.28). **(b)** H_2 production rates under different dosages of $Cu_{SA}(0.9)FT_{111}$ photocatalyst.

Figure 3.11a shows yield-irradiation time plots of H_2 and O_2 evolution for 10 hr for $Cu_{SA}(0.9)FT_{111}$ and FT_{111}. It is noted that H_2 generation in FT_{111} (0.33 mmolg^{-1}) is poor and nearly undetected. In contrast, $Cu_{SA}(0.9)FT_{111}$ exhibits an impressive H_2 generation of ~83

$mmolg^{-1}$ in 10 hr of photocatalytic water splitting experiments. The amount of O_2 generated is ~41 $mmolg^{-1}$, indicating a stable stoichiometric decomposition of H_2O to ~2:1 H_2/O_2 in $Cu_{SA}(0.9)FT_{111}$ HAASC. The H_2 generation is quite fast up in the first 6 hr and then gradually slows down, a commonly observed phenomenon in photocatalysis **[201, 202]**.

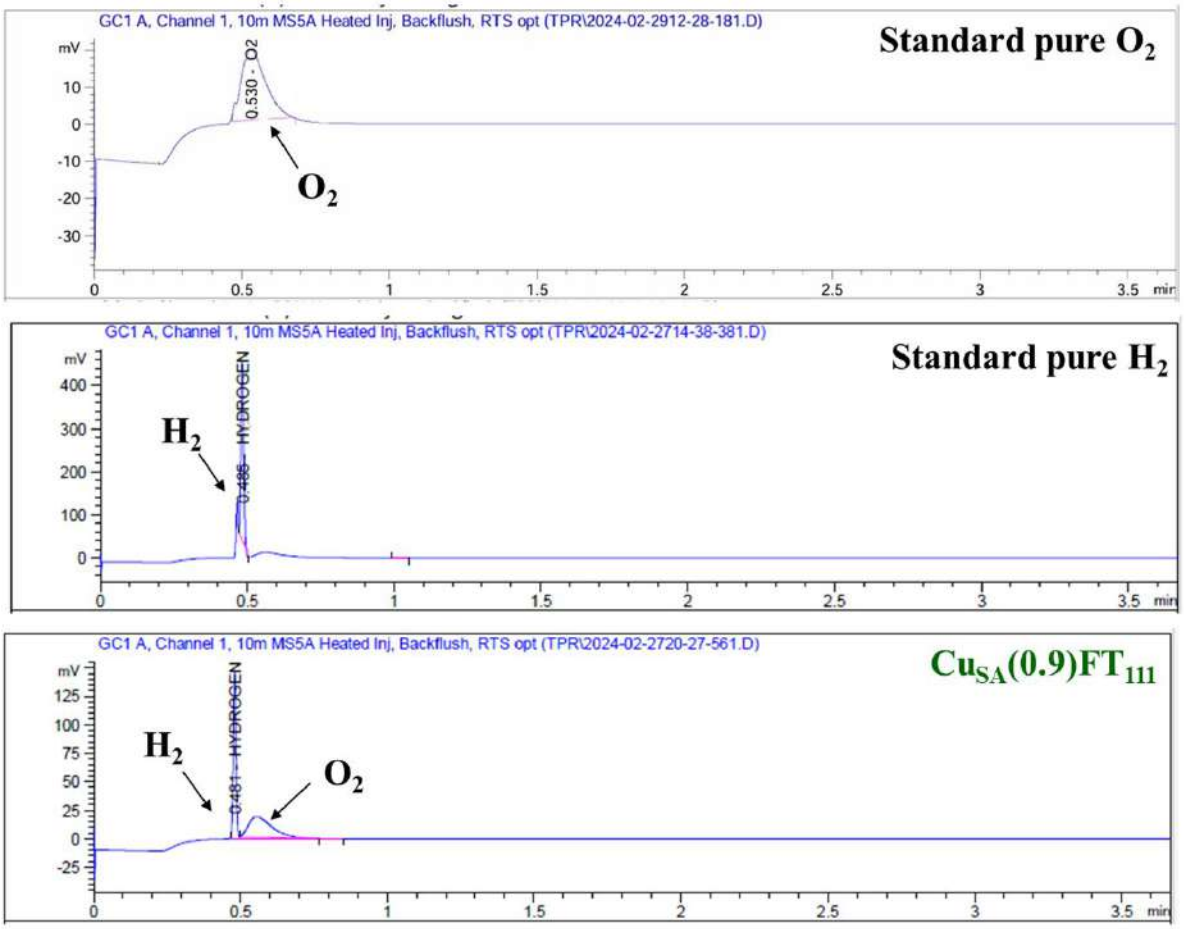

Figure 3.10. The gas products obtained from the photocatalytic water splitting reactions in the presented work, Only H_2 and O_2 are detected in $Cu_{SA}(0.9)FT_{111}$ photocatalyst.

The H_2 production rate in $Cu_{SA}(0.9)FT_{111}$ (8.3 $mmolg^{-1}h^{-1}$) is ~250-fold higher than that of FT_{111} (0.033 $mmolg^{-1}h^{-1}$) as shown in **Figure 3.11b**. The amount of H_2 produced was calculated by comparing the integrated area of the GC peaks with that of the known amounts of standard pure H_2 gas **[203]**

$$PV = nRT \qquad (3.7)$$

Moles (n) of pure hydrogen gas in 10 µl Volume H_2 at normal temperature (27°C) and

pressure (115 bar) is given by,

$$n = \frac{PV}{RT}$$

$$n = \frac{115 \times 10^5 \times 10^{-8}}{8 \cdot 314472 \times 300}$$

$$n = 46 \cdot 104\ \mu mol$$

i.e., 237.21 area of pure H_2 in 10 µl Volume H_2 contains 46.104 μmol of H_2.

Calculation of H_2 Production when 15 ml H_2O is taken in a 50 ml beaker.

237.21 area of pure H_2 in 10 µl Volume H_2 contains 46.104 μmol of H_2.

10.26 area of $Cu_{SA}FT_{111}$ sample in 10 µl Volume H_2 in 4 hours contains

$\frac{46 \cdot 104 \times 10.26}{237.21} = 1 \cdot 9941 \mu mol$ of H_2.

10.26 area of $Cu_{SA}FT_{111}$ sample in 35 ml volume H_2 in 4 hours contains

$\frac{1 \cdot 9941 \times 35}{10} = 6 \cdot 97935$ mmol of H_2.

Hence H_2 production rate of the $Cu_{SA}FT_{111}$ sample in 35 ml volume H_2 is 1.745 $mmolh^{-1}$.

Hence H_2 production rate of the $Cu_{SA}FT_{111}$ sample (per gram) in 35 ml volume H_2 is 17.45 $mmolg^{-1}h^{-1}$. The optimized. 0.1 gm of the photocatalyst was used for photocatalytic reactions. Similarly, the amount of H_2 generated was calculated for 6 h and 10 h of the photocatalytic reactions. The average value calculated after 10 h is 8.27 $mmolg^{-1}h^{-1}$

A similar procedure was utilized for the calculation of H_2 produced from H_2O + CH_3OH (10:1) solution.

These results demonstrate that Cu_{SA}-O_v-Ti_{3c} HAAS are more reactive photocatalytic water-splitting sites than Ti_{5c}-O-Ti_{3c}. It is worth mentioning that the H_2 production rate (8.3 $mmolg^{-1}h^{-1}$) obtained in the presented work in pure water is ~5–35 times higher than the previous reports **(Figure 3.11c) [204-206]**, which may open new avenues towards the development of low-cost, high-performance photocatalytic water splitting systems.

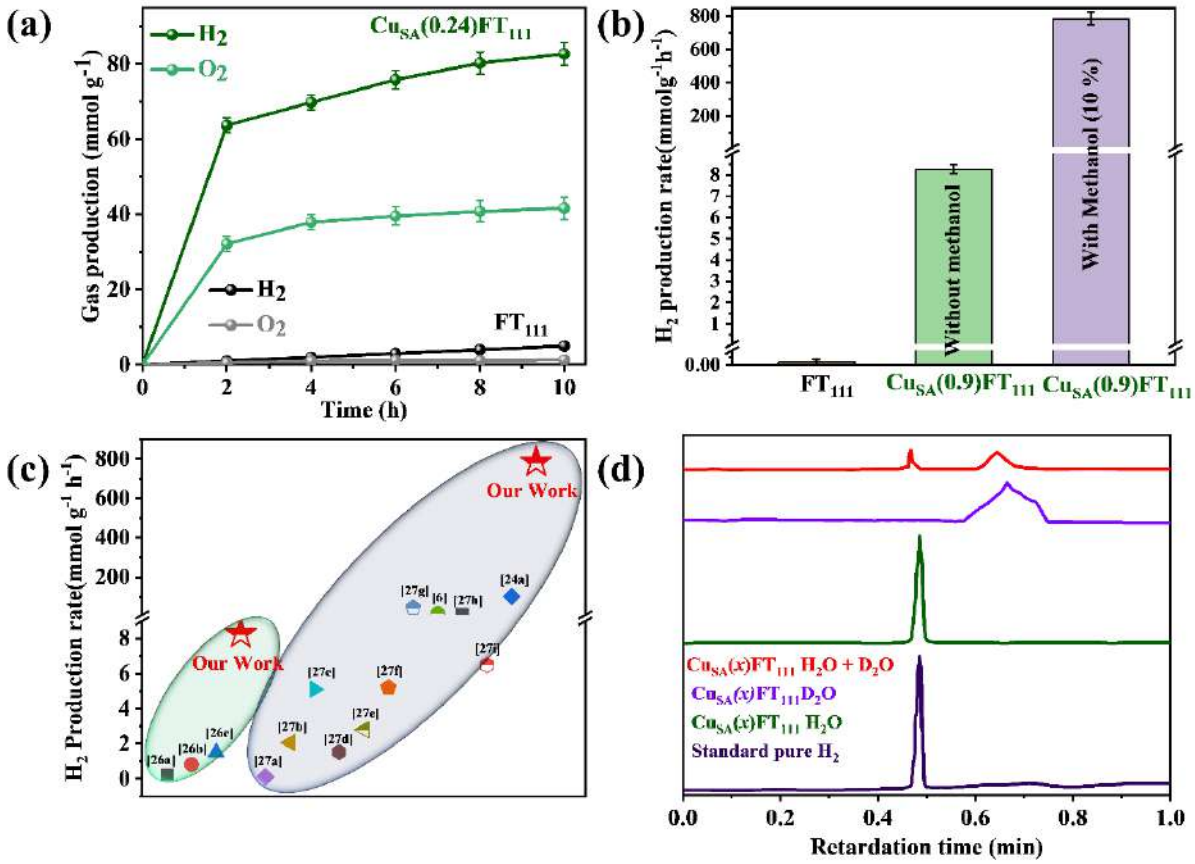

Figure 3.11. (a) H_2 and O_2 yield-irradiation time plots of $Cu_{SA}(0.9)FT_{111}$ and FT_{111}. **(b)** Rate of photocatalytic H_2 gneration in $Cu_{SA}(0.9)FT_{111}$ and FT_{111}. **(c)** Comparison of H_2 production rates achieved in the presented work with the previous reports. **(d)** The signals obtained for the gaseous products from photocatalytic reactions using H_2O, D_2O, and D_2O + H_2O as reaction mixtures (pure H_2 gas is taken as reference).

For better comparison with the previous reports, we performed photocatalytic reactions using water/methanol (10:1; v/v) solution, where an unprecedentedly high H_2 production rate of 784.5 $mmolg^{-1}h^{-1}$ is obtained which is one of the highest reported so far to the best of our knowledge **(Figure 3.11c and Table 3.5) [199, 200, 207-215]**. Notably, a high solar-to-hydrogen conversion efficiency (η_{STH}) of *cal.* 6.64 % was achieved.

Table 3.5. Comparison of photocatalytic H_2 production obtained in the presented work with the previous reports.

Sr. No.	Photocatalyst	Incident light (Light intensity)	Reaction Solution	Cocatalyst	H_2 evolution rate (mmol h^{-1} g^{-1})	References
1	BiOBr/C	Xe lamp (300W)	Water	No	0.24	**[204]**
2	BDCNN350/BDCNN425	Xe lamp (300W)	Water	Pt and Co	0.823	**[205]**
3	Ni_2P/ PCOS	Xe lamp (300W)	Water	No	1.507	**[206]**
4	**Cu_SAFT_{111}**	**Xe lamp (450W)**	**Water**	**No**	**8.3**	**This work**
5	Ni/TiO_2	300 W Xe lamp	Water + 10% methanol	Ni	0.11	**[207]**
6	MoS_2/graphene/TiO_2	350 W Xe lamp (80.0 mW cm^{-2})	Water + 25% methanol	MoS_2/graphene	2.066	**[208]**
7	Cu-TiO_2 nanowire	4×3 W UV-LEDs (80.0 mW cm^{-2})	Water + 25% methanol	Cu metal	5.104	**[209]**
8	Cu_2O/TiO_2	300 W Xe lamp (80.0 mW cm^{-2})	Water + 20% methanol	Cu_2O	1.523	**[210]**
9	Cu/TiO_2	300 W Xe lamp (80.0 mW cm^{-2})	Water + 10% methanol	Cu metal	2.8	**[211]**
10	Pt/black TiO_2	300 W Xe lamp	Water + 20% methanol	Pt	5.2	**[212]**
11	Pt/brookite TiO_2	4 W Hg lamp	100% methanol	Pt	45	**[213]**
12	Cu/TiO_2	300 W Xe lamp (100.0 mW cm^{-2})	Water + 25% methanol	No	16.6	**[90]**
13	Co/NGC@$ZnIn_2S_4$	Xe lamp (300W)	Water + triethanolamine (1 ml)	No	11. 27	**[214]**
14	$ZnIn_2S_4$@MXene	Xe lamp (300W)	Water + 10% triethanolamine	No	6.482	**[215]**
15	Cu/TiO_2	Xe lamp (500W)	Water + methanol	No	101.7	**[199]**
16	Pt/TiO_2	Xe lamp (450W)	Water + methanol	Pt	11.2	**[216]**
17	**Cu_SAFT_{111}**	**Xe lamp (450W)**	**Water + 10% methanol**	**No**	**784.53**	**This work**

The presented work establishes the concept of HAAS as highly reactive centers to achieve unparalleled H_2 generation results. The solar-to-hydrogen conversion efficiency (η_{STH}) was calculated by using equation 3.2 **[182]**:

For a round bottom flask of 50 ml, surface area = 81.67 cm^2

Total H_2 produced = 8.3 mmol per hour

P_{Total} = 100 mW/cm^2 (AM 1.5G)

$$\eta_{STH}(\%) = \left[\frac{\left(\frac{8.3}{3600}\ mmol\ H_2\ per\ s\right) \times (237000\ Jmol^{-1})}{(100\ mW\ cm^{-2}) \times (81.67\ cm^2)}\right] \times 100$$

$$\eta_{STH} = 6.69\ \%$$

Controlled experiments confirm the nature of reactions in the presented work **(Table 3.6)**. No H_2 is detected in the absence of visible light, and in the absence of photocatalyst confirming that H_2 generation is purely photocatalytic in nature. Controlled Isotopic tracing experiments are performed on $Cu_{SA}(0.9)FT_{111}$ to confirm the H-source in evolved H_2 during photocatalytic reactions.

Table 3.6. Controlled photocatalytic experiments and results.

Experimental No.	Photocatalyst	Reaction solution	Visible Light source	H_2 detection
1	NONE	NONE	NONE	NONE
2	YES	NONE	NONE	NONE
3	NONE	YES	YES	NONE
4	YES	YES	NONE	NO
5	YES	YES	YES	YES

Figure 3.11d shows the signals obtained for the gaseous products resulting from the photocatalytic reactions using H_2O, D_2O (heavy water), and D_2O + H_2O as reaction mixtures (signal received from pure H_2 gas is taken as reference). In the case of H_2O, the retention time of the product is the same as that of standard H_2 gas while the retention time of the product from D_2O is different from H_2. The product obtained from D_2O + H_2O mixtures showed two peaks one similar to the H_2O product and the second as that of the product obtained from D_2O **[199]**. These results prove that the H_2 produced in the presented work comes from photo-splitting of water only, consistent with others **[199]**. Controlled experiments were performed to check the possibility of hydrogen peroxide (H_2O_2) generation during photocatalytic water-splitting reactions. We performed a quantitative analysis to check hydrogen peroxide generation during photocatalytic water splitting experiments. For quantitative analysis, we performed titration using potassium permanganate ($KMNO_4$) solution, a common laboratory technique for the determination of H_2O_2 **[217]**. Firstly, a solution of potassium permanganate ($KMnO_4$) at a concentration of 0.02 M was prepared by dissolving 0.316 g of $KMnO_4$ in 100 mL of distilled water, which was then transferred to a burette.

Figure 3.12. Photographs of the photocatalytic reaction solution at various time points (t = 0 sec, 30 sec, 1 min, and 2 min) after titration.

To assess the concentration of hydrogen peroxide (H_2O_2) in the reaction mixture, 1 mL of the reaction mixture was extracted after 4 hours of photocatalytic water-splitting experiments and diluted with 100 mL of water. Subsequently, 20 mL of the prepared aqueous sulfuric acid (1:3) solution was added to the sample. The resulting solution, comprising 1 mL of the photocatalytic reaction mixture, 100 mL of water, and 20 mL of the sulfuric acid (1:3) solution, was gently mixed and titrated with the $KMnO_4$ solution under continuous stirring. Photographs provided in **Figure 3.12** depict the solution at various time points (t = 0 sec, 30 sec, 1 min, and 2 min) after titration. It was observed that upon adding a few drops of $KMnO_4$ solution to the reaction mixture, the deep pink color of $KMnO_4$ did not disappear, which indicated the absence of hydrogen peroxide in the solution. These results affirm that H_2O_2 is not generated during photocatalytic water splitting over HAASC in the presented work.

It is accepted that H_2O_2 can be generated during water splitting through either water oxidation reaction (WOR) or oxygen reduction reaction (ORR) as represented by equations (3.8) and (3.9) respectively **[217, 218]**. We will discuss each possibility in our experiments one by one.

$$2H_2O \rightarrow H_2O_2 + 2H^+ + 2e^- \quad (1.76 \text{ V versus NHE}) \qquad (3.8)$$

$$O_2 + 2H^+ + 2e^- \rightarrow H_2O_2 \quad (0.695 \text{ V versus NHE}) \qquad (3.9)$$

$$2H_2O + 4H^+ \rightarrow O_2 + 4H^+ \quad (1.23 \text{ V versus NHE}) \qquad (3.10)$$

Equation 3.8 describes the WOR reaction, a two-electron process converting water molecules into H_2O_2 with a standard redox potential ($E°$) of 1.76 V. However, due to its lower thermodynamic feasibility compared to the four-electron process of O_2 generation ($E°$=1.23 V) during water splitting (Equation 3.10), this reaction is considered unlikely based on thermodynamic feasibility. Hence, our experiments did not detect H_2O_2 generation.

ORR involves the reduction of O_2 to produce H_2O_2 through a $2e^-$ process (equation 3.9). One possible route for this process is supplying O_2 as an additional source, reacting with H^+ to generate H_2O_2 **[219]**. However, since our experiments did not involve using O_2 as feed, the likelihood of H_2O_2 generation is dismissed. Another potential pathway is consuming the O_2 produced during photocatalytic water splitting, reacting with H^+ to form H_2O_2. Recent studies suggest that single-atom catalysts (SACs) with d^{10} electronic configuration are optimal for H_2O_2 synthesis via the $2e^-$ ORR **[191-195]**. However, as our system possesses a d^9 configuration for Cu_{SA}, similar to studies suggesting d^{10} electronic configuration SACs are optimal for H_2O_2 synthesis via ORR, H_2O_2 generation through this process is also unlikely. Furthermore, the adsorption of O_2 on the catalyst surface is vital for H_2O_2 generation during catalysis **[220]**. We performed adsorption energy calculations for O_2-adsorbed structural models for FT_{111} and $Cu_{SA}FT_{111}$ using DFT calculations. Firstly, the most favorable adsorption sites (low-energy adsorption sites) were identified using the adsorption locator module.

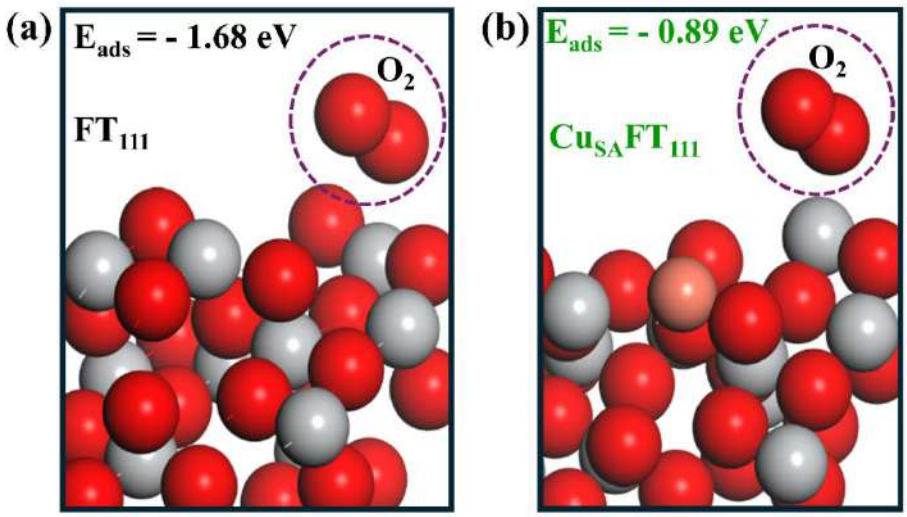

Figure 3.13. O_2-adsorbed optimized structural models for **(a)** FT_{111} and **(b)** $Cu_{SA}FT_{111}$ with corresponding adsorption energy values.

Figure 3.13a, b represents the optimized structures for O_2-adsorbed FT_{111} and O_2-adsorbed $Cu_{SA}FT_{111}$ with corresponding adsorption energy values, i.e., weak O_2 adsorption on $Cu_{SA}FT_{111}$ surfaces compared to FT_{111}. These results support the absence of H_2O_2 generation in our experiments. Additionally, experimental results and theoretical computations suggest significant modulation of band edges and *d*-band center in $Cu_{SA}(x)FT_{111}$ compared to FT_{111}, providing further explanation for the lack of H_2O_2 detection in our experiments **[221]**.

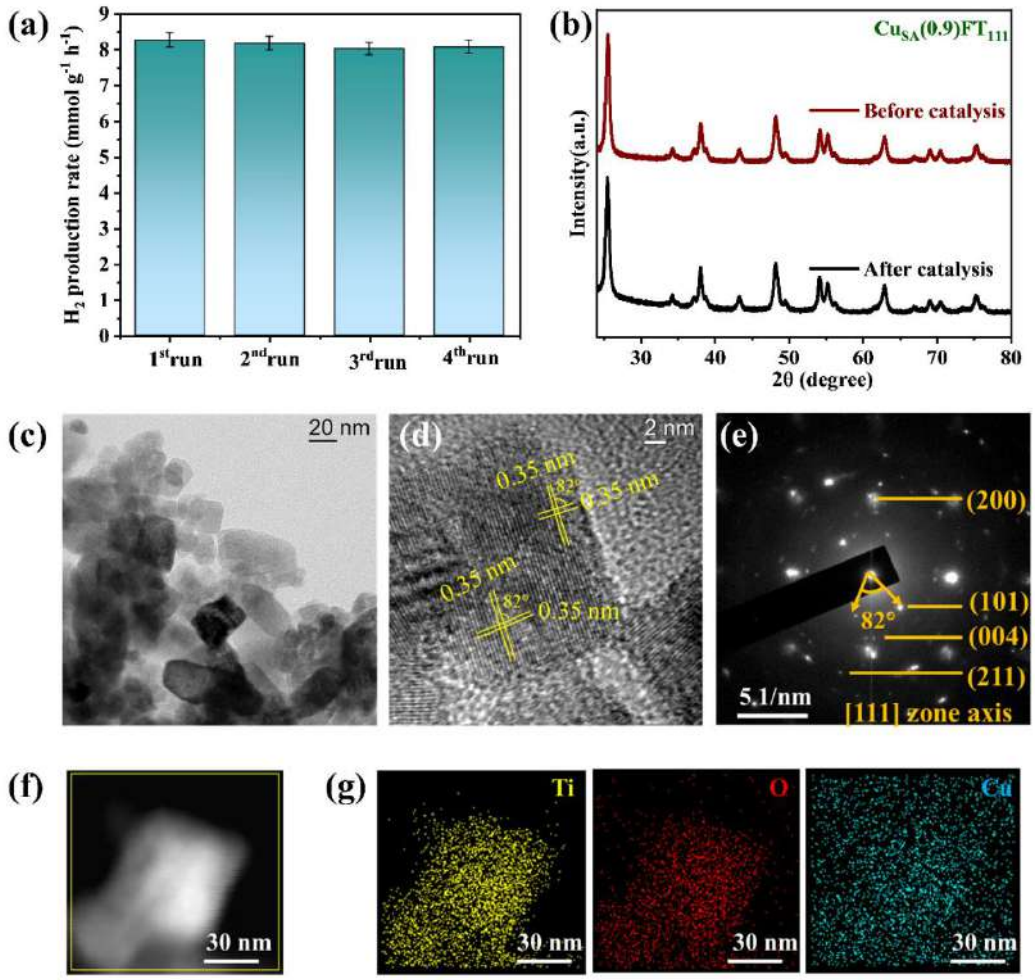

Figure 3.14. (a) Photocatalytic activity of $Cu_{SA}(0.9)FT_{111}$ for four cyclic water splitting experiments, showing the stable activity. (b) XRD patterns of $Cu_{SA}(0.9)FT_{111}$ before and after four cycles of photocatalytic water splitting experiments. No obvious change in the XRD patterns indicates excellent structural stability of $Cu_{SA}(0.9)FT_{111}$ in photocatalytic systems. Analysis of $Cu_{SA}(0.9)FT_{111}$ after 10 hr of photocatalytic reaction. **(c)** TEM image. **(d)** Lattice-resolved HR-TEM image. **(e)** SAED. **(f)** HAADF-STEM. **(g)** EDS elementals maps for Ti, O, and Cu.

For quantitative assessment, titration was carried out using a potassium permanganate ($KMnO_4$) solution **[217]**. The titration findings **(Figure 3.12)**, demonstrate that no H_2O_2 is produced during the photocatalytic reactions investigated in our study **[218,219]**. Notably, $Cu_{SA}(0.9)FT_{111}$ shows high durability in photocatalytic tests and maintains a similar H_2 evolution rate without any noticeable change even after four consecutive cycles of photocatalytic water-splitting experiments **(Figure 3.14a)**. Furthermore, characterization results of $Cu_{SA}(0.9)FT_{111}$ after 1 cyclic (10 hr) of photocatalytic reactions indicate no signs of structural deformation and no loss of Cu content. XRD shows no change in the crystal structure after photocatalysis **(Figure 3.14b)**. TEM and HAADF-STEM results **(Figure 3.14c-e)** signify the stability of (111) exposed facets and Cu single atoms in $Cu_{SA}(0.9)FT_{111}$. EDS elemental maps **(Figure 3.14f, g)** reveal that Cu_{SA} are still well dispersed.

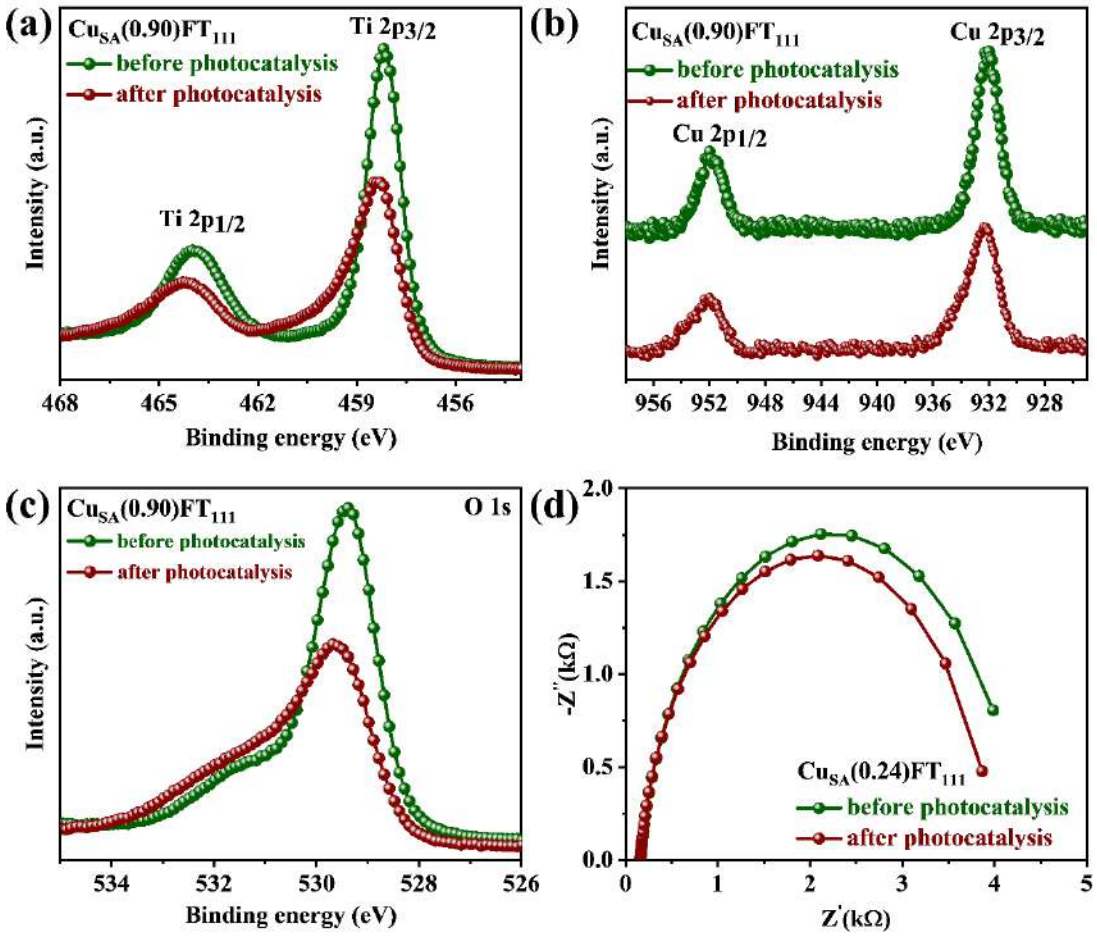

Figure 3.15 (a) High-resolution XPS spectra of Ti2p. **(b)** High-resolution XPS spectra of Cu2p. **(c)** High-resolution XPS spectra of O1s of $Cu_{SA}(0.9)FT_{111}$. No detectable change in the oxidation state of Cu is observed. **(d)** EIS Nyquist plots for $Cu_{SA}(0.9)FT_{111}$ catalyst before and after conducting 10 hr of photocatalytic water splitting experiments.

XPS analysis indicates no detectable change in the oxidation state as well as in the concentration of Cu_{SA} **(Figure 3.15a-c and Table 3.7).** Furthermore, a minor variance observed between the electrochemical impedance spectroscopy (EIS) Nyquist plots **(Figure 3.15d)** indicates the remarkable stability of HAASC for photocatalytic applications. All these results confirm the excellent structural integrity of HAASC, which should be the key reason for high and durable H_2 generation in the presented work.

Table 3.7. Cu content (at%)* in $Cu_{SA}(0.9)FT_{111}$ sample before and after 10 hr of photocatalytic experiments.

Sample	Before photocatalysis	After photocatalysis
$Cu_{SA(}0.9)FT_{111}$	0.9	0.86

*obtained from XPS results

3.3.4. Optical, electronic, and charge transfer properties of HAASC

The optical and electronic properties of the photocatalysts were systematically investigated. The UV-vis diffused reflectance spectra **(Figure 3.16a)** indicate that the visible light harvesting ability of $Cu_{SA}(0.9)FT_{111}$ is better than FT_{111}. In addition to the intrinsic interband absorption around 400 nm of TiO_2, $Cu_{SA}(0.9)FT_{111}$ shows two additional absorption bands; (i) 390 to 500 nm, which is due to the interfacial charge transfer from VB of TiO_2 to Cu_{SA}, and (ii) absorption band from 550 to 800 nm which can be attributed to the *d-d* transitions in Cu^{2+} species in Cu_{SA}-O_v-Ti_{3c} HAASC. The Tau's plots are shown in the inset of **Figure 3.16a**. The optical band gaps (E_g) of $Cu_{SA}(0.9)FT_{111}$ and FT_{111} are determined to be about 2.7 and 3.2 eV respectively. A significant bandgap narrowing in $Cu_{SA}(0.9)FT_{111}$ reveals its potential for visible light photocatalysis **[222]**. **Figure 3.16b** shows the valence band (VB) XPS spectra. The VB edges of FT_{111} and $Cu_{SA}(0.9)FT_{111}$ are determined at 2.55 eV and 1.95 eV respectively. Mott-Schottky (M-S) analysis is a powerful method to determine the flat-

band potential (E_{fb}) and doping density (N_D) of the semiconductors which are the key factors that govern the photocatalytic activity of the material **[180, 223]**.

The positive slopes of the M-S plots **(Figure 3.16c)** confirm that $Cu_{SA}(0.9)FT_{111}$ and FT_{111} are *n*-type semiconductors.

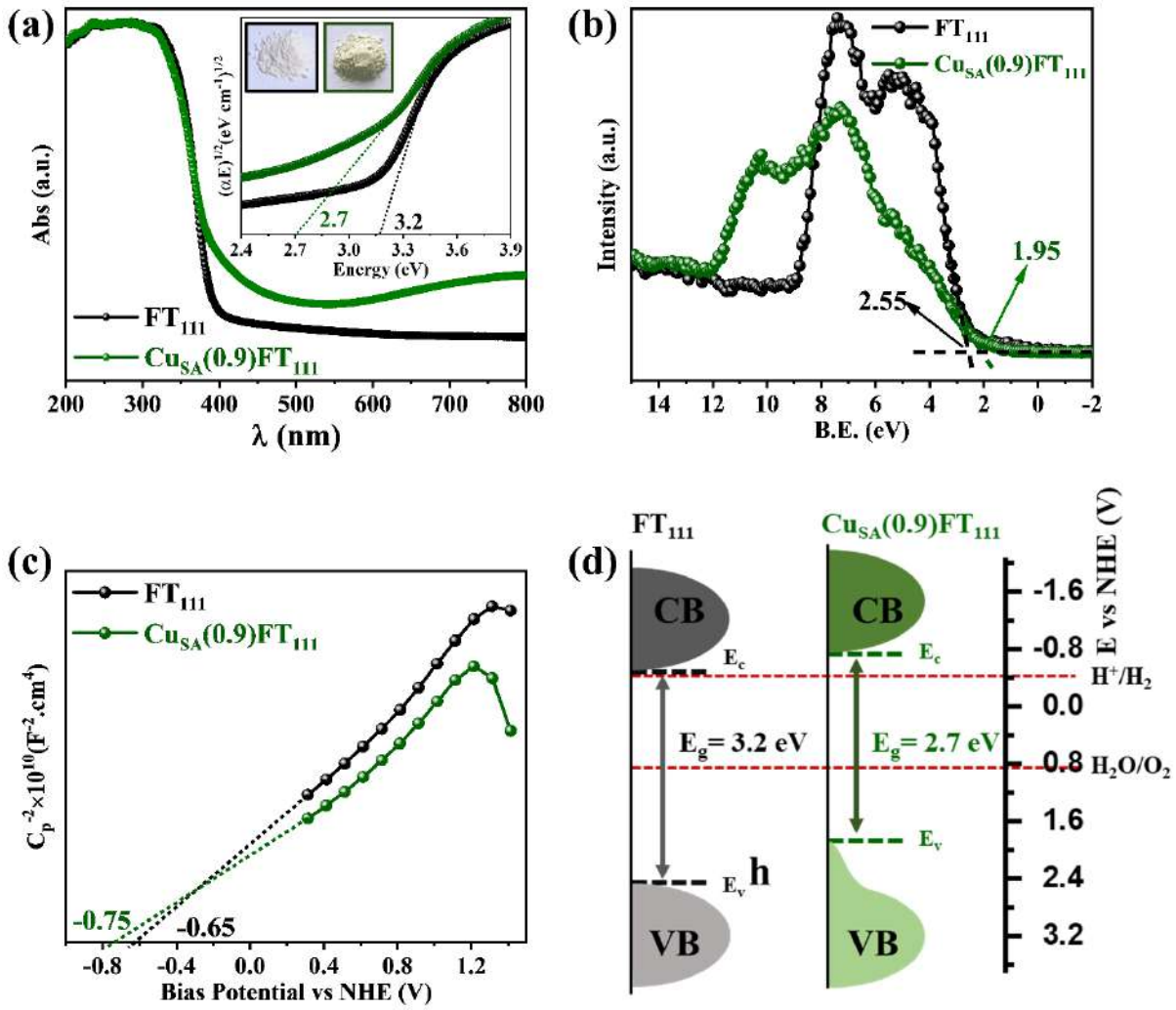

Figure 3.16. Optical, electronic, and charge transfer in HAASC. **(a)** UV-vis DRS spectra of FT_{111} and $Cu_{SA}(0.9)FT_{111}$. The inset shows Tau's plot and band gap values. **(b)** Valance band XPS spectra. **(c)** Mott-Schottky plots (@1 kHz). Flat band potentials (E_{fb}) were obtained from the *x*-intercepts. **(d)** Energy band diagrams of FT_{111} and $Cu_{SA}(0.9)FT_{111}$.

It is important to note that the estimated donor density using equation 3.1 in $Cu_{SA}(0.9)FT_{111}$ ($4.5 \times 10^{20}\ cm^{-3}$) is significantly higher than that of FT_{111}($3.0 \times 10^{20}\ cm^{-3}$), which is believed to be the result of O_v in Cu_{SA}-O_v-Ti_{3c} HAASC **[223]**. For an *n*-type semiconductor,

the conduction band (CB) edge lies 0.3 V lower than E_{fb} **[223]**. The CB edge in $Cu_{SA}(0.9)FT_{111}$ and FT_{111} is determined at -0.75 V and -0.65 V versus normal hydrogen electrode (NHE, *p*H = 7) respectively. A negatively shifted CB potential in $Cu_{SA}(0.9)FT_{111}$ verifies that Cu_{SA} decoration greatly improves the redox capability of photogenerated electrons in the excitation process. It might be concluded that Cu_{SA} doping-induced modulation of CB in $Cu_{SA}(0.9)FT_{111}$ endows enhanced driving force to trigger the H^+/H_2 reduction process. **Figure 3.16d** illustrates the band structures of $Cu_{SA}(0.9)FT_{111}$ HAASC and FT_{111} AASC based on the obtained experimental results.

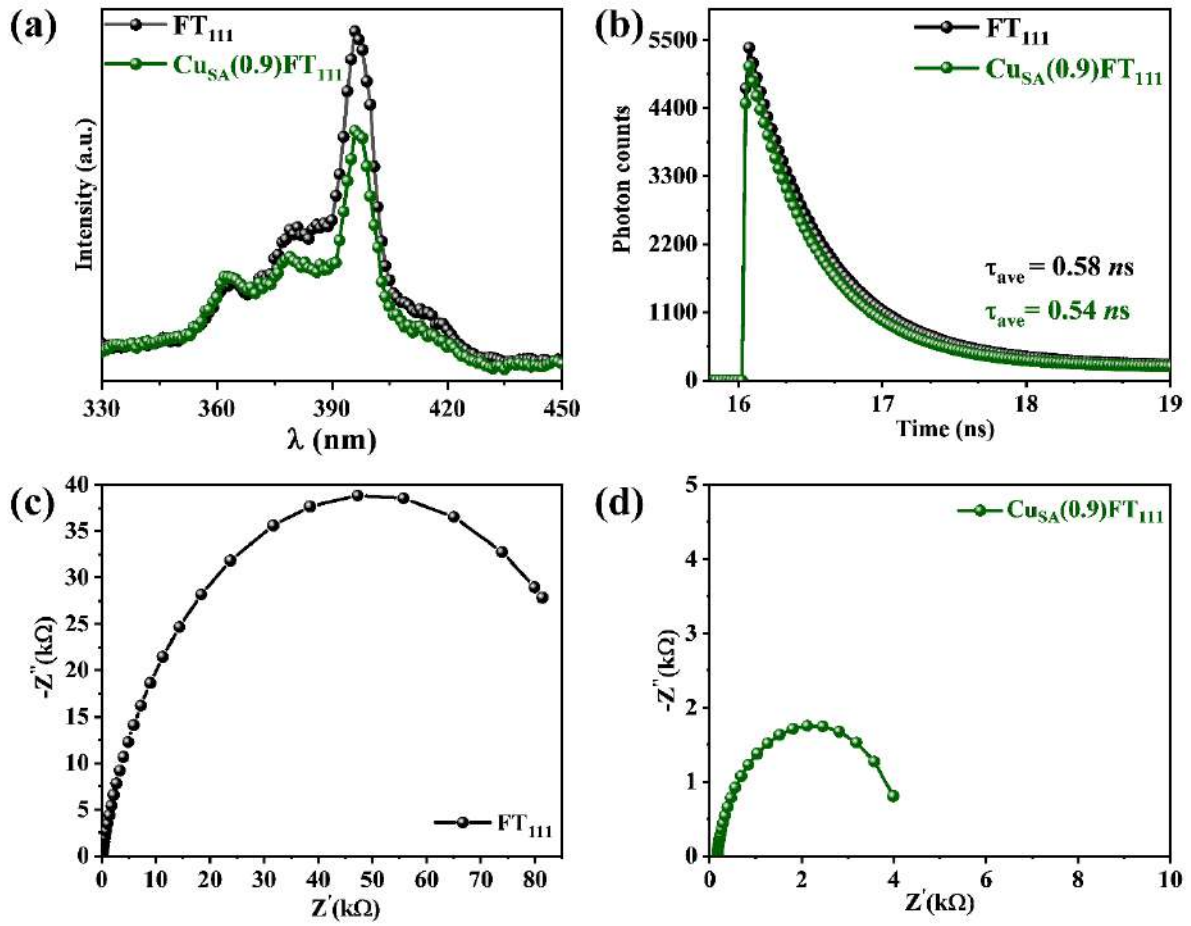

Figure 3.17. (a) Steay-state photoluminescence spectra ($\lambda_{ext} = 260\ nm$). **(b)** Time-resolved photoluminescence spectra of FT_{111} and $Cu_{SA}(0.9)FT_{111}$. **(c, d)** Nyquist plots of FT_{111} and $Cu_{SA}(0.9)FT_{111}$.

The charge transfer dynamics in the samples are studied by steady-state photoluminescence spectra (PL) and Time-resolved PL (TRPL). The diminished PL emission in $Cu_{SA}(0.9)FT_{111}$ **(Figure 3.17a)** indicates lower recombinations of photogenerated charge carriers **[224]**. Moreover, as revealed by TRPL curves **(Figure 3.17b)**, the $Cu_{SA}(0.9)FT_{111}$ displays a shortened average PL lifetime (~0.54 *ns*) than that of FT_{111} (~0.58 *ns*) **(Table 3.8)**, confirming that Cu_{SA}-O_v-Ti_{3c} sites can enhance the separation of photo-generated charge carriers **[172]**. The charge-transfer properties of $Cu_{SA}(0.9)FT_{111}$ and FT_{111} were further investigated by EIS. As shown in the Nyquist plots **(Figure 3.17c, d)** $Cu_{SA}(0.9)FT_{111}$ has a smaller semicircle, indicating significantly improved electronic conductivity as well as enhanced charge transfer at the interface **[224, 225]**. These results confirm the positive effects of Cu_{SA}-O_v-Ti_{3c} HAAS in promoting the separation and transportation of photogenerated charge carriers during the excitation process.

Table 3.8. Obtained best-fitted parameters[$] from TRPL curves.

Sample	τ_1 (*n*s)	Amplitude τ_1 (%)	τ_2 (*n*s)	Amplitude τ_2 (%)	$\tau_{average}$ (*n*s)
FT_{111}	0.5188	56.64	10.1884	43.36	0.5763
$Cu_{SA}(0.9)FT_{111}$	0.4906	58.28	10.1180	41.72	0.5426

[$]The TRPL (Time-Resolved Photoluminescence) curves are fitted using a bi-exponential equation expressed mathematically as **[226]**:

$$I(t) = A_1 exp(-t/\tau_1) + A_2(-t/\tau_2) \quad (3.11)$$

Where *I(t)* denote the PL intensity at a given time, τ_1 denotes the lifetime constant of the radiative component and τ_2 denotes the lifetime constant of the non-radiative component, and A_1 and A_2 are the PL intensities (amplitudes) of the radiative and non-radiative components.

3.3.5. Mechanistic Insights into H_2O Splitting at HAAS

DFT calculations were performed to disclose the role of Cu_{SA}-O_v-Ti_{3c} sites on the electronic structure and the photocatalytic activity of $Cu_{SA}FT_{111}$ HAASC.

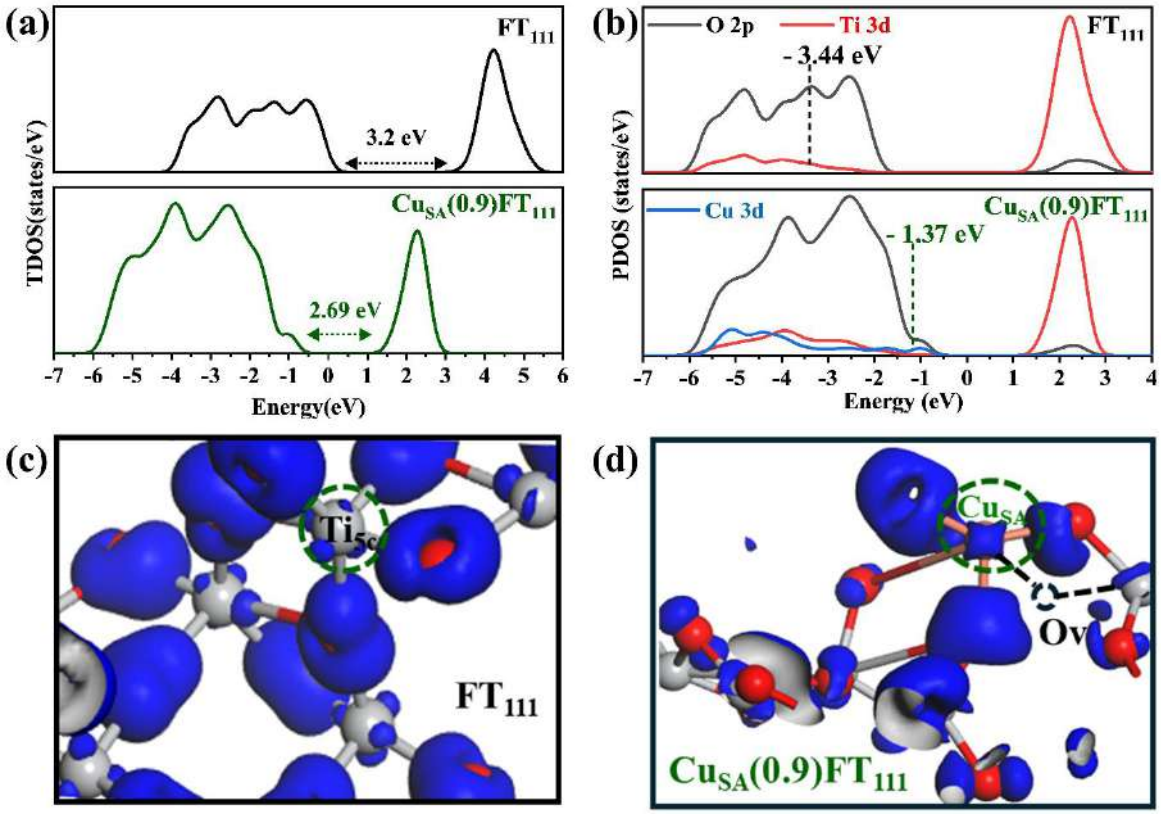

Figure 3.18. Role of HAAS in electronic band structure modulation**. (a)** Calculated TDOS of FT_{111} and $Cu_{SA}(0.9)FT_{111}$. **(b)** Calculated PDOS of FT_{111} and $Cu_{SA}(0.9)FT_{111}$. The black, red, and blue lines stand for PDOS for Ti, O, and Cu respectively. The *d*-band centers are also highlighted in the DOS curves by dotted lines. Charge density difference (CDD) maps for **(c)** Ti_{5c}-O-Ti_{3c} sites (FT_{111}); Ti_{5c} is selected as the center point of CDD; **(d)** Cu_{SA}-O_v-Ti_{3c} site ($Cu_{SA}FT_{111}$), Cu_{SA} is selected as the center point of CDD. The blue color represents the accumulation of electrons. Ti, Cu, and O are shown in grey, brown, and red colors respectively.

Figure 3.18a shows the total density of states (TDOS), indicating a significantly reduced band gap in $Cu_{SA}(0.9)FT_{111}$ (agrees well with the experimental results) due to the presence of Cu_{SA}-O_v-Ti_{3c} HAAS. Furthermore, a negative shift in TDOS of $Cu_{SA}(0.9)FT_{111}$ signifies the modulation of CB and/or VB edges, which is in excellent agreement with the M-S results **(Figure 3.16c)**. In addition, the projected density of states (PDOS) as shown in **Figure 3.18b** in $Cu_{SA}(0.9)FT_{111}$ indicates that Cu_{SA} doping induced *Cu 3d* band which mainly contributes to valence band modulation of the hybrid. The *d*-band center (E_d) of FT_{111} and $Cu_{SA}(0.9)FT_{111}$ relative to E_f is calculated to be −3.44 eV and −1.37 eV, respectively. Importantly, the *d*-band center is significantly shifted toward the Fermi level after trapping of Cu_{SA}. It is well established that the upward shifting of the *d*-band promotes the adsorption of the active intermediates during catalytic reactions **[227, 228]**. It might be concluded that modulation of the *d*-band center facilitates the adsorption of the reaction intermediates. To study the charge heterogeneity at HAAS, the charge density difference (CDD) maps are obtained for Cu_{SA}-O_v-Ti_{3c} and Ti_{5c}-O-Ti_{3c} sites **(Figure 3.18c, d)**.

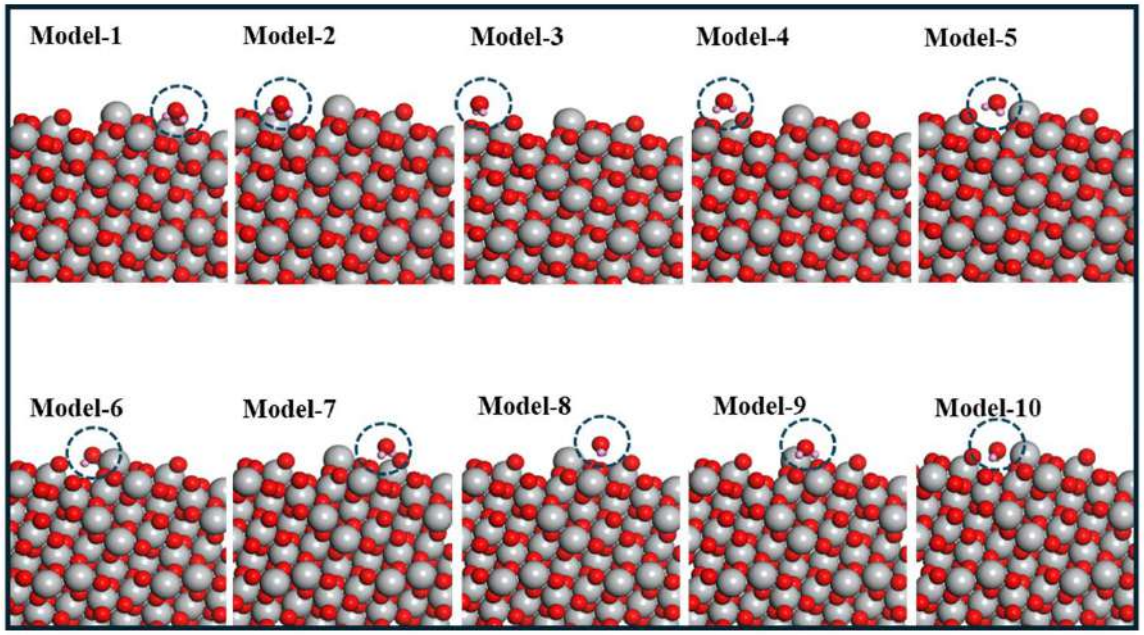

Figure 3.19. Identification of the most preferable active site on the FT_{111} surface for H_2O adsorption. Ti, O, and H atoms are shown in grey, red, and pink colors respectively. The dotted circle refers to the location and orientation of the H_2O molecule**.**

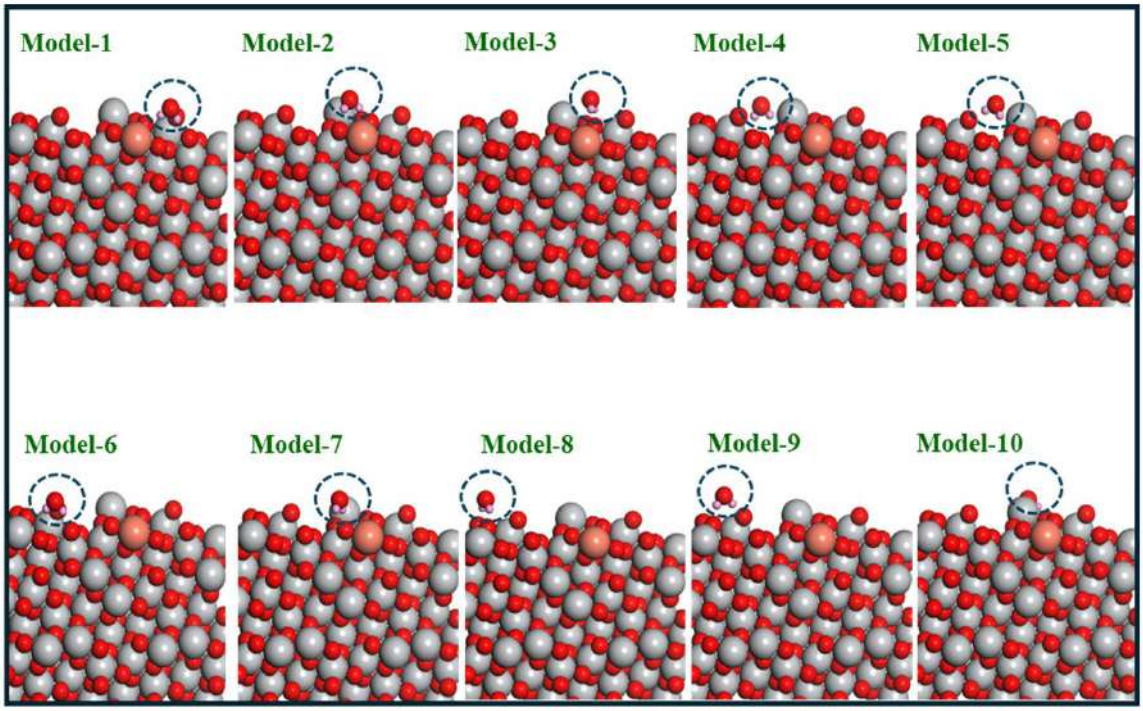

Figure 3.20. Identification of the most preferable active site on the $Cu_{SA}FT_{111}$ surface for H_2O adsorption. Ti, Cu, O, and H atoms are shown in grey, brown, red, and pink colors respectively. The dotted circle refers to the location and orientation of the H_2O molecule..

The CDD maps indicate higher charge concentration at HAAS around Cu_{SA} which should be favorable for better adsorption and activation of H_2O molecules **[97, 100, 172]**. To prove this, adsorption energy calculations were performed for various H_2O-adsorbed structural models for FT_{111} and $Cu_{SA}(0.9)FT_{111}$. Firstly, the most favorable adsorption sites (low-energy adsorption sites) for H_2O were identified using the adsorption locator module **(Figures 3.19, 3.20 and Table 3.9)**

Table 3.9. The obtained formation energy values for all the possible configurations for H_2O adsorption on $Cu_{SA}FT_{111}$ and FT_{111} surfaces.

	Structures		Formation Energy (eV)	
Sr. No.	FT_{111}	$Cu_{SA}FT_{111}$	FT_{111}	$Cu_{SA}FT_{111}$
1	Model-1	Model-1	-48.48	-54.56
2	Model-2	Model-2	-47.75	-53.06
3	Model-3	Model-3	-45.60	-52.07
4	Model-4	Model-4	-44.45	-51.10
5	Model-5	Model-5	-44.41	-50.36
6	Model-6	Model-6	-43.28	-49.12
7	Model-7	Model-7	-42.80	-48.44
8	Model-8	Model-8	-41.60	-46.86
9	Model-9	Model-9	-40.30	-45.98
10	Model-10	Model-10	-39.86	-44.23

The obtained formation energy for all possible configurations indicates that Cu_{SA}-O_v-Ti_{3c} HAAS and Ti_{5c}-O-Ti_{3c} are more favorable sites for H_2O adsorption in $Cu_{SA}FT_{111}$ and FT_{111} respectively. **Figures 3.21a, b** represent optimized configurations for H_2O adsorbed on Ti_{5c}-O-Ti_{3c} and Cu_{SA}-O_v-Ti_{3c} HAASC using DMol3. Notably, the adsorption energy calculated using equation 3.3 in the case of Cu_{SA}-O_v-Ti_{3c} sites ($\Delta E_{ads} = -1.72\ eV$) is more negative than Ti_{5c}-O-Ti_{3c} sites ($\Delta E_{ads} = -0.44\ eV$), which indicates that the Cu_{SA}-O_v-Ti_{3c} site catalyst has high water absorption capability **[229]**. CDD maps were further obtained to elucidate the electron distribution on Cu_{SA}-O_v-Ti_{3c} sites before **(Figure 3.21c)** and after H_2O adsorption **(Figure 3.21d)**. A significant depletion of charge density at Cu_{SA} after H_2O adsorption is observed, indicating efficient transfer of charge from Cu_{SA}-O_v-Ti_{3c} HAASC sites to the adsorbed H_2O molecules; which is highly desirable for activation of water molecules for catalytic reactions **[100, 199]**. These simulation results establish the positive effects of Cu_{SA}-O_v-Ti_{3c} HAAS sites in $Cu_{SA}FT_{111}$ for desired electronic structure modulation, enhanced

adsorption as well as activation of H_2O molecules, thus guaranteeing the high photo-splitting of water molecules at HAAS.

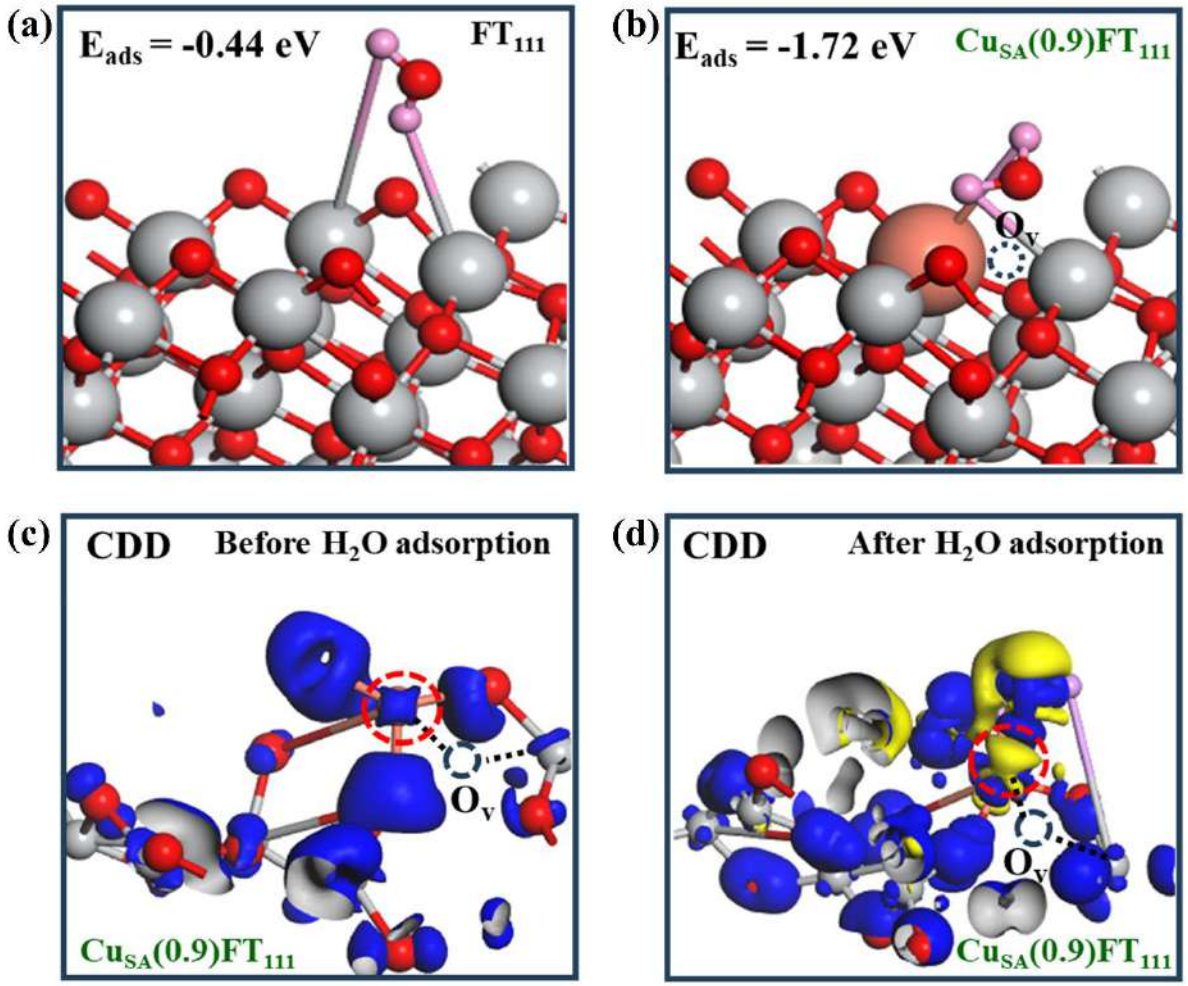

Figure 3.21. (a, b) H_2O adsorbed on Ti_{5c}-O-Ti_{3c} site and Cu_{SA}-O_v-Ti_{3c} and corresponding adsorption energies.. Ti, Cu, O, and H atoms are shown in grey, brown, red, and pink colors respectively. **(c, d)** Charge density difference (CDD) maps on Cu_{SA}-O_v-Ti_{3c} before and after H_2O adsorption. The blue and yellow regions represent the accumulation and depletion of electrons, respectively.

In addition to H_2O adsorption, adsorption/desorption of H are the key factors that determine the hydrogen evolution reaction (HER) activity in the catalytic/photocatalytic reactions. Gibbs free energy calculations using equation 3.4 were performed for H_2 formation on Cu_{SA}-O_v-Ti_{3c} and Ti_{5c}-O-Ti_{3c} sites and the corresponding free-energy diagram is shown in **Figure**

3.22a. Notable, ΔG value of the H_{ads} on Cu_{SA}-O_v-Ti_{3c} sites ($-0.18\ eV$) of $CuFT_{111}$ surface is less negative than that of Ti_{5c}-*O*-Ti_{3c} sites ($-1.4\ eV$) on FT_{111} surface suggesting that HAAS sites are more favorable for H_2 formation **[230, 231]**. These results in combination with the electronic band modulation support the high HER activity obtained in $Cu_{SA}(0.9)FT_{111}$ HAASC. To establish H_2O activation mechanism on HAASC, we further carried out first-principal calculations for various steps including H_2O adsorption, transition state, and H_2 desorption, and corresponding energies are calculated to obtain Gibbs free-energy-diagrams **(Figure 3.22b).** The dark green and black paths represent H_2O activation mechanisms on Cu_{SA}-O_v-Ti_{3c} and Ti_{5c}-O-Ti_{3c} sites, respectively. The more negative adsorption energy of H_2O (from step I to step II) on the Cu_{SA}-O_v-Ti_{3c} sites indicates that the H_2O adsorption efficiency on Cu_{SA}-O_v-Ti_{3c} sites is significantly higher. Step II to III, represents an intermediate state with *H on Cu_{SA} and *OH adsorbed on Ti_{3c}. The transition energy for this step at Cu_{SA}-O_v-Ti_{3c} ($\Delta E_{trans} = -1.58\ eV$) is much higher than Ti_{5c}-O-Ti_{3c} site ($\Delta E_{trans} = -0.47\ eV$), demonstrating that adsorption of intermediates (*i.e.,**H and *OH) is energetically more favourable at Cu_{SA}-O_v-Ti_{3c} sites **[232]**. Interestingly, the upslope for *H (Cu_{SA})-O_v-(Ti_{3c})*OH to *H (Cu_{SA})-O_v-(Ti_{3c}) in the step III to IV indicates the better retention capability of *OH **[161, 233]** which may convert to H_2 in addition to the H_2 coming from *H and likely to achieve more H_2 generation at HAAS **[232]**. In step IV to V (which is rate-limiting step), the H_2 desorption energy at Cu_{SA}-O_v-Ti_{3c} sites ($\Delta E_{des} = 0.18\ eV$) is less than that of Ti_{5c}-O-Ti_{3c} sites ($\Delta E_{des} = 1.4\ eV$) which indicate better H_2 desorption at HAAS and guarantees more H_2 production in HAASC. The DFT results **(Figure 3.13a, b)** for O_2 adsorption on Cu_{SA}-O_v-Ti_{3c} and Ti_{5c}-O-Ti_{3c} sites support the experimental observation of no H_2O_2 detection in the presented work. Based on the above experimental results and DFT calculations, we propose a mechanism for the photocatalytic water-splitting activity of our HAASC, as illustrated in **Figure 3.22c**. In the first step (i), the HAAS serve as active sites to adsorb H_2O molecules

with higher E_{ads}. Due to the intrinsic charge heterogeneity at Cu_{SA}-O_v-Ti_{3c} sites, H_2O molecules are polarized and redistribution of charge occurs.

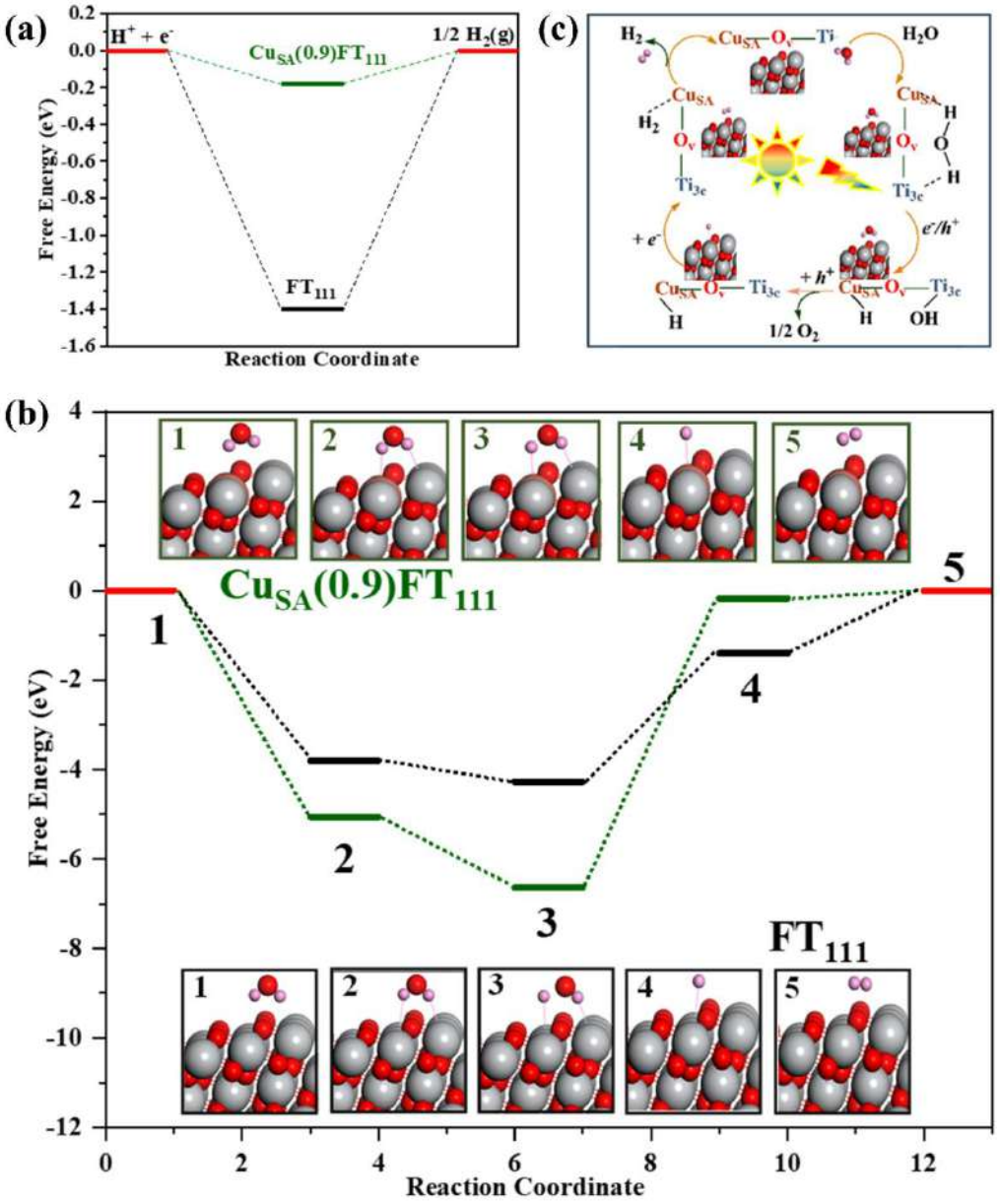

Figure 3.22. DFT calculations of possible reaction paths of H_2O activation and proposed mechanism. **(a)** Free-energy diagram for HER at Cu_{SA}-O_v-Ti_{3c} (green line) and Ti_{5c}-O-Ti_{3c} sites (black line). **(b)** The proposed H_2O activation route and free energy profile of reaction intermediates for Cu_{SA}-O_v-Ti_{3c} HAAS (green line) and Ti_{5c}-O-Ti_{3c} AAS (black line) are shown. Insets represent corresponding intermediate optimized structures for each step. **(c)** The proposed reaction mechanism for photocatalytic water splitting at Cu_{SA}-O_v-Ti_{3c} HAASC. Ti, Cu, O, and H atoms are shown in grey, brown, red, and pink colors respectively.

Under visible light (ii) irradiation, e^-/h^+ pairs are generated and transferred from HAAS sites to adsorbed H_2O molecules, dissociating the H–OH bonds and generating the *H(Cu_{SA})-O_v-(Ti_{3c})*OH intermediate state. The third step (iii) involves the transfer of h^+ to *H(Cu_{SA})-O_v-(Ti_{3c})*OH sites to produce O_2 and *H(Cu_{SA})-O_v-Ti_{3c}. In the fourth step (iv), transfer of e^- occurs to *H(Cu_{SA})-O_v-Ti_{3c} to produce H_2.

3.2.6. Correlation between Cu_{SA} concentration and photocatalytic H_2 production in $Cu_{SA}(x)FT_{111}$

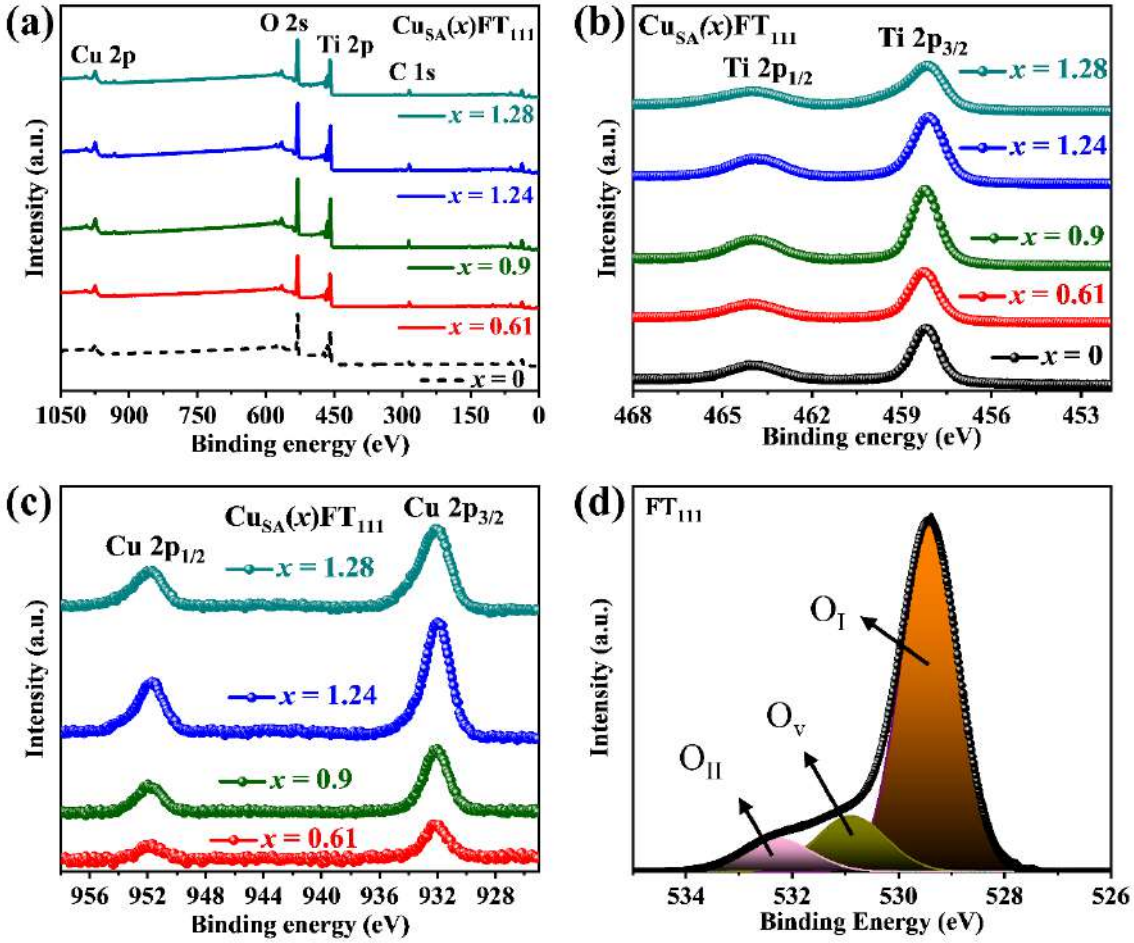

Figure 3.23. Characterization of $Cu_{SA}(x)FT_{111}$ series. (a) XPS Survey Spectra of $Cu_{SA}(x)FT_{111}$ series. (b) High-resolution XPS spectra of Ti2p. (c) High-resolution XPS spectra of Cu2p of $Cu_{SA}(x)FT_{111}$ series. (d) High-resolution XPS spectra of O1s of FT_{111}.

To elucidate the connection between Cu_{SA} concentration, O_v, and photocatalytic H_2 generation, we investigated $Cu_{SA}(x)FT_{111}$ samples using XPS analysis and calculated the concentration of O_v in different samples. Survey spectra confirm Ti, O, and Cu elements in $Cu_{SA}(x)FT_{111}$ **(Figure 3.23a)**. High-resolution XPS spectra of Ti **(Figure 3.23b)** displayed two peaks corresponding to $Ti2p_{3/2}$ (458.4 eV) and $Ti2p_{1/2}$ (464.2 eV). The Cu2p spectra **(Figure 3.23c)** exhibited two peaks corresponding to $Cu2p_{3/2}$ (933.5 eV) and $Cu2p_{1/2}$ (953.6 eV), without any satellite peak, indicating atomically dispersed Cu^{2+} species in $Cu_{SA}(x)FT_{111}$. **Figure 3.23d** show the high-resolution XPS spectra of O*1s* of FT_{111}.

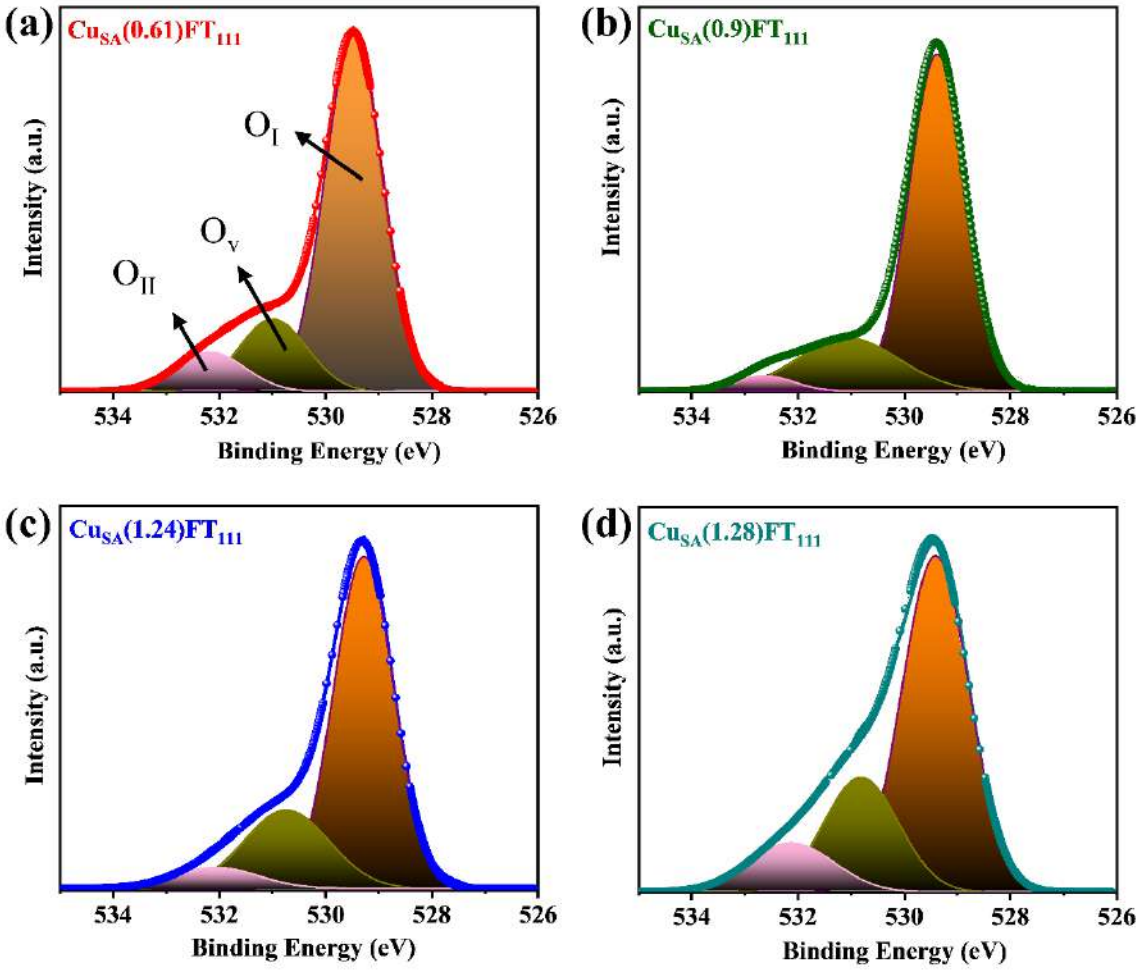

Figure 3.24. High-resolution XPS spectra of O*1s* of **(a)** $Cu_{SA}(0.61)FT_{111}$. **(b)** $Cu_{SA}(0.9)FT_{111}$ **(c)** $Cu_{SA}(1.24)FT_{111}$ and **(d)** $Cu_{SA}(1.28)FT_{111}$

Figure 3.24a-d represents O1s spectra for $Cu_{SA}(x)FT_{111}$ series, revealing characteristic peaks corresponding to lattice oxygen (O_I), oxygen vacancies (O_v), and surface adsorbed water or hydrocarbons (O_{II}) **[192, 193]**. **Table 3.10**, shows atomic percentages of Ti, Cu, and O elements in $Cu_{SA}(x)FT_{111}$ samples, obtained from XPS analysis. The slightly high O/Ti ratio (>2) in all $Cu_{SA}(x)FT_{111}$ samples may be due to the undesired oxygen-containing organic contaminants (carbon contamination is detected in survey spectra **(Figure 3.23a)** and surface adsorbed water is detected in O1s spectra **(Figure 3.23d and 3.24a-d),** an inherent problem with high-pressure systems as elucidated in many reports **[234-236]**.

Table 3.10. The atomic composition* of the HAASC samples

Sample	FT_{111}	$Cu_{SA}(0.61)FT_{111}$	$Cu_{SA}(0.9)FT_{111}$	$Cu_{SA}(1.24)FT_{111}$	$Cu_{SA}(1.28)FT_{111}$
Ti (*at %*)	30.43	29.61	29.54	29.18	28.88
Cu (*at %*)	0	0.61	0.90	1.24	1.28
O (*at %*)	69.57	69.78	69.56	69.58	69.84

**atomic composition is obtained from XPS analysis*

From the O1s spectra **(Figure 3.23d and 3.24a-d)**, the concentration of O_v is calculated **(Table 3.11)**. It is important to note that O_v concentration increases with Cu_{SA} doping, which can be attributed to the formation of more Cu_{SA}-O_v-Ti_3c sites in $Cu_{SA}(x)FT_{111}$ HAASC. **Table 3.11.** Oxygen vacancy (Ov) percentage (%)# in different CuSA(x)FT111 HAASC sample

Sample Name	O_v (%)
FT_{111}	14.69
$Cu_{SA}(0.61)FT_{111}$	17.30
$Cu_{SA}(0.9)FT_{111}$	21.32
$Cu_{SA}(1.24)FT_{111}$	23.50
$Cu_{SA}(1.28)FT_{111}$	24.21

#calculated from the ratio of the integrated peak areas of lattice oxygen (O_I), oxygen vacancies (O_v), and surface adsorbed water or hydrocarbons (O_{II}) in the O1s spectra.

Table 3.12. The Ti/Cu atomic ratio in different $Cu_{SA}(x)FT_{111}$ HAASC samples

Sample Name	Ti/Cu*	Ti/Cu@
FT_{111}	No Cu	No Cu
$Cu_{SA}(0.61)FT_{111}$	48.54	134.36
$Cu_{SA}(0.9)FT_{111}$	32.82	55.48
$Cu_{SA}(1.24)FT_{111}$	23.53	40.54
$Cu_{SA}(1.28)FT_{111}$	22.56	36.78

**calculated from XPS results*
@calculated from ICP-OES results

However, for high Cu loading (1.28 at%), the concentration of O_v does not increase significantly and gets saturated. A similar trend was observed for the Ti/Cu atomic ratio (obtained from XPS, **Table 3.12)**, which initially decreases and then reaches saturation at 1.28 at% Cu. It is important to note that the quantity of copper precursors employed in $Cu_{SA}(1.28)FT_{111}$ is the highest compared to all other samples. Nevertheless, the O_v concentration and Ti/Cu ratio were nearly similar in $Cu_{SA}(1.28)FT_{111}$ and $Cu_{SA}(1.24)FT_{111}$ samples. This suggests that excessive Cu loading might lead to defects or Cu nanocluster formation rather than the creation of new active sites in HAASC.

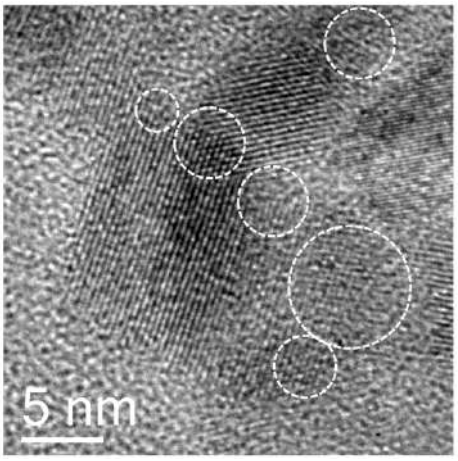

Figure 3.25. High-resolution TEM image $Cu_{SA}(1.28)FT_{111}$ showing abundant disordered atom arrangements highlighted by dash circles.

To check this, we obtained a lattice-resolved HRTEM image of $Cu_{SA}(1.28)FT_{111}$ **(Figure 3.25)**, where abundant disordered atom arrangements (indicated by circles) are clearly visible. This observation is further supported by a slight decrease in the XRD peak intensity of $Cu_{SA}(1.28)FT_{111}$ compared to the other samples **(Figure 3.26a)**. These observations suggest that lattice defects are generated in the $Cu_{SA}FT_{111}$ HAASC when a high concentration of 1.28 at % Cu is used, with a Ti/Cu ratio of less than 23, as determined from XPS analysis. This phenomenon aligns with previous studies that have suggested that high concentrations of metal single atoms in SACs can introduce defects and/or Cu accumulation in the form of nanoclusters that are detrimental to the catalytic activity of these materials **[199, 237, 238]**. The UV-vis spectra **(Figure 3.26b)** show gradual red-shifting of the absorption edge towards the longer wavelength region with increasing Cu loading, indicating the narrowing of the band gap. A gradual reduction of the band gap from 3.2 to 2.65 eV is observed **(Figure 3.26c)**. In particular, there is a noticeable enhancement in visible light absorption ranging from 550 to 800 nm, which is attributed to the *d-d* transition in Cu^{2+}, observed specifically in the sample with 0.9 at% of Cu. This unique feature may result from the efficient entrapment of Cu_{SA} on the 111-faceted TiO_2 surface at this particular concentration of Cu. On the contrary, very poor visible-light harvesting behavior is observed for the sample with 0.61 at% of Cu. Furthermore, charge transfer dynamics in $Cu_{SA}(x)FT_{111}$ samples were studied by steady-state PL spectra **(Figure 3.26d)**. The PL peak intensity relatively decreases with increasing Cu contents, implying the suppression of electron-hole recombination. However, beyond 0.9 at% of Cu, increased charge recombination is observed in HAASC. This trend is likely due to an excess of Cu, leading to lattice disorders observed in HRTEM, which could serve as recombination centers for photogenerated electrons and holes. The EIS Nyquist plots **(Figure 3.26e)** exhibit a similar trend, where a higher charge transfer resistance is evident in $Cu_{SA}(1.28)FT_{111}$ compared to $Cu_{SA}(0.9)FT_{111}$.

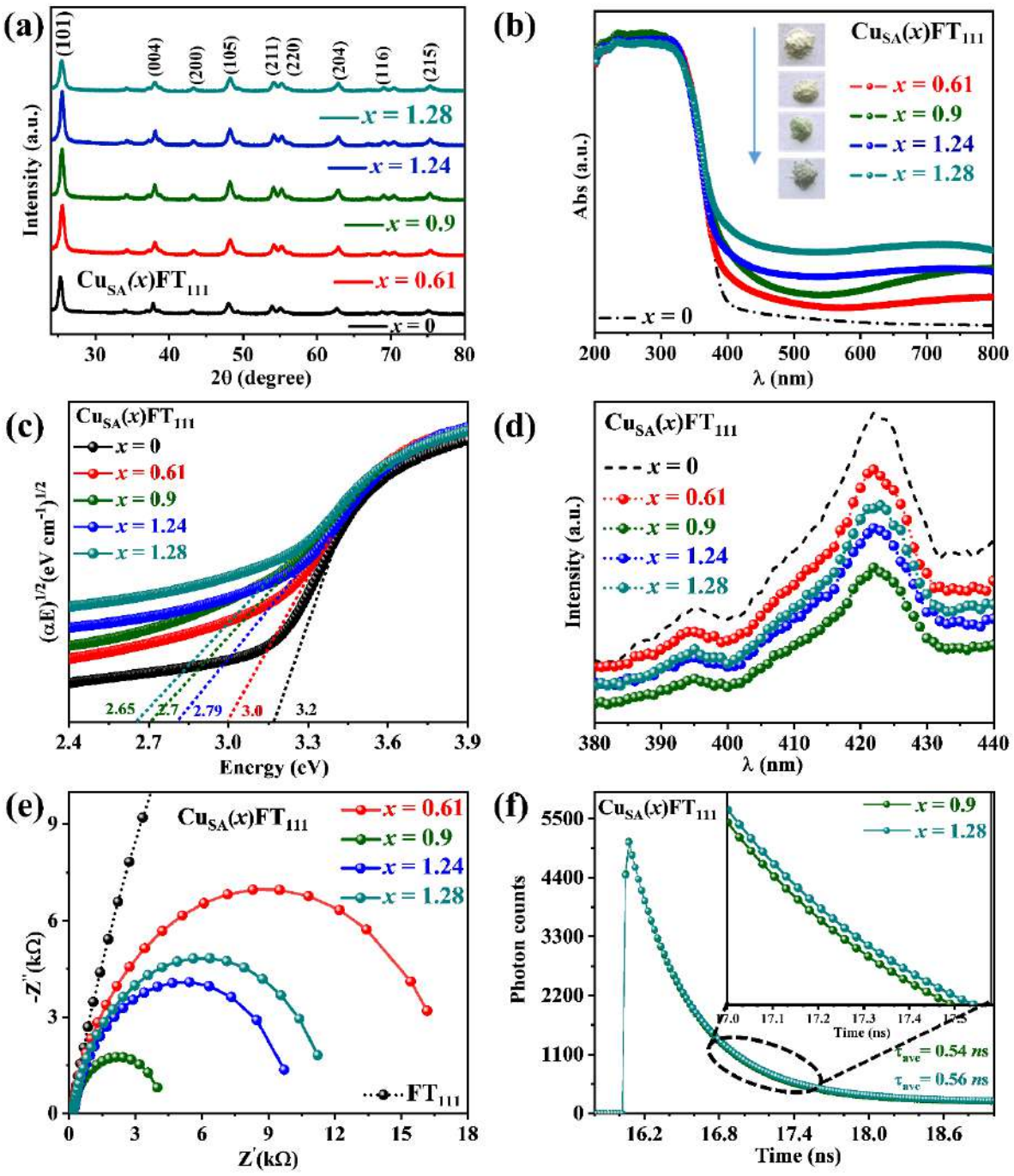

Figure 3.26. **(a)** Powder XRD patterns. **(b)** UV-vis DRS spectra. **(c)** Tau's plot and corresponding band gap values of $Cu_{SA}(x)FT_{111}$ series. **(d)** Room-temperature steady-state photoluminescence spectra ($\lambda_{ext} = 260\,nm$). **(e)** EIS Nyquist plots. **(f)** Time-resolved photoluminescence spectra of $Cu_{SA}(0.9)FT_{111}$ and $Cu_{SA}(1.28)FT_{111}$ HAASC. τ_{ave} represents the average PL lifetime of the samples.

These experimental findings allow us to elucidate the trend observed in the $Cu_{SA}(x)FT_{111}$ series regarding photocatalytic activity, as depicted in **Figure 3.9a**. It is important to note that our experimental and theoretical investigations have already shown that in $Cu_{SA}FT_{111}$ HAASC, Cu_{SA}-O_v-Ti_{3c} are active sites for photo-splitting of water. These sites are formed when Cu_{SA} replaces specific $Ti_{5c}(1)$ atoms on the (111) faceted TiO_2, leading to the creation of O_v. The charge heterogeneity induced by O_v facilitates favorable adsorption and activation of water molecules, ultimately promoting H_2 production. Furthermore, O_v in Cu_{SA}-O_v-Ti_{3c} HAAS facilitates efficient transfer of charge to the adsorbed H_2O molecules. Similar results have been shown by previous reports, where O_v are reported to accelerate charge transfer between catalysts and targeted molecules, resulting in higher catalytic activity **[239, 240]**. The reduced activity observed in the 0.61 at% Cu_{SA}-doped sample can be attributed to the formation of fewer Cu_{SA}-O_v-Ti_{3c} active sites compared to the 0.9 at% Cu_{SA}-doped sample. Additionally, the poor visible-light absorption, increased charge recombination, and high charge transfer resistance associated with the 0.61 at% Cu content contribute to its significantly lower photocatalytic activity. Our findings suggest that optimal photocatalytic H_2 generation is achieved with Cu_{SA} loading amounts of 0.9 and 1.24 at%, as these concentrations offer the desired optical and electronic properties. Conversely, the diminished photocatalytic activity observed in $Cu_{SA}(1.28)FT_{111}$ may result from the lattice defects induced by excessive Cu accumulation, serving as trap centers for charge carriers, as supported by the PL results. The average PL lifetime obtained from the TRPL curve of $Cu_{SA}(1.28)FT_{111}$ **(Figure 3.26f)** further corroborates these conclusions (*i.e.*, delayed charge transportation at high Cu loading) **[172, 187]**. It is conclusive that the optimized Cu_{SA} concentration is a crucial factor in accounting for photocatalytic H_2 production in HAASC.

3.4. Conclusions

In this chapter, a novel highly asymmetric atomic sites catalyst by strategic trapping of Cu single atoms on high-index (111) faceted TiO_2 for markedly enhanced H_2 generation. Experimental and theoretical investigations reveal that Cu single atoms specifically replace Ti_{5c} atoms next to the Ti_{3c} with the creation of O_v resulting in the formation of Cu_{SA}-O_v-Ti_{3c} HAAS. The Cu_{SA}-O_v-Ti_{3c} HAAS act as active sites for the better adsorption and activation of H_2O molecules, when compared with Ti_{5c}-O-Ti_{3c} conventional AAS. More importantly, HAAS gives rise to enhanced light harvesting, improved charge transfer dynamics, and high redox capability of photoexcited electrons in HAASC. Meanwhile, HAAS elevates the *d*-band center towards the Fermi level, which triggers the better adsorption of intermediates. As a result of these multi-synergetic effects, the HAASC achieves an H_2 production rate of 8.3 $mmolh^{-1}g^{-1}$ in pure water and 784.5 $mmolh^{-1}g^{-1}$ in water/methanol (10:1, v/v) mixture, 250-fold higher than Ti_{5c}-O-Ti_{3c} AASC under stimulated AM 1.5G light irradiation. The concept and realization of HAASC in the presented work are expected to open new avenues for developing high-performance photocatalysts for energy conversion and storage.

Chapter: 4
Cu Single Atom (Cu_{SA}) Doped Faceted TiO_2 Thin Films Electrodes for Enhanced PEC Water Splitting

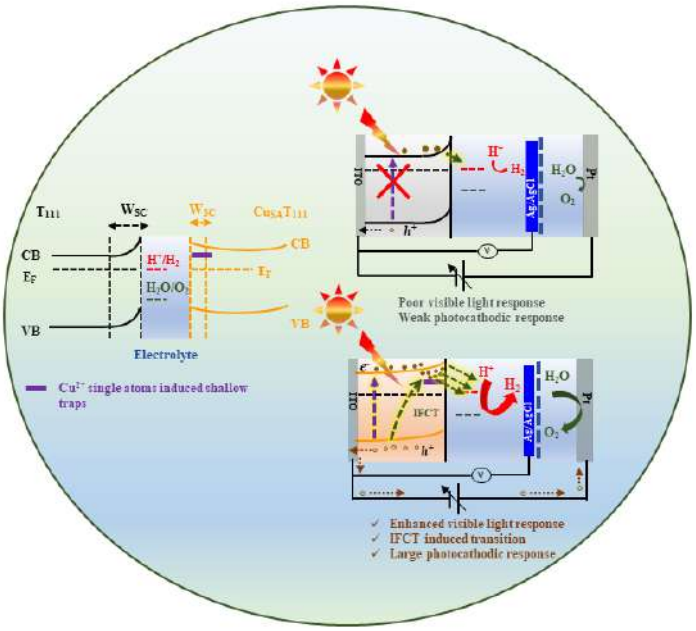

This chapter presents the fabrication of Cu single atom doped TiO_2 thin-film electrodes with (101) and (111) facets for PEC water splitting. The electrodes were prepared via single-step spray pyrolysis deposition technique and evaluated for PEC water splitting. The fabricated electrodes were tested using linear cyclic voltammetry (LCV) and chronoamperometry (CA) techniques to assess their performance in photoelectrochemical (PEC) water splitting. Despite their n-type semiconducting nature, $Cu_{SA}(0.85)T_{101}$ and $Cu_{SA}(0.85)T_{111}$ exhibit cathodic response. The optimized electrode $Cu_{SA}(0.85)T_{111}$ (with 0.85 at% Cu) (~50 µm thickness) delivers a photocurrent density of -2.22 mA cm^{-2} at −1.0 V vs reversible hydrogen electrode (RHE) under AM 1.5G illumination, approximately 2.92 times higher than its {101}-faceted analogue ($Cu_{SA}(0.85)T_{101}$). It further exhibits a low onset potential (−0.22 V vs RHE), a small overpotential (−0.28 V), and an incident photon-to-current efficiency (IPCE) of 27.1% at 420 nm. The enhanced PEC performance of $Cu_{SA}(0.85)T_{111}$ photoelectrode is due to the presence of Cu^{2+} single a and high concentration of O_v, which introduce shallow donor states, narrow the band gap, and improve visible-light absorption. The increased donor density reduces band bending and the depletion width, while defect-induced surface states partially pin the Fermi level. Together, these effects promote efficient charge separation and direct interfacial charge transfer (IFCT), leading to superior PEC performance. Furthermore, a comparative analysis with previously reported Cu/TiO_2-based photocathodes is provided to highlight the superior performance of the developed system for developing low-cost, solar-driven hydrogen production.

4.1. Introduction

Hydrogen (H_2) is a clean fuel with high energy density, offering a sustainable solution to meet growing global energy demands and support the transition to a carbon-neutral future **[42,165]**. Among the various hydrogen production strategies, photoelectrochemical (PEC) water splitting has emerged as an environmentally friendly and sustainable approach that directly converts solar energy into hydrogen fuel through the splitting of water **[42]**. A critical component in PEC systems is the photoelectrode material, which absorbs solar light and generates electron–hole pairs that drive the electrochemical reactions required for water splitting. Among available photoelectrode materials, metal oxides are particularly attractive due to their chemical stability, earth abundance, low cost, and suitable band-edge positions **[241–244]**. Titanium dioxide (TiO_2), first demonstrated as a photoanode by Fujishima and Honda in 1972, remains a benchmark PEC material **[23]**. Its intrinsic n-type character induces upward band bending at the semiconductor–electrolyte interface, leading to surface hole accumulation and favoring photoanodic water oxidation **[245]**. Despite these advantages, the practical application of TiO_2 in PEC systems is limited by several intrinsic challenges, including wide band gaps, suboptimal conduction and valence band alignments, low charge carrier mobility, rapid electron–hole recombination, limited visible-light absorption, and sluggish surface reaction kinetics, all of which reduce PEC efficiency **[245]**. To overcome these limitations, extensive research efforts have focused on modifying TiO_2 through various strategies. These approaches include metal and non-metal doping, heterostructure engineering, noble metal decoration, and facet-specific modifications, aim to improve visible-light absorption, enhance charge separation, and accelerate surface catalytic reactions to enhance the PEC performance of TiO_2-based photoelectrodes **[246-248]**.

Interestingly, although TiO_2 inherently exhibits photoanodic behavior, recent studies have revealed that its PEC characteristics can be significantly altered through heteroatom doping,

enabling it to function as a photocathode under certain conditions. For example, Wardhana and co-workers reported that Cu(II) nanoclusters–modified TiO_2 facilitates direct interfacial charge transfer (IFCT) from the TiO_2 valence band to Cu active sites **[249]**. This interfacial charge-transfer pathway enables the generation of cathodic photocurrents under visible-light irradiation. In their PEC configuration, a Cu(II)/TiO_2/Fluorine-doped tin oxide (FTO) coated glass electrode was employed as the working electrode, while a Pt sheet and Ag/AgCl electrode served as the counter and reference electrodes, respectively. Similarly, Madan and co-workers reported photocathodic behavior in Mn/Fe co-doped TiO_2 nanotube arrays, evaluated using a conventional three-electrode PEC configuration, with Mn/Fe co-doped TiO_2/Ti foil acted as the working electrode, Ag/AgCl as the reference electrode, and a Pt foil acting as the counter electrode **[250]**. In addition to TiO_2-based systems, recent reports have demonstrated that photocathodic responses can also be induced in other n-type semiconductors through appropriate defect engineering. For example, Ruan et al. demonstrated that defect-induced shallow trap states in graphitic carbon nitride (g-C_3N_4) can trigger photocathodic behavior **[251]**. In another study, Madan and co-workers observed a similar response in N-doped, Ti^{3+}-rich $SrTiO_3$, further highlighting the critical role of defect states in modulating charge transport dynamics **[252]**. Collectively, these studies underscore the importance of dopant incorporation and defect engineering in tailoring the electronic structure of semiconductors, thereby enabling control over the direction of photocurrent generation. Such strategies significantly expand the functional versatility of n-type materials, indicating that systems traditionally employed as photoanodes can be rationally redesigned to operate as efficient photocathodes for solar-driven hydrogen evolution.

Building on these advances, I demonstrate that copper single-atom–doped {111}-faceted TiO_2 (Cu_SAT_{111}) thin films exhibit an efficient photocathodic response in PEC water splitting. The electrodes were fabricated by a scalable spray pyrolysis deposition method. The

optimized $Cu_{SA}(0.85)T_{111}$ electrode (~50 μm thickness) delivers a photocurrent density of −2.22 mA cm^{-2} at −1.0 V vs RHE under AM 1.5G illumination, approximately 2.92 times higher than its {101}-faceted analogue. It further exhibits a low onset potential (−0.22 V vs RHE), a small overpotential (−0.28 V), and a high IPCE efficiency of 27.1% at 420 nm. The enhanced PEC performance of $Cu_{SA}(0.85)T_{111}$ photoelectrode is due to the presence of Cu^{2+} single atoms and abundant oxygen vacancies (O_v), which introduce shallow donor states, narrow the band gap, and improve visible-light absorption. The increased donor density reduces band bending and the depletion width, while defect-induced surface states partially pin the Fermi level. Together, these effects promote efficient charge separation and direct IFCT, leading to superior PEC performance. These results substantially outperform previously reported Cu/TiO_2-based photocathodes, highlighting the promise of $Cu_{SA}T_{111}$ for low-cost, solar-driven hydrogen production.

4.2. Experimental

4.2.1. Synthesis of $Cu_{SA}(x)T_{111}$ and $Cu_{SA}(x)T_{101}$

The $Cu_{SA}(x)T_{111}$ catalyst (where x denotes the atomic Cu content, as determined by XPS) was prepared via a facile sol-gel assisted hydrothermal method, as described in chapter 3.2.1.

The $Cu_{SA}(0.85)T_{101}$ catalyst was synthesized using the same procedure as $Cu_{SA}(0.85)T_{111}$, but without adding NH_3 and HF solutions. A variety of $Cu_{SA}(x)T_{111}$ and $Cu_{SA}(x)T_{101}$ nanostructures with varying Cu concentrations (x = 0.67, 0.85, 1.26, and 1.30 at%).

T_{111} sample was prepared following identical steps as $Cu_{SA}(0.85)T_{111}$, but without using the copper precursor solution. T_{101} sample was prepared following identical steps as $Cu_{SA}(0.85)T_{101}$, but without using the copper precursor solution.

4.2.2. Photoelectrochemical Measurements

All potentials were calibrated and converted to the reversible hydrogen electrode (RHE)

scale using an Ag/AgCl reference electrode according to equation 4.1. **[254]**:

$$E_{RHE} = E_{Ag/AgCl} + E^{o}_{Ag/AgCl} + 0.059 \times pH \quad (4.1)$$

Where $E^{o}_{Ag/AgCl}$ is the standard potential of the Ag/AgCl reference electrode (0.197 V vs standard hydrogen potential for saturated KCl at 25 °C).

To determine the incident photon-to-current efficiency (IPCE), photocurrents were recorded under various wavelength filters (350 – 800 nm), and CA measurements were subsequently performed at an applied potential of −1.0 V vs RHE using the equation 4.2. **[5]**:

$$IPCE = \frac{1240 \times I}{\lambda \times J_{SC}} \quad (4.2)$$

Where I is the photocurrent density (mA cm^{-2}), λ is the wavelength of the incident light (nm), J_{SC} is incident light 200 intensity (mW cm^{-2}).

4.2.3. Electrochemical Impedance Spectroscopy (EIS) Measurements

EIS was performed on Metrohm Nova 2.1 Autolab workstation using a three-electrode system using $Cu_{SA}(0.85)T_{111}$ as the working electrode, platinum mesh (1.5 × 1.5 cm) served as the counter electrode, and a saturated KCl Ag/AgCl electrode as the reference. The electrolyte was an aqueous solution of 0.1 M H_2SO_4 (pH ≈ 1). The working electrodes were prepared by the spray pyrolysis deposition technique. EIS measurements were carried out in the dark at an applied potential of –0.256 to –0.756 V (vs. Ag/AgCl) over a frequency range of 0.1 Hz to 100 kHz. Mott–Schottky analyses were conducted at 1 kHz frequency with applied potentials ranging from +0.2 V to –0.8 V vs. Ag/AgCl.

4.2.4. Density Function Theory (DFT) Calculations

DFT simulations were carried out using the Perdew-Burke-Ernzerhof (PBE) exchange-correlation functional within the $DMol^3$ module of Materials Studio **[183]**. In addition, spin-polarized calculations were performed using a plane-wave pseudopotential

approach under the generalized gradient approximation (GGA) **[183, 184]**. Dispersion interactions were accounted for using the DFT-D correction with the Tkatchenko-Scheffler (TS) scheme. A Monkhorst–Pack k-point mesh of 4 × 4 × 1 was used for Brillouin zone integration throughout all calculations. The structural model for the T_{111} catalyst (anatase TiO_2 exposing the (111) facets, space group I41/amd) was constructed as a 1 × 2 × 1 supercell with lattice parameters a = 5.3 Å, b = 10.2 Å, and c = 22.6 Å. To avoid interactions between periodic images, a vacuum layer of 15 Å was introduced along the slab direction. To represent the $Cu_{SA}(0.85)T_{111}$ system and $Cu_{SA}(0.85)T_{101}$ system, copper atoms were incorporated onto the (111) faceted and (101) anatase TiO_2 model respectively. The crystal structures and atomic positions of all models were fully optimized by minimizing the total energy. The geometry optimizations adhered to stringent convergence criteria: an energy tolerance of 1.0×10^{-4} eV, maximum atomic forces below 0.02 Ha/Å, and maximum atomic displacements under 0.05 Å, ensuring stable and accurate structural configurations. During optimization, the bottom layers were kept fixed while only the surface atoms were allowed to relax.

4.3. Results and Discussion

4.3.1. Photoelectrodes Characterization

$Cu_{SA}(x)T_{101}$ and $Cu_{SA}(x)T_{111}$ photoelectrodes were fabricated by first synthesizing the corresponding Cu single-atom–doped TiO_2 nanostructures as reported in chapter 3.2.1. **[179]**, which were subsequently processed into thin-film electrodes. A schematic overview of the synthesis is shown in **Figure 4.1**. $Cu_{SA}(x)T_{111}$ nanostructures were synthesized by tuning the Cu precursor concentration, where x denotes the atomic Cu content determined by XPS. In contrast, omitting HF and NH_3 during synthesis yielded $Cu_{SA}(x)T_{101}$. Control samples prepared without Cu precursors produced pristine TiO_2 with dominant {111} facets (T_{111}) when HF and NH_3 were present, and {101} facets (T_{101}) when HF and NH_3 were omitted.

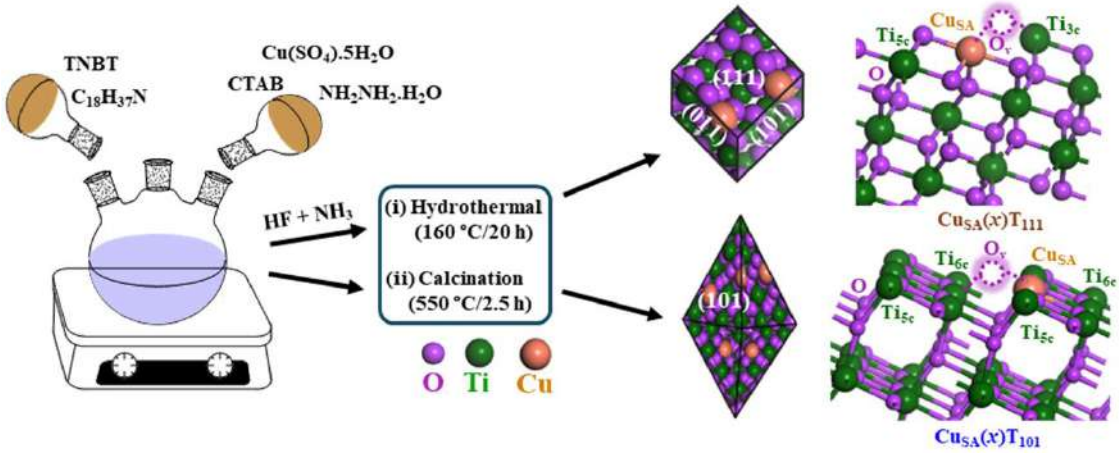

Figure 4.1. Schematic illustration of synthesis process for $Cu_{SA}T_{101}$ and $Cu_{SA}T_{111}$ nanostructures. The structural model of $Cu_{SA}T_{101}$ and $Cu_{SA}T_{111}$ nanostructures is shown, with Ti, O, and Cu atoms represented in green, purple, and rust-orange colors, respectively.

T_{111} and T_{101} exhibit distinct surface atomic configurations. On the {101} facet, Ti atoms are partially five- or six-coordinated (Ti_{5c}/Ti_{6c}) and O atoms are two- or three-coordinated (O_{2c}/O_{3c}) **[73, 255]**. In contrast, the {111} facet is more under-coordinated, consisting of Ti_{5c} and Ti_{3c} sites in a 1:3 ratio and exclusively O_{2c} atoms, which enhances surface reactivity. In Cu_{SA} doped TiO_2 samples, Cu_{SA} preferentially occupy under-coordinated Ti sites, generating O_v. Specifically, in $Cu_{SA}(x)T_{111}$, Cu substitutes Ti_{3c} sites adjacent to Ti_{5c}, whereas in $Cu_{SA}(x)T_{101}$, Cu replaces surface Ti_{5c} atoms **[256]**. The exposed facets were confirmed by HR-TEM and SAED. $Cu_{SA}(0.85)T_{111}$ forms nanocuboids with lattice fringes of 0.35 nm and an interfacial angle of 82°, corresponding to the (101) and (011) planes and confirming predominant {111} exposure **(Figure 4.2a, b) [179]**. $Cu_{SA}(0.85)T_{101}$ displays tetragonal bipyramidal nanoparticles dominated by the (101) plane **(Figure 4.2c, d)**, with no evidence of Cu aggregation. Aberration-corrected high-angle annular dark-field scanning transmission electron microscopy (HAADF-STEM) was further utilized to investigate the detailed spatial distribution of copper species.

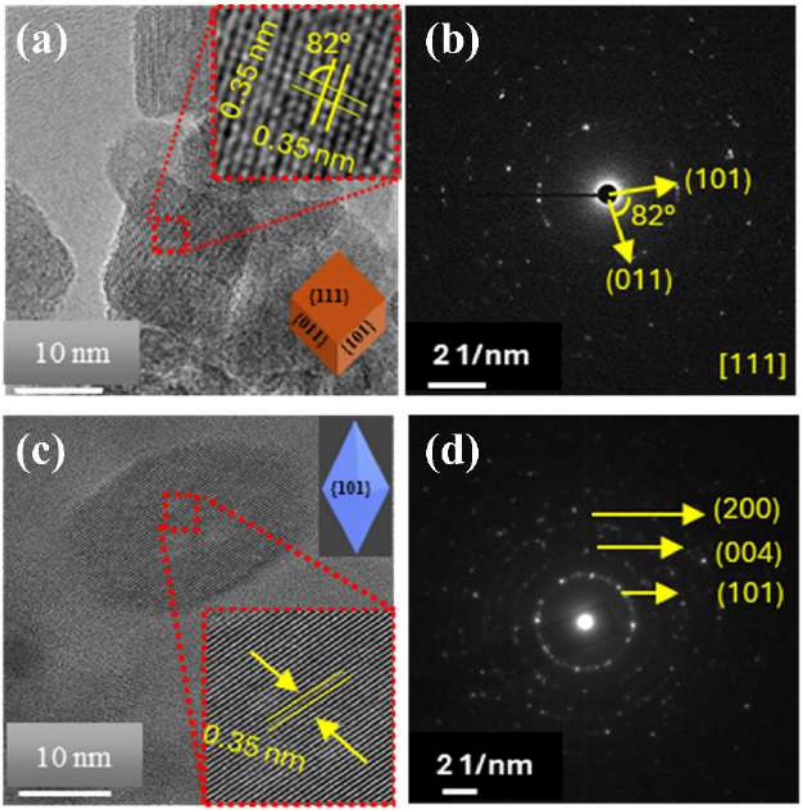

Figure 4.2. (a, b) HR-TEM image and corresponding SAED pattern of $Cu_{SA}(0.85)T_{111}$. Inset on the right shows a zoomed-in view of the area marked by a red dotted circle. The inset on the right corner shows a model of the cuboid shape characteristic of the particle. **(c, d)** HR-TEM image of $Cu_{SA}T_{101}$ and corresponding SAED pattern. The inset on the right shows a zoomed-in view of the area marked by a red dotted circle. The Inset on the left shows a model of the tetragonal bipyramidal shape characteristic of the particle.

However, due to instrumental constraints, atomically resolved HAADF-STEM images could not be obtained for the $Cu_{SA}T_{111}$ and $Cu_{SA}T_{101}$ samples, as shown in **Figure 4.3a** and **Figure 4.3b**. Nevertheless, complementary EDX elemental mapping provides compelling evidence for a homogeneous and well-dispersed distribution of single-atom copper (Cu_{SA}) throughout both $Cu_{SA}(0.85)T_{111}$ and $Cu_{SA}(0.85)T_{101}$ samples. This observation strongly supports the proposed hypothesis of isolated Cu single-atom incorporation within the host matrix, which will be further validated through extended X-ray absorption fine structure (EXAFS) analysis. While the Ti and O, EDX signals closely mimic the shape of the particles observed in the

HAADF-STEM images, the apparent extension of the copper signal beyond the cubic boundaries of the particles is attributed to background interference originating from the copper TEM grid used during analysis. After the exposed facets confirmation, the obtained nanostructures were used for fabrication of thin film electrodes. For thin-film electrode fabrication, the as-synthesized $Cu(x)T_{101}$ and $Cu(x)T_{111}$ powders were dispersed in IPA containing PVA as a binding agent **[253]**.

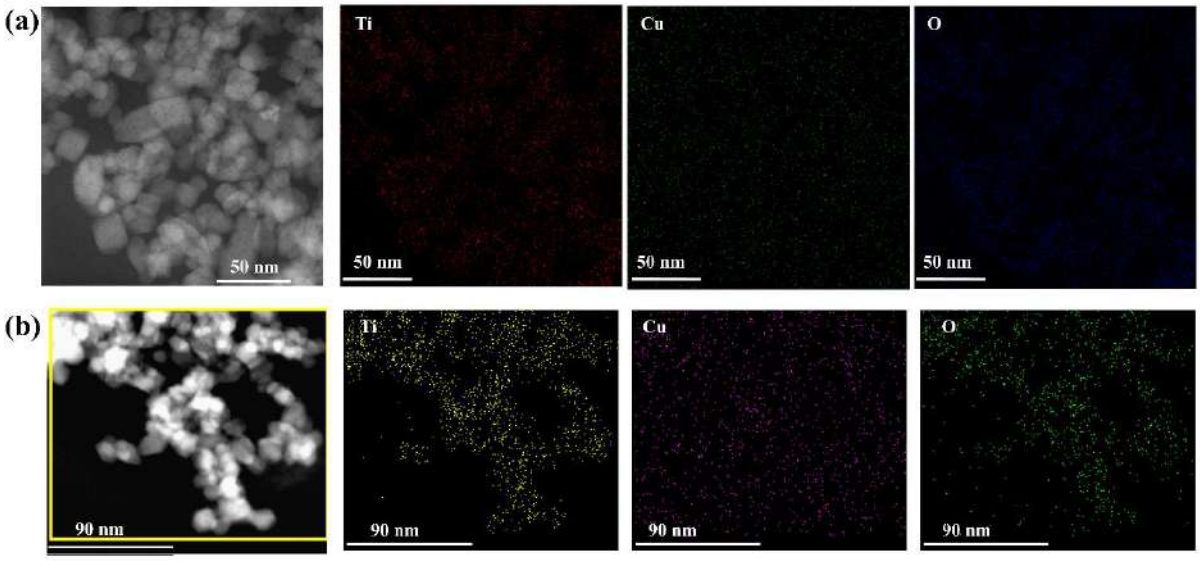

Figure 4.3.(a) HAADF-STEM image and corresponding selected-area EDX elemental maps of Ti, Cu, and O for the $Cu_{SA}(0.85)T_{111}$ sample. **(b)** HAADF-STEM image and corresponding selected-area EDX elemental maps of Ti, Cu, and O for the $Cu_{SA}(0.85)T_{101}$ sample.

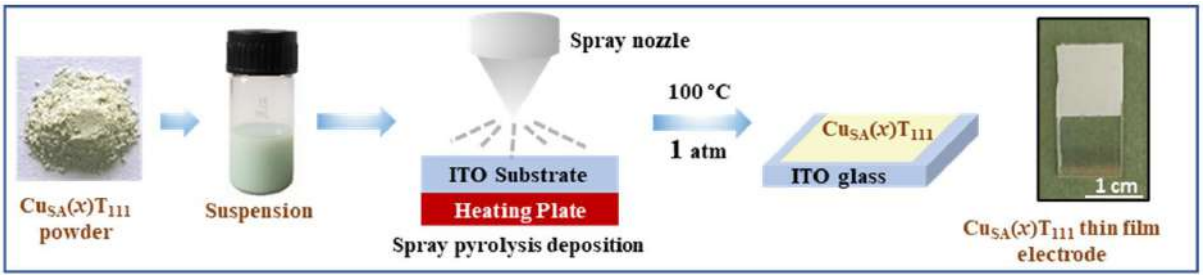

Figure 4.4. Diagram showing the fabrication process of thin film electrodes through the spray-pyrolysis deposition technique.

The resulting suspension was deposited onto ITO glass substrates using a facile spray pyrolysis method followed by calcination **(Figure 4.4)**. Spray pyrolysis is a widely used

method for depositing thin films of metal oxides, metals, and organic semiconductors **[253, 256]**.

Thin film photoelectrodes were prepared using a spray pyrolysis deposition system (Model HO-TH-04, HolmarcOpto Mechatronics Pvt. Ltd., India) **[253]**. The setup features a 20 mL syringe pump for precursor delivery, an ultrasonic atomizing nozzle, an air compressor for carrier gas, and a heated base plate to maintain a consistent substrate temperature. Prior to the deposition process, a homogeneous catalyst suspension was prepared. Specifically, made by mixing 0.2 g of catalyst powder and 0.05 g of PVA in 8 mL of IPA to form a uniform slurry. The mixture was magnetically stirred at 600 rpm for 7 h at room temperature to ensure proper dissolution and mixing of the components. Subsequently, the suspension was ultrasonicated for 1 h to further enhance dispersion and eliminate agglomerates, resulting in a well-dispersed precursor solution suitable for spray deposition. Nozzle movement and spray parameters were precisely controlled via a 2D motorized traverse system powered by a stepper motor. The syringe pump continuously supplied the catalyst solution to the nozzle, while a pressure regulator maintained a steady carrier air flow. ITO-coated glass was used as the substrate. During deposition, the nozzle was positioned 80 mm above the substrate and moved at programmed speeds of 10 mm/s along the X-axis and 5 mm/s along the Y-axis. The catalyst solution was delivered at 200 μL/min, with nozzle air pressure set at 1 atm and the base plate temperature maintained at 100 °C **[17]**. After spraying, the films were calcined at 150 °C for 1 h to complete thin film formation.

Figure 4.5a and **4.5b** display the cross-sectional FE-SEM image of $Cu_{SA}(0.85)T_{111}$ and $Cu_{SA}(0.85)T_{101}$ thin-film electrodes prepared under identical conditions. The films exhibit a uniform morphology with an average thickness of approximately ~50 μm. Notably, both the electrodes exhibit similar thicknesses, indicating good consistency in film fabrication process.

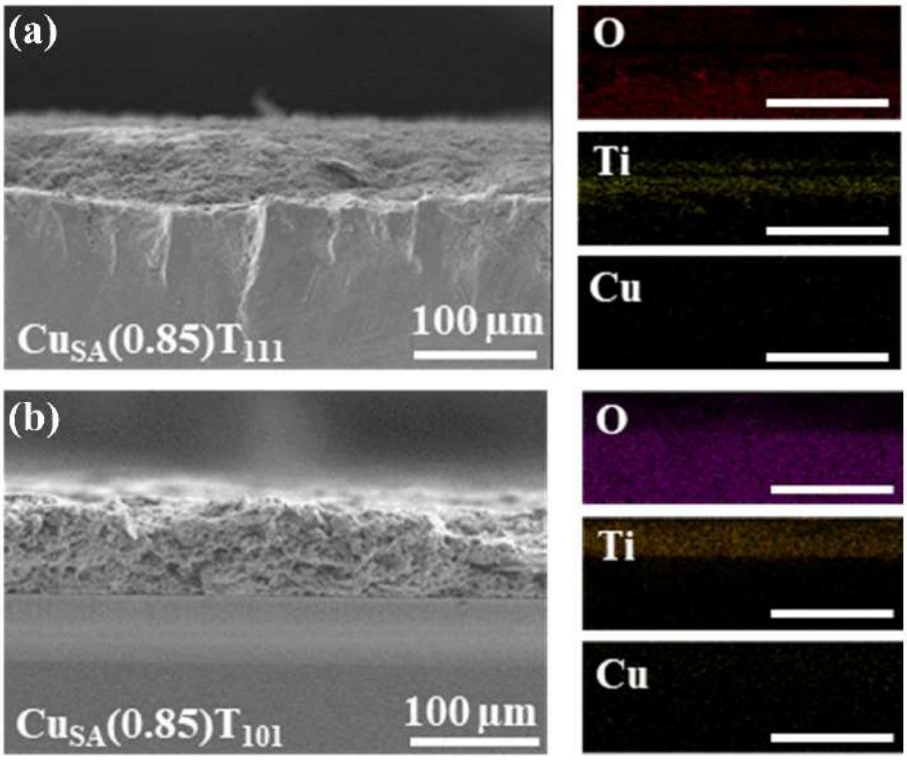

Figure 4.5. (a, b) Cross-sectional FE-SEM images along with corresponding elemental maps.

Elemental distribution obtained via EDX confirms the presence of Ti, Cu, and O. XRD analysis **(Figure 4.6a)** shows that $Cu_{SA}(0.85)T_{101}$ and $Cu_{SA}(0.85)T_{111}$ match anatase TiO_2 (JCPDS 21-2172) with no peaks for Cu, CuO, or Cu_2O, indicating atomic dispersion or lattice incorporation of Cu **[199]**.

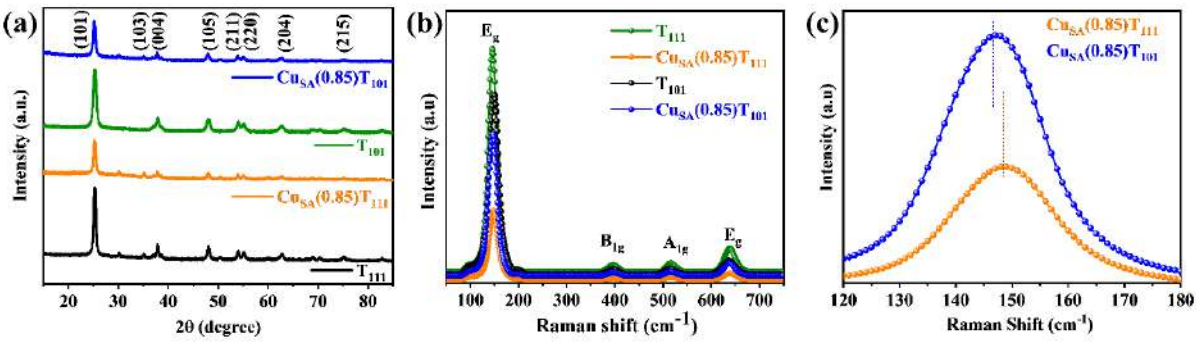

Figure 4.6. (a) XRD patterns of T_{111}, T_{101}, $Cu_{SA}(0.85)T_{111}$, and $CuSA(0.85)T_{101}$ thin-film electrodes. **(b)** Raman spectra of T_{111}, T_{101}, $Cu_{SA}(0.85)T_{111}$, and $CuSA(0.85)T_{101}$ thin-film electrodes. **(c)** Raman spectra of $Cu_{SA}(0.85)T_{101}$ and $Cu_{SA}(0.85)T_{111}$ in the 120–180 cm^{-1} region.

The slight decrease in peak intensities indicates the introduction of lattice defects, specifically O_v, due to Cu incorporation **[257]**. Raman spectra **(Figure 4.6b)** reveal E_g, B_{1g}, and A_{1g} modes corresponding to O–Ti–O vibrations **[187]**. In Cu-doped samples, decreased B_{1g} and A_{1g} intensities indicate Cu substituting surface Ti, altering local coordination and creating O_v, likely because the ionic radius of Cu^{2+} (0.73 Å) is larger than that of Ti^{4+} (0.677 Å).

The E_g mode shift to higher wavenumbers **(Figure 4.6c)** in $Cu_{SA}(0.85)T_{111}$ implies a higher O_v concentration compared to $Cu_{SA}(0.85)T_{101}$ **[187, 188]**. XPS was employed to investigate the elemental oxidation states and quantify O_v in the Cu_{SA}-doped TiO_2 thin films. Survey spectra **(Figure 4.7a, b)** confirm the presence of Ti, O, and Cu. High-resolution Ti 2p spectra **(Figure 4.7c)** display characteristic peaks at 458.48 eV (Ti $2p_{3/2}$) and 464.22 eV (Ti $2p_{1/2}$) **[108]**. A discernible shift toward lower binding energies for $Cu_{SA}(0.85)T_{111}$ indicates an increased surface Ti^{3+} concentration, consistent with a higher density of O_v **[239]**. The Cu 2p spectra **(Figure 4.7d)** show peaks at 932.28 eV and 952.38 eV corresponding to Cu $2p_{3/2}$ and Cu $2p_{1/2}$, respectively, without shake-up satellite features, confirming the presence of atomically dispersed Cu^{2+} species **[258]**. Deconvolution of the O 1s spectra **(Figures 4.7e, f)** reveals contributions from lattice oxygen (O_L, ~529.38 eV), oxygen vacancies (O_v, ~531.03 eV), and surface-adsorbed oxygen species (O_S, ~532.56 eV). Quantitative analysis **(Table 4.1)** shows that the O_v concentration in $Cu_{SA}(0.85)T_{111}$ is nearly twice that in $Cu_{SA}(0.85)T_{101}$. This pronounced generation of O_v defects is likely a key contributor to the enhanced visible-light absorption capacity of $Cu_{SA}(0.85)T_{111}$, as evidenced by the UV-Vis absorption spectra as shown in **Figure 4.8a**.

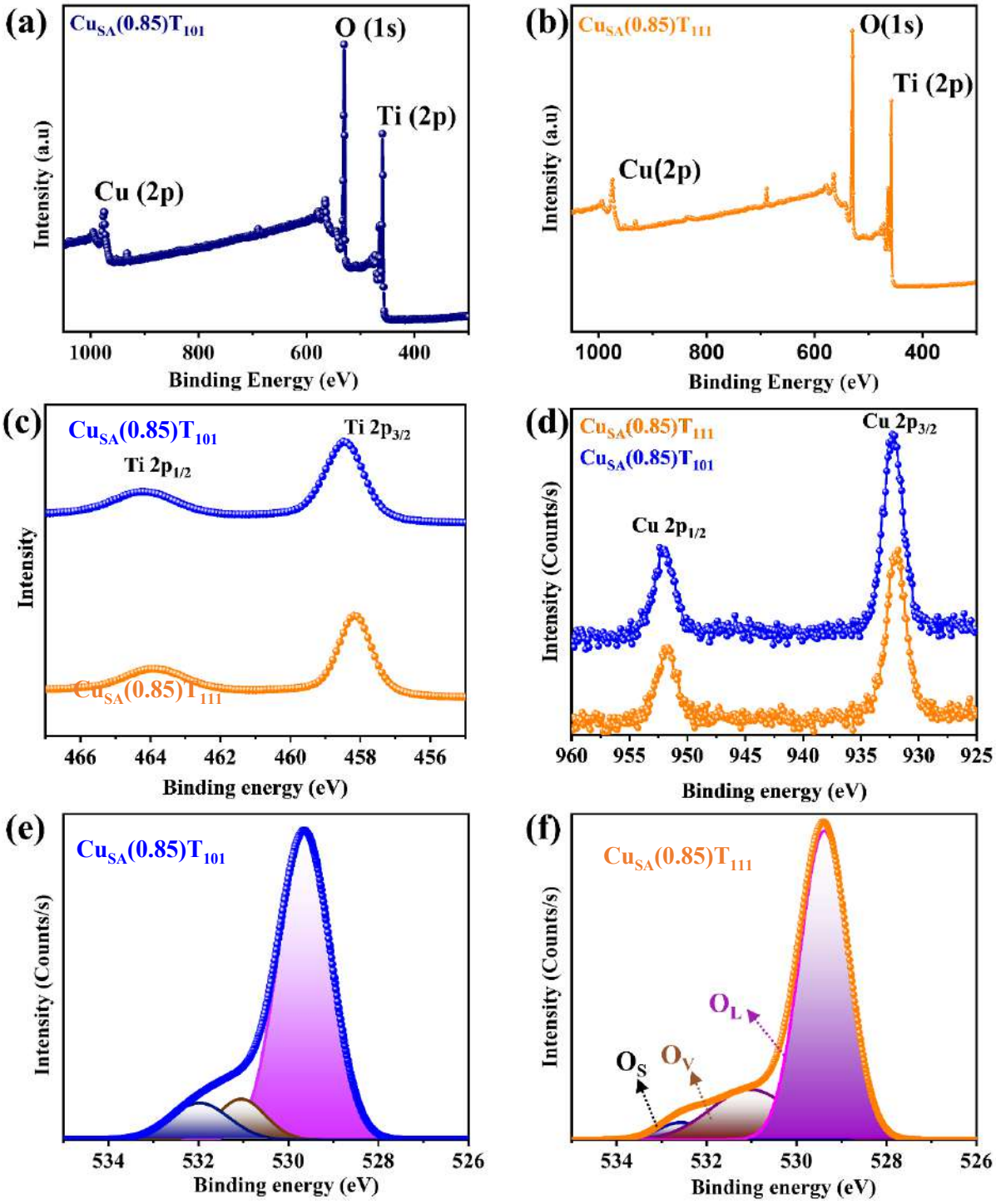

Figure 4.7. Structural and chemical characterization of materials**. (a, b)** XPS survey spectra of $Cu_{SA}(0.85)T_{101}$ and $Cu_{SA}(0.85)T_{111}$ thin-film electrodes, confirming the presence of Ti, O, and Cu elements. **(c)** High-resolution XPS spectra of Ti 2p. **(d)** High-resolution XPS spectra of Cu 2p. **(e, f)** High-resolution XPS spectra of O 1s of $Cu_{SA}T_{101}$ and $Cu_{SA}T_{111}$ thin films, respectively.

Table 4.1. Oxygen vacancy (O_v) percentage (%) in different samples, calculated from the ratio of the integrated peak areas of lattice oxygen (O_L), oxygen vacancies (Ov), and surface adsorbed water or hydrocarbons (O_S) in the O1s XPS spectra.

Sample Name	O_v (%)
T_{111}	10.87
T_{101}	4.6
$Cu_{SA}(0.85)T_{101}$	10.59
$Cu_{SA}(0.85)T_{111}$	20.4

In contrast, the pristine T_{101} and T_{111} photoelectrodes exhibit minimal response in the visible region, which can be attributed to their inherently wide optical bandgaps ~3.05 eV and 3.11 eV respectively, as calculated from Tauc's plots **(Figure 4.8b)**. Despite comparable Cu loading in both samples, $Cu_{SA}(0.85)T_{111}$ (E_g = 2.68 eV) displays a narrower bandgap than $Cu_{SA}(0.85)T_{101}$ (E_g = 2.85 eV), suggesting that the introduction of Cu_{SA} and the higher density of O_v synergistically contribute to electronic structure modification **[259]**.

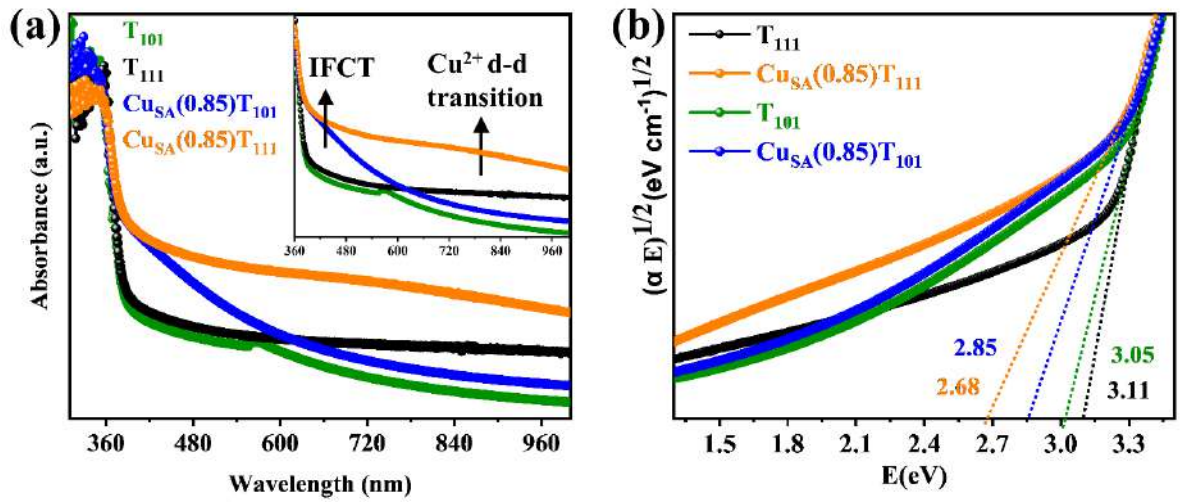

Figure 4.8. (a) UV-Vis absorption spectra of TiO_2 and Cu_{SA}-doped TiO_2 samples. The inset shows the enlarged view of the spectra. **(b)** Tauc plots derived from UV–vis absorption spectra for T_{111}, T_{101}, $Cu_{SA}(0.85)T_{111}$, and $CuSA(0.85)T_{101}$ thin-film photoelectrodes.

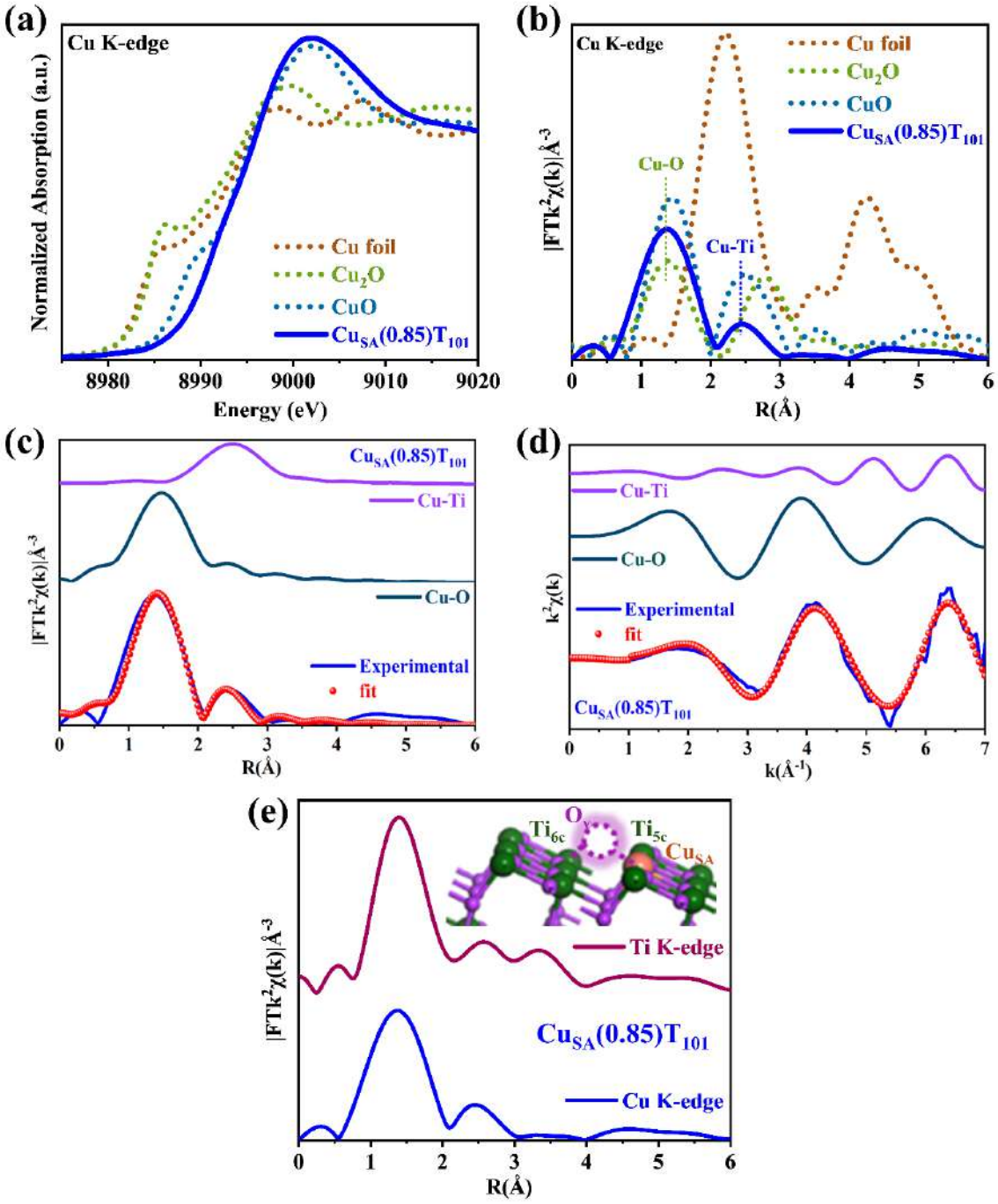

Figure 4.9.(a) Normalized XANES spectra of Cu K-edge for Cu foil, CuO, Cu_2O, and $Cu_{SA}(0.85)T_{101}$. **(b)** Cu *K*-edge k^2-weighted Fourier transform EXAFS spectra. Experimental (solid blue line) and fitted (red circles) Cu K-edge EXAFS spectra of $Cu_{SA}(0.85)T_{101}$ in **(c)** R-space and **(d)** k-space. The fitted contributions from Cu–O (dark cyan) and Cu–Ti (light purple) coordination are also shown. **(e)** Fitted EXAFS spectra of the first coordination shell for Ti *K*-edge and Cu *K*-edge in $Cu_{SA}(0.85)T_{101}$. The inset presents a schematic illustration of the Cu_{SA}-O_v-Ti_{6c} coordination environment derived from XAFS analysis**.**

This bandgap narrowing is particularly advantageous, as it facilitates more effective harvesting of visible light and improved charge carrier excitation, both of which are essential for enhancing PEC water splitting performance **[240]**. Additionally, two new absorption features appear UV-Vis spectra of Cu_{SA}-doped TiO_2 samples: (i) a band near 430 nm, attributed to the interfacial charge transfer (IFCT) from the valance band of TiO_2 to isolated Cu_{SA}, consistent with previous reports **[249, 260]**; and (ii) a broad absorption in the 800 – 900 nm region, associated with the d-d transition of Cu^{2+} dopants **[258]**. As shown in the **Figure 4.8a**, the $Cu_{SA}(0.85)T_{111}$ photoelectrode exhibits a more pronounced IFCT feature and stronger Cu^{2+} d-d transitions, underscoring its enhanced light-harvesting and charge-transfer capability. The isolated nature of Cu in $Cu_{SA}(0.85)T_{111}$ has been demonstrated in our previous work, where Cu_{SA} substitutes surface Ti_{3c} atoms and generates O_v, forming Cu_{SA}–O_v–Ti_{5c} surface sites **[252]**. Normalized Cu K-edge XANES spectra of $Cu_{SA}(0.85)T_{101}$ **(Figure 4.9a)** align with CuO, confirming +2 oxidation state, while differences from Cu foil rule out Cu–Cu coordination. EXAFS analysis **(Figure 4.9b)** shows a dominant Cu–O peak at ~1.36 Å and a minor Cu–Ti peak at ~2.43 Å, with no evidence of Cu–Cu or Cu–O–Cu bonds, indicating atomic Cu substitution for Ti. EXAFS fitting results for $Cu_{SA}(0.85)T_{101}$ give a coordination number (CN) of 4 for Cu-O contribution in the first coordination sphere with a bond length of ~1.92 Å and CN of 4 for Cu-Ti contribution in the second coordination sphere with a bond length of ~2.94 Å **(Figure 4.9c, d and Table 4.2)**. Comparison of Ti and Cu K-edge spectra **(Figure 4.9e)** shows similarity in the first coordination shell, suggesting Cu occupies Ti_{5c} sites, forming Cu_{SA}–O_v–Ti_{6c} in $Cu_{SA}(0.85)T_{101}$, consistent with previous Cu_{SA}/TiO_2 studies **[199, 90]**.

Table 4.2. Detailed information on M-O and Ti-M contributions from EXAFS fitting.

Sample	Scattering Path	N	R (Å)	σ^2 (Å^2)	R-factor (%)
$Cu_{SA}(0.85)T_{101}$	Cu-O	4	1.92 ± 0.005	0.004	0.012
	Cu-Ti	4	2.94 ± 0.054	0.012	

N= Coordination number, *R*= Interatomic distance, σ^2 = Debye-Waller factor (bond disorder)
R-factor = A measure of the quality of EXAFS fitting

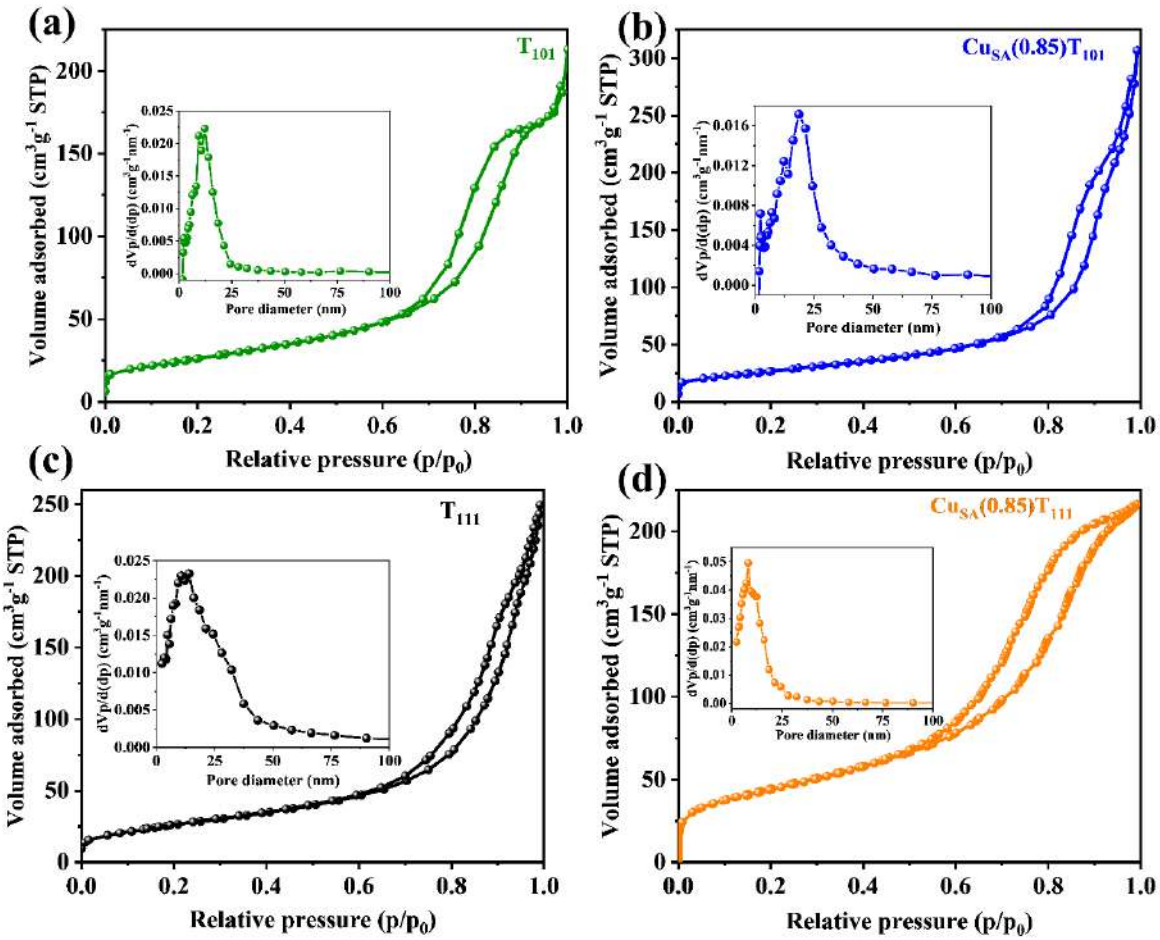

Figure 4.10. Nitrogen adsorption–desorption isotherms of **(a)** T_{101}, **(b)** $Cu_{SA}(0.85)T_{101}$, **(c)** T_{111} and **(d)** $Cu_{SA}(0.85)T_{111}$; insets show corresponding pore size (BJH) distributions.

Figure 4.10 a-d presents the N_2 adsorption–desorption isotherms along with the corresponding pore size distributions of T_{101}, $Cu_{SA}(0.85)T_{101}$, T_{111}, and $Cu_{SA}(0.85)T_{111}$., respectively. All samples exhibit type IV isotherms accompanied by H3 hysteresis loops, which are characteristic features of mesoporous materials. The hysteresis loop appears at a relatively higher relative pressure ($P/P_0 \approx 0.6$), indicating the presence of capillary condensation within mesopores **[189]**. Such adsorption behavior is typically associated with the aggregation of nanoparticles, leading to the formation of slit-shaped pores. The textural parameters, including specific surface area, pore size, and pore volume of all samples, are summarized in **Table 4.3**. Notably, $Cu_{SA}(0.85)T_{111}$ exhibits the highest specific surface area

among all the samples. This enhanced surface area is expected to provide a larger number of active sites and facilitate improved mass transport, which can be beneficial for photoelectrochemical performance **[261]**.

Table 4.3. Surface areas, pore volumes, and pore diameters of samples measured from N_2 adsorption-desorption isotherms.

Sample	Surface area (S_{BET}) (m^2/g)	Mean pore diameter (<*d*>) (nm)	Pore volume (cm^3/g)
T_{101}	95.0	11.8	0.31
$Cu_{SA}(0.85)T_{101}$	99.2	18.5	0.47
T_{111}	100.3	14	0.38
$Cu_{SA}(0.85)T_{111}$	125.7	8.2	0.33

4.3.2. PEC Water Splitting Results

PEC water-splitting performance of the fabricated electrodes was evaluated by LSV using a three-electrode configuration with a Pt mesh counter electrode under dark and simulated solar illumination (AM 1.5G). **Figure 4.11a** compares the LSV curves of pristine T_{101} and T_{111}, as well as $Cu_{SA}(0.85)T_{101}$ and $Cu_{SA}(0.85)T_{111}$ photoelectrodes, all with a thickness of ~20 μm, measured in 0.1 M H_2SO_4 over wide range of voltage from −1 V to 1.5 V. While pristine T101 and T111 exhibit negligible cathodic photocurrent, both CuSA-doped electrodes display pronounced cathodic responses that increase with increasingly negative bias, characteristic of hydrogen evolution reaction (HER) activity [262, 263]. Among all samples, $Cu_{SA}(0.85)T_{111}$ delivers the highest photocurrent density (−0.72 mA cm^{-2}), nearly twice that of $Cu_{SA}(0.85)T_{101}$ (−0.50 mA cm^{-2}), indicating that the {111} facet provides a more favorable surface for PEC water splitting when combined with Cu single-atom doping.

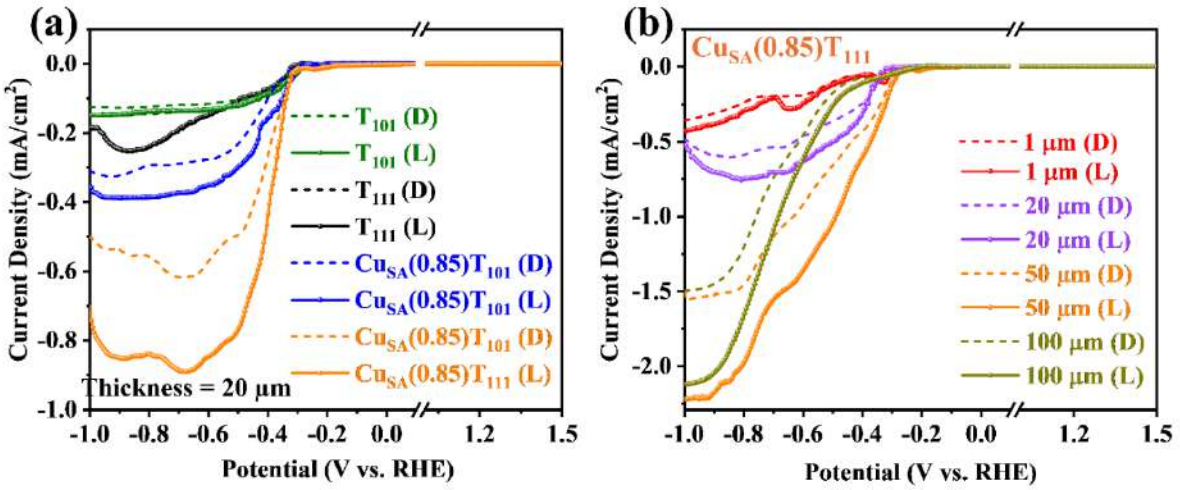

Figure 4.11. PEC water splitting results. **(a)** LSV curves of T_{101}, T_{111}, $Cu_{SA}(0.85)T_{101}$, and $Cu_{SA}(0.85)T_{111}$ photoelectrodes (each ~20 µm thick), recorded in 0.1 M H_2SO_4 under simulated sunlight (AM 1.5G) at ambient temperature. **(b)** LSV responses of $Cu_{SA}(0.85)T_{111}$ electrodes with varying film thicknesses.

To further optimize performance, the influence of film thickness was systematically investigated. The $Cu_{SA}(0.85)T_{111}$ electrodes with thicknesses of ~1, 20, 50, and 100 µm were fabricated **(Figure 4.12a, b, c)** and evaluated under identical conditions **(Figure 4.11b)**.

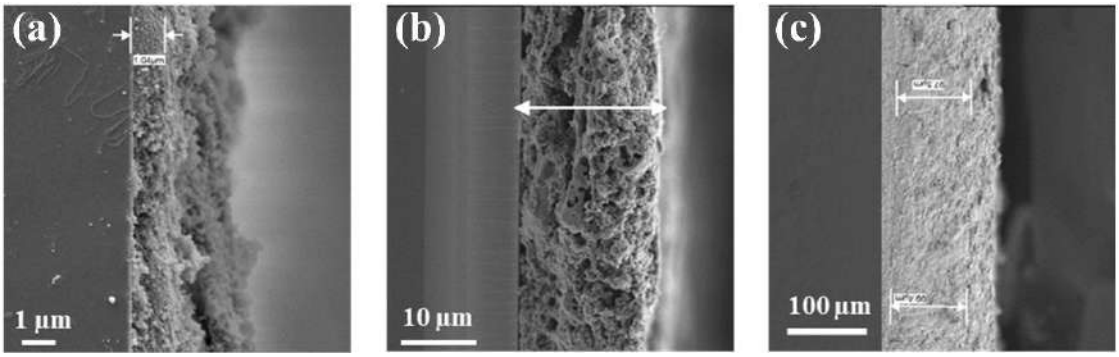

Figure 4.12. (a, b, c) Cross-sectional FESEM images of $Cu_{SA}(0.85)T_{111}$ photoelectrodes with thicknesses of approximately 1, 20, and 100 µm.

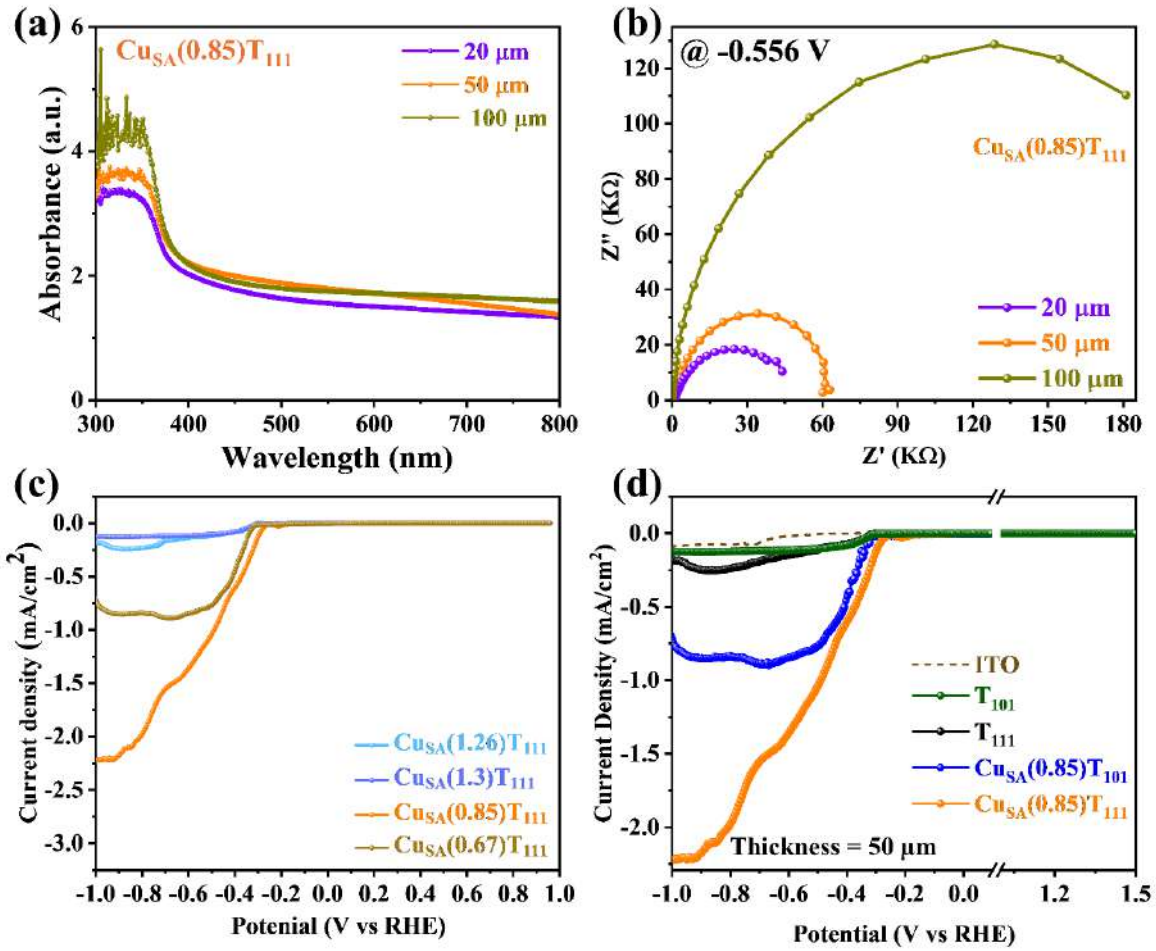

Figure 4.13. (a) UV–vis absorption spectra of $Cu_{SA}(0.85)T_{111}$ photoelectrodes with thicknesses of approximately 1, 20, and 100 µm. **(b)** EIS Nyquist plots of $Cu_{SA}(0.85)T_{111}$ photoelectrodes with different thicknesses at an applied potential of –0.556 V. **(c)** Linear sweep voltammetry (LSV) curves of $Cu_{SA}(x)T_{111}$ photoelectrodes with varying Cu concentrations at a constant thickness of ~50 µm. **(d)** LSV curves of $Cu_{SA}(0.85)T_{101}$, and $Cu_{SA}(0.85)T_{111}$ photoelectrodes, each at optimized thickness ~50 µm.

The reduced performance of thinner films is attributed to insufficient light harvesting, as evidenced by the UV–Vis spectra of $Cu_{SA}(0.85)T_{111}$ films with varying thicknesses **(Figure 4.13a)**. In contrast, thicker films show diminished performance due to enhanced charge-carrier recombination arising from extended transport pathways, as supported by the Nyquist plots **(Figure 4.13b)**. Notably, the ~50 µm thick film demonstrates efficient light absorption while maintaining relatively low charge recombination, leading to its superior photoelectrochemical performance. Subsequently, the effect of Cu loading was examined by fabricating $Cu_{SA}(x)T_{111}$ photoelectrodes with Cu contents of 0.67, 0.85, 1.26, and 1.30 at%, while maintaining a constant film thickness (~50 µm) to eliminate thickness-related effects.

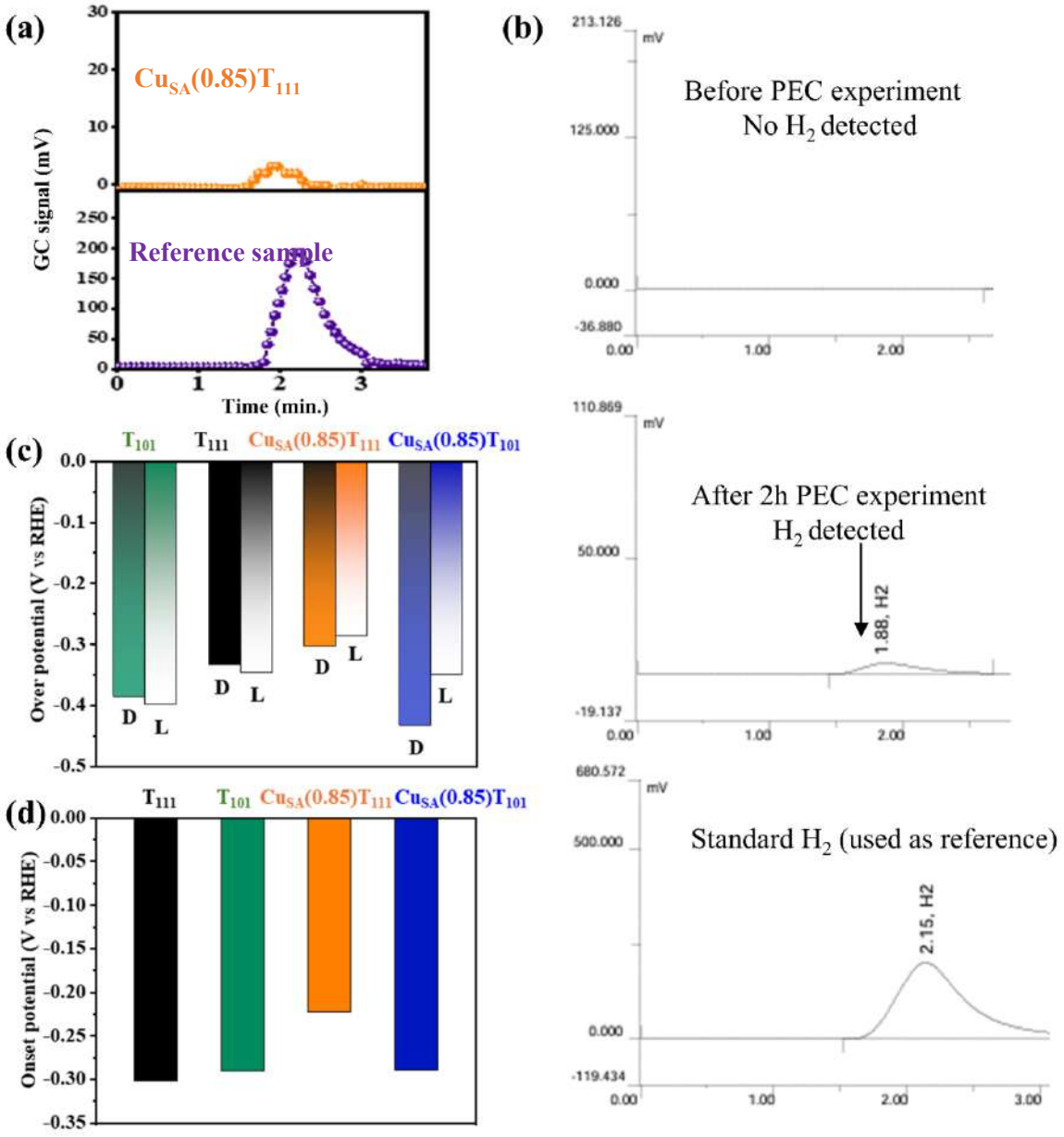

Figure 4.14.(a) GC signals for the gaseous product collected after 2 hr from the headspace of the $Cu_{SA}(0.85)T_{111}$ electrode compartment in an H-cell configuration, with pure H_2 gas as reference. **(b)** Gas chromatography (GC) signals of gaseous products collected from the headspace of the $Cu_{SA}(0.85)T_{111}$ photoelectrode compartment in an H-cell configuration. **(c)** Bar charts comparing overpotentials under dark and illuminated conditions for T_{101}, T_{111}, $Cu_{SA}(0.85)T_{101}$, and $Cu_{SA}(0.85)T_{111}$ photoelectrodes (~50 µm thick), measured in 0.1 M H_2SO_4 under AM 1.5G illumination at ambient temperature. **(d)** Onset potentials of T_{101}, T_{111}, $Cu_{SA}(0.85)T_{101}$, and $Cu_{SA}(0.85)T_{111}$ under illumination. The symbols "D" and "L" in the figures stand for dark and light conditions, respectively.

As shown in **Figure 4.13c**, the photocurrent density increases with Cu content up to 0.85 at% and then decreases at higher loadings. The $Cu_{SA}(0.85)T_{111}$ electrode exhibits the optimal PEC performance, indicating that excessive Cu incorporation introduces defect states that act as recombination centers and slow charge-carrier dynamics **[253, 199]**. **Figure 4.13d** compares the optimized T_{101}, T_{111}, $Cu_{SA}(0.85)T_{101}$ and $Cu_{SA}(0.85)T_{111}$ electrodes, both with ~50 μm thickness. Notably, $Cu_{SA}(0.85)T_{111}$ achieves a photocurrent density of −2.22 mA cm^{-2} at −1.0 V vs. RHE, approximately 2.92 times higher than that of $Cu_{SA}(0.85)T_{101}$ (−0.76 mA cm^{-2}). To directly confirm hydrogen evolution, controlled PEC experiments were conducted in an H-type cell with cathodic and anodic compartments separated by a Nafion membrane to prevent product crossover. After 2 h of PEC experiments, gas chromatography analysis of the headspace from the $Cu_{SA}(0.85)T_{111}$ compartment revealed a distinct H_2 signal **(Figure 4.14a and Figure 4.14b),** which was absent prior to illumination, unambiguously confirming photocathodic H_2 generation. The electrocatalytic properties were further assessed by determining the overpotential (η) required to reach a current density of 0.1 mA cm^{-2}. $Cu_{SA}(0.85)T_{111}$ exhibits the lowest overpotential, decreasing from −0.31 V in the dark to −0.28 V under illumination, along with a more positive HER onset potential (−0.22 V vs. −0.35 V for $Cu_{SA}(0.85)T_{101}$), indicating improved thermodynamic favorability **(Figures 4.14c, d) [264]**. Both the overpotential and the onset potential were influenced by the Cu concentration **(Figures 4.15a and 4.15b)**, with $Cu_{SA}(0.85)T_{111}$ exhibiting the lowest values among all tested electrodes. Electrolyte optimization revealed that 0.1 M H_2SO_4 yields the highest photocurrent **(Figure 4.15c)**, owing to enhanced ionic conductivity and interfacial charge transfer, whereas higher acidity leads to surface corrosion and reduced TiO_2 stability, consistent with Pourbaix diagram predictions **[265]**. Transient photocurrent responses measured by chronoamperometry at −1.0 V vs. RHE show rapid and reversible photocurrent

switching upon light on/off cycles **(Figure 4.15d)**, indicative of efficient charge separation and low recombination.

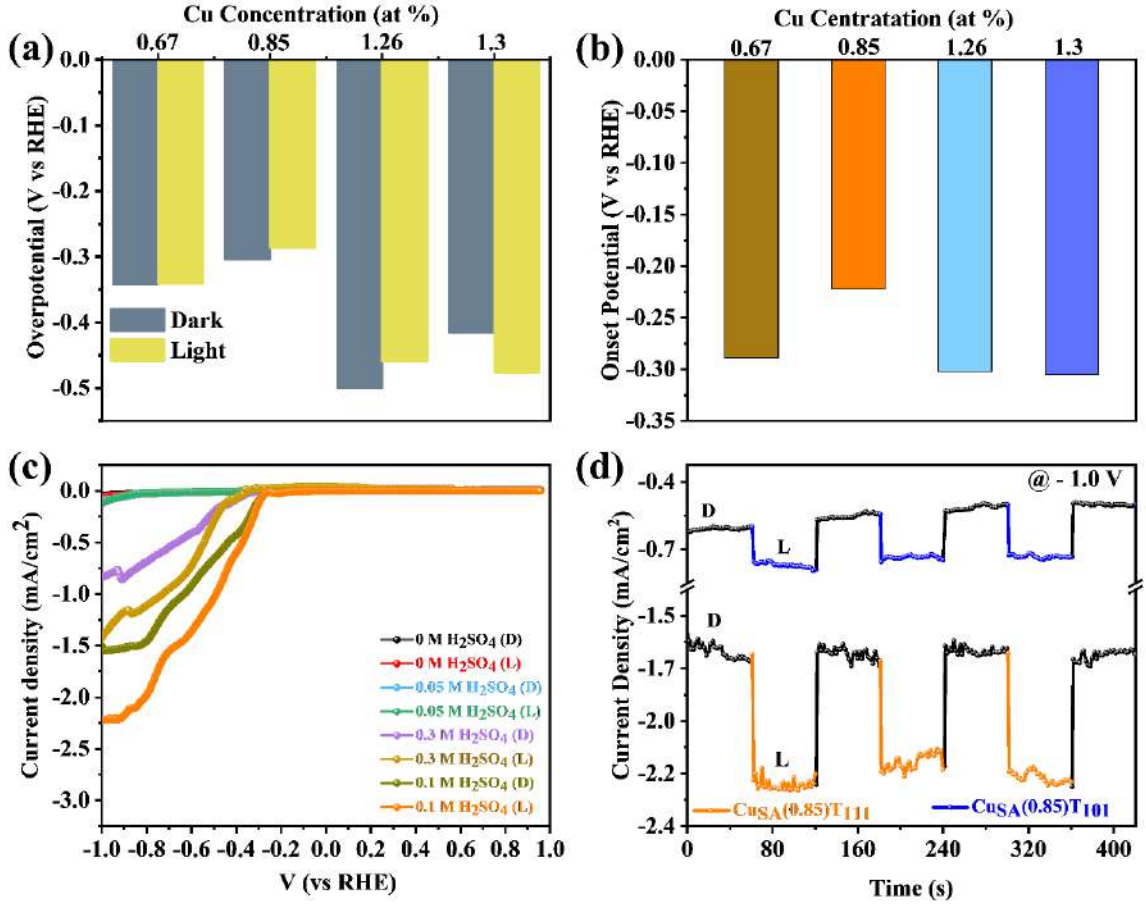

Figure 4.15. (a) Overpotentials of $Cu_{SA}(x)T_{111}$ photoelectrodes as a function of Cu content. **(b)** Onset potentials of $Cu_{SA}(x)T_{111}$ photoelectrodes as a function of Cu content. **(c)** LSV curves of $Cu_{SA}(0.85)T_{111}$ photoelectrodes measured in H_2SO_4 electrolytes with varying concentrations. **(d)** CA measurements for $Cu_{SA}(0.85)T_{101}$ and $Cu_{SA}(0.85)T_{111}$ electrodes performed under intermittent light irradiation with 180-second on/off cycles. The symbols "D" and "L" in the figures stand for dark and light conditions, respectively.

In contrast, pristine TiO_2 electrodes (T_{101} and T_{111}) exhibited a significantly weaker photoresponse under identical conditions, with negligible variation between illuminated and dark states **(Figure 4.16a, b)**.

Extended PEC stability tests were conducted to evaluate the durability of the photoelectrodes. The Cu-doped TiO2 samples exhibit a stable and sustained photocurrent over a period of 1 h

(Figure 4.16c), conversely, T_{101} and T_{111} samples showed no appreciable change in photocurrent over time (Figure 4.16a, b).

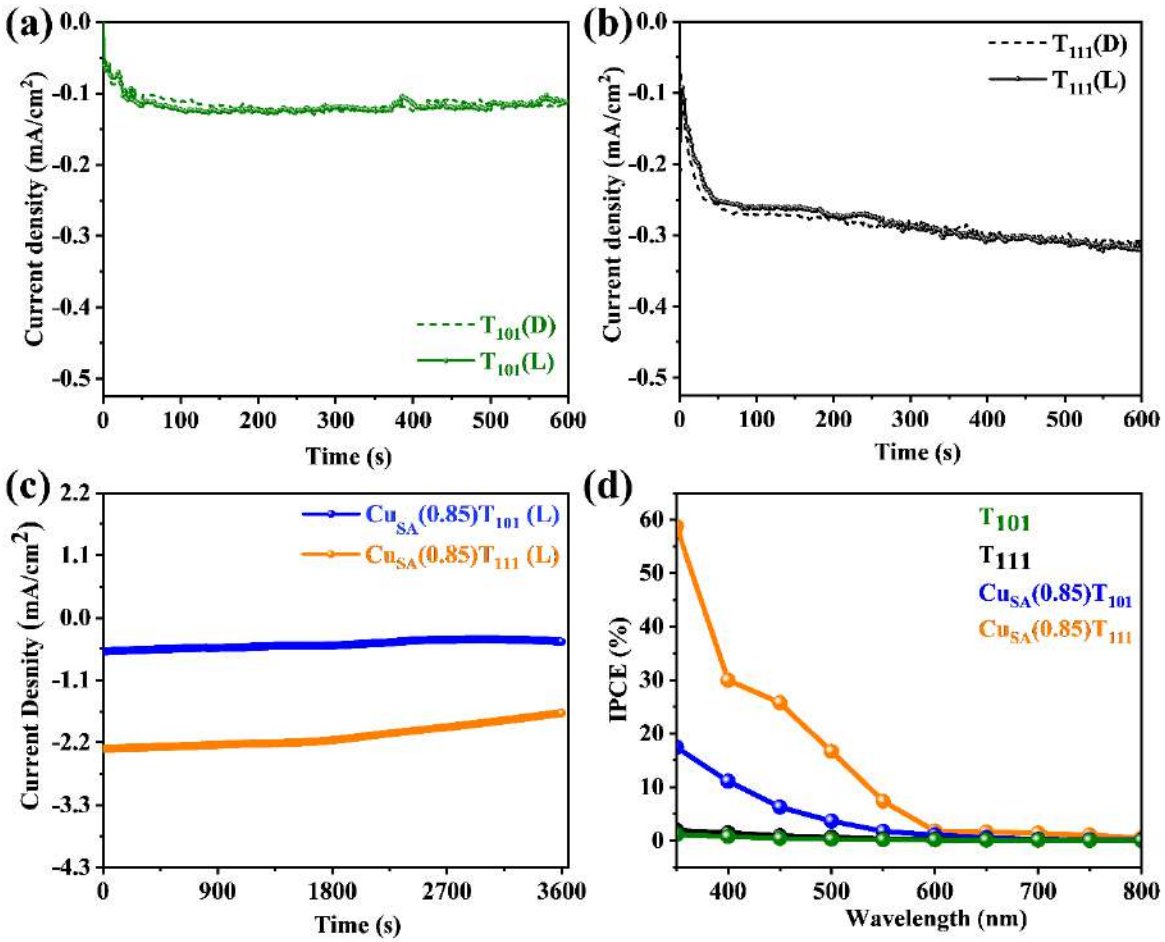

Figure 4.16. (a, b) Extended chronoamperometry (CA) measurements of T_{101} and T_{111} photoelectrodes. The symbols "D" and "L" in the figures stand for dark and light conditions, respectively. **(c)** Extended CA measurements on $Cu_{SA}(0.85)T_{101}$ and $Cu_{SA}(0.85)T_{111}$ electrodes performed over a period of 1 h. **(d)** IPCE spectra of T_{101}, T_{111}, $Cu_{SA}(0.85)T_{101}$, and $Cu_{SA}(0.85)T_{111}$ photoelectrodes measured at –1.0 V vs. RHE across the 350–800 nm wavelength range in 0.1 M H_2SO_4.

To further verify the stability of the materials, post-reaction characterization was performed. XRD analysis confirms that the crystal structure of the $Cu_{SA}(0.85)T_{111}$ remains intact after the stability test **(Figure 4.17a)**. In addition, XPS results indicate that the oxidation state of Cu is largely preserved **(Figure 4.17b, c)**. Although a slight loss of Cu is observed **(Table 4.4)**, the overall structural integrity and chemical stability of the $Cu_{SA}(0.85)T_{111}$ are maintained. These

results collectively demonstrate the good operational stability of the Cu-doped system under PEC conditions.

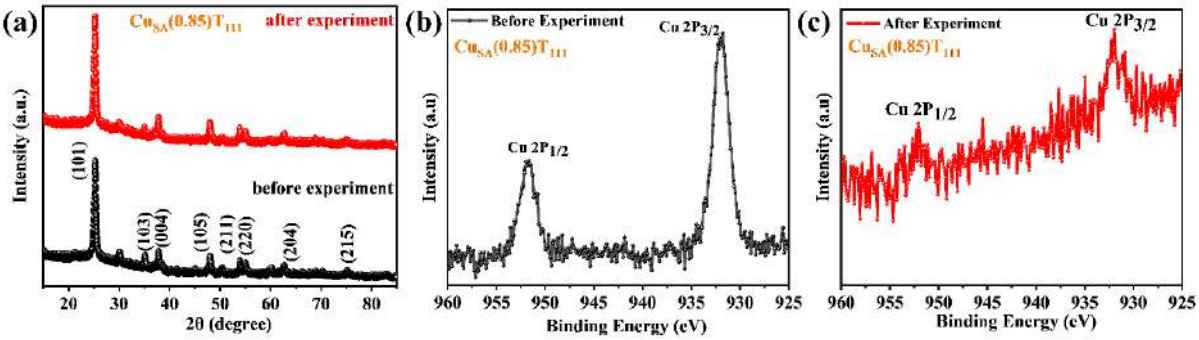

Figure 4.17. (a) XRD patterns of Cu$_{SA}$(0.85)T$_{111}$ photoelectrodes before and after PEC measurements. **(b, c)** High-resolution Cu 2p XPS spectra of Cu$_{SA}$(0.85)T$_{111}$ photoelectrodes after extended CA measurements.

Table 4.4. Cu content (at%) in Cu$_{SA}$(0.85)T$_{111}$ sample before and after 1 hour of photoelectrochemical water splitting experiments.

Sample	Before experiment	After experiment
Cu$_{SA}$(0.85)T$_{111}$	0.85	0.48

*obtained from XPS results

Finally, incident photon-to-current efficiency (IPCE) measurements **(Figure 4.16d)** reveal a maximum IPCE of 27.1% at 420 nm for Cu$_{SA}$(0.85)T$_{111}$, significantly exceeding those of Cu$_{SA}$(0.85)T$_{101}$ (9.0%), T$_{111}$ (1.2%) and T$_{101}$ (0.98%). This substantial enhancement in IPCE reflects the improved light-harvesting capability and more efficient charge separation and transfer in the Cu$_{SA}$(0.85)T$_{111}$ electrode. The superior photoconversion performance observed here is in excellent agreement with the LSV and CA results, further confirming the effectiveness of single-atom Cu incorporation and facet engineering in boosting PEC activity.

Table 4.5. PEC performance comparison of various Cu-doped TiO_2 photoelectrodes reported in the literature

Sr. No.	Materials	Nature of the electrodes	Electrolyte	Device structure (photoanode/electrolyte/photocathode)	Light source	Photocurrent density (mA cm^{-2})	Potential (V vs RHE)	References
1	Cu-doped TiO_2-B (bronze phase) nanowires	Photoanode	1 mol L^{-1} KOH	Cu-TiO_2-B/KOH/Pt	Xenon lamp 500 W	0.8	1.567	[269]
2	Cu-doped TiO_2 TF	Photoanode	1 M NaOH	Cu-TiO_2 TF/NaOH/Pt	Xenon lamp 500 W	0.018	1.42	[270]
3	Core–shell TiO_2@Cu_2O NW array	Photoanode	0.5 M Na_2SO_4	TiO_2@Cu_2O NW /Na_2SO_4/Pt	Xenon lamp 300 W	4.66	1.23	[271]
4.	Cu_2O/TiO_2	Photoanode	0.1 M NaOH	Cu_2O/TiO_2/NaOH/Pt	Xenon lamp 500 W	0.0018	1.68	[272]
5.	Copper(II) oxide NC-loaded TiO_2 (Cu(II)/TiO_2)	Photocathode	0.5M $KHCO_3$	Cu(II)/TiO_2/$KHCO_3$/Pt	Xenon lamp 150 W	−0.0024	0.44	[249]
6.	Cu_2O NW array-coated TiO_2 (Cu_2O NW/TiO_2)	Photocathode	0.1 M K_2SO_4	Cu_2O NW/TiO_2/K_2SO_4/Pt	Xenon lamp 150 W	−0.23	−0.17	[266]
7.	Cu_2O/CuO/TiO_2	Photocathode	0.1 M Na_2SO_4	$BiVO_4$/NiOOH/FeOOH–Cu_2O/CuO/TiO_2/Na_2SO_4/Pt	Ozone-free Xenon lamp	−2.25	0.1	[267]

					300 W			
8.	Mn/Fe co-doped TiO_2 NT arrays (Mn/Fe-TNT@Ti)	Photocathode	0.5 M Na_2SO_4	Mn/Fe-TNT@Ti-500/Na_2SO_4/Pt	Xenon lamp 270 W	−0.331	−0.4	[250]
9.	TiO_2/Sb_2Se_3	Photocathode	0.5M H_2SO_4	TiO_2/Sb_2Se_3/H_2SO_4/Pt		−0.1	0.3	[268]
10.	Cu_{SA}-doped doped {111}-faceted TiO_2	Photocathode	0.1 M H_2SO_4	$Cu_{SA}(0.85)T_{111}$/M H_2SO_4/Pt	Xenon lamp 70 W	−2.22	−1.0	This work

TF- Thin film, NW – Nanowire, NC- nanoclusters, NT- nanotubes, SA- Single atoms

Table 4.5 presents a comprehensive comparison of our results with earlier Cu/TiO_2-based photoanodes, along with recent reports demonstrating photocathodic behavior in TiO_2-based materials **[249, 250, 266-272]**. Remarkably, the current density obtained in this work ranks among the highest for both photoanodic and photocathodic configurations. In particular, the photocathodic current density achieved using single-layer $Cu_{SA}T_{111}$ electrodes (−2.22 mA/cm²) is significantly higher than that reported for Cu(II)TiO_2 electrodes (−0.0024 mA/cm²), and Cu_2O NW array-coated TiO_2 (−0.23 mA/cm^2) **[249, 266]**. Furthermore, the performance closely approaches that of more complex Cu_2O/CuO/TiO_2 tandem architecture (−2.3 mA/cm^2) **[267]**, despite the simple design of the present system. Beyond Cu/TiO_2-based materials, the photocathodic current density also surpasses that of TiO_2/Sb_2Se_3 electrodes (−0.1 mA/cm^2) incorporating rare-earth elements, reported by Xavier et al. **[268]**, as well as Mn/Fe co-doped TiO_2 nanotubes (−0.331 mA/cm^2) reported by Madan et al.**[250]** These comparisons clearly highlight the significance of this work in advancing the development of efficient and cost-effective photocathodes for PEC water splitting.

4.3.3. DFT Results

The adsorption of H_2O molecules on the catalyst surface and the efficient transfer of charge carriers are critical factors that significantly influence catalytic performance. DFT calculations were conducted to investigate H_2O adsorption and interfacial charge transfer on $Cu_{SA}T_{101}$ and $Cu_{SA}T_{111}$ surfaces. In both systems, Cu atoms replace surface Ti atoms, generating O_v and forming Cu_{SA}–O_v–Ti_{6c} sites on T_{101} and Cu_{SA}–O_v–Ti_{3c} sites on T_{111} **[253]**. Using the Adsorption Locator module, the most stable adsorption sites for H_2O were identified: on $Cu_{SA}T_{101}$, one H atom interacts with the Cu site and the other with a Ti_{6c} atom **(Figure 4.18)**, whereas on $Cu_{SA}T_{111}$, one H atom binds to Cu and the other to Ti_{3c} **(Figures 4.19)** with corresponding energy values summarized in **Table 4.6**.

Table 4.6. Formation energy of different configurations of $Cu_{SA}(0.85)T_{101}$ and $Cu_{SA}(0.85)T_{111}$ samples.

Sr.No	Structures $Cu_{SA}(0.85)T_{101}$	Formation Energy (eV) $Cu_{SA}(0.85)T_{101}$	Structures $Cu_{SA}(0.85)T_{111}$	Formation Energy (eV) $Cu_{SA}(0.85)T_{111}$
1	Configuration_1	-11.84	Configuration_1	-12.43
2	Configuration_2	-11.82	Configuration_2	-11.62
3	Configuration_3	-11.77	Configuration_3	-11.27
4	Configuration_4	-10.99	Configuration_4	-11.17
5	Configuration_5	-10.59	Configuration_5	-11.16
6	Configuration_6	-10.56	Configuration_6	-11.12
7	Configuration_7	-10.28	Configuration_7	-10.99
8	Configuration_8	-10.24	Configuration_8	-10.59
9	Configuration_9	-10.07	Configuration_9	-10.16
10	Configuration_10	-9.88	Configuration_10	-10.04

Geometry optimization revealed stronger adsorption calculated using equation 3.3 on $Cu_{SA}T_{111}$ (ΔE_{ads} = –1.63 eV) compared to $Cu_{SA}T_{101}$ (ΔE_{ads} = –0.76 eV) **(Figure 4.20a)**. Charge density difference (CDD) analyses further indicate significant electron redistribution

at the $Cu_{SA}T_{111}/H_2O$ interface **(Figure 4.20b)**, demonstrating enhanced charge transfer from the surface to the adsorbed molecule **[183]**. This pronounced electron transfer is critical for water activation, a key step in photocatalytic and catalytic processes. Collectively, these results highlight that $Cu_{SA}T_{111}$ not only provides stronger H_2O adsorption but also promotes more efficient interfacial charge transfer, which underpins its superior catalytic activity and faster reaction kinetics in water-involved processes. DFT calculations predict more efficient charge transfer from $Cu_{SA}(0.85)T_{111}$ to adsorbed H_2O molecules compared to $Cu_{SA}(0.85)T_{101}$. These simulation results demonstrate that the $Cu_{SA}T_{111}$ surface provides favorable conditions for H_2O adsorption as well as effectively promotes its activation.

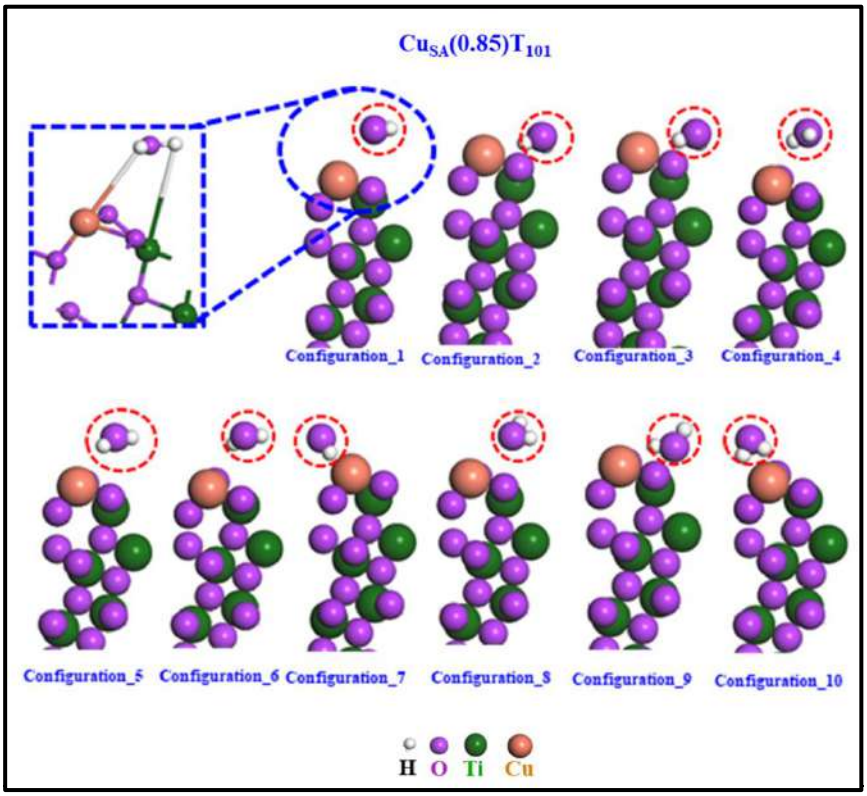

Figure 4.18. DFT analysis of H_2O adsorption and activation on $Cu_{SA}(0.85)T_{101}$. The most favorable adsorption sites are identified, with Ti, O, and Cu atoms shown in green, purple, and rust-orange, respectively. The red dotted circle highlights the adsorption configuration of H_2O**.** The inset shows the most stable configuration.

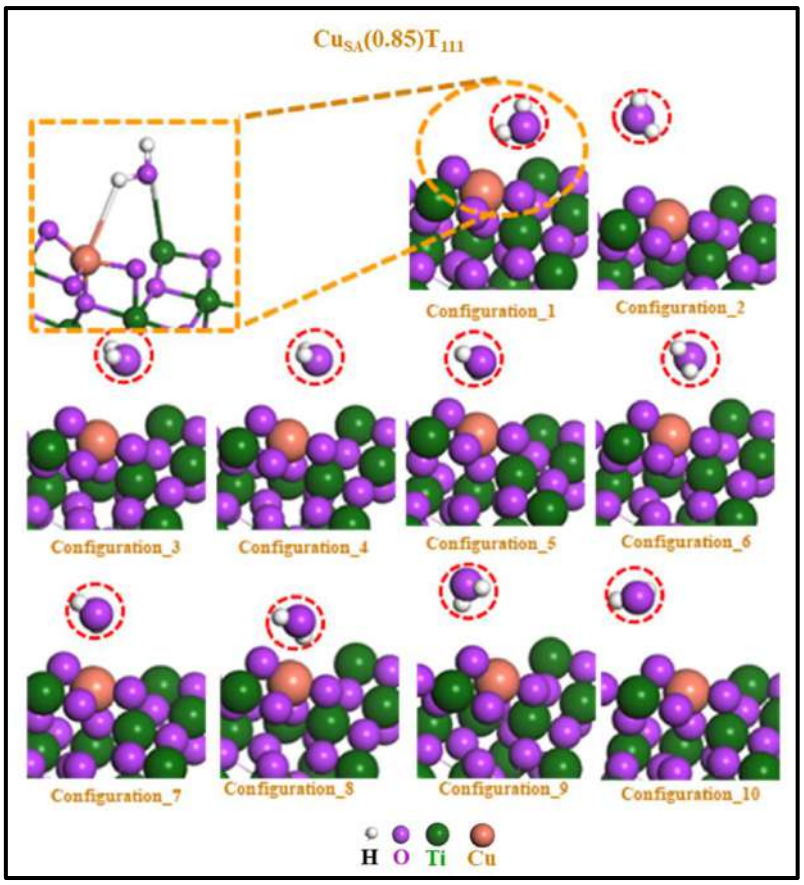

Figure 4.19. DFT analysis of H_2O adsorption and activation on $Cu_{SA}(0.85)T_{111}$, the inset shows the most stable configuration.

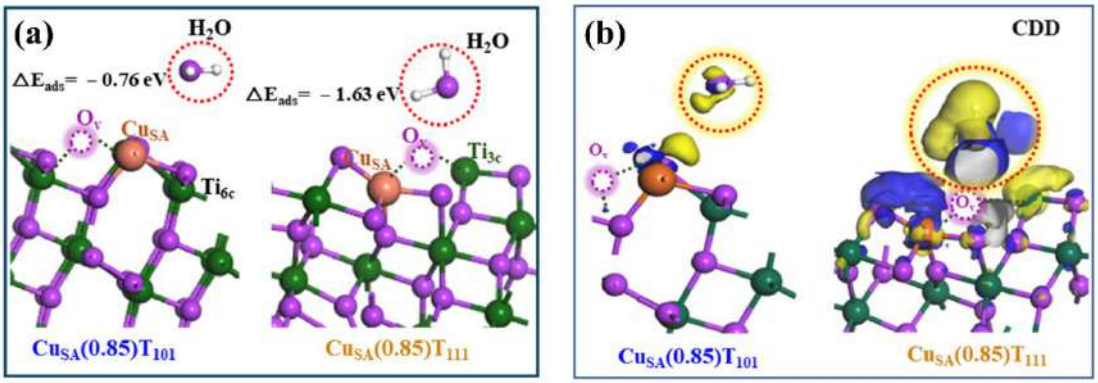

Figure 4.20. DFT Analysis of H_2O adsorption and activation. **(a)** Optimized structures of H_2O adsorbed on the active sites of $Cu_{SA}(0.85)T_{101}$ and $Cu_{SA}(0.85)T_{111}$, along with the corresponding adsorption energy values. **(b)** CDD plots, with yellow and blue regions indicating electron depletion and accumulation, respectively. Ti, O, and Cu atoms are shown in green, purple, and rust-orange.

4.3.4. EIS Results

As supported by the DFT results, $Cu_{SA}T_{111}$ demonstrates more effective charge transfer to adsorbed H_2O molecules than $Cu_{SA}T_{101}$. To experimentally validate this prediction, EIS measurements were conducted to investigate the charge transfer behavior.

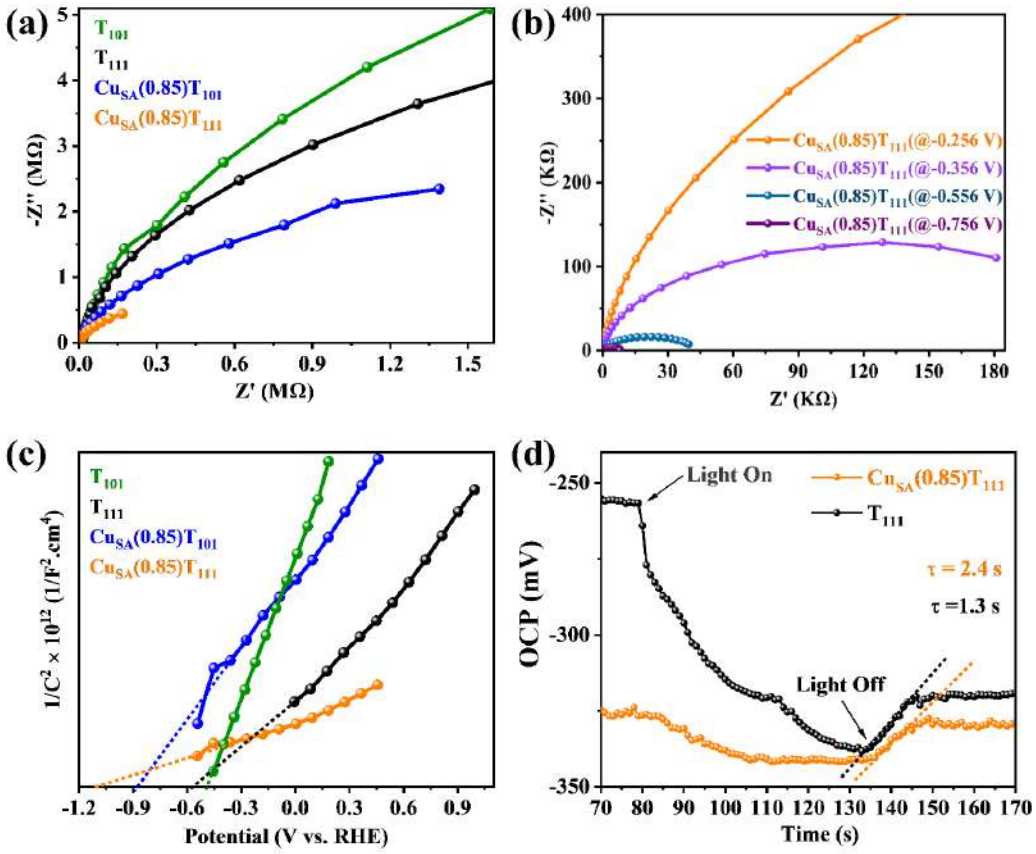

Figure 4.21. (a) EIS Nyquist plots of T_{101}, T_{111} and $Cu_{SA}(0.85)T_{101}$ and $Cu_{SA}(0.85)T_{111}$ measured at an applied potential of –0.256 V. **(b)** Nyquist plots of $Cu_{SA}(0.85)T_{111}$ photoelectrodes measured at different applied bias potentials. **(c)** Mott-Schottky plots of T_{101}, T_{111} and $Cu_{SA}(0.85)T_{101}$ and $Cu_{SA}(0.85)T_{111}$ recorded at 1 kHz. **(d)** OCVD curves of T_{111} and $Cu_{SA}(0.85)T_{111}$ electrodes.

The Nyquist plots shown in **Figure 4.21a** compare the electrochemical responses of T_{101}, T_{111}, $Cu_{SA}(0.85)T_{111}$, and $Cu_{SA}(0.85)T_{101}$ photoelectrodes, measured using a standard three-electrode configuration at an applied potential of –0.256 V. Notably, the semicircle observed for $Cu_{SA}(0.85)T_{111}$ displays a significantly smaller diameter than that of $Cu_{SA}(0.85)T_{101}$. This reduction in semicircle size corresponds to a lower charge transfer resistance (R_{ct}) at the

semiconductor–electrolyte interface, indicating that $Cu_{SA}(0.85)T_{111}$ enables more efficient interfacial electron transfer **[97,172]**. This enhanced charge transfer efficiency directly contributes to the superior PEC performance observed in $Cu_{SA}(0.85)T_{111}$. Furthermore, the Nyquist plots of $Cu_{SA}(0.85)T_{111}$ performed under different negative bias show a progressive decrease in the semicircle diameter with increasingly negative applied bias **(Figure 4.21b)**, reflecting a corresponding reduction in the R_{ct}. This decline in R_{ct} signifies that interfacial electron transport becomes more efficient as the potential becomes more cathodic. Mott–Schottky (M–S) analysis was performed to evaluate the flat band potential (E_{fb}) and donor density (N_d) of T_{101}, T_{111}, $Cu_{SA}(0.85)T_{101}$ and $Cu_{SA}(0.85)T_{111}$. As shown in **Figure 4.21c**, the M–S plots ($1/C^2$ vs. applied potential, with C representing the capacitance associated with the space charge region) exhibit positive slopes, confirming the n-type semiconducting behavior of both electrodes. Measurements at a frequency of 1 kHz revealed flat band potentials of –0.48 V for T_{101}, –0.57 V for T_{111}, –0.88 V for $Cu_{SA}(0.85)T_{101}$ and –1.06 V for $Cu_{SA}(0.85)T_{111}$. The more negative E_{fb} of $Cu_{SA}(0.85)T_{111}$ indicates improved charge carrier separation, likely due to stronger band bending at the semiconductor/electrolyte interface. This enhanced internal electric field promotes more effective separation of photogenerated electron–hole pairs, contributing to the superior photocurrent observed in $Cu_{SA}(0.85)T_{111}$ photoelectrode **[225]**. Further insights into the electronic properties were gained by calculating the N_d using equation 3.1 **[223]**:

Notably, the N_d in $Cu_{SA}(0.85)T_{111}$ was determined to be 4.56×10^{19} cm^{-3}, approximately four-times higher than that of $Cu_{SA}(0.85)T_{101}$ (9.9×10^{18} cm^{-3}) and about five-times higher than that of T_{111} (8.85×10^{18} cm^{-3}). This higher donor density is attributed to the increased concentration of O_v in $Cu_{SA}(0.85)T_{111}$, as confirmed by XPS analysis. These O_v act as electron donors, thereby enhancing free carrier density and improving charge transport within the semiconductor. Overall, the M–S analysis highlights the superior electronic properties of

the $Cu_{SA}(0.85)T_{111}$ surface, which contribute directly to its improved photoelectrochemical performance through enhanced charge separation and greater carrier availability. Notably, tailing in the M–S plots indicate the presence of surface states that partially pin the surface Fermi level **[273]**. These surface states can significantly influence band bending and alter the charge transfer dynamics at the semiconductor–electrolyte interface **[273]**. The depletion-layer width (W_{sc}), calculated from M–S data, using the equation 4.3 **[251]**:

$$W_{sc} = \sqrt{\frac{2\epsilon\epsilon_0}{eN_d}\left(E - E_{fb} - \frac{k_B T}{e}\right)} \qquad (4.3)$$

Importantly, the W_{sc} is markedly reduced for $Cu_{SA}(0.85)T_{111}$ (~8 nm) compared to pristine T_{111} (~83 nm), indicating effective electrostatic screening at the interface. This pronounced reduction in depletion width indicates enhanced electrostatic screening at the interface. Such screening facilitates more efficient charge separation and accelerates interfacial charge transfer processes, ultimately improving the overall charge transport across the semiconductor–electrolyte junction **[250,251]**.

4.3.5. Open-Circuit Voltage Decay (OCVD) Measurements Results

To investigate the contribution of O_V-induced surface trap states to the photocathodic behavior of $Cu_{SA}(0.85)T_{111}$, open-circuit voltage decay (OCVD) measurements were performed. As shown in **Figure 4.21d**, the OCVD curves of T_{111} and $Cu_{SA}(0.85)T_{111}$ exhibit negative photovoltage under illumination, confirming their n-type semiconductor behavior, which is consistent with the EIS results. Notably, $Cu_{SA}(0.85)T_{111}$ exhibited a reduced photovoltage variation between illuminated and dark conditions compared to pristine T_{111}. This behavior can be attributed to Cu_{SA}-induced surface trap states located below the conduction band, which modulate band bending and consequently weaken the built-in electric field **[251]**. Upon switching off the light source, the open-circuit voltage decreases, and a

similar trend is observed for T_{101} and $Cu_{SA}(0.85)T_{101}$. Importantly, $Cu_{SA}(0.85)T_{111}$ exhibits a significantly slower photovoltage decay than T_{111}, indicating improved charge carrier dynamics **[251,274]**. The average lifetime (τ) of the majority charge carriers can be derived from the OCV decay curves using the relation 4.4 [274]:

$$\tau = -\frac{k_B T}{q}\left(\frac{dV}{dt}\right)^{-1} \quad (4.4)$$

Where k_B the Boltzmann is constant, T is the temperature, t is the time, and q is elementary charge.

The calculated electron lifetimes for T_{111} and $Cu_{SA}(0.85)T_{111}$ are 1.3 s and 2.4 s, respectively. This enhancement is attributed to efficient electron trapping at Cu_{SA} sites in conjunction with O_v, which prolongs carrier lifetime and promotes effective charge separation.

4.3.6. Proposed Reaction Mechanism

Although M–S and OCVD analyses confirm that the materials retain n-type semiconducting behavior, where upward band bending typically causes surface electron depletion and results in photoanodic activity, the Cu_{SA} doped TiO_2 photoelectrodes ($Cu_{SA}T_{101}$ and $Cu_{SA}T_{111}$) exhibit a pronounced photocathodic response. This unusual behavior can be attributed to the combined effects of defect-induced modifications to the band structure, partial surface Fermi-level pinning, and an efficient IFCT in Cu_{SA}-doped TiO_2 photoelectrodes. Structural and spectroscopic analyses provide clear insight into the origin of this phenomenon. XPS and EXAFS measurements confirm the presence of Cu^{2+} single atoms and O_v in Cu_{SA} doped TiO_2 photoelectrodes. Taking $Cu_{SA}(0.85)T_{111}$ as a representative, this material exhibits the highest O_v concentration. These O_v introduce shallow donor states near the conduction-band edge, leading to the band-gap narrowing, as also evidenced by UV–Vis absorption spectra, where the band gap decreases from 3.11 eV for T_{111} to 2.68 eV for $Cu_{SA}(0.85)T_{111}$. Furthermore,

M–S analysis reveals a significantly higher donor density in $Cu_{SA}(0.85)T_{111}$. The increased electron concentration enhances electrostatic screening at the semiconductor–electrolyte interface, thereby reducing the extent of band bending **[250,251]**. Consequently, the effective space-charge barrier is substantially diminished, resulting in a much narrower depletion width in $Cu_{SA}(0.85)T_{111}$ (~8 nm) compared to pristine T_{111} (~83 nm). In addition, the noticeable tailing behavior observed in the M–S plots indicates the presence of surface states that partially pin the surface Fermi level, further wreaking the band bending in $Cu_{SA}(0.85)T_{111}$. **Figure 4.22a** illustrates the band alignment of TiO_2 and $Cu_{SA}(0.85)T_{111}$ derived from XPS, EIS, and UV–Vis results. The $Cu_{SA}(0.85)T_{111}$ exhibits a smaller optical band gap, shallow electronic states near the conduction band, a reduced effective space-charge barrier, and a more negative conduction-band edge accompanied by partial Fermi-level pinning **[273]**. During the LSV measurements, the potential was scanned from −1.0 V to +1.5 V vs RHE. Under dark conditions **(Figure 4.22b)**, in $Cu_{SA}(0.85)T_{111}$, it begins to exhibit a cathodic current when the potential reaches the negative region, i.e., −0.22 V vs RHE, and increases progressively as the scan proceeds toward more negative potentials. This behavior can be attributed to a relatively narrow depletion width (~8 nm) and a high donor density arising from O_v in $Cu_{SA}(0.85)T_{111}$. At sufficiently negative potentials, electrons in the semiconductor gain enough energy to overcome the interfacial charge-transfer barrier, enabling cathodic current generation. This response primarily reflects the electrocatalytic activity of Cu-doped TiO_2 electrodes, similar to the previous reports **[275]**. In contrast, pristine TiO_2 (T_{111}) remains essentially electrochemically inactive over the same potential range.

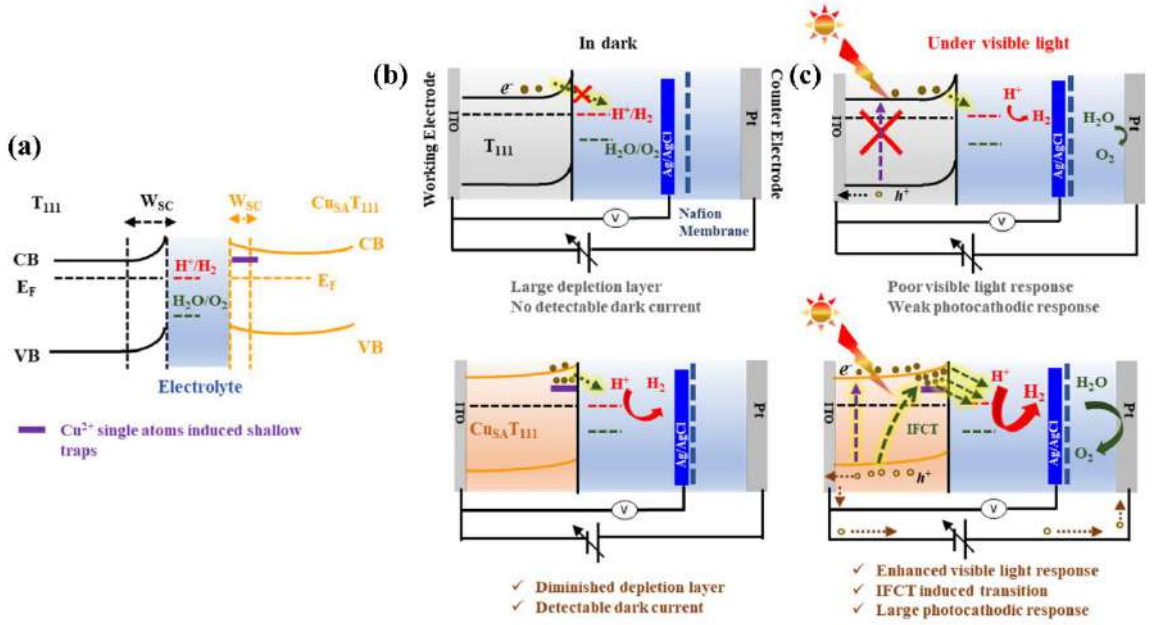

Figure 4.22. (a) Schamtic diagram showing the band structures of T_{111} and $Cu_{SA}(0.85)T_{111}$. **(b)** Illustration of the charge transport processes under dark conditions. **(c)** Representation of the charge transport mechanism in both materials under visible light, emphasizing IFCT-driven generation and separation of charge carriers.

This inactivity is attributed to its much wider depletion region (~83 nm) and lower electron density, which creates a larger space-charge barrier and limits electron transport towards the semiconductor–electrolyte interface, thereby suppressing cathodic charge-transfer processes under dark conditions as schematically illustrated in **(Figure 4.22b)**.

Upon visible-light irradiation **(Figure 4.22c)**, $Cu_{SA}(0.85)T_{111}$ efficiently generates electron (e^-)–hole (h^+) pairs due to its reduced optical band gap (~2.7 eV) compared with pristine TiO_2, enabling enhanced visible-light absorption and a higher population of photogenerated charge carriers. In addition to improved light harvesting, IFCT from the TiO_2 lattice to atomically dispersed Cu centers plays a key role in modulating charge-carrier dynamics. UV–Vis absorption spectra provide evidence for this IFCT process, where photoexcitation induces electron transfer from the TiO_2 matrix to Cu single-atom sites. DFT results signify that e H_2O molecules are adsorbed on $Cu_{SA}T_{111}$ surface through interaction with Cu_{SA}-O_v-Ti_{3c} surface

sites. These Cu_{SA}–O_v–Ti_{3c} centers act as electron-accepting sites, facilitating efficient electron trapping and promoting electron accumulation near the semiconductor surface while suppressing bulk recombination. As a result, photogenerated electrons (e^-) preferentially migrate to these surface sites at the semiconductor–electrolyte interface, where they react with adsorbed H_2O molecules to drive the HER at the working electrode. The Charge density difference results from DFT results have already established the facile activation of H_2O molecules on Cu_{SA}–O_v–Ti_{3c} centers **(Figure 4.20b)**. Meanwhile, the photogenerated holes (h^+) remain in the TiO_2 valence band and are transferred to the Pt counter electrode, where water oxidation occurs, producing oxygen (O_2) gas. Similar mechanisms have been reported in the earlier studies **[249, 276-278]**. Notably, the photocurrent begins to emerge only when the potential enters the negative region (~−0.22 V vs RHE) and increases progressively as the scan proceeds toward more negative potentials, reaching approximately −2.22 mA cm^{-2} at −1.0 V vs RHE. This behavior indicates that electron accumulation at the Cu single-atom sites becomes sufficient in the cathodic potential region to overcome the interfacial charge-transfer barrier, thereby enabling proton reduction and hydrogen evolution. The increasing applied negative bias promotes charge separation and suppresses recombination. This mechanism is corroborated by Nyquist plots showing a systematic decrease in charge-transfer resistance with increasingly negative bias **(Figure 4.21b)**. Notably, the role of Cu^{2+}-induced IFCT in Cu/TiO_2 systems has been suggested in several studies on Cu-TiO_2 photocatalysts, particularly in the context of environmental remediation applications **[279]**. Overall, the enhanced photocathodic performance of the Cu_{SA}-doped TiO_2 photoelectrodes originates from the synergistic interplay of reduced band bending, partial surface Fermi-level pinning, and efficient IFCT. Compared with $Cu_{SA}T_{101}$, the superior PEC performance of $Cu_{SA}T_{111}$ can be attributed to its stronger H_2O adsorption and activation capability, as indicated by DFT calculations. In addition, the relatively higher surface area of $Cu_{SA}T_{111}$ (125.7 m^2 g^{-1})

compared with $Cu_{SA}T_{101}$ (99.2 m^2 g^{-1}) may further contribute to the improved HER activity.

4.4. Conclusions

In this chapter, I have demonstrated that Cu_{SA}–doped {111}-faceted TiO_2 thin-films electrodes exhibit an unusual yet highly efficient photocathodic response despite their *n*-type character. The optimized electrode, fabricated via scalable spray pyrolysis, delivers a photocurrent density of −2.22 mA cm^{-2} at −1.0 V vs RHE under AM 1.5G illumination, 2.92 times higher than its {101}-faceted analogue, along with a low onset potential (−0.22 V), small overpotential (−0.28 V), and high IPCE (27.1% at 420 nm). The enhanced photocathodic response of $Cu_{SA}(0.85)T_{111}$ arises from Cu^{2+} single atoms and abundant O_v, which create shallow donor states, narrow the band gap, and improve visible-light absorption. Increased donor density reduces band bending and depletion width, while defect-induced surface states partially pin the Fermi level, together promoting efficient charge separation and interfacial charge transfer. These results substantially outperform previously reported Cu/TiO_2-based photocathodes, highlighting the promise of $Cu_{SA}T_{111}$ for low-cost, solar-driven H_2 production.

Chapter: 5
Conclusion and Future Scope

This chapter summarizes the results and outlines the future scope of the work.

Solar water splitting for hydrogen (H_2) production is a clean and sustainable energy However, the performance of most of the photocatalysts developed so far is still poor due to unsuitable band structures, fast recombination of photogenerated charge carriers and slow surface reactions.

Single-atom catalysts (SACs) where isolated metal atoms are anchored on the semiconductor supports have shown excellent atomic utilisation efficiency and outstanding catalytic activity. To stabilise these single atoms, specific anchoring sites such as unsaturated surface atoms, surface defects or heteroatoms are needed, providing strong metal-support interactions. Defect-rich metal oxides including TiO_2, In_2O_3, $W_{18}O_{49}$, and Fe_2O_3 have emerged as suitable supports in which oxygen or metal vacancies act as trap centers for the doping of single atoms.

More specifically, asymmetric atomic sites (AAS) of the $M_{SA}–O_v–M_2$ form are found to be particularly active catalytic configurations. However, despite these advances, the practical use of asymmetric atomic site catalysts (AASCs) for H_2 production is still limited. Existing approaches rely on metal oxides with high defect concentration, which require H_2 or H_2/Ar gas during preparation, making them incompatible with H_2 production systems. This limitation can be overcome by selecting an alternative support with intrinsic well-defined defect sites.

The high-index faceted nanostructures intrinsically contain undercoordinated surface atoms, which are inherently defective without treatment. The interesting intrinsic asymmetric atomic site is $Ti_{5c}–O–Ti_{3c}$ on the (111) facet of anatase TiO_2. Building on this, a novel highly asymmetric atomic-site catalyst (HAASC) was designed by anchoring Cu single atoms (Cu_{SA}) on high-index (111) faceted TiO_2, exploiting its unique surface chemistry for improved solar water splitting for H_2 production. In HAASC, replace Ti_{5c} adjacent to Ti_{3c} sites, creating oxygen vacancies (O_v) and forming $Cu_{SA}–O_v–Ti_{3c}$ HAAS.

These HAASC serve as highly active sites, enhancing adsorption and activation of H_2O molecules compared to conventional Ti_{5c}–O–Ti_{3c} sites in photocatalytic water splitting for H_2 production. In addition, it improves light harvesting, charge transfer dynamics, and redox capability of photoexcited electrons. The HAASC achieves H_2 production rates are **8.3 mmol h^{-1} g^{-1}** in pure water and **784.5 mmol h^{-1} g^{-1}** in water/methanol (10:1 v/v).

To explore this more, HAASC developed some limitations in photocatalytic H_2 production, like H_2 & O_2 gas mixing, which makes the thin-film electrodes of Cu_{SA}-doped (111)-faceted TiO_2 for photoelectrochemical (PEC) water splitting. Cu_{SA}-doped (111)-faceted TiO_2 thin-film electrodes show an unusual but efficient photocathodic response despite their n-type semiconductor. The optimized elelctrode of $Cu_{SA}(0.85)T_{111}$ shows, (i) high photocurrent of **−2.22 mA cm^{-2} at −1.0** V vs RHE under AM 1.5G light, (ii) Low onset potential (−0.22 V), (iii) Low overpotential (−0.28 V) , and (iv) High IPCE (27.1% at 420 nm)

The enhanced photocathodic response of $Cu_{SA}(0.85)T_{111}$ arises from Cu^{2+} single atoms and a high concentration of O_v, which create shallow donor states, narrow the band gap, and improve visible-light absorption. Increased donor density reduces band bending and depletion width, while defect-induced surface states partially pin the Fermi level, together promoting efficient charge separation through direct IFCT to the surface for proton reduction into hydrogen.

Future Scope

- Future research will focus on dual-atom doping in the developed material to enhance solar water splitting efficiency. recently, Dual-atom catalysts (DACs) have attracted great interest for solar energy applications. DACs contain two linked metal active sites that coupled together to lower the energy required for reactions and improve selectivity of the desired products. This unique two active site allows multiple

reaction intermediates to be activated simultaneously. In addition, DACs have shown great potential for solar driven application **[280]**.

- The developed catalyst can be used for photocatalyst CO_2 reduction due to their excellent visible light harvesting capabilities, reduced charge recombination, fast kinetics, high number of atomic sites and easy synthesis method.
- Cu-doped faceted TiO_2 semiconductor can be used in other applications, like from light sensors and photodiodes to gas detectors and memory chips; Cu-doped TiO_2 is steadily moving from the laboratory into real electronic products **[281, 282]**. Its ability to be tuned optically and electrically by simply adjusting the Cu doping level makes it a flexible and cost-effective material for the next generation of smart electronic devices.

Reference:

[1] L. Pang, L. Liu, X. Zhou, M. Hafeez, S. Ullah, and M. T. Sohail, "How Does Natural Resource Depletion Affect Energy Security Risk? New Insights from Major Energy Consuming Countries," *Energy Strategy Reviews* 54 (2024): 101460, https://doi.org/10.1016/j.esr.2024.101460.

[2] I. Roger, M. A. Shipman, and M. D. Symes, "Earth-Abundant Catalysts for Electrochemical and Photoelectrochemical Water Splitting," Nature Reviews Chemistry 1 (2017): 0003, https://doi.org/10.1038/s41570-016-0003.

[3] https://www.energyinst.org/statistical-review

[4] M. K. Ekoue, M. Woerman, and C. Clastres, "Intermittency and Uncertainty in Wind and Solar Energy: Impacts on the French Electricity Market," *Energy Economics* 142 (2025): 108176, https://doi.org/10.1016/j.eneco.2024.108176.

[5] C. S. Kaunda, C. Z. Kimambo, and T. K. Nielsen, "Hydropower in the Context of Sustainable Energy Supply: A Review of Technologies and Challenges," *International Scholarly Research Notices* 2012 (2012): 730631, https://doi.org/10.5402/2012/730631.

[6] J. J. Wimhurst, C. C. Nsude, and J. S. Greene, "Standardizing the Factors Used in Wind Farm Site Suitability Models: A Review," *Heliyon* 9 (2023): e15903, https://doi.org/10.1016/j.heliyon.2023.e15903.

[7] H. H. Pourasl, R. Vatankhah Barenji, and V. M. Khojastehnezhad, "Solar Energy Status in the World: A Comprehensive Review," *Energy Reports* 10 (2023): 3474–3493, https://doi.org/10.1016/j.egyr.2023.10.022.

[8] T. M. Razykova, C. S. Ferekides, D. Morel, E. Stefanakos, H. S. Ullal, and H. M. Upadhyaya, "Solar Photovoltaic Electricity: Current Status and Future Prospects," *Solar Energy* 85 (2011): 1580–1608, https://doi.org/10.1016/j.solener.2010.12.002.

[9] O. Khaselev and J. A. Turner, "A Monolithic Photovoltaic-Photoelectrochemical Device for Hydrogen Production via Water Splitting," *Science* 280 (1998): 425–427, https://doi.org/10.1126/science.280.5362.425.

[10] M. Grätzel, "Mesoscopic Solar Cells for Electricity and Hydrogen Production from Sunlight," *Chemistry Letters* 34 (2005): 8–13, https://doi.org/10.1246/cl.2005.8.

[11] A. A. Bayod-Rújula, "Solar Photovoltaics (PV)," in *Solar Hydrogen Production* (2019): 237–295, https://doi.org/10.1016/b978-0-12-814853-2.00008-4.

[12] A. Polman, M. Knight, E. C. Garnett, B. Ehrler, and W. C. Sinke, "Photovoltaic Materials: Present Efficiencies and Future Challenges," *Science* 352 (2016): aad4424, https://doi.org/10.1126/science.aad4424.

[13] C. Yang, W. Hu, J. Liu, C. Han, Q. Gao, A. Mei, Y. Zhou, F. Guo, and H. Han, "Achievements, Challenges, and Future Prospects for Industrialization of Perovskite Solar Cells," *Light: Science & Applications* 13 (2024): 227, https://doi.org/10.1038/s41377-024-01461-x.

[14] B. T. Son, N. V. Long, and N. T. N. Hang, "Fly Ash-, Foundry Sand-, Clay-, and Pumice-Based Metal Oxide Nanocomposites as Green Photocatalysts," *RSC Advances* 11 (2021): 30805–30826, https://doi.org/10.1039/D1RA05647F.

[15] P. V. Kamat, "Unsung Heroes of Energy Research," *ACS Energy Letters* 3 (2018): 1394–1395, https://doi.org/10.1021/acsenergylett.8b00792.

[16] H. Song, S. Luo, H. Huang, B. Deng, and J. Ye, "Solar-Driven Hydrogen Production: Recent Advances, Challenges, and Future Perspectives," *ACS Energy Letters* 7 (2022): 1043–1065, https://doi.org/10.1021/acsenergylett.1c02591.

[17] M. S. Dresselhaus and I. L. Thomas, "Alternative Energy Technologies," *Nature* 414 (2001): 332–337, https://doi.org/10.1038/35104599.

[18] J. A. Turner, "Sustainable Hydrogen Production," *Science* 305 (2004): 972–974, https://doi.org/10.1126/science.1103197.

[19] https://h2fcp.org/stationmap.

[20] S. Chen, T. Takata, and K. Domen, "Particulate Photocatalysts for Overall Water Splitting," *Nature Reviews Materials* 2 (2017): 17050, https://doi.org/10.1038/natrevmats.2017.50.

[21] S. Shen, J. Shi, P. Guo, and L. Guo, "Visible-Light-Driven Photocatalytic Water Splitting on Nanostructured Semiconducting Materials," *International Journal of Nanotechnology* 8 (2011): 523–591,https://doi.org/10.1504/IJNT.2011.040192.

[22] T. Bak, J. Nowotny, M. Rekas, and C. Sorrell, "Photo-Electrochemical Hydrogen Generation from Water Using Solar Energy: Materials-Related Aspects," *International Journal of Hydrogen Energy* 27 (2002): 991–1022, https://doi.org/10.1016/S0360-3199(02)00022-8.

[23] A. Fujishima and K. Honda, "Electrochemical Photolysis of Water at a Semiconductor Electrode," *Nature* 238 (1972): 37–38, https://doi.org/10.1038/238037a0.

[24] C. V. Niveditha, A. C. Nizamudeen, R. Ramanarayanan, M. J. Jabeen Fatima, and S. Swaminathan, "Showcasing Electrode–Electrolyte Interfacial Potential as a Vital Parameter in the Hydrogen Generation by Metal Oxide Electrodes," *Materials Research Express* 5 (2018): 035504, https://doi.org/10.1088/2053-1591/aab076.

[25] K. Maeda, "Photocatalytic Water Splitting Using Semiconductor Particles: History and

Recent Developments," *Journal of Photochemistry and Photobiology C: Photochemistry Reviews* 12 (2011): 237–268, https://doi.org/10.1016/j.jphotochemrev.2011.07.001.

[26] L. Gnanasekaran, S. Rajendran, H. Karimi-Maleh, A. K. Priya, J. Qin, M. Soto-Moscoso, S. Ansar, and C. Bathula, "Surface Modification of TiO_2 by Adding V_2O_5 Nanocatalytic System for Hydrogen Generation," *Chemical Engineering Research and Design* 182 (2022): 114–119, https://doi.org/10.1016/j.cherd.2022.03.046.

[27] N. Zhang, H. Li, K. Yu, and Z. Zhu, "Differently Structured MoS_2 for the Hydrogen Production Application and a Mechanism Investigation," *Journal of Alloys and Compounds* 685 (2016): 65–69, https://doi.org/10.1016/j.jallcom.2016.05.228.

[28] F. Qureshi and M. Tahir, "Photoelectrochemical Water Splitting with Engineering Aspects for Hydrogen Production: Recent Advances, Strategies and Challenges," *International Journal of Hydrogen Energy* 69 (2024): 760–776, https://doi.org/10.1016/j.ijhydene.2024.05.039.

[29] C. Acar, I. Dincer, and G. F. Naterer, "Review of Photocatalytic Water-Splitting Methods for Sustainable Hydrogen Production," *International Journal of Energy Research* 40 (2016): 1449–1473, https://doi.org/10.1002/er.3549.

[30] M. G. Walter, E. L. Warren, J. R. McKone, S. W. Boettcher, Q. Mi, E. A. Santori, and N. S. Lewis, "Solar Water Splitting Cells," *Chemical Reviews* 110 (2010): 6446–6473, https://doi.org/10.1021/cr1002326.

[31] L. M. Peter, "Energetics and Kinetics of Light-Driven Oxygen Evolution at Semiconductor Electrodes: The Example of Hematite," *Journal of Solid State Electrochemistry* 17 (2013): 315–326, https://doi.org/10.1007/s10008-012-1957-3.

[32] K. Sivula and R. van de Krol, "Semiconducting Materials for Photoelectrochemical Energy Conversion," *Nature Reviews Materials* 1 (2016): 15010, https://doi.org/10.1038/natrevmats.2015.10.

[33] T. Hisatomi, J. Kubota, and K. Domen, "Recent Advances in Semiconductors for Photocatalytic and Photoelectrochemical Water Splitting," *Chemical Society Reviews* 43 (2014): 7520–7535, https://doi.org/10.1039/C3CS60378D.

[34] H. G. Yang, C. H. Sun, S. Z. Qiao, J. Zou, G. Liu, S. C. Smith, H. M. Cheng, and G. Q. Lu, "Anatase TiO_2 Single Crystals with a Large Percentage of Reactive Facets," *Nature* 453 (2008): 638–641, https://doi.org/10.1038/nature06964.

[35] B. Qiao, A. Wang, X. Yang, L. F. Allard, Z. Jiang, Y. Cui, J. Liu, J. Li, and T. Zhang, "Single-Atom Catalysis of CO Oxidation Using Pt_1/FeO_x," *Nature Chemistry* 3 (2011): 634–641, https://doi.org/10.1038/nchem.1095.

[36] J. Low, J. Yu, M. Jaroniec, S. Wageh, and A. A. Al-Ghamdi, "Heterojunction Photocatalysts," *Advanced Materials* 29 (2017): 1601694, https://doi.org/10.1002/adma.201601694.

[37] F. Jiao and H. Frei, "Nanostructured Cobalt Oxide Clusters in Mesoporous Silica as Efficient Oxygen-Evolving Catalysts," *Angewandte Chemie International Edition* 48 (2009): 1841–1844, https://doi.org/10.1002/anie.200805534.

[38] J. A. Turner, "A Realizable Renewable Energy Future," *Science* 285 (1999): 687–689, https://doi.org/10.1126/science.285.5428.687.

[39] X. Chen, S. Shen, L. Guo, and S. S. Mao, "Semiconductor-Based Photocatalytic Hydrogen Generation," *Chemical Reviews* 110 (2010): 6503–6570, https://doi.org/10.1021/cr1001645.

[40] K. Maeda and K. Domen, "Solid Solution of GaN and ZnO as a Stable Photocatalyst for Overall Water Splitting under Visible Light," *Chemistry of Materials* 22 (2010): 612–623, https://doi.org/10.1021/cm901917a.

[41] Q. Wang and K. Domen, "Particulate Photocatalysts for Light-Driven Water Splitting: Mechanisms, Challenges, and Design Strategies," *Chemical Reviews* 120 (2020): 919–985, https://doi.org/10.1021/acs.chemrev.9b00201.

[42] A. Kudo and Y. Miseki, "Heterogeneous Photocatalyst Materials for Water Splitting," *Chemical Society Reviews* 38 (2009): 253–278, https://doi.org/10.1039/B800489G.

[43] X. Chen and S. S. Mao, "Titanium Dioxide Nanomaterials: Synthesis, Properties, Modifications, and Applications," *Chemical Reviews* 107 (2007): 2891–2959, https://doi.org/10.1021/cr0500535.

[44] W. Maziarz, A. Kusior, and A. Trenczek-Zajac, "Nanostructured TiO_2-Based Gas Sensors with Enhanced Sensitivity to Reducing Gases," *Beilstein Journal of Nanotechnology* 7 (2016): 1718–1726, https://doi.org/10.3762/bjnano.7.164.

[45] A. Kay, I. Cesar, and M. Grätzel, "New Benchmark for Water Photooxidation by Nanostructured α-Fe_2O_3 Films," *Journal of the American Chemical Society* 128 (2006): 15714–15721, https://doi.org/10.1021/ja064380l.

[46] Y. Park, K. J. McDonald, and K.-S. Choi, "Progress in Bismuth Vanadate Photoanodes for Use in Solar Water Oxidation," *Chemical Society Reviews* 42 (2013): 2321–2337, https://doi.org/10.1039/C2CS35260E.

[47] T. W. Kim and K.-S. Choi, "Nanoporous $BiVO_4$ Photoanodes with Dual-Layer Oxygen Evolution Catalysts for Solar Water Splitting," *Science* 343 (2014): 990–994, https://doi.org/10.1126/science.1246913.

[48] L. Wang, H. Hu, J. Xu, S. Zhu, A. Ding, and C. Deng, "WO_3 Nanocubes: Hydrothermal Synthesis, Growth Mechanism, and Photocatalytic Performance," *Journal of Materials Research* 34 (2019): 2955–2963, https://doi.org/DOI:%2010.1557/jmr.2019.189.

[49] R. Asahi, T. Morikawa, T. Ohwaki, K. Aoki, and Y. Taga, "Visible-Light Photocatalysis in Nitrogen-Doped Titanium Oxides," *Science* 293 (2001): 269–271, https://doi.org/10.1126/science.1061051.

[50] X. Li, J. Yu, J. Low, Y. Fang, J. Xiao, and X. Chen, "Engineering Heterogeneous Semiconductors for Solar Water Splitting," *Journal of Materials Chemistry A* 3 (2015): 2485–2534, https://doi.org/10.1039/C4TA04461D.

[51] J. Yu and J. Ran, "Facile Preparation and Enhanced Photocatalytic H_2-Production Activity of $Cu(OH)_2$ Cluster Modified TiO_2," *Energy & Environmental Science* 4 (2011): 1364–1371, https://doi.org/10.1039/C0EE00729C.

[52] Q. Zhu, Q. Xu, M. Du, X. Zeng, G. Zhong, B. Qiu, and J. Zhang, "Recent Progress of Metal Sulfide Photocatalysts for Solar Energy Conversion," *Advanced Materials* 34 (2022): 2202929, https://doi.org/10.1002/adma.202202929.

[53] M. Zubair, I.-H. Svenum, M. Ronning, and J. Yang, "Facile Synthesis Approach for Core-Shell TiO_2-CdS Nanoparticles for Enhanced Photocatalytic H_2 Generation from Water," *Catalysis Today* 328 (2019): 15–20, https://doi.org/10.1016/j.cattod.2018.10.070.

[54] I. Tsuji, H. Kato, and A. Kudo, "Visible-Light-Induced H_2 Evolution from an Aqueous Solution Containing Sulfide and Sulfite over a ZnS–$CuInS_2$–$AgInS_2$ Solid-Solution Photocatalyst," *Angewandte Chemie International Edition* 44 (2005): 3565–3568, https://doi.org/10.1002/anie.200500314.

[55] Y. Yan, Z. Chen, X. Cheng, and W. Shi, "Research Progress of $ZnIn_2S_4$-Based Catalysts for Photocatalytic Overall Water Splitting," *Catalysts* 13 (2023): 967, https://doi.org/10.3390/catal13060967.

[56] D. Abeysinghe and S. E. Skrabalak, "Toward Shape-Controlled Metal Oxynitride and Nitride Particles for Solar Energy Applications," *ACS Energy Letters* 3 (2018): 1331–1344, https://doi.org/10.1021/acsenergylett.8b00518.

[57] X. Wang, K. Maeda, A. Thomas, K. Takanabe, G. Xin, J. M. Carlsson, K. Domen, and M. Antonietti, "A Metal-Free Polymeric Photocatalyst for Hydrogen Production from Water under Visible Light," *Nature Materials* 8 (2009): 76–80, https://doi.org/10.1038/nmat2317.

[58] Y. Lei, F. Yang, Y. Si, C. Guo, J. Liu, M. Li, and Z. Xiong et al., "Boosting Oxygen Reduction Catalysis with Tailorable Active-N-Dominated Doped Defective CNTs," *Applied Surface Science* 499 (2020): 143844, https://doi.org/10.1016/j.apsusc.2019.143844.

[59] Z. Zhang, L. Zhang, M. N. Hedhili, H. Zhang, and P. Wang, "Plasmonic Gold Nanocrystals Coupled with Photonic Crystal Seamlessly on TiO_2 Nanotube Photoelectrodes for Efficient Visible Light Photoelectrochemical Water Splitting," *Nano Letters* 13 (2013): 14–20, https://doi.org/10.1021/nl3029202.

[60] X. Pan, M.-Q. Yang, X. Fu, N. Zhang, and Y.-J. Xu, "Defective TiO_2 with Oxygen Vacancies: Synthesis, Properties and Photocatalytic Applications," *Nanoscale* 5 (2013): 3601–3614, https://doi.org/10.1039/C3NR00476G.

[61] G. Wang, Y. Ling, and Y. Li, "Oxygen-deficient metal oxide nanostructures for photoelectrochemical water oxidation and other applications," *Nanoscale* **4** (2012): 6682–6691, https://doi.org/10.1039/C2NR32222F.

[62] X. Liu, Y. Liu, T. Liu, Y. Jia, H. Deng, W. Wang, and F. Zhang, "Alkali-mediated dissolution-recrystallization strategy for in situ construction of a $BiVO_4/BiVO_{40}$ heterojunction with promoted interfacial charge transfer: Formation mechanism and photocatalytic tetracycline degradation studies," *Chemical Engineering Journal* **431** (2022): 134181, https://doi.org/10.1016/j.cej.2021.134181.

[63] Q. Xu, L. Zhang, B. Cheng, J. Fan, and J. Yu, "S-Scheme heterojunction photocatalyst," *Chem* **6** (2020): 1543–1559, https://doi.org/10.1016/j.chempr.2020.06.010.

[64] A. J. Bard, "Photoelectrochemistry and heterogeneous photocatalysis at semiconductors," *Journal of Photochemistry* **10** (1979): 59–75, https://doi.org/10.1016/0047-2670(79)80037-4.

[65] X. Li, C. Garlisi, Q. Guan, S. Anwer, K. Al-Ali, G. Palmisano, and L. Zheng, "A review of material aspects in developing direct Z-scheme photocatalysts," *Materials Today* **47** (2021): 75–107, https://doi.org/10.1016/j.mattod.2021.02.017.

[66] J. Fu, Q. Xu, J. Low, C. Jiang, and J. Yu, "Ultrathin 2D/2D WO_3/g-C_3N_4 Step-Scheme H_2-Production Photocatalyst," *Applied Catalysis B: Environmental* 243 (2019): 556–565, https://doi.org/10.1016/j.apcatb.2018.11.011.

[67] F. Li, G. Zhu, J. Jiang, L. Yang, F. Deng, Arramel, and X. Li, "A Review of Updated S-Scheme Heterojunction Photocatalysts," *Journal of Materials Science & Technology* 177 (2024): 142–180, https://doi.org/10.1016/j.jmst.2023.08.038.

[68] E. M. Akinoglu, D. A. Hoogeveen, C. Cao, A. N. Simonov, and J. J. Jasieniak, "Prospects of Z-Scheme Photocatalytic Systems Based on Metal Halide Perovskites," *ACS Nano* 15 (2021): 7860–7878, https://doi.org/10.1021/acsnano.0c10387.

[69] J. Li, L. Li, J. Wang, A. Cabot, and Y. Zhu, "Boosting Hydrogen Evolution by Methanol Oxidation Reaction on Ni-Based Electrocatalysts: From Fundamental Electrochemistry to

Perspectives," *ACS Energy Letters* 9 (2024): 853–879, https://doi.org/10.1021/acsenergylett.3c02678.

[70] G. Liu, J. Yu, G. Q. Lu, and H.-M. Cheng, "Crystal Facet Engineering of Semiconductor Photocatalysts: Motivations, Advances and Unique Properties," *Chemical Communications* 47 (2011): 6763–6783, https://doi.org/10.1039/C1CC10665A.

[71] Y. Zhai, P. Han, Q. Yun, Y. Ge, X. Zhang, Y. Chen, and H. Zhang, "Phase Engineering of Metal Nanocatalysts for Electrochemical CO_2 Reduction," *eScience* 2 (2022): 467–485, https://doi.org/10.1016/j.esci.2022.09.002.

[72] S. Liu, J. Yu, and M. Jaroniec, "Anatase TiO_2 with Dominant High-Energy {001} Facets: Synthesis, Properties, and Applications," *Chemistry of Materials* 23 (2011): 4085–4093, https://doi.org/10.1021/cm200597m.

[73] H. Xu, P. Reunchan, S. Ouyang, H. Tong, N. Umezawa, T. Kako, and J. Ye, "Anatase TiO_2 Single Crystals Exposed with High-Reactive {111} Facets Toward Efficient H_2 Evolution," *Chemistry of Materials* 25 (2013): 405–411, https://doi.org/10.1021/cm303502b.

[74] G. Liu, H. G. Yang, J. Pan, Y. Q. Yang, G. Q. Lu, and H.-M. Cheng, "Titanium Dioxide Crystals with Tailored Facets," *Chemical Reviews* 114 (2014): 9559–9612, https://doi.org/10.1021/cr400621z.

[75] J. Zeng, Y. Xia, M. Rycenga, J. Tao, Z.-Y. Li, Q. Zhang, Y. Zhu, and Y. Xia, "Controlling the Shapes of Silver Nanocrystals with Different Capping Agents," *Journal of the American Chemical Society* 132 (2010): 8552–8553, https://doi.org/10.1021/ja103655f.

[76] D. Wang, H. Jiang, X. Zong, Q. Xu, Y. Ma, G. Li, and C. Li, "Crystal Facet Dependence of Water Oxidation on $BiVO_4$ Sheets under Visible Light Irradiation," *Chemistry – A European Journal* 17 (2011): 1275–1282, https://doi.org/10.1002/chem.201001636.

[77] H. Zhang, Y. Wang, P. Liu, Y. Han, X. Yao, J. Zou, H. Cheng, and H. Zhao, "Anatase TiO_2 Crystal Facet Growth: Mechanistic Role of Hydrofluoric Acid and Photoelectrocatalytic Activity," *ACS Applied Materials & Interfaces* 3 (2011): 2472–2478, https://doi.org/10.1021/am200363p.

[78] D.-F. Zhang, H. Zhang, L. Guo, K. Zheng, X.-D. Han, and Z. Zhang, "Delicate Control of Crystallographic Facet-Oriented Cu_2O Nanocrystals and the Correlated Adsorption Ability," *Journal of Materials Chemistry* 19 (2009): 5220–5225, https://doi.org/10.1039/B816349A.

[79] R. Li, F. Zhang, D. Wang, J. Yang, M. Li, J. Zhu, X. Zhou, H. Han, and C. Li, "Spatial Separation of Photogenerated Electrons and Holes among {010} and {110} Crystal Facets of

$BiVO_4$," *Nature Communications* 4 (2013): 1432, https://doi.org/10.1038/ncomms2401.

[80] N. Tian, Z.-Y. Zhou, S.-G. Sun, Y. Ding, and Z. L. Wang, "Synthesis of Tetrahexahedral Platinum Nanocrystals with High-Index Facets and High Electro-Oxidation Activity," *Science* 316 (2007): 732–735, https://doi.org/10.1126/science.1140484.

[81] C. Wang, Q. Zhang, B. Yan, B. You, J. Zheng, L. Feng, C. Zhang, S. Jiang, W. Chen, and S. He, "Facet Engineering of Advanced Electrocatalysts Toward Hydrogen/Oxygen Evolution Reactions," *Nano-Micro Letters* **15** (2023): 52, https://doi.org/10.1007/s40820-023-01024-6.

[82] S. Bai, W. Jiang, Z. Li, and Y. Xiong, "Surface and Interface Engineering in Photocatalysis," *ChemNanoMat* **1** (2015): 223–239, https://doi.org/10.1002/cnma.201500069.

[83] X.-F. Yang, A. Wang, B. Qiao, J. Li, J. Liu, and T. Zhang, "Single-Atom Catalysts: A New Frontier in Heterogeneous Catalysis," *Accounts of Chemical Research* **46** (2013): 1740–1748. https://doi.org/10.1021/ar300361m.

[84] X. Li, W. Bi, L. Zhang, S. Tao, W. Chu, Q. Zhang, Y. Luo, C. Wu, and Y. Xie, "Single-Atom Pt as Co-Catalyst for Enhanced Photocatalytic H_2 Evolution," *Advanced Materials* **28** (2016): 2427–2431, https://doi.org/10.1002/adma.201505281.

[85] P. Qi, J. Wang, X. Djitcheu, D. He, H. Liu, and Q. Zhang, "Techniques for the Characterization of Single Atom Catalysts," *RSC Advances* **12** (2022): 1216–1227, https://doi.org/10.1039/D1RA07799F.

[86] Y. Li, Z. Wang, T. Xia, H. Ju, K. Zhang, R. Long, Q. Xu, C. Wang, L. Song, J. Zhu, J. Jiang, and Y. Xiong, "Implementing Metal-to-Ligand Charge Transfer in Organic Semiconductor for Improved Visible-Near-Infrared Photocatalysis," *Advanced Materials* **28** (2016): 6959–6965, https://doi.org/10.1002/adma.201601960.

[87] C. Gao, J. Low, R. Long, T. Kong, J. Zhu, and Y. Xiong, "Heterogeneous Single-Atom Photocatalysts: Fundamentals and Applications," *Chemical Reviews* **120** (2020): 12175–12216, https://doi.org/10.1021/acs.chemrev.9b00840.

[88] L. Zeng and C. Xue, "Single Metal Atom Decorated Photocatalysts: Progress and Challenges," *Nano Research* **14** (2021): 934–944, https://doi.org/10.1007/s12274-020-3099-8.

[89] Y. Sui, S. Liu, T. Li, Q. Liu, T. Jiang, Y. Guo, and J.-L. Luo, "Atomically Dispersed Pt on Specific TiO_2 Facets for Photocatalytic H_2 Evolution," *Journal of Catalysis* **353** (2017): 250–255, https://doi.org/10.1016/j.jcat.2017.07.024.

[90] B.-H. Lee, S. Park, M. Kim, A. K. Sinha, S. C. Lee, E. Jung, W. J. Chang, K.-S. Lee, J.

H. Kim, S.-P. Cho, H. Kim, K. T. Nam, and T. Hyeon, "Reversible and Cooperative Photoactivation of Single-Atom Cu/TiO_2 Photocatalysts," *Nature Materials* **18** (2019): 620–626, https://doi.org/10.1038/s41563-019-0344-1.

[91] Y. Wang, Q. Wang, J. Wu, X. Zhao, Y. Xiong, F. Luo, and Y. Lei, "Asymmetric Atomic Sites Make Different: Recent Progress in Electrocatalytic CO_2 Reduction," *Nano Energy* **103** (2022): 107815. https://doi.org/10.1016/j.nanoen.2022.107815.

[92] Y. Zhang, L. Jiao, W. Yang, C. Xie, and H.-L. Jiang, "Rational Fabrication of Low-Coordinate Single-Atom Ni Electrocatalysts by MOFs for Highly Selective CO_2 Reduction," *Angewandte Chemie International Edition* **60** (2021): 7607–7611, https://doi.org/10.1002/anie.202016219.

[93] K. Ma, Z. Wang, W. Gao, Y. Chen, H. Li, Y. Gao, H. Zhang, O. Ruzimuradov, J. Low, and Y. Li, "Modulating the Coordination Environment in CeO_{2-x} towards Enhanced Photocatalytic CO_2 Conversion Stability and Performance," *Advanced Powder Materials* **5** (2026): 100362. https://doi.org/10.1016/j.apmate.2025.100362

[94] M. Sun, Y. Chen, X. Fan, D. Li, J. Song, K. Yu, and Z. Zhao, "Electronic Asymmetry of Lattice Oxygen Sites in ZnO Promotes the Photocatalytic Oxidative Coupling of Methane," *Nature Communications* **15** (2024): 9900, https://doi.org/10.1038/s41467-024-54226-w.

[95] H. Zeng, S. Yoshioka, W. Wang, Z. Han, I. G. Ivanov, H. Liang, V. Darakchieva, and J. Sun, "Manipulating Electron Structure through Dual-Interface Engineering of 3C-SiC Photoanode for Enhanced Solar Water Splitting," *Journal of the American Chemical Society* **147** (2025): 14815–14823, https://doi.org/10.1021/jacs.5c04005.

[96] A. Zindrou, L. Belles, and Y. Deligiannakis, "Interactions of Oxygen Vacancies with Photoinduced {Hole/Electron} Pairs in $SrTiO_{3-x}$: Their Key Role in Photocatalytic H_2 Production," *The Journal of Physical Chemistry C* **129** (2025): 15309–15321, https://doi.org/10.1021/acs.jpcc.5c03464.

[97] K. Yu, L.-L. Lou, S. Liu, and W. Zhou, "Asymmetric Oxygen Vacancies: the Intrinsic Redox Active Sites in Metal Oxide Catalysts," *Advanced Science* **7** (2020): 1901970, https://doi.org/10.1002/advs.201901970.

[98] Z. Tao, N. Lv, H. Zhao, X. Luo, Z. Li, J. Yu, L. Chen, X. Liu, and S. Mu, "Dual Active Site-Mediated Ir Single-Atom-Doped RuO_2 Catalysts for Highly Efficient and Stable Water Splitting," *Chemical Science* **15** (2024): 16796–16803, https://doi.org/10.1039/D4SC04909H.

[99] C. Wang, K. Wang, Y. Feng, C. Li, X. Zhou, L. Gan, Y. Feng, H. Zhou, B. Zhang, X. Qu, H. Li, J. Li, A. Li, Y. Sun, and S. Zhang, "Co and Pt Dual-Single-Atoms with Oxygen-Coordinated Co–O–Pt Dimer Sites for Ultrahigh Photocatalytic Hydrogen Evolution

Efficiency," *Advanced Materials* **33** (2021): 2003327. https://doi.org/10.1002/adma.202003327

[100] Z. Zhao, Dr. P. Wang, C. Song, T. Zhang, Prof. S. Zhan, and Prof. Y. Li, "Enhanced Interfacial Electron Transfer by Asymmetric Cu-Ov-In Sites on In_2O_3 for Efficient Peroxymonosulfate Activation,"*Angewandte Chemie International Edition* **62** (2023): e202216403, https://doi.org/10.1002/anie.202216403.

[101] L. Nie, D. Mei, H. Xiong, B. Peng, Z. Ren, X. I. P. Hernandez, A. DeLaRiva, M. Wang, M. H. Engelhard, L. Kovarik, A. K. Datye, and Y. Wang, "Activation of Surface Lattice Oxygen in Single-Atom Pt/CeO_2 Catalysts for Low-Temperature CO Oxidation," *Science* 358 (2017): 1419–1423, https://doi.org/10.1126/science.aao2109.

[102] R. Gao, J. Wang, Z. Huang, R. Zhang, W. Wang, L. Pan, J. Zhang, W. Zhu, X. Zhang, C. Shi, J. Lim, and J.-J. Zou, "Pt/Fe2O3 with Pt–Fe pair sites as a catalyst for oxygen reduction with ultralow Pt loading," *Nature Energy* 6 (2021): 614–623, https://doi.org/10.1038/s41560-021-00826-5.

[103] Wei Jun Ong, Lai Ling Tan, Siang-Piao Chai, Siew-Teng Yong, and Abdul Rahman Mohamed, "Facet-Dependent Photocatalytic Properties of TiO_2-Based Composites for Energy Conversion and Environmental Remediation," *ChemSusChem* 7 (2014): 690–719, https://doi.org/10.1002/cssc.201300924.

[104] J. Pan, X. Wu, L. Wang, G. Liu, G. Q. Lu, and H. M. Cheng, "Synthesis of Anatase TiO_2 Rods with Dominant Reactive {010} Facets for the Photoreduction of CO_2 to CH_4 and Use in Dye-Sensitized Solar Cells," *Chemical Communications* **47** (2011): 8361–8363, https://doi.org/10.1039/C1CC13034J.

[105] C. T. Dinh, T. D. Nguyen, F. Kleitz, and T.-O. Do, "Shape-Controlled Synthesis of Highly Crystalline Titania Nanocrystals," *ACS Nano* **3** (2009): 3737–3743, https://doi.org/10.1021/nn900940p.

[106] E. Hosono, S. Fujihara, K. Kakiuchi, and H. Imai, "Growth of Submicrometer-Scale Rectangular Parallelepiped Rutile TiO_2 Films in Aqueous $TiCl_3$ Solutions under Hydrothermal Conditions," *Journal of the American Chemical Society* **126** (2004): 7790–7791, https://doi.org/10.1021/ja048820p.

[107] T. Li, B. Tian, J. Zhang, R. Dong, T. Wang, and F. Yang, "Facile Tailoring of Anatase TiO_2 Morphology by Use of H_2O_2: From Microflowers with Dominant {101} Facets to Microspheres with Exposed {001} Facets," *Industrial & Engineering Chemistry Research* **52** (2013): 6704–6712, https://doi.org/10.1021/ie3030714.

[108] V. Amoli, M. G. Sibi, B. Banerjee, M. Anand, A. Maurya, S. A. Farooqui, A. Bhaumik,

and A. K. Sinha, “Faceted Titania Nanocrystals Doped with Indium Oxide Nanoclusters as a Superior Candidate for Sacrificial Hydrogen Evolution without Any Noble-Metal Cocatalyst under Solar Irradiation,” *ACS Applied Materials & Interfaces* **7** (2015): 810–822, https://doi.org/10.1021/am507293b.

[109] P. Debye and P. Scherrer, “Interferenz an regellos orientierten Teilchen im Röntgenlicht,” *Physikalische Zeitschrift* **17** (1916): 277–283.

[110] B. D. Cullity and S. R. Stock, *Elements of X-Ray Diffraction*, 3rd ed. Upper Saddle River, NJ, USA: Prentice-Hall Inc., 2001. ISBN: 0-201-61091-4

[111] A. L. Patterson, “The Scherrer Formula for X-Ray Particle Size Determination,” *Physical Review* **56** (1939): 978–982. https://doi.org/10.1103/PhysRev.56.978

[112] D. S. Su, B. Zhang, and R. Schlögl, “Electron Microscopy in Heterogeneous Catalysis,” *Chemical Reviews* 115 (2015): 2818–2882, https://doi.org/10.1021/cr500084c.

[113] D. McMullan, “Scanning Electron Microscopy 1928–1965,” *Scanning* 17 (1995): 175–185, https://doi.org/10.1002/sca.4950170309.

[114] D. J. Stokes, “Recent Advances in Electron Imaging, Image Interpretation and Applications: Environmental Scanning Electron Microscopy,” *Philosophical Transactions of the Royal Society of London. Series A: Mathematical, Physical and Engineering Sciences* 361 (2003): 2771–2787, https://doi.org/10.1098/rsta.2003.1279.

[115] J. C. Meier, I. Katsounaros, C. Galeano, H. J. Bongard, A. A. Topalov, A. Kostka, A. Karschin, F. Schüth, and K. J. J. Mayrhofer, “Independent Evaluation of the Electrochemical Characteristics of Anisotropic Structured Pt Nanoparticles,” *Energy & Environmental Science* 5 (2012): 9319–9330, https://doi.org/10.1039/C2EE22550F.

[116] J. Goldstein, D. Newbury, P. Echlin, D. Joy, C. Fiori, and E. Lifshin, *Scanning Electron Microscopy and X-Ray Microanalysis*, 3rd ed. New York, NY, USA: Springer, 2003. ISBN: 978-0-306-47292-3. https://doi.org/10.1007/978-1-4615-0215-9.

[117] H. H. Rose, “Optics of High-Performance Electron Microscopes,” *Science and Technology of Advanced Materials* **9** (2008): 014107, https://doi.org/10.1088/0031-8949/9/1/014107.

[118] https://en.wikipedia.org/wiki/Energy-dispersive_X-ray_spectroscopy.

[119] J. M. Yoon, D. O. Shin, Y. Yin, H. K. Seo, D. Kim, Y. I. Kim, J. H. Jin, Y. T. Kim, B. Bae, S. O. Kim, and J. Y. Lee, “Fabrication of high-density In3Sb1Te2 phase change nanoarray on glass-fabric reinforced flexible substrate,” *Nanotechnology* **23** (2012): 255301, https://doi.org/10.1088/0957-4484/23/25/255301.

[120] D. B. Williams and C. B. Carter, *Transmission Electron Microscopy: A Textbook for*

Materials Science, Vol. 1 – Basics. New York, NY, USA: Plenum Press, 1996. ISBN: 0-306-45324-X.

[121] D. S. Su, B. Zhang, and R. Schlögl, "Electron Microscopy of Solid Catalysts—Transforming from a Challenge to a Toolbox," *Chemical Reviews* **115** (2015): 2818–2882, https://doi.org/10.1021/cr500084c.

[122] J. C. Yang, M. W. Small, R. V. Grieshaber, and R. G. Nuzzo, "Recent developments and applications of electron microscopy to heterogeneous catalysis," *Chemical Society Reviews* **41** (2012): 8179–8194, https://doi.org/10.1039/C2CS35371G.

[123] B. Zhang, X. Ni, W. Zhang, L. Shao, Q. Zhang, F. Girgsdies, C. Liang, R. Schlögl, and D. S. Su, "Structural rearrangements of Ru nanoparticles supported on carbon nanotubes under microwave irradiation," *Chemical Communications* **47** (2011): 10716–10718, https://doi.org/10.1039/C1CC13858H.

[124] P. A. Buffat, "Electron diffraction and HRTEM studies of multiply-twinned structures and dynamical events in metal nanoparticles: facts and artefacts," Materials Chemistry and Physics 81 (2003): 368–375, https://doi.org/10.1016/S0254-0584(03)00024-5.

[125] W. Zhou and J. M. Thomas, "HRTEM surface profile imaging of solids," *Current Opinion in Solid State and Materials Science* **5** (2001): 75–83, https://doi.org/10.1016/S1359-0286(00)00037-1.

[126] P. M. Voyles, D. A. Muller, J. L. Grazul, P. H. Citrin, and H. J. L. Gossmann, "Atomic-scale imaging of individual dopant atoms and clusters in highly n-type bulk Si," *Nature* **416** (2002): 826–829. https://doi.org/10.1038/416826a.

[127] A. Velazquez-Palenzuela, E. Brillas, C. Arias, F. Centellas, J. A. Garrido, R. M. Rodríguez, and P. L. Cabot, "Structural Characterization of Ru-Modified Carbon-Supported Pt Nanoparticles Using Spontaneous Deposition with CO Oxidation Activity," *The Journal of Physical Chemistry C* **116** (2012): 18469–18478, https://doi.org/10.1021/jp304232u.

[128] J. Liu, "Advanced Electron Microscopy Characterization of Nanostructured Heterogeneous Catalysts," *Microscopy and Microanalysis* **10** (2004): 55–76, https://doi.org/10.1017/S1431927604040310.

[129] D. S. Su, R. Schloegl, S. Kujawa, B. Freitag, Microscopy and microanalysis 2005, 11,1550.

[130] J. M. Thomas and P. A. Midgley, "The Merits of Static and Dynamic High-Resolution Electron Microscopy (HREM) for the Study of Solid Catalysts," *ChemCatChem* **2** (2010): 783–798, https://doi.org/10.1002/cctc.201000059.

[131] J. C. Yang, M. W. Small, R. V. Grieshaber, and R. G. Nuzzo, "Recent developments

and applications of electron microscopy to heterogeneous catalysis," *Chemical Society Reviews* **41** (2012): 8179–8194, https://doi.org/10.1039/C2CS35371G.

[132] D. A. Muller, Y. Tzou, R. Raj, and J. Silcox, "Mapping Sp^2 and Sp^3 States of Carbon at Sub-nanometre Spatial Resolution," *Nature* **366** (1993): 725–727. https://doi.org/10.1038/366725a0.

[133] P. E. Batson, "Simultaneous STEM Imaging and Electron Energy-Loss Spectroscopy with Atomic-Column Sensitivity," *Nature* **366** (1993): 727–728. https://doi.org/10.1038/366727a0.

[134] P. Wang, A. J. D'Alfonso, S. D. Findlay, L. J. Allen, and A. L. Bleloch, "Contrast Reversal in Atomic-Resolution Chemical Mapping," *Physical Review Letters* **101** (2008): 236102. https://doi.org/10.1103/PhysRevLett.101.236102.

[135] C. Dwyer, "Multislice theory of fast electron scattering incorporating atomic inner-shell ionization," *Ultramicroscopy* **104** (2005): 141–151, https://doi.org/10.1016/j.ultramic.2005.03.005.

[136] G. Leofanti, M. Padovan, G. Tozzola, and B. Venturelli, "Surface Area and Pore Texture of Catalysts," *Catalysis Today* **41** (1998): 207–219. https://doi.org/10.1016/S0920-5861(98)00050-9.

[137] M. Kruk and M. Jaroniec, "Gas Adsorption Characterization of Ordered Organic–Inorganic Nanocomposite Materials," *Chemistry of Materials* **13** (2001): 3169–3183. https://doi.org/10.1021/cm0101069.

[138] K. S. W. Sing, D. H. Everett, R. A. W. Haul, L. Moscou, R. A. Pierotti, J. Rouquérol, and T. Siemieniewska, "Reporting Physisorption Data for Gas/Solid Systems with Special Reference to the Determination of Surface Area and Porosity," *Pure and Applied Chemistry* **57** (1985): 603–619, https://doi.org/10.1351/pac198557040603.

[139] C. G. V. Burgess, D. H. Everett, and S. Nuttall, "Adsorption hysteresis in porous materials," *Pure and Applied Chemistry* **61** (1989): 1845–1856, https://doi.org/10.1351/pac198961111845.

[140] W. Haiss, N. T. K. Thanh, J. Aveyard, and D. G. Fernig, "Determination of Size and Concentration of Gold Nanoparticles from UV−Vis Spectra," *Analytical Chemistry* **79** (2007): 4215–4221. https://doi.org/10.1021/ac0702084.

[141] V. Srikant and D. R. Clarke, "On the Optical Band Gap of Zinc Oxide," Journal of Applied Physics 83 (1998): 5447–5451. https://doi.org/10.1063/1.367375.

[142] D. C. Koningsberger, S. M. A. M. Bouwens, J. A. R. van Veen, V. H. J. de Beer, and R. Prins, "EXAFS Determination of the Structure of Cobalt in Carbon-Supported Cobalt and

Cobalt-Molybdenum Sulfide Hydrodesulfurization Catalysts," *The Journal of Physical Chemistry* **95** (1991): 123–134. https://doi.org/10.1021/j100154a028.

[143] J. Tauc, "Optical Properties and Electronic Structure of Amorphous Ge and Si," *Materials Research Bulletin* **3** (1968): 37–46. https://doi.org/10.1016/0025-5408(68)90023-8.

[144] K. R. Nemade and S. A. Waghuley, "UV–Visible Spectroscopic Study of One Pot Synthesized Strontium Oxide Quantum Dots," *Results in Physics* **3** (2013): 52–54, https://doi.org/10.1016/j.rinp.2013.03.001.

[145] J. R. Lakowicz, *Principles of Fluorescence Spectroscopy*, 3rd ed. Berlin, Germany: Springer, 2006, https://doi.org/10.1007/978-0-387-46312-4.

[146] A. Meldrum, "Time-Resolved Photoluminescence Spectroscopy of Semiconductor Nanocrystals and Other Fluorophores," *Journal of Visualized Experiments* (JoVE) (2022), https://doi.org/10.3791/64101.

[147] L. Zeiri, B. V. Bronk, Y. Shabtai, J. Eichler, and S. Efrima, "Surface-Enhanced Raman Spectroscopy as a Tool for Probing Specific Biochemical Components in Bacteria," *Applied Spectroscopy* **58** (2004): 33–40, https://doi.org/10.1366/000370204322729441.

[148] P. Colomban, G. Sagon, and X. Faurel, "Differentiation of antique ceramics from the Raman spectra of their coloured glazes and paintings," Journal of Raman Spectroscopy 32 (2001): 351–360, https://doi.org/10.1002/jrs.704.

[149] P. Colomban, G. Gouadec, and L. Mazerolles, "Raman analysis of materials corrosion: the example of SiC fibers," *Materials and Corrosion* **53** (2002): 306–315, https://doi.org/10.1002/1521-4176(200205)53:5<306::AID-MACO306>3.0.CO;2-W.

[150] U. Lavrenčič-Štangar, B. Orel, A. S. Vuk, G. Sagon, P. Colomban, E. Statthatos, and P. Lianos, "In Situ Resonance Raman Microspectroscopy of a Solid-State Dye-Sensitized Photoelectrochemical Cell," *Journal of The Electrochemical Society* **149** (2002): E413–E418, https://doi.org/10.1149/1.1509071.

[151] J. Jiang, K. Bosnick, M. Maillard, and L. Brus, "Single Molecule Raman Spectroscopy at the Junctions of Large Ag Nanocrystals," *The Journal of Physical Chemistry B* **107** (2003): 9964–9972, https://doi.org/10.1021/jp034632u.

[152] C. V. Raman, "A New Radiation," *Indian Journal of Physics* **2** (1928): 387–398

[153] https://en.wikipedia.org/wiki/X-ray_photoelectron_spectroscopy.

[154] https://www.phi.com/surface-analysis-techniques/xps-esca.html.

[155] Weil, J.A., Bolton, J.R. — Electron Paramagnetic Resonance: Elementary Theory and Practical Applications, 2nd ed., Wiley-Interscience, 2007.

[156] F. Fabregat-Santiago, J. Bisquert, E. Palomares, S. A. Haque, J. R. Durrant,

"Impedance spectroscopy study of dye-sensitized solar cells with undoped spiro-OMeTAD as hole conductor," *Journal of Applied Physics* **100** (2006): 034510, https://doi.org/10.1063/1.2222063.

[157] J. Nissfolk, K. Fredin, A. Hagfeldt, and G. Boschloo, "Recombination and Transport Processes in Dye-Sensitized Solar Cells Investigated under Working Conditions," *The Journal of Physical Chemistry B* **110** (2006): 17715–17718, https://doi.org/10.1021/jp064046b.

[158] Q. Wang, S. Ito, M. Grätzel, F. Fabregat-Santiago, I. Mora-Seró, J. Bisquert, T. Bessho, and H. Imai, "Characteristics of High Efficiency Dye-Sensitized Solar Cells," *The Journal of Physical Chemistry B* **110** (2006): 25210–25221, https://doi.org/10.1021/jp064256o.

[159] J. W. Ondersma and T. W. Hamann, "Impedance Investigation of Dye-Sensitized Solar Cells Employing Outer-Sphere Redox Shuttles," *The Journal of Physical Chemistry C* **114** (2010): 638–645, https://doi.org/10.1021/jp908442p.

[160] M. Grätzel, R. A. J. Janssen, D. B. Mitzi, and E. H. Sargent, "Materials Interface Engineering for Solution-Processed Photovoltaics," *Nature* **488** (2012): 304–312. https://doi.org/10.1038/nature11476.

[161] A. K. Poswal, A. Agrawal, H. K. Poswal, D. Bhattacharyya, S. N. Jha, and N. K. Sahoo, "Augmentation of the step-by-step Energy-Scanning EXAFS beamline BL-09 to continuous-scan EXAFS mode at INDUS-2 SRS," *Journal of Synchrotron Radiation* **23** (2016): 1518–1527, https://doi.org/10.1107/S160057751601362X.

[162] B. Delley, "An All-Electron Numerical Method for Solving the Local Density Functional for Polyatomic Molecules," *The Journal of Chemical Physics* **92** (1990): 508–517. https://doi.org/10.1063/1.458452.

[163] S. Thomas and N. S. Haider, ""A Study on Basics of a Gas Analyzer," *International Journal of Advanced Research in Electrical, Electronics and Instrumentation Engineering* **2** (2013): 6016–6020.

[164] http://encyclopedia2.thefreedictionary.com/Gas+Analyzers.

[165] M. Wang, Y. Zuo, J. Wang, Y. Wang, X. Shen, B. Qiu, L. Cai, F. Zhou, S. P. Lau, and Y. Chai, "Remarkably Enhanced Hydrogen Generation of Organolead Halide Perovskites via Piezocatalysis and Photocatalysis," *Advanced Energy Materials* 9 (2019): 1901801, https://doi.org/10.1002/aenm.201901801.

[166] T. Takata, J. Jiang, Y. Sakata, M. Nakabayashi, N. Shibata, V. Nandal, K. Seki, T. Hisatomi, and K. Domen, "Photocatalytic Water Splitting with a Quantum Efficiency of Almost Unity," *Nature* 581 (2020): 411–414, https://doi.org/10.1038/s41586-020-2278-9.

[167] B. Samanta, Á. Morales-García, F. Illas, N. Goga, J. A. Anta, S. Calero, A. Bieberle-Hütter, F. Libisch, A. B. Muñoz-García, M. Pavone, and M. C. Toroker, "Challenges of Modeling Nanostructured Materials for Photocatalytic Water Splitting," *Chemical Society Reviews* 51 (2022): 3794–3818, https://doi.org/10.1039/D1CS00648G.

[168] C.-F. Fu, X. Wu, and J. Yang, "Material Design for Photocatalytic Water Splitting from a Theoretical Perspective," *Advanced Materials* 30 (2018): 1802106, https://doi.org/10.1002/adma.201802106.

[169] Y. Qi, J. Zhang, Y. Kong, Y. Zhao, S. Chen, D. Li, W. Liu, Y. Chen, T. Xie, J. Cui, C. Li, K. Domen, and F. Zhang, "Unraveling of Cocatalysts Photodeposited Selectively on Facets of $BiVO_4$ to Boost Solar Water Splitting," *Nature Communications* 13 (2022): 484, https://doi.org/10.1038/s41467-022-28146-6.

[170] A. Wang, J. Li, and T. Zhang, "Heterogeneous Single-Atom Catalysis," *Nature Reviews Chemistry* 2 (2018): 65–81, https://doi.org/10.1038/s41570-018-0010-1.

[171] C. Cheng, W.-H. Fang, R. Long, and O. V. Prezhdo, "Water Splitting with a Single-Atom Cu/TiO_2 Photocatalyst: Atomistic Origin of High Efficiency and Proposed Enhancement by Spin Selection," *JACS Au* 1 (2021): 550–559, https://doi.org/10.1021/jacsau.1c00004.

[172] H. Zhang, Y. Wang, S. Zuo, W. Zhou, J. Zhang, and X. W. D. Lou, "Isolated Cobalt Centers on W18O49 Nanowires Perform as a Reaction Switch for Efficient CO2 Photoreduction," *Journal of the American Chemical Society* 143 (2021): 2173–2177, https://doi.org/10.1021/jacs.0c08409.

[173] S. Hejazi, S. Mohajernia, B. Osuagwu, G. Zoppellaro, P. Andryskova, O. Tomanec, S. Kment, R. Zbořil, and P. Schmuki, "On the Controlled Loading of Single Platinum Atoms as a Co-Catalyst on TiO_2 Anatase for Optimized Photocatalytic H_2 Generation," *Advanced Materials* 32 (2020): 1908505, https://doi.org/10.1002/adma.201908505.

[174] Y. Shen, C. Ren, L. Zheng, X. Xu, R. Long, W. Zhang, Y. Yang, Y. Zhang, Y. Yao, H. Chi, J. Wang, Q. Shen, Y. Xiong, Z. Zou, and Y. Zhou, "Room-temperature photosynthesis of propane from CO_2 with Cu single atoms on vacancy-rich TiO_2," *Nature Communications* 14 (2023): 1117, https://doi.org/10.1038/s41467-023-36778-5.

[175] K. Zhang, L. Wang, J. K. Kim, M. Ma, G. Veerappan, C.-L. Lee, K.-J. Kong, H. Lee, and J. H. Park, "An order/disorder/water junction system for highly efficient co-catalyst-free photocatalytic hydrogen generation," *Energy & Environmental Science* 9 (2016): 499–503, https://doi.org/10.1039/C5EE03100A.

[176] R. Belgamwar, R. Verma, T. Das, S. Chakraborty, P. Sarawade, and V. Polshettiwar,

"Defects Tune the Strong Metal–Support Interactions in Copper Supported on Defected Titanium Dioxide Catalysts for CO_2 Reduction," *Journal of the American Chemical Society* 145 (2023): 8634–8645, https://doi.org/10.1021/jacs.3c01336.

[177] J. Yu, J. Low, W. Xiao, P. Zhou, and M. Jaroniec, "Enhanced Photocatalytic CO_2-Reduction Activity of Anatase TiO_2 by Co exposed {001} and {101} Facets," *Journal of the American Chemical Society* 136 (2014): 8839–8842, https://doi.org/10.1021/ja5044787.

[178] L. Zhang, J. Ran, S.-Z. Qiao, and M. Jaroniec, "Characterization of Semiconductor Photocatalysts," *Chemical Society Reviews* 48 (2019): 5184–5206, https://doi.org/10.1039/C9CS00172G.

[179] V. Amoli, S. Bhat, A. Maurya, B. Banerjee, A. Bhaumik, and A. K. Sinha, "Tailored Synthesis of Porous TiO_2 Nanocubes and Nanoparallelepipeds with Exposed {111} Facets and Mesoscopic Void Space: A Superior Candidate for Efficient Dye-Sensitized Solar Cells," *ACS Applied Materials & Interfaces* 7 (2015): 26022–26035, https://doi.org/10.1021/acsami.5b07954.

[180] K. Gelderman, L. Lee, and S. W. Donne, "Flat-Band Potential of a Semiconductor: Using the Mott–Schottky Equation," *Journal of Chemical Education* 84 (2007): 685–688, https://doi.org/10.1021/ed084p685.

[181] S. Roberts, "Dielectric Constants and Polarizabilities of Ions in Simple Crystals and Barium Titanate," *Physical Review* 76 (1949): 1215, https://doi.org/10.1103/PhysRev.76.1215.

[182] J. H. Kim, D. Hansora, P. Sharma, J.-W. Jang, and J. S. Lee, "Toward Practical Solar Hydrogen Production — An Artificial Photosynthetic Leaf-to-Farm Challenge," *Chemical Society Reviews* 48 (2019): 1908–1971, https://doi.org/10.1039/C8CS00699G.

[183] M. Xie, S. Tang, Z. Li, M. Wang, Z. Jin, P. Li, X. Zhan, H. Zhou, and G. Yu, "Intermetallic Single-Atom Alloy In–Pd Bimetallene for Neutral Electrosynthesis of Ammonia from Nitrate," *Journal of the American Chemical Society* 145 (2023): 13957–13967, https://doi.org/10.1021/jacs.3c03432.

[184] B. Delley, "From Molecules to Solids with the DMol³ Approach," *Journal of Chemical Physics* 113 (2000): 7756–7764, https://doi.org/10.1063/1.1316015.

[185] C. X. Bezuidenhout, C. Esterhuysen, and L. J. Barbour, "Solvatochromism as a Probe to Observe the Solvent Exchange Process in a 1-D Porous Coordination Polymer with 1-D Solvent Accessible Channels," *Chemical Communications* 53 (2017): 5618–5621, https://doi.org/10.1039/C7CC02492D.

[186] L. Zhao, L. Liu, and H. Sun, "Semi-Ionic Model for Metal Oxides and Their Interfaces

with Organic Molecules," *Journal of Physical Chemistry C* 111 (2007): 10610–10617, https://doi.org/10.1021/jp071775y.

[187] S. Wu, Z. Chen, W. Yue, S. Mine, T. Toyao, M. Matsuoka, X. Xi, L. Wang, and J. Zhang, "Single-Atom High-Valent Fe(IV) for Promoted Photocatalytic Nitrogen Hydrogenation on Porous TiO_2-SiO_2," *ACS Catalysis* 11 (2021): 4362–4371, https://doi.org/10.1021/acscatal.1c00072.

[188] G. Ramadevudu, Md. Shareefuddin, N. S. Bai, M. L. Rao, and M. N. Chary, "Electron Paramagnetic Resonance and Optical Absorption Studies of Cu^{2+} Spin Probe in MgO-Na_2O-B_2O_3 Ternary Glasses," *Journal of Non-Crystalline Solids* 278 (2000): 205–212, https://doi.org/10.1016/S0022-3093(00)00255-6.

[189] V. Amoli, R. Tiwari, A. Dutta, A. Bhaumik, and A. K. Sinha, "Structurally Stabilized Organosilane-Templated Thermostable Mesoporous Titania," *ChemPhysChem* 15 (2014): 187–194, https://doi.org/10.1002/cphc.201300872.

[190] T. Wu, H. Zhao, X. Zhu, Z. Xing, Q. Liu, T. Liu, S. Gao, S. Lu, G. Chen, A. M. Asiri, Y. Zhang, and X. Sun, "Identifying the Origin of Ti^{3+} Activity Toward Enhanced Electrocatalytic N_2 Reduction over TiO_2 Nanoparticles Modulated by Mixed-Valent Copper," *Advanced Materials* 32 (2020): 2000299, https://doi.org/10.1002/adma.202000299.

[191] M. A. Halcrow, "Interpreting and Controlling the Structures of Six-Coordinate Copper (II) Centres — When Is a Compression Really a Compression?" *Dalton Transactions* (2003): 4375–4384, https://doi.org/10.1039/B309242A.

[192] X. Qiu, M. Miyauchi, K. Sunada, M. Minoshima, M. Liu, Y. Lu, D. Li, Y. Shimodaira, Y. Hosogi, Y. Kuroda, and K. Hashimoto, "Hybrid Cu_xO/TiO_2 Nanocomposites as Risk-Reduction Materials in Indoor Environments," *ACS Nano* 6 (2012): 1609–1618, https://doi.org/10.1021/nn2045888.

[193] F. Lei, Y. Sun, K. Liu, S. Gao, L. Liang, B. Pan, and Y. Xie, "Oxygen Vacancies Confined in Ultrathin Indium Oxide Porous Sheets for Promoted Visible-Light Water Splitting," *Journal of the American Chemical Society* 136 (2014): 6826–6829, https://doi.org/10.1021/ja501866r.

[194] Z. Wang, R. Lin, Y. Huo, H. Li, and L. Wang, "Formation, Detection, and Function of Oxygen Vacancy in Metal Oxides for Solar Energy Conversion," *Advanced Functional Materials* 32 (2022): 2109503, https://doi.org/10.1002/adfm.202109503.

[195] G. Li, N. M. Dimitrijevic, L. Chen, T. Rajh, and K. A. Gray, "Role of Surface/Interfacial Cu^{2+} Sites in the Photocatalytic Activity of Coupled CuO–TiO_2 Nanocomposites," *Journal of Physical Chemistry C* 112 (2008): 19040–19044,

https://doi.org/10.1021/jp8068392.

[196] Y.-C. Zhang, N. Afzal, L. Pan, X. Zhang, and J.-J. Zou, "Structure–Activity Relationship of Defective Metal-Based Photocatalysts for Water Splitting: Experimental and Theoretical Perspectives," *Advanced Science* 6 (2019): 1900053, https://doi.org/10.1002/advs.201900053.

[197] M. F. Camellone and S. Fabris, "Reaction Mechanisms for the CO Oxidation on Au/CeO_2 Catalysts: Activity of Substitutional Au^{3+}/Au^{+} Cations and Deactivation of Supported Au^{+} Adatoms," *Journal of the American Chemical Society* 131 (2009): 10473–10483, https://doi.org/10.1021/ja902109k.

[198] J. Low, J. Ma, J. Wan, W. Jiang and Y. Xiong, "Identification and Design of Active Sites on Photocatalysts for the Direct Artificial Carbon Cycle," *Accounts of Materials Research* 3 (2022): 331–342, https://doi.org/10.1021/accountsmr.1c00222.

[199] Y. Zhang, J. Zhao, H. Wang, B. Xiao, W. Zhang, X. Zhao, T. Lv, M. Thangamuthu, J. Zhang, Y. Guo, J. Ma, L. Lin, J. Tang, R. Huang, and Q. Liu, "Single-Atom Cu Anchored Catalysts for Photocatalytic Renewable H_2 Production with a Quantum Efficiency of 56%," *Nature Communications* 13 (2022): 58, https://doi.org/10.1038/s41467-021-27698-3.

[200] L. Zhang, X. Yang, Q. Yuan, Z. Wei, J. Ding, T. Chu, C. Rong, Q. Zhang, Z. Ye, F.-Z. Xuan, Y. Zhai, B. Zhang, and X. Yang, "Elucidating the structure-stability relationship of Cu single-atom catalysts using operando surface-enhanced infrared absorption spectroscopy," *Nature Communications* 14 (2023): 8311, https://doi.org/10.1038/s41467-023-44078-1.

[201] M. Melchionna and P. Fornasiero, "Updates on the Roadmap for Photocatalysis," *ACS Catalysis* 10 (2020): 5493–5501, https://doi.org/10.1021/acscatal.0c01204.

[202] X. Song, G. Wei, J. Sun, C. Peng, J. Yin, X. Zhang, Y. Jiang, and H. Fei, "Overall photocatalytic water splitting by an organolead iodide crystalline material," *Nature Catalysis* 3 (2020): 1027–1035, https://doi.org/10.1038/s41929-020-00543-4.

[203] http://sciencing.com/measure-hydrogen-gas-7768310.html.

[204] X. Zheng, L. Feng, Y. Dou, H. Guo, Y. Liang, G. Li, J. He, P. Liu, and J. He, "High Carrier Separation Efficiency in Morphology-Controlled BiOBr/C Schottky Junctions for Photocatalytic Overall Water Splitting," *ACS Nano* **15** (2021): 13209–13220, https://doi.org/10.1021/acsnano.1c02884.

[205] D. Zhao, Y. Wang, C.-L. Dong, Y.-C. Huang, J. Chen, F. Xue, S. Shen, and L. Guo, "Boron-doped nitrogen-deficient carbon nitride-based Z-scheme heterostructures for photocatalytic overall water splitting," *Nature Energy* **6** (2021): 388–397, https://doi.org/10.1038/s41560-021-00795-9.

[206] X. Yan, M. Xia, H. Liu, B. Zhang, C. Chang, L. Wang, and G. Yang, "An electron-hole rich dual-site nickel catalyst for efficient photocatalytic overall water splitting," *Nature Communications* **14** (2023): 1741, https://doi.org/10.1038/s41467-023-37358-3.

[207] M. Xiao, L. Zhang, B. Luo, M. Lyu, Z. Wang, H. Huang, S. Wang, A. Du, and L. Wang, "Molten-Salt-Mediated Synthesis of an Atomic Nickel Co-catalyst on TiO_2 for Improved Photocatalytic H_2 Evolution," *Angewandte Chemie* 132 (2020): 7297–7301, https://doi.org/10.1002/ange.202001148.

[208] Q. Xiang, J. Yu, and M. Jaroniec, "Synergetic Effect of MoS_2 and Graphene as Cocatalysts for Enhanced Photocatalytic H_2 Production Activity of TiO_2 Nanoparticles," Journal of the American Chemical Society 134 (2012): 6575–6578, https://doi.org/10.1021/ja302846n.

[209] S. Xiao, P. Liu, W. Zhu, G. Li, D. Zhang, and H. Li, "Copper Nanowires: A Substitute for Noble Metals to Enhance Photocatalytic H2 Generation," *Nano Letters* **15** (2015): 4853–4858, https://doi.org/10.1021/acs.nanolett.5b00082.

[210] Y. Liu, B. Zhang, L. Luo, X. Chen, Z. Wang, E. Wu, D. Su, and W. Huang, "TiO2/Cu2O Core/Ultrathin Shell Nanorods as Efficient and Stable Photocatalysts for Water Reduction," *Angewandte Chemie International Edition* 54 (2015): 15260–15265, https://doi.org/10.1002/anie.201509115.

[211] H. Tian, X. L. Zhang, J. Scott, C. Ng, and R. Amal, "TiO2-supported copper nanoparticles prepared via ion exchange for photocatalytic hydrogen production," *Journal of Materials Chemistry A* **2** (2014): 6432–6438, https://doi.org/10.1039/C3TA15254E.

[212] G. Zhu, H. Yin, C. Yang, H. Cui, Z. Wang, J. Xu, T. Lin, and F. Huang, "Black Titania for Superior Photocatalytic Hydrogen Production and Photoelectrochemical Water Splitting," *ChemCatChem* **7** (2015): 2614–2619, https://doi.org/10.1002/cctc.201500488.

[213] M. Cargnello, T. Montini, S. Y. Smolin, J. B. Priebe, J. J. Delgado Jaén, V. V. T. Doan-Nguyen, I. S. McKay, J. A. Schwalbe, M.-M. Pohl, T. R. Gordon, Y. Lu, J. B. Baxter, A. Brückner, P. Fornasiero, and C. B. Murray, "Engineering Titania Nanostructure to Tune and Improve Its Photocatalytic Activity," *Proceedings of the National Academy of Sciences of the United States of America* **113** (2016): 3966–3971. https://doi.org/10.1073/pnas.1524806113.

[214] S. Wang, Y. Wang, S. L. Zhang, S.-Q. Zang, and X. W. Lou, "Supporting Ultrathin $ZnIn_2S_4$ Nanosheets on Co/N-Doped Graphitic Carbon Nanocages for Efficient Photocatalytic H_2 Generation," *Advanced Materials* **31** (2019): 1903404. https://doi.org/10.1002/adma.201903404.

[215] G. Zuo, Y. Wang, W. L. Teo, Prof. A. Xie, Y. Guo, Y. Dai, Dr. W. Zhou, D. Jana, Prof.

Q. Xian, Prof. W. Dong, Prof. Y. Zhao. *Angew. Chem. Int. Ed.* **2020,** 132, 11383.

[216] B. Banerjee, V. Amoli, A. Maurya, A. K. Sinha, and A. Bhaumik, "Green synthesis of Pt-doped TiO_2 nanocrystals with exposed (001) facets and mesoscopic void space for photo-splitting of water under solar irradiation," *Nanoscale* **7** (2015): 10504–10512, https://doi.org/10.1039/C5NR02097B.

[217] B. J. Deadman, K. Hellgardt, and K. Kuok (Mimi) Hii, "A colorimetric method for rapid and selective quantification of peroxodisulfate, peroxomonosulfate and hydrogen peroxide," *Reaction Chemistry & Engineering* **2** (2017): 462–488, https://doi.org/10.1039/C7RE00050B.

[218] Z. Teng, Q. Zhang, H. Yang, K. Kato, W. Yang, Y.-R. Lu, S. Liu, C. Wang, A. Yamakata, C. Su, B. Liu, and T. Ohno, "Atomically dispersed antimony on carbon nitride for the artificial photosynthesis of hydrogen peroxide," *Nature Catalysis* **4** (2021): 374–384, https://doi.org/10.1038/s41929-021-00605-1.

[219] Z. Zhang, T. Tsuchimochi, T. Ina, Y. Kumabe, S. Muto, K. Ohara, H. Yamada, S. L. Ten-no, and T. Tachikawa, "Binary dopant segregation enables hematite-based heterostructures for highly efficient solar H_2O_2 synthesis," *Nature Communications* **13** (2022): 1499, https://doi.org/10.1038/s41467-022-28944-y.

[220] S. Wu and X. Quan, "Design Principles and Strategies of Photocatalytic H2O2 Production from O_2 Reduction," *ACS ES&T Engineering* **2** (2022): 1068–1079, https://doi.org/10.1021/acsestengg.1c00456.

[221] H. Hou, X. Zeng, and X. Zhang, "Production of Hydrogen Peroxide by Photocatalytic Processes," *Angewandte Chemie International Edition* 59 (2020): 17356–17376, https://doi.org/10.1002/anie.201911609.

[222] H. Tong, S. Ouyang, Y. Bi, N. Umezawa, M. Oshikiri, and J. Ye, "Nano-Photocatalytic Materials: Possibilities and Challenges," *Advanced Materials* **24** (2012): 229–251. https://doi.org/10.1002/adma.201102752.

[223] L. Liao, Q. Zhang, Z. Su, Z. Zhao, Y. Wang, Y. Li, X. Lu, D. Wei, G. Feng, Q. Yu, X. Cai, J. Zhao, Z. Ren, H. Fang, F. Robles-Hernandez, S. Baldelli, and J. Bao, "Efficient solar water-splitting using a nanocrystalline CoO photocatalyst," *Nature Nanotechnology* **9** (2014): 69–73. https://doi.org/10.1038/nnano.2013.272.

[224] P. Sun, Y. Zhou, H. Li, H. Zhang, L. Feng, Q. Cao, S. Liu, T. Wågberg, and G. Hu, "Round-the-clock bifunctional honeycomb-like nitrogen-doped carbon-decorated Co_2P/Mo_2C-heterojunction electrocatalyst for direct water splitting with 18.1% STH efficiency," *Applied Catalysis B: Environmental* **310** (2022): 121354.

https://doi.org/10.1016/j.apcatb.2022.121354.

[225] H. Ben, G. Yan, H. Liu, C. Ling, Y. Fan, and X. Zhang, "Local Spatial Polarization Induced Efficient Charge Separation of Squaraine-Linked COF for Enhanced Photocatalytic Performance," *Advanced Functional Materials* **32** (2022): 2104519. https://doi.org/10.1002/adfm.202104519.

[226] T. Wei, Y.-N. Zhu, X. An, L.-M. Liu, X. Cao, H. Liu, and J. Qu, "Defect Modulation of Z-Scheme TiO_2/Cu_2O Photocatalysts for Durable Water Splitting," *ACS Catalysis* **9** (2019): 8346–8354, https://doi.org/10.1021/acscatal.9b01786.

[227] Z. Chen, Y. Song, J. Cai, X. Zheng, D. Han, Y. Wu, Y. Zang, S. Niu, Y. Liu, J. Zhu, X. Liu, and G. Wang, "Tailoring the d-Band Centers Enables Co_4N Nanosheets To Be Highly Active for Hydrogen Evolution Catalysis," *Angewandte Chemie International Edition* **57** (2018): 5076–5080, https://doi.org/10.1002/anie.201801834.

[228] N. Wang, D. Chen, S. Ning, J. Lao, J. Xu, M. Luo, W. Zhang, J. Chen, M. Yang, F. Xie, Y. Jin, S. Sun, H. Meng, "Fe Cluster Modified Co_9S_8 Heterojunction: Highly Efficient Photoelectrocatalyst for Overall Water Splitting and Flexible Zinc-Air Batteries," *Advanced Materials* **36** (2024): 2306138. https://doi.org/10.1002/adma.202306138.

[229] K. Fan, W. Xie, J. Li, Y. Sun, P. Xu, Y. Tang, Z. Li, and M. Shao, "Active hydrogen boosts electrochemical nitrate reduction to ammonia," *Nature Communications* **13** (2022): 7958, https://doi.org/10.1038/s41467-022-35664-w.

[230] J. Ding, H. Yang, S. Zhang, Q. Liu, H. Cao, J. Luo, and X. Liu, "Advances in the Electrocatalytic Hydrogen Evolution Reaction by Metal Nanoclusters-based Materials," *Small* **18** (2022): 2204524. https://doi.org/10.1002/smll.202204524.

[231] H. Zhang, G. Meng, T. Wei, J. Ding, Q. Liu, J. Luo, and X. Liu, "Co doping promotes the alkaline overall seawater electrolysis performance over $MnPSe_3$ nanosheets," *Chemical Communications* **59** (2023): 12144–12147, https://doi.org/10.1039/D3CC03434H.

[232] T. Wei, G. Meng, Y. Zhou, Z. Wang, Q. Liu, J. Luo, and X. Liu, "Amorphous Fe–Co oxide as an active and durable bifunctional catalyst for the urea-assisted H_2 evolution reaction in seawater," *Chemical Communications* **59** (2023): 9992–9995, https://doi.org/10.1039/D3CC02419A.

[233] M. Maji, S. Dutta, R. Jena, A. Dey, T. K. Maji, S. K. Pati, and S. Bhattacharyya, "Hydrogen Evolution in Neutral Media by Differential Intermediate Binding at Charge-Modulated Sites of a Bimetallic Alloy Electrocatalyst," *Angewandte Chemie International Edition* **63** (2024): e202403697. https://doi.org/10.1002/anie.202403697.

[234] G. Ketteler, S. Yamamoto, H. Bluhm, K. Andersson, D. E. Starr, D. F. Ogletree, H.

Ogasawara, A. Nilsson, and M. Salmeron, "The Nature of Water Nucleation Sites on TiO_2(110) Surfaces Revealed by Ambient Pressure X-ray Photoelectron Spectroscopy," *The Journal of Physical Chemistry C* **111** (2007): 8278–8282, https://doi.org/10.1021/jp068606i.

[235] M. J. Jackman, A. G. Thomas, and C. Muryn, "Photoelectron Spectroscopy Study of Stoichiometric and Reduced Anatase TiO_2(101) Surfaces: The Effect of Subsurface Defects on Water Adsorption at Near-Ambient Pressures," *The Journal of Physical Chemistry C* **119** (2015): 13682–13690, https://doi.org/10.1021/acs.jpcc.5b02732.

[236] Y. Wang, Y. Lü, W. Zhan, Z. Xie, Q. Kuang, and L. Zheng, "Synthesis of porous Cu_2O/CuO cages using Cu-based metal–organic frameworks as templates and their gas-sensing properties," *Journal of Materials Chemistry A* **3** (2015): 12796–12803, https://doi.org/10.1039/C5TA01108F.

[237] N. Zhang, A. Jalil, D. Wu, S. Chen, Y. Liu, C. Gao, W. Ye, Z. Qi, H. Ju, C. Wang, X. Wu, L. Song, J. Zhu, and Y. Xiong, "Refining Defect States in $W_{18}O_{49}$ by Mo Doping: A Strategy for Tuning N_2 Activation towards Solar-Driven Nitrogen Fixation," *Journal of the American Chemical Society* **140** (2018): 9434–9443, https://doi.org/10.1021/jacs.8b02076.

[238] A. Wang, J. Li, and T. Zhang, "Heterogeneous Single-Atom Catalysis," *Nature Reviews Chemistry* **2** (2018): 65–81. https://doi.org/10.1038/s41570-018-0010-1.

[239] R. Zhang, Q. Wu, P. Sherrell, D. Li, K. Huang, J. Chen, and X. Yao, "Dynamic investigation of oxygen defects on transition metal-based electrocatalysts: formation, characterization, and mechanism during alkaline oxygen evolution reaction," *Science China Chemistry* **66** (2023): 2221–2243, https://doi.org/10.1007/s11426-023-1649-y.

[240] R. Qiang, H. Wang, K. Xu, Q. Yuan, Y. Yu, L. Li, J. Wang, L. Zheng, P. C. Sherrell, J. Chen, and X. Bi, "Available Active Sites on ε-Fe_3N Nanoparticles Synthesized by a Facile Route for Hydrogen Evolution Reaction," *Advanced Materials Interfaces* **8** (2021): 2100070. https://doi.org/10.1002/admi.202100070.

[241] D. Gunawan, J. Zhang, Q. Li, C. Y. Toe, J. Scott, M. Antonietti, J. Guo, and R. Amal, "Materials Advances in Photocatalytic Solar Hydrogen Production: Integrating Systems and Economics for a Sustainable Future," *Advanced Materials* **36** (2024): 2404618, https://doi.org/10.1002/adma.202404618.

[242] M. G. Idris, H. Y. Hafeez, J. Mohammed, Y. Mohammed, A. B. Suleiman, and C. E. Ndikilar, "Recent Developments on Metal Oxide-Based Photocatalysts for Effective Solar Fuel (Hydrogen) Production via Photocatalytic Water-Splitting," *Journal of Alloys and Compounds Communications* **7** (2025):100080,

https://doi.org/10.1016/j.jacomc.2025.100080.

[243] M. Kumar, B. Meena, P. Subramanyam, D. Suryakala, and C. Subrahmanyam, "Recent trends in photoelectrochemical water splitting: the role of cocatalysts," *NPG Asia Materials* **14** (2022): 88, https://doi.org/10.1038/s41427-022-00436-x.

[244] A. G. Tamirat, J Rick, A. A. Dubale, W-N Su, and B-J Hwang, "Using Hematite for Photoelectrochemical Water Splitting: A Review of Current Progress and Challenges," *Nanoscale Horizons* **1** (2016): 243–267, https://doi.org/10.1039/C5NH00098J.

[245] X. Zhang, S. Zhang, X. Cui, W. Zhou, W. Cao, D. Cheng, and Y. Sun, "Recent Advances in TiO_2-Based Photoanodes for Photoelectrochemical Water Splitting," *Chemistry An Asian Journal* **17** (2022): e202200668, https://doi.org/10.1002/asia.202200668.

[246] J. Liu, Z. Wei, and W. Shangguan, "Defects Engineering in Photocatalytic Water Splitting Materials," *ChemCatChem* **11** (2019): 6177-6189, https://doi.org/10.1002/cctc.201901579.

[247] C. Phawa, S. Prayoonpokarach, K. Sinthiptharakoon, P. Chakthranont, W. Sangkhun, K. Faungnawakij, and T. Butburee, "Effects of Matching Facet Pairs of TiO_2 on Photoelectrochemical Water Splitting Behaviors," *ChemCatChem* **12** (2020): 2116-2124, https://doi.org/10.1002/cctc.201901857.

[248] S. E. Jun, J. K. Lee, S. Ryu, and H. W. Jang, "Single Atom Catalysts for Photoelectrochemical Water Splitting," ChemCatChem **15** (2023): e202300926, https://doi.org/10.1002/cctc.202300926.

[249] A. C. Wardhana, A. Yamaguchi, K. Adachi, D. Hashizume, and M. Miyauchi, "Direct Interfacial Excitation from TiO_2 to Cu(II) Nanoclusters Enables Cathodic Photoresponse for Hydrogen Evolution Under Visible-Light Irradiation," *Small* **19** (2023): 2206893, https://doi.org/10.1002/smll.202206893.

[250] K. Madan, S. Guru, M. Madan, R. Shanmugam, H.S. Rao, and G.R. Rao, "Mn/Fe Co-doped TiO_2 Nanotube Arrays for Photoelectrochemical Water Splitting in Neutral Medium," *Journal of Photochemistry & Photobiology A: Chemistry* **456** (2024): 115816, https://doi.org/10.1016/j.jphotochem.2024.115816.

[251] Q. Ruan, T. Miao, H. Wang, and J. Tang, "Insight on Shallow Trap States-Introduced Photocathodic Performance in N-Type Polymer Photocatalysts," *Journal of the American Chemical Society* **142** (2020): 2795–2802, https://doi.org/10.1016/j.cattod.2015.08.017.

[252] K. Madan, H. S. Rao, R. B. Harikrishna, and G. R. Rao, "N-doped Ti^{3+} Rich $SrTiO_3$ for Efficient Photoelectrochemical Water Splitting," *Catalysis Today* **445** (2025): 115055, https://doi.org/10.1016/j.cattod.2024.115055.

[253] Hemant, Shubham, D. Kumar, C. Yadav, P. Raj, Amandeep, and V. Amoli, "Highly Deformable and Durable PEDOT:PSS Printed Electrodes via Tailored Chemistry and Fabrication Synergy for Scalable Wearable Electronics," *Advanced Materials Technologies* **11** (2025): e01625, https://doi.org/10.1002/admt.202501625.

[254] D. R. Chowdhury, L. Spiccia, S. S. Amritphale, A. Paul, and A. Singh, "A Robust Iron Oxyhydroxide Water Oxidation Catalyst Operating Under Near Neutral and Alkaline Conditions," *Journal of Materials Chemistry A* **4** (2016): 3655-3660, https://doi.org/10.1039/C6TA00313C.

[255] T. Wu, X. Kang, M. W. Kadi, I. Ismail, G. Liu, and H-M. Cheng, "Enhanced Photocatalytic Hydrogen Generation of Mesoporous Rutile TiO_2 Single Crystal with Wholly Exposed {111} Facets," *Chinese Journal of Catalysis* **36** (2015): 2103–2108, https://doi.org/10.1016/S1872-2067(15)60996-2.

[256] D. Kumar, A. Mishra, Shubham, Hemant, S. Bhattacharjee, R. R. Urkude, B. Ghosh, A. Bhaumik, A. K. Sinha, A. S. K. Sinha, and V. Amoli, "Highly Asymmetric Cu_{SA}-O_v-Ti_{3c} Atomic Sites Catalyst for Unprecedented Solar Hydrogen Generation," *Advanced Energy Materials* **14** (2024): 2401964, https://doi.org/10.1002/aenm.202401964.

[257] H. Zhang, M. Wang, and F. Xu, "Generating Oxygen Vacancies in Cu^{2+} -Doped TiO_2 Hollow Spheres for Enhanced Photocatalytic Activity and Antimicrobial Activity," *Micro & Nano Letters* **15** (2020): 535–539, https://doi.org/10.1049/mnl.2019.0781.

[258] X. Qiu, M. Miyauchi, K. Sunada, M. Minoshima, M. Liu, M. Lu, D. Li, Y. Shimodaira, Y. Hosogi, Y. Kuroda, and K. Hashimoto, "Hybrid Cu(x)O/TiO_2 Nanocomposites as Risk-Reduction Materials in Indoor Environments," *ACS Nano* **6** (2012): 1609–1618, https://doi.org/10.1039/B800489G.

[259] R. Fernández-Climent, S. Giménez, and M. García-Tecedor, "The Role of Oxygen Vacancies in Water Splitting Photoanodes," *Sustainable Energy & Fuels* **4** (2020): 5916–5926. https://doi.org/10.1039/D0SE01305F.

[260] Y. Nosaka, S. Takahashi, H. Sakamoto, and A. Y. Nosaka, "Reaction Mechanism of Cu(II)-Grafted Visible-Light Responsive TiO_2 and WO_3 Photocatalysts Studied by Means of ESR Spectroscopy and Chemiluminescence Photometry," *The Journal of Physical Chemistry C* **115** (2011): 21283–21290, https://doi.org/10.1021/jp2070634.

[261] A. L. Sangle, S. Singh, J. Jian, S. R. Bajpe, H. Wang, N. Khare, and J. L. MacManus-Driscoll, "Very High Surface Area Mesoporous Thin Films of $SrTiO_3$ Grown by Pulsed Laser Deposition and Application to Efficient Photoelectrochemical Water Splitting," *Nano Letters* **16** (2016): 7338–7345, https://doi.org/10.1021/acs.nanolett.6b02487.

[262] S. Wu, Q. Peng, W. Deng, F. Zhi, M. He, M. Wang, J. Wang, G. Peng, and S. Cao, "Recent Progress of Graphitic Carbon Nitride Films and Their Application in Photoelectrochemical Water Splitting," *Sustainable Energy Fuels* **7** (2023**)**: 4708–4726, https://doi.org/10.1039/D3SE00780D.

[263] K. Wenderich, W. Kwak, A. Grimm, G. J. Kramer, G. Mul, and B. Mei, "Industrial Feasibility of Anodic Hydrogen Peroxide Production Through Photoelectrochemical Water Splitting: A Techno-Economic Analysis," *Sustainable Energy & Fuels* **4** (2020): 3143–3156, https://doi.org/10.1039/D0SE00524J.

[264] Z. Guo, Z. Xu, F. Xie, J. Jiang, K. Zheng, S. Alabidun, M. Crespo-Ribadeneyra, Y-S. Hu, H. Au, and M.-M. Titirici, "Investigating the Superior Performance of Hard Carbon Anodes in Sodium-Ion Compared With Lithium- and Potassium-Ion Batteries," *Advanced Materials* **35** (2023): 2305742, https://doi.org/10.1002/adma.202304091.

[265] P. Acevedo-Peña, J. Vazquez-Arenas, R. Cabrera-Sierra, L. Lartundo-Rojas, and I. González, "Ti Anodization in Alkaline Electrolyte: The Relationship Between Transport of Defects, Film Hydration and Composition," *Journal of The Electrochemical Society* **160** (2013): C277-C284, https://doi.org/10.1149/2.063306jes.

[266] F. Yang, C. Schröck, J. Kugelstadt, S. Zhang, C. Scheu, C. Trautmann, A. W. Maijenburg, and M. E. Toimil-Molares, "Cu_2O/TiO_2 Nanowire Assemblies as Photocathodes for Solar Hydrogen Evolution: Influence of Diameter, Length and Number Density of

Wires," *Zeitschrift für Physikalische Chemie* **234** (2020): 1205–1221, https://doi.org/10.1515/zpch-2019-1529.

[267] S. R. Sitaaraman, A. N. Grace, J. Zhu, and R. Sellappan, "Photoelectrochemical Performance of a Nanostructured $BiVO_4$/NiOOH/FeOOH–Cu_2O/CuO/TiO_2 Tandem Cell for Unassisted Solar Water Splitting," *Nanoscale Advances* **6** (2024): 2407-2418, https://doi.org/10.1039/D4NA00088A.

[268] T. P. Xavier, M. Piraviperumal, C.-Y. Kuo, and M. Govindasamy, "TiO_2 Hole Transport Layer Incorporated in a Thermally Evaporated Sb_2Se_3 Photoelectrode Exhibiting Low Onset Potential for Photoelectrochemical Applications," *Energy & Fuels* **38** (2024): 16936–16948, https://doi.org/10.1021/acs.energyfuels.4c02083.

[269] J. Su, Z. Li, Y. Zhang, Y. Wei, and X. Wang, "N-Doped and Cu-Doped TiO_2-B Nanowires with Enhanced Photoelectrochemical Activity," *RSC Advances* **6** (2016): 16177, https://doi.org/10.1039/C5RA26309C.

[270] I. Ganesh, P. P. Kumar, I. Annapoorna, J. M. Sumliner, M. Ramakrishnaa, N. Y. Hebalkar, G. Padmanabhama, and G. Sundararajan, "Preparation and Characterization of Cu-Doped TiO_2 Materials for Electrochemical, Photoelectrochemical, and Photocatalytic Applications," *Applied Surface Science* **293** (2014): 229-247, https://doi.org/10.1016/j.apsusc.2013.12.140.

[271] W. Yuan, J. Yuan, J. Xie, and C. M. Li, "Polymer-Mediated Self-Assembly of TiO_2@Cu_2O Core−Shell Nanowire Array for Highly Efficient Photoelectrochemical Water Oxidation," *ACS Applied Materials & Interfaces* **8** (2016): 6082−6092, https://doi.org/10.1021/acsami.6b00030.

[272] T. Gao, T.-T. Li, X. Liao, J.-H. Lin, B.-C. Shiu, and C.-W. Lou, "Construction of Cu_2O/TiO_2 Heterojunction Photoelectrodes for Photoelectrochemical Determination of Glucose," *Journal of Materials Research and Technology* **21** (2022): 798-809, https://doi.org/10.1016/j.jmrt.2022.09.043.

[273] J. Wang, G. Ni, W. Liao, K. Liu, J. Chen, F. Liu, Z. Zhang, M. Jia, J. Li, J. Fu, E. Pensa, L. Jiang, Z. Bian, E. Cortés, and M. Liu, "Subsurface Engineering Induced Fermi Level De-Pinning in Metal Oxide Semiconductors for Photoelectrochemical Water Splitting," *Angewandte Chemie International Edition* **62** (2023): e202217026, https://doi.org/10.1002/anie.202217026.

[274] J. Bisquert, F. Fabregat-SantiagoIván, I. Mora-Seró, G. Garcia-Belmonte, and S.

Giménez, “Electron Lifetime in Dye-Sensitized Solar Cells: Theory and Interpretation of Measurements,” *The Journal of Physical Chemistry C* **113** (2009): 17278–17290, https://doi.org/10.1021/jp9037649.

[275] M. Fazil, S. M. Alshehri, Y. Mao, and T. Ahmad, “Enhanced Photo/Electrocatalytic Hydrogen Evolution by Hydrothermally Derived Cu-Doped TiO_2 Solid Solution Nanostructures,” *Langmuir* **40** (2024): 4063–4076, https://doi.org/10.1021/acs.langmuir.3c02860.

[276] K. Iizuka, T. Kumeda, K. Suzuki, H. Tajiri, O. Sakata, N. Hoshi, and M. Nakamura, “Tailoring the Active Site for the Oxygen Evolution Reaction on a Pt Electrode,” *Communications Chemistry* **5** (2022): 126, https://doi.org/10.1038/s42004-022-00748-7.

[277] X. Xu, G. Zhou, X. Dong, and J. Hu, “Interface Band Engineering Charge Transfer for 3D MoS_2 Photoanode to Boost Photoelectrochemical Water Splitting,” *ACS Sustainable Chemistry & Engineering* **5** (2017): 3829–3836, https://doi.org/10.1021/acssuschemeng.6b02883.

[278] F. Niu, D. Wang, F. Li, Y. Liu, S. Shen, and T. J. Meyer, “Hybrid Photoelectrochemical Water Splitting Systems: From Interface Design to System Assembly,” *Advanced Energy Materials* **10** (2020): 1900399, https://doi.org/10.1002/aenm.201900399.

[279] M. Miyauchi, H. Irie, M. Liu, X. Qiu, H. Yu, K. Sunada, and K. Hashimoto, “Visible-Light-Sensitive Photocatalysts: Nanocluster-Grafted Titanium Dioxide for Indoor Environmental Remediation,” *The Journal of Physical Chemistry Letters* **7** (2016): 75-84, https://doi.org/10.1021/acs.jpclett.5b02041.

[280] X. Chen, H. Cheng, R. Shi, T. Zhou, T. He, and Q. Liu, “Recent Advances in Data-Driven Design of Dual-Atom Catalysts,” Advanced Functional Materials 36 (2026): 202510647, https://doi.org/10.1002/adfm.202510647.

[281] J. Bai and B. Zhou, "Titanium Dioxide Nanomaterials for Sensor Applications," *Chemical Reviews* 114 (2014): 10131–10176, **https://doi.org/10.1021/cr400625j.**

[282] C. Ghosh, A. Dey, and I. Biswas, "CuO–TiO_2 Based Self-Powered Broad Band Photodetector," *Nano Materials Science* 6 (2024): 345–354, https://doi.org/10.1016/j.nanoms.2023.11.003.

List of Research Publications:

1. ***D. Kumar***, A. Mishra, Shubham, Hemant, S. Bhattacharjee, R. R. Urkude, B. Ghosh, A. Bhaumik, A. K. Sinha*, A.S.K. Sinha and V. Amoli*, "Highly Asymmetric Cu_{SA}-O_v-Ti_{3c} Atomic Sites Catalyst for Unprecedented Solar Hydrogen Generation," ***Advanced Energy Materials, 2024, 14, 2401964 (Impact Factor 27.8),*** https://doi.org/10.1002/aenm.202401964.

2. ***D. Kumar,*** Hemant, A. K. Verma, Siddhi Agrawal, Jaswant Singh Bhati, Shubham, Shikha Singh, Vipin Amoli*, "Defect-Induced Band Bending Mitigation Enables Bias and Photo-assisted Cathodic Response in Cu Single Atom Doped Faceted TiO_2 Thin Films Electrodes," ***ChemCatChem, 2026, 18, e70818 (Impact Factor 3.9),*** https://doi.org/10.1002/cctc.70818.

3. A. Mishra, V. Verma, A. Khan, ***D. Kumar***, T. S. Khan, V. Amoli*, A. K. Sinha*, "Waste Ilmenite Sludge-derived Low-cost Mesoporous Fe-doped TiO_2: A Versatile Photocatalyst for Enhanced Visible Light Photocatalysis Without a Cocatalyst," ***Journal of Environmental Chemical Engineering, 2023, 11, 110319 (Impact Factor 7.7),*** https://doi.org/10.1016/j.jece.2023.110319.

4. P. K. Prajapati, D. Garg, A. Malik, ***D. Kumar***, V. Amoli, S. L Jain*, "A Novel Ternary Metal Oxide Cascade Z-scheme Heterojunction for Efficient CO_2 Photoconversion Without a Co-catalyst," ***Journal of Environmental Chemical Engineering, 2023, 10, 108147 (Impact Factor 7.7),*** https://doi.org/10.1016/j.jece.2022.108147.

5. Akash Mandal, Neelanjana Ghosh, Bhabani Malakar, ***Dileep Kumar***, Vipin Amoli*, Asim Bhaumik*, Biswajit Chowdhury*, "Efficient Synthesis of Propylene Carbonate over Bimetallic Fe-Cu/SBA-15 Catalyst from CO_2 and Propylene Oxide,"***Asian Journal of Organic Chemistry 2025, 10, 202500432 (Impact Factor 2.7),*** https://doi.org/10.1002/ajoc.202500432.

6. Hemant, Shubham, ***Dileep Kumar***, Chaitanya Yadav, Pushkar Raj, Amandeep, Vipin Amoli*, "Highly Deformable and Durable PEDOT:PSS Printed Electrodes via Tailored Chemistry and Fabrication Synergy for Scalable Wearable Electronics,"

Advanced Materials Technologies, 2025, 0, e01625 (Impact Factor 6.2), https://doi.org/10.1002/admt.202501625.

Conferences:

1. International conference on Shaping the Energy Future: Challenges and Opportunities (SEFCO) at CSIR-IIP, Dehradun, India (April 23-25, 2025).
   Oral Presentation: Single-atom Cu doped TiO_2 photocatalyst for Photocatalytic Hydrogen Generation.

2. CoE International Conference Molecular Materials and Functions at IIT Madars, India (December 9 – 11, 2024).
   Poster Presentation: Strategic Doping of Single Atom in High Energy Faceted Nanostructures (SA-HEF) for Unprecedented Hydrogen Generation.

Academic Visits:

1. CSIR–Indian Institute of Petroleum for conducting density functional theory (DFT) calculations and gaining experimental support in photocatalytic studies.
2. Raja Ramanna Centre for Advanced Technology, Indore for beamline experiments.
3. Indian Institute of Technology, Delhi for carrying out in-situ EPR experiments.